



ISSN 2959-0663 (Print)  
ISSN 2959-0671 (Online)  
ISSN-L 2959-0663

# EURASIAN JOURNAL OF CHEMISTRY

2025. Vol. 30 No. 3(119)

**Special Issue**

## TRACK-ETCHED MEMBRANES: Future Prospects, Opportunities and Challenges

**Guest Editors:**

Anastassiya A. Mashentseva, Alexander N. Nechaev,  
Murat Barsbay, Pavel Yu. Apel



ISSN 2959-0663 (Print)  
ISSN 2959-0671 (Online)  
ISSN-L 2959-0663

# EURASIAN JOURNAL OF CHEMISTRY

**2025**

**Volume 30, No. 3 (119)**

**Special Issue**

## **Track-Etched Membranes: Future Prospects, Opportunities and Challenges**

**Guest Editors: *Anastassiya A. Mashentseva, Alexander N. Nechaev, Murat Barsbay,  
Pavel Yu. Apel***

September 30<sup>th</sup>, 2025

Founded in 1996

Published 4 times a year

Karaganda  
2025

**Publisher: Karagandy University of the name of academician E.A. Buketov**

*Postal address:* 28, Universitetskaya Str., Karaganda, 100024, Kazakhstan

E-mail: [chemistry.vestnik@ksu.kz](mailto:chemistry.vestnik@ksu.kz);  
[irina.pustolaikina@ksu.kz](mailto:irina.pustolaikina@ksu.kz);  
[ipustolaikina@gmail.com](mailto:ipustolaikina@gmail.com)

Tel./fax: +7(7212) 34-19-40.

Web-site: <https://ejc.buketov.edu.kz>

*Guest Editors*

- A.A. Mashentseva,** Professor, PhD, Head of the Technological Track-Etched Membranes Laboratory, Institute of Nuclear Physics of the Republic of Kazakhstan, Almaty (Kazakhstan);
- A.N. Nechaev,** Candidate of Chemical Sciences, Deputy Head of the Centre of Applied Physics, Joint Institute for Nuclear Research, Dubna, Moscow region (Russia);
- M. Barsbay,** Professor, PhD, Department of Chemistry, Hacettepe University, Beytepe Campus, Kimya Bolumu, Ankara (Turkiye);
- P.Yu. Apel,** Doctor of Chemical Sciences, Head of Centre of Applied Physics, Flerov Laboratory of Nuclear Reactions, Joint Institute for Nuclear Research, Dubna, Moscow region (Russia)

*Editor-in-Chief*

**Ye.M. Tazhbayev,** Doctor of Chemical sciences

*Executive Editor*

**I.A. Pustolaikina,** Candidate of Chemical sciences

*Editorial board*

- Z.M. Muldakhmetov,** Academician of NAS RK, Doctor of chem. sciences, Institute of Organic Synthesis and Coal Chemistry of the Republic of Kazakhstan, Karaganda (Kazakhstan);
- S.M. Adekenov,** Academician of NAS RK, Doctor of chem. sciences, International Research and Production Holding "Phytochemistry", Karaganda (Kazakhstan);
- S.E. Kudaibergenov,** Doctor of chem. sciences, Institute of Polymer Materials and Technologies, Almaty (Kazakhstan);
- V. Khutoryanskiy,** Professor, University of Reading, Reading (United Kingdom);
- Fengyun Ma,** Professor, Xinjiang University, Urumqi (PRC);
- Xintai Su,** Professor, South China University of Technology, Guangzhou (PRC);
- R.R. Rakhimov,** Doctor of chem. sciences, Norfolk State University, Norfolk (USA);
- N. Nuraje,** Associate Professor, Nazarbayev University, Astana (Kazakhstan);
- S.A. Beznosyuk,** Doctor of phys.-math. sciences, Altai State University, Barnaul (Russia);
- B.F. Minaev,** Doctor of chem. sciences, Bohdan Khmelnytsky National University of Cherkasy, Cherkasy (Ukraine);
- I.V. Kulakov,** Doctor of chem. sciences, University of Tyumen (Russia);
- R.P. Bhole,** PhD, Associate Professor, Dr. D.Y. Patil Institute of Pharmaceutical Sciences and Research, Sant Tukaram Nagar, Pimpri, Pune (India);
- S.S. Gurav,** PhD, Professor, Goa College of Pharmacy, Panaji (India);
- A.A. Atakhanov,** Doctor of techn. sciences, Institute of Polymer Chemistry and Physics, Tashkent (Uzbekistan);

<b>I.V. Korolkov,</b>	PhD, Associated Professor, Astana branch, Institute of Nuclear Physics of the Republic of Kazakhstan, Astana (Kazakhstan);
<b>A.M. Makasheva,</b>	Doctor of techn. sciences, Zh. Abishev Chemical-Metallurgical Institute, Karaganda (Kazakhstan);
<b>M.I. Baikenov,</b>	Doctor of chem. sciences, Karagandy University of the name of acad. E.A. Buketov (Kazakhstan);
<b>L.K. Salkeeva,</b>	Doctor of chem. sciences, Karagandy University of the name of acad. E.A. Buketov (Kazakhstan);
<b>G.I. Dzhardimalieva,</b>	Doctor of chem. sciences, Federal Research Center of Problems of Chemical Physics and Medicinal Chemistry, Russian Academy of Sciences, Chernogolovka, Moscow Region (Russia);
<b>S.K. Filippov,</b>	PhD, Project Leader, DWI-Leibniz Institute for Interactive Materials, Aachen, North Rhine-Westphalia, (Germany);
<b>S.A. Ivasenko,</b>	Doctor of pharm. sciences, Karaganda Medical University (Kazakhstan).

*Proofreader* I.N. Murtazina

*Computer layout* V.V. Butyaikin

**Eurasian Journal of Chemistry. — 2025. — Vol. 30, No. 3(119). — Special Issue “Track-Etched Membranes: Future Prospects, Opportunities and Challenges”. — 154 p.**

**ISSN 2959-0663 (Print). ISSN 2959-0671 (Online). ISSN-L 2959-0663**

Proprietary: NLC “Karagandy University of the name of academician E.A. Buketov”.

Registered by the Ministry of Information and Social Development of the Republic of Kazakhstan. Re-registration certificate No. KZ95VPY00063697 dated 30.01.2023.

Signed in print 30.09.2025. Format 60×84 1/8. Offset paper. Volume 19,25 p.sh. Circulation 200 copies. Price upon request. Order № 126.

Printed in the Publishing house of NLC “Karagandy University of the name of academician E.A. Buketov”. 28, University Str., Karaganda, 100024, Kazakhstan. Tel.: +7(7212) 35-63-16. E-mail: izd\_karu@buketov.edu.kz

© Karagandy University of the name of academician E.A. Buketov, 2025



---

# CONTENTS

## PREFACE

<i>Mashentseva, A.A., Nechaev, A.N., Barsbay, M., &amp; Apel, P.Yu.</i> Preface to the Special Issue “Track-Etched Membranes: Future Prospects, Opportunities and Challenges” .....	5
---	---

## ADVANCED REVIEWS ON TEMs

<i>Sütekin, S.D., Rakisheva, S.R., Mashentseva, A. A., &amp; Barsbay, M.</i> A Mini Review on Track-etched Membranes Potential for Sensors Development.....	7
<i>Rossouw, A., Petrik, L.F., Nechaev, A.N., &amp; Apel, P.Yu.</i> Advancing Functionalized Track-Etched Membranes: Composite and Hybrid Materials through the JINR–South Africa Partnership .....	23

## MODIFICATION AND DEVELOPMENT OF NEW TYPES OF TEMs

<i>Kryukova-Seliverstova, A.V., Orelovich, O.L., Altynov, V.A., Akimov, A.V., Shmakov, A.S., Nikolskaya, D.V., Kirilkin, N.S., &amp; Pinaeva, U.V.</i> Radiation Grafting of PVDF Track-Etched Membranes: A Study for Nanoscale Pore Functionalization.....	40
<i>Yeszhanov, A.B., Korolkov, I.V., &amp; Zdorovets, M.V.</i> Graft Polymerization of Octadecyl Acrylate on PET Track-Etched Membranes for Direct Contact Membrane Distillation .....	56
<i>Ponomar, M.A., Sarapulova, V.V., Guliaeva, V.V., Apel, P.Yu., &amp; Pismenskaya, N.D.</i> Transport Properties of Cation-Exchange Membranes Obtained by Pore Filling of Track-Etched Membranes with Perfluorosulfonic Acid Polymer .....	65
<i>Shakayeva, A.Kh., Omertasov, D.D., Zhatkanbayeva, Zh.K., Zhumazhanova, A.T., Zdorovets, M.V., &amp; Korolkov, I.V.</i> Graft Polymerization of Allylamine for the Modification of PET Track-Etched Membrane.....	85

## PROSPECTIVE APPLICATIONS OF TEMs

<i>Mitrofanov, A.V., Apel, P.Yu., Ivanov, O.M., &amp; Pudonin, F.A.</i> A New Application of Track-Etched Membranes in X-Ray and Vacuum Ultraviolet Optics.....	93
<i>Balyasin, M.V., Serpionov, G.V., Krashennnikov, M.E., Lyundup, A.V., &amp; Nechaev, A. N.</i> Biological Compatibility of Polyethylene Terephthalate Track Membranes: Growth, Proliferation, and Viability of Cells in Culture Systems .....	99
<i>Bedin, S.A., Kozhina, E.P., Doludenko, I.M., &amp; Drachev, V.P.</i> Track-Etched Membranes for Gold Nanowire SERS Substrates .....	110

## TEMs BASED COMPOSITES AND ITS PRACTICAL APPLICATIONS



<i>Drozhzhin, N.A., Ponomareva, O.Yu., Vinogradov, I.I., Serpionov, G.V., Kanet, A., Nikolskaya, D.V., &amp; Vershinina, T.N.</i> Nickel (II) Based Metal-Organic Framework Consolidated on Nanofibers Modified Track-Etched Membrane for Dye Removal.....	118
<i>Rakisheva, S.R., Nurpeisova, D.T., Zhumabayev, A.M., Parmanbek, N., Barsbay, M. &amp; Mashentseva, A.A.</i> Galvanic Replacement-Assisted Synthesis of Cu–Ag Composite Membrane Catalysts for Potassium Ferricyanide Reduction .....	129
<i>Andreev, E.V., Fadeikina, I.N., Mutali, A.K., &amp; Kukushkin, V.I.</i> Comparison of SERS Effect on Composite Track-Etched Membranes with Silver Nanostructures Obtained by Vacuum Deposition and Chemical Synthesis .....	143

## PREFACE

Editorial

Received: 9 September 2025 | Published online: 20 September 2025

<https://doi.org/10.31489/2959-0663/3-25-0>

Anastassiya A. Mashentseva<sup>1</sup>, Alexander N. Nechaev<sup>2</sup>,  
Murat Barsbay<sup>3\*</sup>, Pavel Yu. Apel<sup>2</sup>

<sup>1</sup>*Institute of Nuclear Physics of the Republic of Kazakhstan, Almaty, Kazakhstan;*

<sup>2</sup>*Joint Institute for Nuclear Research, Dubna, Moscow region, Russia;*

<sup>3</sup>*Department of Chemistry, Hacettepe University, Ankara, Türkiye*

(\*Corresponding author's e-mail: [mbarSBay@hacettepe.edu.tr](mailto:mbarSBay@hacettepe.edu.tr))

### Preface to the Special Issue “Track-Etched Membranes: Future Prospects, Opportunities and Challenges”

Track-etched membranes (TeMs) represent a unique class of materials whose precise pore geometry and adaptable surface chemistry have made them indispensable in many areas of modern science and technology. Originally developed as filters for biological and analytical applications, they are now widely recognized as versatile functional platforms in separation processes, energy devices, sensors, and biomedical technologies. Their ability to combine reproducible nanoscale structure with tunable chemical modification explains the sustained interest in this field and provides the motivation for this Special Issue.

The present volume brings together contributions that reflect both the maturity of TeM research and the ongoing search for new directions. It includes **two review articles**. The first offers a concise overview of the potential of TeMs in sensor development, highlighting how controlled pore structures can be integrated into devices for highly sensitive detection. The second review, prepared within the framework of an international collaboration, discusses the progress in functionalized composite and hybrid membranes, emphasizing the role of TeMs as reliable supports for advanced materials. Together, these articles provide context and perspective for the original works presented in this collection.

A central part of this Special Issue is devoted to the **modification and development of new types of TeMs**. The papers in this section describe radiation-induced pore-confined grafting of PVDF membranes, graft polymerization of long-chain acrylates on PET membranes for distillation applications, and the preparation of cation-exchange membranes by pore filling with perfluorosulfonic acid polymers. Other contributions examine the functionalization of PET membranes with amine-containing polymers. These studies collectively illustrate the wide range of strategies now available for tailoring TeMs at the nanoscale, with direct implications for transport behavior and selectivity.

The collection also includes contributions under the theme of **prospective applications**. Here, the use of TeMs is explored in fields that extend well beyond their traditional role in filtration. Examples include the design of membranes for X-ray and vacuum ultraviolet optics, studies of the biological compatibility of PET membranes in cell culture systems, and the use of TeMs as substrates for surface-enhanced Raman scattering (SERS) with gold nanowires. These works underscore the breadth of application spaces where TeMs are proving to be effective and reliable.

A further group of papers focuses on **TeM-based composites**. These include the immobilization of nickel-based metal–organic frameworks on modified TeMs for dye removal, the preparation of copper–silver composite catalysts supported on TeMs for electrochemical reduction processes, and comparative studies of SERS effects on composite membranes with silver nanostructures obtained by different fabrication routes.

Such examples highlight how the intrinsic structure of TeMs can be combined with functional materials to generate composites with enhanced catalytic and sensing properties.

Taken together, the contributions in this Special Issue document the steady progress of TeM research, from methodological advances in membrane modification to the demonstration of new applications in diverse areas. They also reflect the collaborative and international nature of the field, with studies carried out by research groups from various countries, such as Kazakhstan, Russia, South Africa, and Türkiye.

It is a privilege to present this Special Issue to the scientific community. We hope that the collection of articles will be of value to researchers working with membranes, nanostructured materials, and applied technologies, and that it will serve as a reliable source of current knowledge in this dynamic and interdisciplinary area.

#### *Information about Guest Editors\**

---

*\*The editors' names are presented in the following order: First Name, Middle Name and Last Name*



**Anastassiya Alexandrovna Mashentseva** — Prof., PhD, Head of the Technological Track-etched Membranes Laboratory, The Institute of Nuclear Physics of the Republic of Kazakhstan, Ibragimov street, 1, 050032 Almaty, Kazakhstan; e-mail: [a.mashentseva@inp.kz](mailto:a.mashentseva@inp.kz); <http://orcid.org/0000-0003-4393-5845>



**Alexander Nikolaevich Nechaev** — Candidate of Chemical Sciences, Deputy Head of Centre of Applied Physics, Joint Institute for Nuclear Research, Dubna, Joliot-Curie street 6, 141980, Moscow region, Russian Federation; e-mail: [nechaeffalexander@yandex.ru](mailto:nechaeffalexander@yandex.ru); <https://orcid.org/0000-0002-5138-4265>



**Murat Barsbay** (*corresponding author*) — Prof., PhD, Department of Chemistry, Hacettepe University, Beytepe Campus, Kimya Bolumu, 06800, Beytepe, Ankara, Türkiye; e-mail: [mbarsbay@hacettepe.edu.tr](mailto:mbarsbay@hacettepe.edu.tr); <https://orcid.org/0000-0003-0788-4446>



**Pavel Yurievich Apel** — Doctor of Chemical Sciences, Head of Centre of Applied Physics, Flerov Laboratory of Nuclear Reactions, Joint Institute for Nuclear Research, Dubna, Joliot-Curie street 6, 141980, Moscow region, Russian Federation; e-mail: [apel@jinr.ru](mailto:apel@jinr.ru); <https://orcid.org/0000-0003-1259-163X>

## ADVANCED REVIEWS ON TEMs

Review

Received: 27 May 2025 | Revised: 21 August 2025 |  
Accepted: 3 September 2025 | Published online: 21 September 2025

UDC 544.42+519.242.7

<https://doi.org/10.31489/2959-0663/3-25-12>

Semiha D. Sütekin<sup>1</sup>, Saniya R. Rakisheva<sup>2, 3\*</sup>,  
Anastassiya A. Mashentseva<sup>2, 3</sup>, Murat Barsbay<sup>1</sup>

<sup>1</sup>Department of Chemistry, Hacettepe University, Ankara, Türkiye;

<sup>2</sup>Institute of Nuclear Physics of the Republic of Kazakhstan, Almaty, Kazakhstan;

<sup>3</sup>Department of Nuclear Physics, New Materials, and Technologies,  
L.N. Gumilyov Eurasian National University, Astana, Kazakhstan

(\*Corresponding author's e-mail: [saniya.rakisheva58@gmail.com](mailto:saniya.rakisheva58@gmail.com))

### A Mini Review on Track-Etched Membranes Potential for Sensors Development

Track-etched membranes (TEMs) have emerged as a promising class of nanostructured materials for the development of advanced sensing platforms. Owing to their highly uniform pore architecture, controllable dimensions, and versatile surface chemistry, TEMs can be used to create highly sensitive, selective, and robust sensors. This review provides a comprehensive overview of recent advances in the use of TEMs for sensor development, with a particular emphasis on functionalization strategies and application domains. The review discusses stimuli-responsive TEMs in detail which are capable of dynamic switching in response to environmental triggers such as pH, temperature, light, or redox. Functional nanochannels engineered through various modifications, such as polymer grafting or metal-organic frameworks incorporation, exhibit unique ionic transport behaviors suitable for real-time detection and biomimetic sensing. TEMs have also shown considerable potential in the detection of toxic metal ions, where tailored chemical groups and hybrid interfaces enable sub-ppb sensitivity in complex matrices. Furthermore, their capacity to host biomolecules like DNA probes, antibodies, or enzymes opens avenues for biosensing applications, including clinical diagnostics, virus detection, and neurotransmitter detecting. Additionally, their integration into wearable devices highlights their potential for flexible, real-time health monitoring. Challenges related to large-scale manufacturing, long-term stability, and standardization remain and are addressed in this review. Looking forward, TEMs have potential to bridge the gap between lab-scale innovation and practical sensor technologies, offering solutions for environmental, biomedical, and industrial applications.

**Keywords:** track-etched membranes (TEMs), composite track-etched membranes (CTEMs), biosensors, hybrid membranes, functional nanomaterials, stimuli-responsive materials

#### Content

##### Review Plan

- 1 Introduction
- 2 Track-Etched Membranes Potential for Sensors Development
  - 2.1 Stimuli-Responsive Sensors Based on TEMs
  - 2.2 Inorganic Pollutants Detection with TEMs
  - 2.3 TEM-Based Biosensors
- 3 Conclusions
- References



**Semiha Duygu Sütekin** is a PhD (2016) and Assistant Professor in Polymer Chemistry since 2023. Dr. Sütekin's research interests include controlled radical polymerization techniques for the synthesis of polymeric nanostructures, the functionalization of polymeric membranes, suitably designed for environmental applications as well as controlled drug delivery systems. In particular, she has conducted extensive studies on the controlled functionalization of track-etched membranes and their utilization as catalysts.



**Saniya Rakisheva** is 3<sup>rd</sup> year PhD student in the "Nanomaterials and Nanotechnologies" major at the Eurasian National University named after L.N. Gumilyov. Since 2025, she has been an engineer of the technological track-etched membranes laboratory in the Astana branch of the Institute of Nuclear Physics of the Republic of Kazakhstan. Saniya Rakisheva's research interests include functionalization of track-etched membranes, development of biodegradable polymeric track-etched membranes, as well as development of composite track-etched membranes for environmental applications.



**Anastassiya Alexandrovna Mashentseva** is a PhD (2011) and Associate Professor (2017) in Chemistry, Full Professor in Nanotechnology (2023). Since 2011, she has been leading the technological track-etched membranes laboratory in the Astana branch of the Institute of Nuclear Physics of the Republic of Kazakhstan, providing expert guidance and leadership in research endeavours. Professor Mashentseva has conducted extensive research in the field of materials science and nanomaterials, with a particular focus on their environmental applications. The primary areas of scientific research also involve pioneering the development of new, promising applications of polymer track-etched membranes in water purification processes using catalysis and sorption methods, as well as the creation of all-solid-state supercapacitors based on track-etched membranes.



**Murat Barsbay** is a PhD (2009) and Associate Professor (2014) in Polymer Chemistry, Full Professor in Chemistry (2021). Professor Murat Barsbay's research centers on radiation-induced polymerization and polymer surface modification, with a strong focus on controlling structure and functionality at the nano- and micro-scale. His expertise covers the design and fabrication of radiation-grafted membranes, nanogels, and other functional polymer materials, achieved through advanced grafting and cross-linking techniques. Building on this core competency, he has developed applications in energy storage, including all-solid-state supercapacitors; biomedical technologies, such as nano-sized drug carriers and antimicrobial surfaces; environmental remediation through adsorptive and catalytic polymeric materials; and sustainable materials based on radiation-modified natural polymers. He has led numerous national and international research projects, and continues to contribute to advancing polymer science through both fundamental studies and application-driven innovations.

### *Review Plan*

**Inclusion and Exclusion Criteria:** This review summarises the latest advancements (mainly 2021–2025) in TeM-based sensors for detecting organic/inorganic analytes. Foundational studies from 2001 to 2012 are also included to provide historical context. Over 63 peer-reviewed articles were selected from Scopus, Web of Science, and Google Scholar using the following keywords: track-etched membranes, biosensors, heavy metal detection, composite TeMs, and stimuli-responsive sensors. Emphasis was placed on functionalization techniques, sensor mechanisms, and applications, excluding non-peer-reviewed sources or studies lacking experimental validation.

The review begins with an introduction that highlights the significance of TeMs in modern sensor technology. It highlights the limitations of conventional sensors, such as low sensitivity, slow response times,

and instability under varying conditions, and explains how TeMs address these challenges through their unique structural and chemical properties.

The main body is divided into three thematic subsections, each exploring a critical aspect of TeM-based sensors. Section 2.1 presents stimuli-responsive sensors, emphasizing how TeMs can be engineered to react dynamically to pH, temperature, and chemical stimuli. Case studies, such as poly-L-lysine (PLL)-modified PET nanochannels, illustrate how these membranes mimic biological ion channels, enabling precise control over ionic transport. The discussion extends to light- and redox-responsive systems, including azobenzene-functionalized metal-organic frameworks (MOFs), which exhibit high on-off ratios for ion gating. Section 2.2 shifts focus to TeMs for inorganic pollutant detection, particularly heavy metals like  $\text{Pb}^{2+}$ ,  $\text{Cd}^{2+}$ , and  $\text{Cu}^{2+}$ . It critiques traditional analytical methods (e.g., ICP-MS) for their cost and complexity, contrasting them with TeM-based electrochemical sensors that offer portability and sub-ppb detection limits. Notable examples include grafted membranes and interpolyelectrolyte complexes, which enhance adsorption and signal amplification. The section also addresses challenges, such as interference from competing ions, and proposes solutions like selective chelating ligands. Section 2.3 explores biosensing applications, showcasing TeMs' versatility in immobilizing enzymes, antibodies, and DNA probes. Examples range from dopamine detection using poly(3-aminobenzylamine)-functionalized nanochannels to SARS-CoV-2 antibody monitoring with optical-fiber-integrated membranes. The subsection highlights innovations in real-time monitoring, such as wearable TeM-based sensors for physiological signals, while acknowledging limitations like the need for Raman spectrometers in certain SERS-based designs.

The Conclusion summarises these themes, reiterating the advantages of TeMs, such as modularity, stability, and scalability, while identifying unresolved challenges, such as the sophisticated fabrication method. It calls for future research into low-cost fabrication methods and biocompatible compositions to enable commercialization. The section ends by envisioning TeMs as foundational tools for next-generation diagnostics and environmental sensors, particularly in resource-limited settings.

### *1 Introduction*

Polymers materials have demonstrated extraordinary potential across scientific and technological applications due to their versatile chemical structures and tunable physical properties [1–3]. Among these, stimuli-responsive “smart” polymers stand out for their ability to dynamically alter their behavior in response to environmental changes, finding applications in drug delivery, actuators, and sensing systems [4–8]. Particularly promising are porous polymer membranes, where controlled nanostructuring can amplify these responsive behaviors. Track-etched membranes (TeMs) represent a unique class of such materials, fabricated by irradiating polymer films with accelerated heavy ions followed by selective chemical etching [9–11]. This precise fabrication method creates membranes with uniform, well-defined nanopores (typically 10–1000 nm in diameter) while maintaining excellent mechanical stability [12–14]. The combination of high surface area, tailorable pore geometry, and narrow size distribution makes TeMs ideal substrates for integrating smart functionalities through functionalization with various ligands or grafting of monomers [15–18]. Critically, their abundant surface chemistry allows extensive functionalization with responsive polymers, nanoparticles, and biomolecules, creating hybrid systems that merge the advantages of porous scaffolds with smart material responses [19–22].

The nanochannels within TeMs demonstrate unparalleled functionality in sensing applications due to their ability to precisely modulate ionic currents in response to diverse stimuli. By engineering the surface chemistry and physical properties of these nanochannels, researchers can create highly selective sensors capable of detecting targets ranging from small ions to complex biomolecules like DNA and proteins. For instance, single nanochannel systems have achieved extraordinary sensitivity in detecting trace biomarkers, such as liver cancer-associated microRNAs (miRNAs), with detection limits as low as 97.2 aM [23]. The dynamic “on-off” switching behavior of these nanochannels in response to molecular interactions enables real-time monitoring of biological processes, offering transformative potential for diagnostic and therapeutic applications [24]. This biomimetic gating mechanism, which closely resembles natural ion channel regulation, positions TeMs as ideal candidates for developing next-generation nanofluidic devices, including logic circuits and stimulus-responsive drug delivery systems [25, 26].

Stimuli-responsive sensors based on TeMs represent a significant advancement in functional materials engineering. Surface modification with responsive polymers such as poly(acrylic acid) (PAA), poly(N-isopropylacrylamide) (PNIPAM), or poly(L-lysine) (PLL) enables precise control over ionic transport in response to environmental changes in pH, temperature, or redox potential [27]. When combined with asym-



metric pore geometries (e.g., conical or bullet-shaped nanochannels), these functionalized TeMs exhibit advanced phenomena like current rectification and molecular gating, closely mimicking the sophisticated regulation observed in biological systems [28]. Their exceptional mechanical stability and chemical versatility make them robust platforms for real-time, in situ analysis of complex chemical and biological environments [29].

Beyond biomedical applications, TeMs show tremendous promise for environmental monitoring, particularly in detecting hazardous heavy metal ions. While conventional analytical techniques like ICP-MS offer high accuracy, their high cost, complex operation, and lack of portability limit widespread use [30]. In contrast, TeM-based sensors provide an attractive alternative, combining low cost, portability, and exceptional sensitivity. Functionalization with specific chelating groups (e.g., carboxyl, amine, or pyridyl moieties) enables selective preconcentration of toxic metals such as  $\text{Pb}^{2+}$ ,  $\text{Cd}^{2+}$ , and  $\text{Cu}^{2+}$ . When integrated with advanced electrochemical techniques like square wave anodic stripping voltammetry (SWASV), these systems achieve detection limits at parts-per-billion (ppb) and even sub-ppb levels. Furthermore, hybrid membranes incorporating nanoparticles demonstrate enhanced performance through improved electron transfer at the pore-electrolyte interface [31].

The biosensing applications of TeMs have attracted growing interest due to their exceptional capacity for precise surface engineering. By immobilizing biological recognition elements — including enzymes, nucleic acids, and antibodies — onto nanochannel surfaces, these membranes enable highly specific interactions with target analytes [32]. The combination of structural precision and chemical adaptability makes TeMs ideal scaffolds for constructing biosensing interfaces with superior selectivity, sensitivity, and customizability [33]. Recent innovations have further expanded their capabilities through incorporation of molecular imprinting techniques and metal-organic frameworks (MOFs), enabling detection of ultra-trace analytes in complex biological fluids. This modular design approach not only enhances performance but also facilitates integration with emerging technologies like lab-on-a-chip systems and wearable sensors [34, 35].

This review provides a focused examination of track-etched membrane (TeM)-based sensors, building upon our previous comprehensive analysis of composite TeM (CTeM) fabrication and functionalization techniques [36]. Rather than revisiting fundamental grafting methods or material synthesis, which were thoroughly covered in our prior review, we concentrate here on three groundbreaking sensor applications: (1) stimuli-responsive systems exploiting pH-, temperature-, and chemically-triggered nanochannel gating mechanisms, (2) inorganic pollutants, e.g. heavy metal ions, detection platforms achieving sub-ppb sensitivity through interfacial engineering, and (3) advanced biosensors integrating biorecognition elements like enzymes, antibodies, and DNA probes. Through critical analysis of recent studies (2021–2025), we demonstrate how TeMs' nanoporous architecture enables unprecedented sensor performance, from biomimetic ionic rectification to single-molecule detection, while addressing limitations in stability and reproducibility. The discussion culminates in a forward-looking perspective on emerging hybrid designs (e.g., MOF-integrated TeMs, wearable sensor interfaces) and unmet challenges in scalable manufacturing and real-world deployment.

## *2 Track-Etched Membranes Potential for Sensors Development*

### *2.1 Stimuli-Responsive Sensors Based on TeMs*

Track-etched membranes (TeMs) featuring stimuli-responsive nanochannels have expanded the borders of sensor design by merging precision-engineered pores with environmentally adaptive materials. The nanochannels of TeMs can be tailored via surface modification to regulate ionic and molecular transport [36]. A notable example involves modifying PET-based conical nanopores with poly-L-lysine (PLL), a biocompatible polymer known for its sensitivity to pH and temperature. As shown in the work by Li et al., such PLL-functionalized nanopores exhibit a dual-responsive behavior, with their ionic conductance modulated by external stimuli [37]. The mechanism of operation relies on the transformation of surface charge characteristics within the nanochannels. Pristine PET nanopores typically display carboxyl groups on their inner surfaces, imparting a negative surface charge under neutral conditions. However, PLL modification converts these surfaces to amine-rich environments, which become protonated and positively charged at physiological pH values. This fundamental alteration in surface chemistry leads to a complete reversal of current rectification behavior, significantly expanding the operational range compared to unmodified nanopores [36]. Most remarkably, these modified nanopores exhibit sharp, reversible transitions between nonconductive (“OFF”) states at high pH (11.5) and elevated temperature (70 °C) to conductive (“ON”) states under lower pH or temperature conditions (Figure 1). The switching behavior shows exceptional reproducibility over multiple cycles,

maintaining >90 % of initial response amplitude after 50 switching events, making these systems highly suitable for applications requiring robust, repeatable performance.

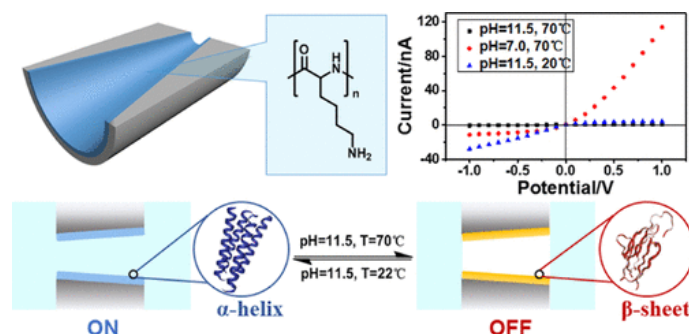


Figure 1. Chemical equilibrium of the PLL layer in nanopores of PET TEMs is associated with the pH-dependent behavior of PET TEMs. Adapted with permission from [37]. Copyright 2020 American Chemical Society OMEGA

Fluorescence-based TeM sensors represent another important class of responsive systems. Soto Espinoza et al. developed an innovative platform using track-etched PET membranes functionalized with fluorescent reporters [38]. While conventional fluorescein tags showed limited pH sensitivity in this configuration, Green Fluorescent Protein (GFP) demonstrated remarkable pH-dependent fluorescence changes across the physiologically relevant range of pH 4–8. The modification process, achieved through radical-initiated grafting polymerization, selectively altered the inner pore walls while preserving the bulk membrane properties. The resulting biosensor not only detected buffer pH with high accuracy but also successfully monitored pH changes in real-time during *E. coli* cell culture, demonstrating its potential for biological and microbiological applications.

For specific molecular recognition, Li's research group created an advanced glucose-sensing system using conical PET nanochannels functionalized with 3-aminobenzenboronic acid [39]. This design capitalized on the pH-dependent binding affinity of boronic acid moieties for glucose molecules. The fabrication process involved initial generation of carboxyl groups on the nanochannel surfaces through chemical etching, followed by covalent attachment of the sensing moieties via EDC/NHSS coupling chemistry. The resulting sensor exhibited exceptional selectivity for glucose, with minimal interference from common biological molecules like ascorbic acid and urea. The operational principle relies on reversible transitions between “on” and “off” states triggered by pH changes: glucose binding at neutral pH (7.38) decreases ionic current (“off” state), while acidic conditions (pH 4.45) release glucose and restore conductivity (“on” state). This system maintained stable performance through multiple cycles, demonstrating its potential for continuous glucose monitoring applications.

Multimodal sensing platforms achieved significant advancement through the work of Lou et al., who developed a “smart gate” nanochannel system combining electrical and optical detection modalities [40]. The design incorporated aggregation-induced emission (AIE) fluorophores that become highly fluorescent upon interaction with target molecules. In this system, 1,2-diphenylethene-1,2-diyl-*bis*(1,4-phenylene)-1,1'-diboronic acid (TPEDB) served as both the glucose recognition element and fluorescence reporter. The modification process involved UV irradiation and chemical etching of PET membranes, followed by sequential functionalization steps to create stable boronic acid recognition sites. When glucose molecules interact with these sites, they induce fluorophore aggregation, producing a strong fluorescence signal while simultaneously altering ionic current through the nanochannels (Figure 2). This dual-output system provided built-in signal verification, significantly enhancing detection reliability.

Recent advances in polyelectrolyte-modified TeMs by Wiedenhöft et al. demonstrated remarkable adsorption capabilities for environmental pollutants [41]. The study compared two polyelectrolytes — poly(2-acrylamido glycolic acid) (PAGA) and poly(N-acetyl dehydroalanine) (PNADha) — grafted onto PET track-etched membranes. PAGA-modified membranes exhibited particularly strong responses to both pH changes and  $\text{Cu}^{2+}$  ions, showing complete wettability transitions and efficient methylene blue adsorption following Langmuir isotherm behavior. These systems offer promising platforms for combined detection and removal of environmental contaminants.

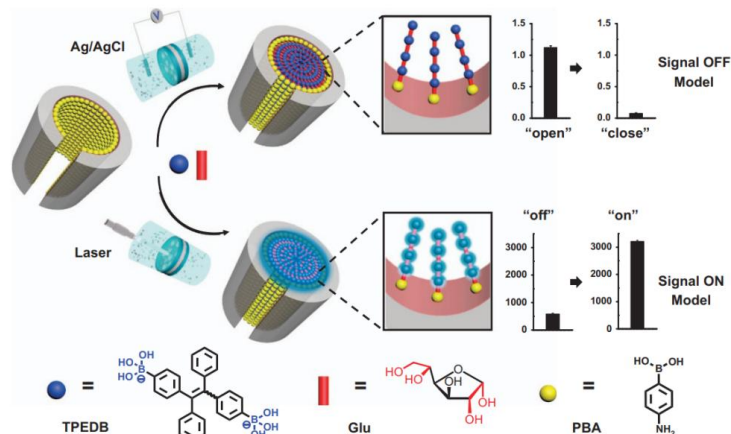


Figure 2. Fluorescent dual-signal-output nanochannels and ionic current during oligomerization. TPEDB interacts with glucose to form oligomers. PET membranes were UV-irradiated, etched, and then immobilized with 4-aminophenyl boronic acid. The sensor displayed high sensitivity and specific glucose recognition. Adapted with permission from [40]. Copyright 2020 NPG Asia Materials with license under CC BY 4.0

The integration of metal-organic frameworks (MOFs) with TeMs has pushed the boundaries of nanofluidic control. Qian et al. achieved unprecedented light-responsive gating by incorporating carboxylated azobenzene-coordinated MOFs (AZO-MOFs) into bullet-shaped PET nanochannels. The UiO-66-AZODC framework, built using azobenzene-4,4'-dicarboxylic acid (AZODC) ligands, demonstrated remarkable light-triggered conformational changes. Under illumination, these MOF-embedded nanochannels achieved staggering on-off ratios up to 40.2 — outperforming conventional AZO-modified systems by 30-fold. The in-situ growth technique used for MOF integration preserved nanochannel integrity while enabling sub-nanometer precision in ion transport control [42].

For ultrasensitive metal detection, Müller et al. developed peptide-functionalized nanopores capable of femtomolar  $\text{Cu}^{2+}$  sensing [43]. The system utilized conical nanopores whose inner surfaces were modified with peptides with strong specificity for copper ions. When exposed to  $\text{Cu}^{2+}$  ions in aqueous media, the ionic transport properties of the pores changed from exhibiting rectifying behavior to becoming selectively permeable to anions. This resulted in distinct, easily measurable changes in ionic current. Notably, the sensor performed reliably even in complex sample environments, such as synthetic urine, without being affected by other metal ions (Figure 3). To enhance accuracy, electrical signals were cross-validated with fluorescence-based measurements, yielding a robust sensing platform suitable for both clinical diagnostics and environmental analysis.

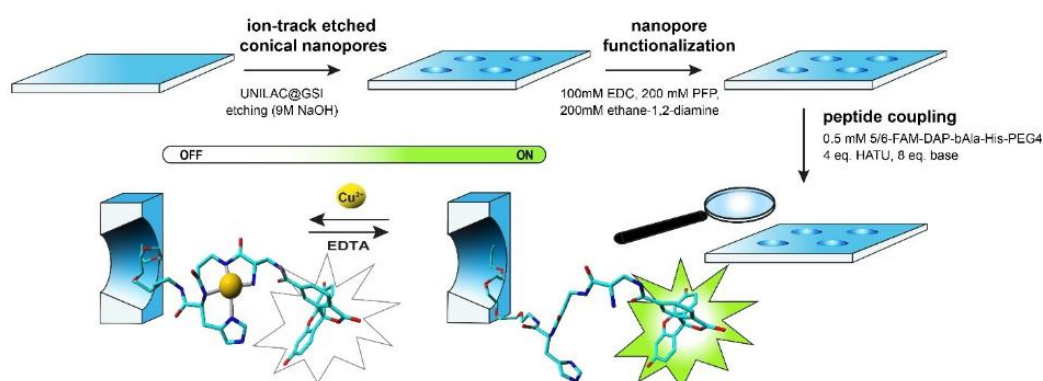


Figure 3. Design and composition of a copper sensor utilizing ion-track etched polyethylene terephthalate (PET) membranes. Adapted from [43]. Copyright (2020) with permission from Wiley-VCH Verlag GmbH & Co. KGaA

These developments highlight how stimuli-responsive track-etched membranes (TeMs) are changing sensor design by integrating precise control over nanofluidics with functional, adaptive surface functionalities. This field is open for further advancements, driven by continual improvements in sensitivity, selectivity, and long-term stability.

## 2.2 Inorganic Pollutant Detection with TeMs

Detecting hazardous heavy metals remains a pressing issue due to their long-term persistence and toxicological risks. Traditional analytical methods like inductively coupled plasma mass spectrometry (ICP-MS) and X-ray fluorescence spectroscopy (XRF) offer accuracy but are hindered by cost, complexity, and infrastructure demands. In contrast, TeM-based sensing approaches are gaining attention for their ability to combine nanoscale selectivity with operational simplicity. By leveraging tunable pore structures and chemical functionalization, TeMs may provide a low-cost and portable alternative for detecting trace metals with high sensitivity.

A pivotal advancement in this field was demonstrated by Shang et al., who engineered asymmetric conical nanochannels in PET films using track-etching techniques [44]. These nanochannels exhibited ionic current rectification due to their geometric asymmetry and surface charge effects, preferentially transporting cations from the narrow to the wide end under applied potential. To achieve selective  $\text{Pb}^{2+}$  detection, the researchers sputter-coated the nanochannel surfaces with gold, enabling subsequent immobilization of the '8-17' DNAzyme through Au-thiol bonding. X-ray photoelectron spectroscopy (XPS) confirmed the successful DNAzyme functionalization, while electrochemical measurements revealed exceptional selectivity for  $\text{Pb}^{2+}$  over competing metal ions, with no observable interference. The sensor demonstrated remarkable stability under varying environmental conditions, outperforming protein-based nanopore systems in robustness. This work established an important paradigm for combining nanofluidic phenomena with biomolecular recognition elements for heavy metal sensing.

Composite track-etched membranes (CTeMs) represent a sophisticated evolution of conventional TeMs, incorporating secondary phases such as metal/metal oxide nanoparticles or carbon-based materials to enhance functionality. These hybrid structures typically consist of a polymeric membrane matrix integrated with nanostructured inorganic components, creating synergistic effects that improve sensitivity and selectivity. While some CTeMs employ physical deposition methods, others utilize advanced grafting techniques to covalently attach functional polymers to the pore walls, followed by a modification step with inorganic functionalities [14]. A notable example is the work by Bessbousse et al., who developed  $\beta$ -poly(vinylidene fluoride) ( $\beta$ -PVDF) track-etched membranes functionalized with poly(acrylic acid) (PAA) brushes for ultrasensitive  $\text{Pb}^{2+}$  detection [45]. To fabricate the sensor, carboxyl groups were first introduced onto the inner surface of the nanochannels through chemical etching, and the sensing molecules were subsequently attached via EDC/NHSS coupling chemistry. The resulting device showed high selectivity for glucose, with minimal interference from typical biological compounds such as ascorbic acid and urea. Its operation relies on reversible switching between "on" and "off" states driven by pH changes: at physiological pH (around 7.4), glucose binds to the boronic acid groups, leading to a reduced ionic current ("off" state), whereas at acidic pH (around 4.5), glucose is released and the ionic conductivity is restored ("on" state). The system demonstrated reliable and effective performance using square wave anodic stripping voltammetry (SWASV) demonstrated sub-parts-per-billion (ppb) detection limits across repeated cycles, making it a promising candidate for continuous glucose monitoring applications.

The same research group later advanced this technology significantly by implementing reversible addition-fragmentation chain-transfer (RAFT) polymerization for controlled PAA grafting within  $\beta$ -PVDF nanochannels. Through RAFT-mediated polymerization, they achieved precise control over grafting densities (5–63 % degree of grafting, DOG), as confirmed by comprehensive characterizations [46]. Size exclusion chromatography and AFM analysis verified the controlled nature of the RAFT process, showing uniform polymer brush growth along pore walls. Interestingly, pore diameter was found to decrease systematically with increasing DOG, with complete pore filling occurring beyond ~40 wt% DOG. The RAFT-derived membranes exhibited superior performance when transformed into functionalized membrane electrodes with gold coatings. In SWASV measurements, these RAFT-prepared sensors demonstrated nearly threefold higher sensitivity at sub-ppb  $\text{Pb}^{2+}$  concentrations compared to conventional free-radically grafted counterparts. This enhancement was attributed to the more uniform and controllable distribution of PAA brushes within the nanochannels, optimizing both metal ion binding capacity and subsequent electrochemical detection efficiency. These developments underscore how controlled polymerization techniques like RAFT can unlock new potential in TeM-based sensors. Controlled surface modification methods such as RAFT-mediated graft copolymerization allow for precise tuning of polymer brush structures within nanochannels, including adjustments to chain length and grafting density. These carefully modified surfaces can significantly enhance properties like adsorption capacity, electrochemical response, and fluid flow behavior. As techniques for surface modification continue to progress, the improvements in sensitivity and selectivity will follow. Integrat-

ing these approaches with advanced electrode materials and tailored pore geometries could further boost performance.

Another example of multicomponent graft copolymer-modified TeMs was reported by Zdorovets et al., who employed UV-induced graft copolymerization technique to functionalize PET TeMs with PAA and poly(4-vinylpyridine) (P4VPy) [47]. This approach enabled the creation of membranes with tailored chelating properties, where AA provided carboxyl groups for cation exchange, while 4-VPy introduced nitrogen-containing ligands for enhanced metal coordination. The optimal performance was achieved with copolymer-grafted membranes (PET TeMs-g-P4VPy/PAA), which demonstrated exceptional sensitivity toward  $\text{Cu}^{2+}$  ( $0.74 \mu\text{g/L}$ ),  $\text{Pb}^{2+}$  ( $1.13 \mu\text{g/L}$ ), and  $\text{Cd}^{2+}$  ( $2.07 \mu\text{g/L}$ ) through SWASV measurements (Figure 4). The platinum-coated electrodes ensured reproducible signal transduction, while the grafted polymer layers significantly improved metal ion adsorption efficiency compared to unmodified TeMs.

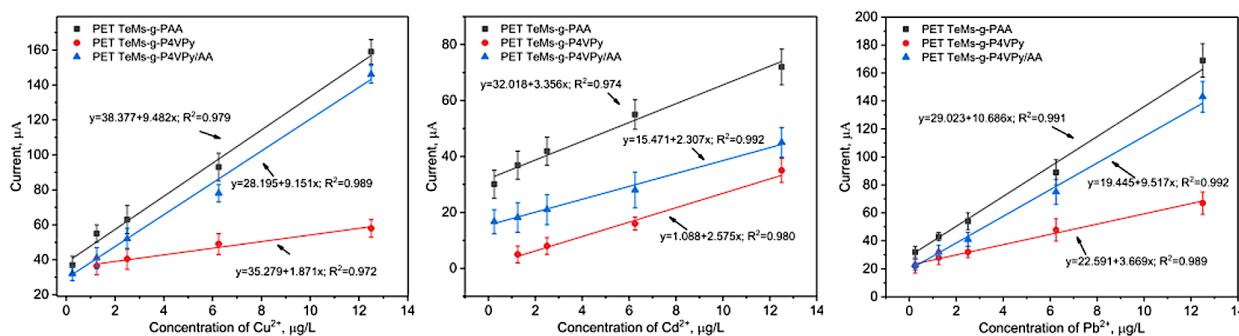


Figure 4. Calibration curves of peak currents for  $\text{Cu}^{2+}$ ,  $\text{Cd}^{2+}$ , and  $\text{Pb}^{2+}$  concentration for the square wave anodic stripping voltammetry after 30 min of adsorption in appropriate heavy metal ion solution in 0.1 M sodium acetate electrolyte. Adapted from [47]. Copyright (2019) with permission from MDPI under CC BY 4.0 license

Another recent advance in this field was demonstrated by Zhumanazar et al. through the implementation of RAFT polymerization for precisely controlled grafting of poly(methacrylic acid) (PMAA) on PET track-etched membranes [48]. Unlike conventional grafting approaches, the RAFT technique enabled exact tuning of polymer brush characteristics within the nanochannels, as illustrated in Figure 5. This controlled functionalization strategy proved critical for optimizing both the binding capacity for  $\text{Cd}^{2+}$  ions and the subsequent electrochemical response characteristics [48].

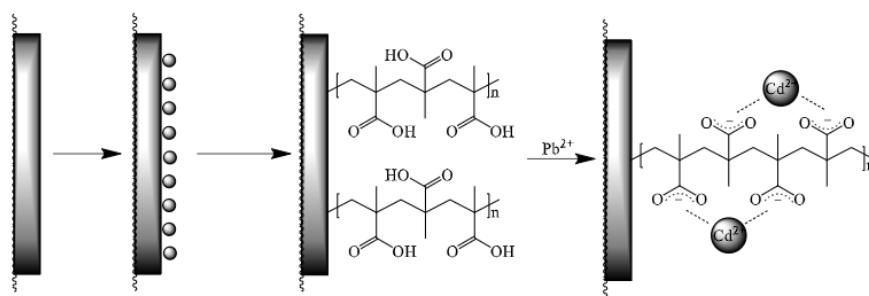


Figure 5. Modification of PET TeM with PMAA. Adapted from [48]. Copyright (2021) with permission from NNC RK Bulletin under CC BY 4.0 license

The sensor fabrication followed a dual-phase approach: First, the RAFT-mediated PMAA grafting created a uniform network of carboxyl groups along the pore walls, serving as selective binding sites for cadmium ions. Subsequently, magnetron sputtering deposited a 40–50 nm gold layer on both membrane surfaces, transforming the entire structure into a high-performance working electrode while maintaining nanochannel accessibility, like previous works [47, 49, 50]. The gold coating allowed flexible configuration, with one side serving as cathode and the other as anode during measurements. The detection protocol involved three carefully optimized stages: (1) 30-minute preconcentration in  $\text{Cd}^{2+}$  solutions ( $0.5\text{--}12.5 \text{ mg/L}$ ), (2) electrodeposition at  $-1 \text{ V}$  for 60 s (vs.  $\text{Ag/AgCl}$  reference) to enhance  $\text{Cd}^0$  accumulation, and (3) anodic stripping voltammetry ( $-1$  to  $+1 \text{ V}$  scan) yielding a distinct oxidation peak at  $-0.7 \text{ V}$  corresponding to  $\text{Cd}^0 \rightarrow \text{Cd}^{2+}$  conversion.

The PMAA-grafted membranes demonstrated tenfold improved sensitivity ( $\text{LOD} = 0.5 \text{ mg/L}$ ,  $R^2 = 0.98$ ) compared to unmodified TeMs ( $\text{LOD} = 5.01 \text{ mg/L}$ ,  $R^2 = 0.985$ ).

Building upon these developments, Korolkov et al. explored photograft polymerization of methacrylic acid (MAA) followed by interpolyelectrolyte complex formation with poly(allylamine) (PAIAm) to further enhance sensor performance [51]. The resulting membranes exhibited a threefold improvement in  $\text{Pb}^{2+}$  detection limits ( $1.25 \text{ }\mu\text{g/L}$ ) compared to unmodified TeMs ( $3.03 \text{ }\mu\text{g/L}$ ), attributed to the synergistic effects of the carboxyl-rich PMAA brushes and the amine-containing PAIAm complexes. This work underscored the importance of multilayer surface engineering in optimizing heavy metal ion sensors.

Collectively, these studies demonstrate the remarkable versatility of TeM-based sensors for environmental monitoring. Through strategic combinations of nanochannel engineering, surface functionalization, and electrochemical detection methods, researchers have achieved promising sensitivity and selectivity for toxic metal ions. The ongoing development of surface modification techniques, well-defined grafting methods, hybrid nanomaterials, and optimized detection protocols continues to push the boundaries of what's possible in this critical field, offering promising solutions for real-world environmental and biomedical applications.

### 2.3 TeM-Based Biosensors

Biosensors based on TeMs have become an emerging tool in analytical research, merging the well-defined structure of nanochannels with selective biorecognition functionalities. The ability to decorate membrane pores with biologically active components, such as nucleic acid sequences, enzymes, or antibodies, has unlocked applications in diagnostics, environmental monitoring, and food safety. These biofunctionalized interfaces offer high specificity and can be adapted for both electrochemical and optical detection platforms. Their structural uniformity and chemical modification potential position TeMs as highly adaptable scaffolds for tailored biosensing devices.

An important study by Laucirica et al. represents a significant advancement in neurotransmitter detection technology through their development of a dopamine-responsive iontronic device [52]. This innovative biosensor utilized bullet-shaped single nanochannels in PET membranes that were carefully functionalized with poly(3-aminobenzylamine) (PABA). The key innovation lies in the PABA modification, which introduces pH-sensitive amino-pendant groups along the inner channel surface. These functional groups enable remarkable reversible switching of charge carrier selectivity — shifting from anion-dominated transport under acidic conditions to cation-selective behavior in basic environments. The biosensor demonstrated exceptional performance in dopamine (DA) detection, achieving sub-nanomolar sensitivity while maintaining excellent specificity against common interferents like ascorbic acid and urea. The working mechanism involves dopamine molecules binding to the immobilized PABA chains, which subsequently alters the nanochannel's current rectification properties in a concentration-dependent manner. Detailed binding analysis revealed a clear correlation between rectification efficiency and dopamine concentration, following a well-defined binding isotherm model. This system not only provides a robust platform for neurotransmitter monitoring but also establishes a generalizable approach for developing other neurotransmitter-specific biosensors.

Ali et al. developed an ingenious chiral biosensor platform using modified conical PET nanopores [53]. Their design creatively combines mussel-inspired surface chemistry with protein-based molecular recognition. The fabrication process involves steps of polydopamine (PDA) coating through immersion in dopamine solution ( $2 \text{ mg/mL}$  in Tris buffer,  $\text{pH } 8.5$ ) and covalent immobilization of bovine serum albumin (BSA) via Michael addition between PDA's benzoquinone groups and BSA's amine residues ( $2 \text{ mg/mL}$  in PBS,  $\text{pH } 8.0$ ). The current-voltage profiles of these modified nanochannels change markedly upon L-tryptophan binding over a concentration range of  $100 \text{ }\mu\text{M}$  to  $1.5 \text{ mM}$ , while showing negligible response to the D-enantiomer or other amino acids. This configuration highlights the potential of TeM-based biosensors for enantioselective detection in pharmaceutical and biochemical analysis.

The field of immunological detection has seen remarkable advances through TeM-based architectures. Ahlawat et al. developed a sophisticated microfluidic electrochemical biosensor using gold-coated polycarbonate TeMs [54]. This system features a multi-layered design where the gold nanolayer is first modified through thiol chemistry, followed by EDC/NHS coupling to immobilize anti-mesothelin antibodies. The biosensor's performance is exceptional, detecting mesothelin antigen across an astonishing concentration range from  $100 \text{ ng/mL}$  down to  $10 \text{ attograms/mL}$  ( $\text{ag/mL}$ ). Sensitivity analysis revealed pore-size dependent detection capabilities, with  $50\text{-nm}$  pores achieving  $0.011 \text{ ag mL}^{-1} \text{ cm}^{-1}$  sensitivity, while  $80\text{-nm}$  and  $100\text{-nm}$  pores



showed 0.027 and 0.017  $\text{ag mL}^{-1}\text{cm}^{-1}$ , respectively. The sensor's stability outperforms conventional electrochemical tools, maintaining consistent performance over extended operational periods.

Parallel work by Habtamu et al. demonstrated another innovative approach for antibody detection [33]. Their electrochemical immunosensor employs gold nanoelectrode ensembles (NEEs) assembled on polycarbonate track-etched membranes. The system utilizes tissue transglutaminase for capturing anti-tTG antibodies, followed by detection with HRP-labeled secondary antibodies in the presence of  $\text{H}_2\text{O}_2$ /hydroquinone. This design achieves a low detection limit of 1.8  $\text{ng/mL}$  for anti-tTG antibodies, with robust selectivity and reproducibility that matches traditional diagnostic methods for celiac disease. The platform's diagnostic accuracy, combined with its potential for miniaturization, makes it particularly valuable for clinical applications.

TeM biosensors have found unexpected applications in art conservation through the work of Gaetani et al. [55]. Their nanoelectrode ensemble platform was specifically designed to detect ovalbumin (OVA) in historical artworks, where it serves as a binding agent in photographic prints and tempera paintings. The detection mechanism involves capturing OVA from aqueous extracts, followed by reaction with glucose oxidase (GOx)-labeled anti-OVA antibodies. When exposed to glucose and a redox mediator, the system generates a characteristic electrocatalytic current. The voltammetric response shows distinct patterns — the mediator's redox peaks diminish while a new catalytic current appears, unambiguously indicating OVA presence. This method has proven particularly valuable for distinguishing between egg white and egg yolk tempera in artworks, providing art conservators with a reliable alternative to FTIR-ATR techniques.

Mizuguchi and colleagues have made significant contributions to flow-based TeM biosensors through two notable designs. Their first innovation was a dual-electrode coulometric detector for microbore HPLC [56]. The system uses platinum-sputtered track-etched membranes (0.40  $\mu\text{m}$  pores, 13 % porosity, 10  $\mu\text{m}$  thickness) arranged in alternating working (2 mm-wide) and counter (6 mm-wide) electrode configurations. The unique flow cell design, with a 0.1 mm diameter inlet channel, creates an extremely small detection volume (0.08 nL per electrode). This architecture achieves near-complete electrolysis conversion below 50  $\mu\text{L/min}$  flow rates, enabling sensitive detection of catecholamines — 0.1  $\mu\text{M}$  for noradrenaline and adrenaline, and 0.2  $\mu\text{M}$  for dopamine.

Their subsequent work introduced an enzyme-free uric acid biosensor using track-etched membrane electrodes (TEMEs) [57]. The system incorporates several innovative features: gold-sputtered TEMEs modified with acetylene black catalyst for enhanced sensitivity, and 2-aminoethanethiol-modified Au-TEMEs as pre-reactor electrodes to eliminate ascorbic acid interference. In flow-injection analysis mode, the biosensor achieves 0.6  $\mu\text{M}$  detection limits for uric acid, with excellent recovery rates in human urine samples. This design establishes an important precedent for non-enzymatic flow-based sensors with improved selectivity.

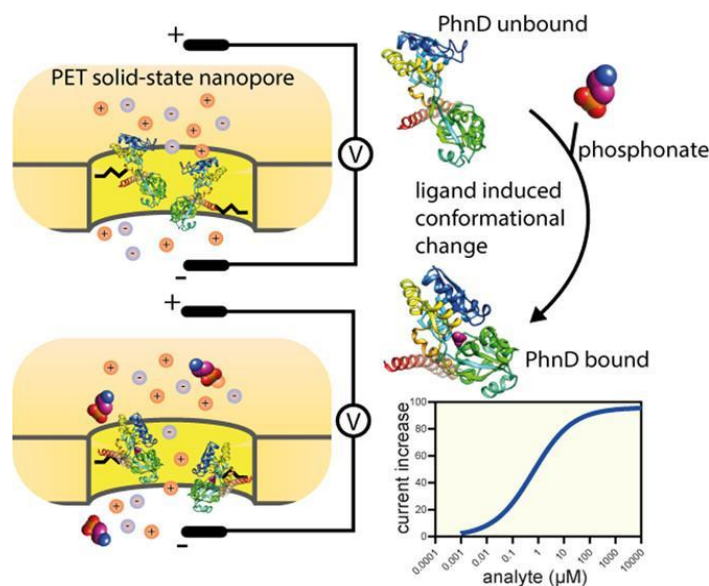


Figure 6. Electrical hybrid nanopore device integrating solid-state nanopores with bacterial binding proteins for the high-affinity detection of phosphonates. Adapted from [58].

Copyright (2020) with permission from American Chemical Society

Bernhard et al. developed a groundbreaking hybrid nanopore device that combines the best features of biological recognition and solid-state stability [58]. Their system integrates phosphonate-binding protein PhnD with P(DMAA-co-NMAS) polymers inside single PET nanopores (Figure 6). The sensor demonstrates remarkable affinity differences; 27 nM for 2-aminoethylphosphonate (2AEP) versus 373 nM for ethylphosphonate (EP). Compared to conventional ion chromatography or pulsed amperometric detection, this approach improves detection limits by factors of 100-1000. The device operates by producing distinct current changes when target phosphonates bind to the immobilized PhnD, enabling real-time monitoring with high specificity. This work represents a significant step toward practical, miniaturized electrical devices for environmental monitoring.

The non-enzymatic glucose sensor developed by Shakaeva et al. demonstrates the versatility of the TeM platform [59]. The fabrication involves multiple sophisticated steps: initial grafting of 2-hydroxyethyl-methacrylate (HEMA), formation of polyelectrolyte complexes with poly(allylamine) (PAIAm), and functionalization with 4-mercaptophenylboronic acid (MPBA). The MPBA's B-OH groups interact with glucose, while its thiol groups anchor gold nanoparticles deposited via magnetron sputtering. Square wave voltammetry analysis reveals a linear response from 0.1 mM to 8 mM glucose, with 0.1 mM detection limits ( $R^2 = 0.999$ ). The sensors demonstrate excellent reproducibility and selectivity against metal ions and ascorbic acid, performing reliably in complex matrices like apple juice and human serum.

The Kukushkin research group has made significant contributions to viral detection through their innovative work on aptamer-functionalized track-etched membranes [56, 57]. Their initial study [60] investigated the robustness of aptamer-coated membranes with nanostructured silver layers for influenza A/B virus detection. While the SERS-active silver nanoislands showed promising enhancement properties, they demonstrated limited stability in biological fluids following aptamer functionalization and virus exposure. Detailed analysis revealed that the strong binding affinity between influenza A viruses and their specific aptamers actually compromised sensor stability; the virus-aptamer interaction energy exceeded the adhesion forces between nanoparticles and membrane surface, leading to displacement of aptamer-functionalized nanoparticles from the sensor interface.

To address these challenges, the team developed an improved chromium-silver coating architecture. This modified design significantly enhanced fluorescence signals from Cyanine-3-labeled aptamers, although it did not support SERS applications. The chromium interlayer improved coating adhesion and stability while maintaining the optical enhancement properties crucial for detection. Building on these findings, Kukushkin et al. subsequently refined their approach through a redesigned aptasensor configuration [61]. The key innovation involved transitioning from two separate aptamers to a single, double-labeled aptamer molecule incorporating both thiol anchoring groups and Cyanine-3 fluorescent reporters. This simplified architecture provided several advantages, including reduced system complexity by eliminating intermolecular coupling effects, enhanced reproducibility through more consistent aptamer orientation, and potential for lower detection limits by minimizing non-specific interactions. The study systematically investigated optimal approaches for presenting SERS-active compounds at the membrane interface and characterized analyte-induced changes in both surface-enhanced Raman and fluorescence spectra. These investigations confirmed the sensor's ability to detect influenza A virus with remarkable sensitivity, achieving limits of detection (LOD) 10–100 times lower than conventional RT-PCR methods. The platform offers exceptional value for rapid testing applications, with estimated costs around \$0.50 per test and significantly streamlined procedural requirements compared to standard diagnostic methods. However, the current requirement for Raman spectroscopy readout remains a limitation for point-of-care deployment.

A comprehensive 2020 review highlighted significant advancements in developing protein-based nanotubes (NTs) for applications in molecule capture, enzyme reactions, and virus/bacteria trapping [62]. The review particularly emphasized the advantages of layer-by-layer (LbL) assembly techniques using nanoporous polycarbonate (PC) membranes as templates. Komatsu (2020) stressed that the wet-template-assisted LbL procedure offers unparalleled flexibility in designing each layer of the nanotube structure. This approach was successfully implemented in several groundbreaking studies, including one focusing on Hepatitis B virus (HBV) trapping [63]. Researchers developed human serum albumin (HSA)-based nanotubes with HBsAb antibodies incorporated in the outer layer, using poly-L-arginine (PLA) as an intermediate layer. This architecture achieved an exceptional 99.9 % trapping ratio after incubation. Similar impressive results were obtained for bacterial capture, with the system demonstrating -7 log reduction for *E. coli* and -5.0 log reduction for influenza A virus [64, 65]. These studies collectively illustrate the powerful synergy between

biological recognition elements and engineered material systems in creating advanced pathogen capture platforms.

The COVID-19 pandemic drove innovative adaptations of TeM technology, particularly in the development of the TEMFIS platform (track-etched microporous membrane filtration microplate with optical fiber immunosensing) for detecting SARS-CoV-2 neutralizing antibodies (NAbs) [66]. This sophisticated system combines several key components: a track-etched microporous membrane filtration microplate for sample processing, optical fibers for signal transmission, and a smartphone-based reader platform. The surrogate virus neutralization test developed on the TEMFIS platform (TEMFIS-sVNT) showed very high performance in practice. It delivered highly consistent results, with low variability between runs (intra-assay CV under 9 %, inter-assay CV under 14 %), and demonstrated strong clinical sensitivity. It detected antibodies in 92.68 % of COVID-19 patients and 76 % of vaccinated individuals. Impressively, it showed 100 % specificity in healthy controls. Unlike conventional methods such as ELISA-based sVNT or pseudovirus neutralization tests, this system doesn't require live viruses or cell cultures, which simplifies things greatly. It runs as a single-step procedure and works well in portable formats, making it ideal for point-of-care testing. Not only does it meet the urgent demand for quick and reliable immunity checks after infection or vaccination, but it also holds promise for broader use in detecting immunity against other infectious diseases down the line.

A recent example in TeM biosensor technology involves innovative wearable applications addressing critical challenges in skin-interfaced sensors, as demonstrated by Zhao et al. [67]. Their research focuses on developing high-performance, breathable electronic interfaces using precisely engineered track-etched membranes. The fabrication process employs controlled ion bombardment techniques to create membranes with smooth surfaces and precisely adjustable pore structures, enabling fine control over permeability, functionality, and durability. Membranes with pore diameters around 12.6  $\mu\text{m}$  exhibit superior breathability and moisture management, with air flow ( $190.6 \text{ mm}\cdot\text{s}^{-1}$ ) and water vapor transmission ( $2051 \text{ g}\cdot\text{m}^{-2}\cdot\text{day}^{-1}$ ) rates surpassing many commercial alternatives. These properties outperform many commercial membranes, enabling the development of comfortable, on-skin sensors for continuous physiological monitoring. These sensors can effectively monitor body movements and capture bioelectrical signals like ECG for heart activity and EMG for muscle function. Their ability to manage heat and wick away sweat makes them more suitable for extended use.

In diagnostics, TeMs have shown strong potential for detecting nucleic acids. When modified with DNA or RNA probes, their narrow channels improve molecular interactions, enabling highly sensitive detection of disease markers. This makes them useful for early diagnosis, point-of-care tests, and liquid biopsies. TeMs have also been used to detect proteins, neurotransmitters, and pathogens. During the COVID-19 pandemic, they enabled fast and accurate antibody testing, showing their value in urgent health situations. Going forward, efforts should focus on improving fabrication and standardization to bring these sensors from the lab to real-world applications.

### 3 Conclusions

Track-etched membranes (TeMs) have demonstrated remarkable potential as versatile sensing platforms, combining precisely engineered nanoarchitectures with robust polymer matrices. Previous works consistently highlight three key advantages of TeM-based sensors: (1) exceptional modularity through diverse surface functionalization approaches, (2) outstanding chemical and mechanical stability across operational conditions, and (3) scalable fabrication potential from single-pore devices to large-area membranes. The demonstrated success of TeM-based systems across healthcare diagnostics, environmental monitoring, and industrial applications underscores their remarkable adaptability and performance reliability.

TeMs have a promising potential especially in biomedical fields, largely thanks to their natural biocompatibility and ability to work well with complex biological environments. By attaching DNA or RNA probes, protein-binding molecules, or even whole-cell capture elements, researchers have managed to create sensors that can detect various markers ranging from individual biomolecules to pathogens. Some of the most advanced TeM-based sensors can detect nucleic acids at attomolar concentrations, an impressive level of sensitivity that makes them ideal for early disease detection and precise diagnostics.

Despite these advancements, there are still some real-world challenges to address before these sensors become a part of everyday medical or commercial use. One major issue is keeping them stable and functional over long periods, especially in clinical or outdoor settings where conditions can vary. Another one is ensuring consistency; as biological elements like enzymes or aptamers are involved, small differences between batches can impact performance. Wearable formats have their own problems too, such as contamination, me-

chanical wear, and sweat can all degrade accuracy. Therefore, there's a clear need for antifouling surfaces and flexible but tough TeM materials.

To move forward, it's necessary to advance smart designs, scalable manufacturing methods, and tight integration with electronics. As this review highlighted, the scientific groundwork is already strong. With the right engineering, TeM-based sensors could have a big impact in fields ranging from healthcare to environmental monitoring. The coming years will be crucial for translating these promising laboratory achievements into tangible solutions that address real-world challenges in healthcare, environmental protection, and industrial quality control.

### Author Information\*

*\*The authors' names are presented in the following order: First Name, Middle Name and Last Name*

**Semiha Duygu Sütekin** — Asst. Prof., PhD, Department of Chemistry, Hacettepe University, Ankara 06800, Turkey; e-mail: [duygu@hacettepe.edu.tr](mailto:duygu@hacettepe.edu.tr); <https://orcid.org/0000-0002-4605-1116>

**Saniya Renatovna Rakisheva** (*corresponding author*) — engineer of the technological track-etched membranes laboratory, The Institute of Nuclear Physics of the Republic of Kazakhstan, Ibragimov street, 1, 050032 Almaty, Kazakhstan; e-mail: [saniya.rakisheva58@gmail.com](mailto:saniya.rakisheva58@gmail.com); <https://orcid.org/0000-0003-3618-4828>

**Anastassiya Alexandrovna Mashentseva** — Prof., PhD, head of the technological track-etched membranes laboratory, The Institute of Nuclear Physics of the Republic of Kazakhstan, Ibragimov street, 1, 050032 Almaty, Kazakhstan; e-mail: [a.mashentseva@inp.kz](mailto:a.mashentseva@inp.kz); <http://orcid.org/0000-0003-4393-5845>

**Murat Barsbay** — Prof., PhD, Department of Chemistry, Hacettepe University, Ankara 06800, Turkey; e-mail: [mbarsbay@hacettepe.edu.tr](mailto:mbarsbay@hacettepe.edu.tr); <https://orcid.org/0000-0003-0788-4446>

### Author Contributions

The manuscript was written through contributions of all authors. All authors have given approval to the final version of the manuscript. **CRedit**: **Semiha Duygu Sütekin** and **Saniya Renatovna Rakisheva** conceptualization, data curation, investigation, methodology, validation, visualization, writing-review & editing; **Anastassiya Alexandrovna Mashentseva** conceptualization, formal analysis, funding acquisition, resources, supervision, validation, writing-original draft, writing-review & editing; **Murat Barsbay** supervision, validation, writing-review & editing

### Acknowledgments

This study was funded by the Ministry of Science and Higher Education of the Republic of Kazakhstan (Grant No AP23487226).

### Declaration of Generative AI and AI-Assisted Technologies in the Writing Process

During the preparation of this work the authors used Grammarly in order to refine the language of the manuscript. After using this service, the authors reviewed and edited the content as needed and take full responsibility for the content of the publication.

### Conflicts of Interest

The authors declare no conflict of interest.

### References

- 1 Brighenti, R., Li, Y., & Vernerey, F. J. (2020). Smart Polymers for Advanced Applications: A Mechanical Perspective Review. *Frontiers in Materials*, 7, 548239. <https://doi.org/10.3389/fmats.2020.00196>
- 2 Dayyoub, T., Maksimkin, A. V., Filippova, O. V., Tcherdyntsev, V. V., & Telyshev, D. V. (2022). Shape Memory Polymers as Smart Materials: A Review. *Polymers* 2022, Vol. 14, Page 3511, 14(17), 3511. <https://doi.org/10.3390/POLYM14173511>
- 3 Alam, M. W., Islam Bhat, S., Al Qahtani, H. S., Aamir, M., Amin, M. N., Farhan, M., ... Souayeh, B. (2022). Recent Progress, Challenges, and Trends in Polymer-Based Sensors: A Review. *Polymers*, 14(11), 2164. <https://doi.org/10.3390/polym14112164>

- 4 Samir, A., Ashour, F. H., Hakim, A. A. A., & Bassyouni, M. (2022). Recent advances in biodegradable polymers for sustainable applications. *npj Materials Degradation* 2022 6:1, 6(1), 1–28. <https://doi.org/10.1038/s41529-022-00277-7>
- 5 Hou, W., Xiao, Y., Han, G., & Lin, J. Y. (2019). The Applications of Polymers in Solar Cells: A Review. *Polymers* 2019, Vol. 11, Page 143, 11(1), 143. <https://doi.org/10.3390/POLYM11010143>
- 6 Laftah, W. A., & Wan Abdul Rahman, W. A. (2025). Polymers for anti-fouling applications: a review. *Environmental Science: Advances*. <https://doi.org/10.1039/D5VA00034C>
- 7 Fattah-alhosseini, A., Chaharmahali, R., Alizad, S., Kaseem, M., & Dikici, B. (2024). A review of smart polymeric materials: Recent developments and prospects for medicine applications. *Hybrid Advances*, 5, 100178. <https://doi.org/10.1016/J.HYBADV.2024.100178>
- 8 Bratek-Skicki, A. (2021). Towards a new class of stimuli-responsive polymer-based materials — Recent advances and challenges. *Applied Surface Science Advances*, 4, 100068. <https://doi.org/10.1016/j.apsadv.2021.100068>
- 9 Lau, W. J., Ismail, A. F., Misdan, N., & Kassim, M. A. (2012). A recent progress in thin film composite membrane: A review. *Desalination*, 287, 190–199. <https://doi.org/10.1016/J.DESAL.2011.04.004>
- 10 Yu, M., Foster, A. B., Kentish, S. E., Scholes, C. A., & Budd, P. M. (2025). Recent progress in thin film composite membranes based on the polymer of intrinsic microporosity PIM-1: Preparation, properties and performance. *Journal of Membrane Science*, 722, 123844. <https://doi.org/10.1016/J.MEMSCI.2025.123844>
- 11 Wu, L., Song, Y., Xing, S., Li, Y., Xu, H., Yang, Q., & Li, Y. (2022). Advances in electrospun nanofibrous membrane sensors for ion detection. *RSC Advances*, 12(54), 34866–34891. <https://doi.org/10.1039/D2RA04911B>
- 12 Korolkov, I. V., Narmukhamedova, A. R., Melnikova, G. B., Muslimova, I. B., Yeszhanov, A. B., Zhatkanbayeva, Z. K., ... Zdorovets, M. V. (2021). Preparation of Hydrophobic PET Track-Etched Membranes for Separation of Oil–Water Emulsion. *Membranes* 2021, Vol. 11, Page 637, 11(8), 637. <https://doi.org/10.3390/MEMBRANES11080637>
- 13 Ma, T., Janot, J. M., & Balme, S. (2020). Track-Etched Nanopore/Membrane: From Fundamental to Applications. *Small Methods*, 4(9), 2000366. <https://doi.org/10.1002/smt.202000366>
- 14 Aimanova, N. A., Almanov, A. A., Alipoori, S., Barsbay, M., Zhumabayev, A. M., Nurpeisova, D. T., Mashentseva, A. A. (2025) Development of the all-solid-state flexible supercapacitor membranes via RAFT-mediated grafting and electrospun nanofiber modification of track-etched membranes. *RSC Advances*, 15(8), 6260–6280. <https://doi.org/10.1039/d4ra08055f>
- 15 Korolkov, I. V., Gorin, Y. G., Yeszhanov, A. B., Kozlovskiy, A. L., & Zdorovets, M. V. (2018). Preparation of PET track-etched membranes for membrane distillation by photo-induced graft polymerization. *Materials Chemistry and Physics*, 205, 55–63. <https://doi.org/10.1016/J.MATCHEMPHYS.2017.11.006>
- 16 Parmanbek, N., Sütekin, D. S., Barsbay, M., Mashentseva, A. A., Zheltov, D. A., Aimanova, N. A., ... Zdorovets, M. V. (2022). Hybrid PET Track-Etched Membranes Grafted by Well-Defined Poly(2-(dimethylamino)ethyl methacrylate) Brushes and Loaded with Silver Nanoparticles for the Removal of As(III). *Polymers*, 14(19), 4026. <https://doi.org/10.3390/polym14194026>
- 17 Barsbay, M., & Güven, O. (2014). Grafting in confined spaces: Functionalization of nanochannels of track-etched membranes. *Radiation Physics and Chemistry*, 105, 26–30. <https://doi.org/10.1016/J.RADPHYSICHEM.2014.05.018>
- 18 Shakayeva, A. K., Yeszhanov, A. B., Zhumazhanova, A. T., Korolkov, I. V., & Zdorovets, M. V. (2024). Fabrication of Hydrophobic PET Track-Etched Membranes using 2,2,3,3,4,4,4-Heptafluorobutyl Methacrylate for Water Desalination by Membrane Distillation. *EURASIAN JOURNAL OF CHEMISTRY*, 29(2 (114)), 81–88. <https://doi.org/10.31489/2959-0663/2-24-5>
- 19 Kececi, K. (2023). A Comparable Study of Single Stranded DNA Sensing Using Track-Etched Nanopore Sensors. *ChemistrySelect*, 8(37), e202302856. <https://doi.org/10.1002/slct.202302856>
- 20 Maity, S., & Tripathi, B. P. (2024). Nanostructured Zwitterionic Membranes: Harnessing Temperature-Responsive Microgels for Tunable Water Filtration and Molecular Separation. *ACS Applied Polymer Materials*, 6(1), 596–606. <https://doi.org/10.1021/acsapm.3c02234>
- 21 Apel, P. Y. (2025). Intersections of pore channels in track-etched polymer templates and membranes. *Materials Chemistry and Physics*, 339, 130681. <https://doi.org/10.1016/J.MATCHEMPHYS.2025.130681>
- 22 Apel, P. (2001). Track etching technique in membrane technology. *Radiation Measurements*, 34(1–6), 559–566. [https://doi.org/10.1016/S1350-4487\(01\)00228-1](https://doi.org/10.1016/S1350-4487(01)00228-1)
- 23 Zhang, S., Cheng, J., Shi, W., Li, K. -B., Han, D. -M., & Xu, J. -J. (2020). Fabrication of a Biomimetic Nanochannel Logic Platform and Its Applications in the Intelligent Detection of miRNA Related to Liver Cancer. *Analytical Chemistry*, 92(8), 5952–5959. <https://doi.org/10.1021/acs.analchem.0c00147>
- 24 Li, M., Xiong, Y., Lu, W., Wang, X., Liu, Y., Na, B., ... Qing, G. (2020). Functional Nanochannels for Sensing Tyrosine Phosphorylation. *Journal of the American Chemical Society*, 142(38), 16324–16333. <https://doi.org/10.1021/jacs.0c06510>
- 25 Li, J., An, P., Qin, C., Sun, C. L., Sun, M., Ji, Z., ... Xie, Y. (2020). Bioinspired dual-responsive nanofluidic diodes by poly-L-lysine modification. *ACS Omega*, 5(9), 4501–4506. <https://doi.org/10.1021/acsomega.9b03850>
- 26 Wang, J., Zhou, Y., & Jiang, L. (2021). Bio-inspired Track-Etched Polymeric Nanochannels: Steady-State Biosensors for Detection of Analytes. *ACS Nano*, 15(12), 18974–19013. <https://doi.org/10.1021/acsnano.1c08582>
- 27 Armstrong, J. A., Bernal, E. E. L., Yaroshchuk, A., & Bruening, M. L. (2013). Separation of ions using polyelectrolyte-modified nanoporous track-etched membranes. *Langmuir*, 29(32), 10287–10296. <https://doi.org/10.1021/la401934v>
- 28 Laucirica, G., Toum Terrones, Y., Cayón, V. M., Cortez, M. L., Toimil-Molares, M. E., Trautmann, C., ... Azzaroni, O. (2020). High-sensitivity detection of dopamine by biomimetic nanofluidic diodes derivatized with poly(3-aminobenzylamine). *Nanoscale*, 12(35), 18390–18399. <https://doi.org/10.1039/D0NR03634J>



- 29 Lalia, B. S., Kochkodan, V., Hashaikeh, R., & Hilal, N. (2013). A review on membrane fabrication: Structure, properties and performance relationship. *Desalination*, 326, 77–95. <https://doi.org/10.1016/J.DESAL.2013.06.016>
- 30 Esfahani, M. R., Aktij, S. A., Dabaghian, Z., Firouzjaei, M. D., Rahimpour, A., Eke, J., ... Koutahzadeh, N. (2019). Nano-composite membranes for water separation and purification: Fabrication, modification, and applications. *Separation and Purification Technology*, 213, 465–499. <https://doi.org/10.1016/j.seppur.2018.12.050>
- 31 Zhumanazar, N., Korolkov, I. V., Yeszhanov, A. B., Shlimas, D. I., & Zdorovets, M. V. (2023). Electrochemical detection of lead and cadmium ions in water by sensors based on modified track-etched membranes. *Sensors and Actuators A: Physical*, 354, 114094. <https://doi.org/10.1016/J.SNA.2022.114094>
- 32 Mizuguchi, H., Fujiki, S., Shibata, T., Oishi, M., Iiyama, M., Takayanagi, T., ... Yeh, M. H. (2023). A flow-based enzyme-free biosensor fabricated using track-etched membrane electrodes: Selective and sensitive detection of uric acid. *Sensors and Actuators B: Chemical*, 383, 133588. <https://doi.org/10.1016/J.SNB.2023.133588>
- 33 Habtamu, H. B., Not, T., De Leo, L., Longo, S., Moretto, L. M., & Ugo, P. (2019). Electrochemical Immunosensor Based on Nanoelectrode Ensembles for the Serological Analysis of IgG-type Tissue Transglutaminase. *Sensors*, 19(5), 1233. <https://doi.org/10.3390/s19051233>
- 34 Kozhina, E., Bedin, S., Martynov, A., Andreev, S., Piryazev, A., Grigoriev, Y., ... Naumov, A. (2023). Ultrasensitive Optical Fingerprinting of Biorelevant Molecules by Means of SERS-Mapping on Nanostructured Metasurfaces. *Biosensors*, 13(1), 46. <https://doi.org/10.3390/BIOS13010046/S1>
- 35 Zhao, J., Kan, Y., Chen, Z., Li, H., & Zhang, W. (2023). MOFs-Modified Electrochemical Sensors and the Application in the Detection of Opioids. *Biosensors 2023, Vol. 13, Page 284*, 13(2), 284. <https://doi.org/10.3390/BIOS13020284>
- 36 Mashentseva, A. A., Sutekin, D. S., Rakisheva, S. R., & Barsbay, M. (2024). Composite Track-Etched Membranes: Synthesis and Multifaced Applications. *Polymers*, 16(18), 2616. <https://doi.org/10.3390/polym16182616>
- 37 Li, J., An, P., Qin, C., Sun, C. L., Sun, M., Ji, Z., ... Xie, Y. (2020). Bioinspired dual-responsive nanofluidic diodes by poly-L-lysine modification. *ACS Omega*, 5(9), 4501–4506. <https://doi.org/10.1021/acsomega.9b03850>
- 38 Soto Espinoza, S., Aguiar, C., Richieri, F., & Grasselli, M. (2019). Track-etched membrane as fluorescence-based pH biosensor. *Reactive and Functional Polymers*, 135, 1–7. <https://doi.org/10.1016/j.reactfunctpolym.2018.11.018>
- 39 Sun, Z., Han, C., Wen, L., Tian, D., Li, H., & Jiang, L. (2012). pH gated glucose responsive biomimetic single nanochannels. *Chemical Communications*, 48(27), 3282. <https://doi.org/10.1039/c2cc17277a>
- 40 Xu, X., Zhao, W., Gao, P., Li, H., Feng, G., Zhao, Z., & Lou, X. (2016). Coordination of the electrical and optical signals revealing nanochannels with an ‘onion-like’ gating mechanism and its sensing application. *NPG Asia Materials*, 8(1), e234–e234. <https://doi.org/10.1038/am.2015.138>
- 41 Wiedenhöft, L., Elleithy, M. M. A., Ulbricht, M., & Schacher, F. H. (2021). Polyelectrolyte functionalisation of track etched membranes: Towards charge-tunable adsorber materials. *Membranes*, 11(7). <https://doi.org/10.3390/membranes11070509>
- 42 Qian, T., Zhao, C., Wang, R., Chen, X., Hou, J., Wang, H., & Zhang, H. (2021). Synthetic azobenzene-containing metal-organic framework ion channels toward efficient light-gated ion transport at the subnanoscale. *Nanoscale*, 13(41), 17396–17403. <https://doi.org/10.1039/D1NR04595D>
- 43 Müller, L. K., Duznovic, I., Tietze, D., Weber, W., Ali, M., Stein, V., ... Tietze, A. A. (2020). Ultrasensitive and Selective Copper(II) Detection: Introducing a Bioinspired and Robust Sensor. *Chemistry — A European Journal*, 26(39), 8511–8517. <https://doi.org/10.1002/chem.202001160>
- 44 Shang, Y., Zhang, Y., Li, P., Lai, J., Kong, X. -Y., Liu, W., ... Jiang, L. (2015). DNAzyme tunable lead(ii) gating based on ion-track etched conical nanochannels. *Chemical Communications*, 51(27), 5979–5981. <https://doi.org/10.1039/C5CC00288E>
- 45 Bessbousse, H., Nandhakumar, I., Decker, M., Barsbay, M., Cuscito, O., Lairez, D., ... Wade, Travis. L. (2011). Functionalized nanoporous track-etched  $\beta$ -PVDF membrane electrodes for lead(ii) determination by square wave anodic stripping voltammetry. *Analytical Methods*, 3(6), 1351. <https://doi.org/10.1039/c1ay05038a>
- 46 Barsbay, M., Güven, O., Bessbousse, H., Wade, T. L., Beuneu, F., & Clochard, M. -C. (2013). Nanopore size tuning of polymeric membranes using the RAFT-mediated radical polymerization. *Journal of Membrane Science*, 445, 135–145. <https://doi.org/10.1016/j.memsci.2013.05.029>
- 47 Zdorovets, M. V., Korolkov, I. V., Yeszhanov, A. B., & Gorin, Y. G. (2019). Functionalization of PET Track-Etched Membranes by UV-Induced Graft (co)Polymerization for Detection of Heavy Metal Ions in Water. *Polymers*, 11(11), 1876. <https://doi.org/10.3390/polym11111876>
- 48 Zhumanazar, N. N., Korolkov, I. V., Eszhanov, A. B., Shakayeva, A. Kh., Tashenov, A. K., & Zdorovets, M. V. (2021). Sensors Based on Track-Etched Membranes for Electrochemical Detection of Cadmium Ions. *NNC RK Bulletin*, (1), 4–8. <https://doi.org/10.52676/1729-7885-2021-1-5-8>
- 49 Omertassov, D. D., Shakayeva, A. Kh., Zhatkanbayeva, Z. K., Shakirzyanov, R. I., Zdorovets, M. V., Güven, O., Korolkov, I. V. (2025). HKUST-1 synthesis in PET Track-Etched membranes via conversion of deposited CU for carbon dioxide capture. *ACS Omega*, <https://doi.org/10.1021/acsomega.5c01493>
- 50 Bessbousse, H., Zran, N., Fauléau, J., Godin, B., Lemée, V., Wade, T., & Clochard, M. -C. (2016). Poly(4-vinyl pyridine) radiografted PVDF track etched membranes as sensors for monitoring trace mercury in water. *Radiation Physics and Chemistry*, 118, 48–54. <https://doi.org/10.1016/j.radphyschem.2015.03.011>
- 51 Korolkov, I. V., Zhumanazar, N., Gorin, Y. G., Yeszhanov, A. B., & Zdorovets, M. V. (2020). Enhancement of electrochemical detection of Pb<sup>2+</sup> by sensor based on track-etched membranes modified with interpolyelectrolyte complexes. *Journal of Materials Science: Materials in Electronics*, 31(22), 20368–20377. <https://doi.org/10.1007/s10854-020-04556-4>



- 52 Laucirica, G., Toum Terrones, Y., Cayón, V. M., Cortez, M. L., Toimil-Molares, M. E., Trautmann, C., ... Azzaroni, O. (2020). High-sensitivity detection of dopamine by biomimetic nanofluidic diodes derivatized with poly(3-aminobenzylamine). *Nanoscale*, 12(35), 18390–18399. <https://doi.org/10.1039/D0NR03634J>
- 53 Ali, M., Nasir, S., & Ensinger, W. (2016). Stereoselective detection of amino acids with protein-modified single asymmetric nanopores. *Electrochimica Acta*, 215, 231–237. <https://doi.org/10.1016/j.electacta.2016.08.067>
- 54 Ahlawat, S., Nehra, A., Pandey, V., & Singh, K. P. (2019). Gold-coated nanoporous polycarbonate track-etched solid platform for the rapid detection of mesothelin. *Ionics*, 25(4), 1887–1896. <https://doi.org/10.1007/s11581-018-2761-6>
- 55 Gaetani, C., Gheno, G., Borroni, M., De Wael, K., Moretto, L. M., & Ugo, P. (2019). Nanoelectrode ensemble immunosensing for the electrochemical identification of ovalbumin in works of art. *Electrochimica Acta*, 312(2019), 72–79. <https://doi.org/10.1016/j.electacta.2019.04.118>
- 56 Mizuguchi, H., Nishimori, D., Kuwabara, T., Takeuchi, M., Iiyama, M., & Takayanagi, T. (2020). Track-etched membrane-based dual-electrode coulometric detector for microbore/capillary high-performance liquid chromatography. *Analytica Chimica Acta*, 1102, 46–52. <https://doi.org/10.1016/j.aca.2019.12.045>
- 57 Mizuguchi, H., Fujiki, S., Shibata, T., Oishi, M., Iiyama, M., Takayanagi, T., ... Yeh, M. H. (2023). A flow-based enzyme-free biosensor fabricated using track-etched membrane electrodes: Selective and sensitive detection of uric acid. *Sensors and Actuators B: Chemical*, 383(February), 133588. <https://doi.org/10.1016/j.snb.2023.133588>
- 58 Bernhard, M., Diefenbach, M., Biesalski, M., & Laube, B. (2020). Electrical Sensing of Phosphonates by Functional Coupling of Phosphonate Binding Protein PhnD to Solid-State Nanopores. *ACS Sensors*, 5(1), 234–241. <https://doi.org/10.1021/acssensors.9b02097>
- 59 Shakayeva, A. Kh., Munasbaeva, K. K., Zhumazhanova, A. T., Zdorovets, M. V., & Korolkov, I. V. (2023). Electrochemical sensors based on modified track-etched membrane for non-enzymatic glucose determination. *Microchemical Journal*, 193, 109003. <https://doi.org/10.1016/j.microc.2023.109003>
- 60 Kukushkin, V. I., Kristavchuk, O. V., Zhdanov, G. A., Keshek, A. K., Gambaryan, A. S., Andreev, Y. V., ... Zavyalova, E. G. (2023). Aptasensors Based on Track-Etched Membranes Coated with a Nanostructured Silver Layer for Influenza A and B Virus Detection. *Bulletin of the Russian Academy of Sciences: Physics*, 87(2), 172–177. <https://doi.org/10.31857/S0367676522700375>
- 61 Kukushkin, V., Kristavchuk, O., Andreev, E., Meshcheryakova, N., Zaborova, O., Gambaryan, A., ... Zavyalova, E. (2023). Aptamer-coated track-etched membranes with a nanostructured silver layer for single virus detection in biological fluids. *Frontiers in Bioengineering and Biotechnology*, 10, 1076749. <https://doi.org/10.3389/fbioe.2022.1076749>
- 62 Komatsu, T. (2020). Protein-based smart microtubes and nanotubes as ultrasmall biomaterials. *Chemistry Letters*, 49(10), 1245–1255. <https://doi.org/10.1246/cl.200433>
- 63 Komatsu, T., Qu, X., Ihara, H., Fujihara, M., Azuma, H., & Ikeda, H. (2011). Virus Trap in Human Serum Albumin Nanotube. *Journal of the American Chemical Society*, 133(10), 3246–3248. <https://doi.org/10.1021/ja1096122>
- 64 Karch, H., Tarr, P. I., & Bielaszewska, M. (2005). Enterohaemorrhagic Escherichia coli in human medicine. *International Journal of Medical Microbiology*, 295(6–7), 405–418. <https://doi.org/10.1016/j.ijmm.2005.06.009>
- 65 Yuge, S., Akiyama, M., Ishii, M., Namkoong, H., Yagi, K., Nakai, Y., ... Komatsu, T. (2017). Glycoprotein Nanotube Traps Influenza Virus. *Chemistry Letters*, 46(1), 95–97. <https://doi.org/10.1246/cl.160805>
- 66 Wang, C., Wu, Z., Liu, B., Zhang, P., Lu, J., Li, J., ... Li, C. (2021). Track-etched membrane microplate and smartphone immunosensing for SARS-CoV-2 neutralizing antibody. *Biosensors and Bioelectronics*, 192(August), 113550. <https://doi.org/10.1016/j.bios.2021.113550>
- 67 Zhao, Y., Wang, T., Li, Y., Zhao, Z., Xue, J., & Wang, Q. (2024). Fabrication of Breathable Multifunctional On-Skin Electronics Based on Tunable Track-Etched Membranes. *ACS Applied Electronic Materials*, 6(2), 969–977. <https://doi.org/10.1021/acsaelm.3c01414>

Arnoux Rossouw<sup>1, 2\*</sup>, Leslie F. Petrik<sup>3</sup>, Alexander N. Nechaev<sup>1</sup>, Pavel Yu. Apel<sup>1</sup>

<sup>1</sup>Joint Institute for Nuclear Research, Dubna, Moscow region, Russia;

<sup>2</sup>Nelson Mandela University, Gqeberha, South Africa;

<sup>3</sup>University of the Western Cape, Bellville, South Africa

(\*Corresponding author's e-mail: [rossouw@jinr.ru](mailto:rossouw@jinr.ru))

## Advancing Functionalized Track-Etched Membranes: Composite and Hybrid Materials through the JINR–South Africa Partnership

Track-etched polymer membranes (TeMs) are precision porous materials widely applied in water purification, sensing, and catalysis. However, their practical use is limited by hydrophobicity, fouling, and lack of functional activity. The purpose of this review is to synthesize the outcomes of the long-standing collaboration between South African institutions and the Flerov Laboratory of Nuclear Reactions of the Joint Institute for Nuclear Research in Dubna, Russia (FLNR, JINR), highlighting their contribution to overcoming these challenges. The objective is to present a focused survey of advances in TeMs functionalization, contextualized within global progress, and to assess their implications for applied membrane science. The methodology involved a structured literature survey (2007–2025) across Scopus, Web of Science, and Google Scholar, combined with critical evaluation of collaborative outputs. Emphasis was placed on peer-reviewed studies of metal sputtering, chemical grafting, and electrospun nanofiber composites. Results indicate that these approaches improve TeMs performance by enhancing hydrophilicity, mechanical stability, and catalytic or sensing functionality. Case studies include Ti/TiO<sub>2</sub> coatings for self-cleaning membranes, silver/gold nanoparticle-modified TeMs for surface-enhanced Raman spectroscopy, and nanofiber/TeMs hybrids for pollutant adsorption. In conclusion, the JINR — South Africa partnership demonstrates how targeted international collaboration can deliver impactful technologies. Future research should prioritize stimuli-responsive “smart” membranes, MOF-integrated hybrids, and roll-to-roll scale-up for industrial deployment.

**Keywords:** Track-etched membranes, Composite membranes, Hybrid materials, functionalisation, sputtering, electrospinning, nanoparticle integration, water purification, biosensing, JINR–South Africa collaboration

### Contents

- 1 Introduction
- 2 Methodology
- 3 South Africa — FLNR, JINR Collaboration Overview
  - 3.1 Origins and Framework
  - 3.2 Metal Sputtering for Functional Coatings
  - 3.3 Electrospun Nanofiber–Track Membrane Composites
- 4 Advances in Track-Etched Membrane Functionalization
  - 4.1 Metal/Metal Oxide Thin-Film Coatings
  - 4.2 Chemical Grafting and In-Pore Deposition
  - 4.3 Polymer Nanofiber Layering (Hybrid Membranes)
- 5 Composite and Hybrid Membranes
  - 5.1 Improved Hydrophilicity and Fouling Resistance
  - 5.2 Catalytic and Reactive Functions
  - 5.3 Enhanced Selectivity and Sensitivity
  - 5.4 Mechanical Stability and Throughput
- 6 Applications in Water Purification And Sensing
  - 6.1 Water Purification Applications
  - 6.2 Sensing Applications
- 7 Gaps and Future Directions
  - 7.1 Stimuli-Responsive “Smart” Membranes
  - 7.2 Broader Application Spectrum

7.3	Advanced Composite Architectures
7.4	Scale-Up and Practical Deployment
7.5	Infrastructure Development
7.6	Outlook
8	Conclusions
9	References



Dr. **Arnoux Rossouw** is a seasoned engineer and materials scientist, currently serving as Senior Scientific Researcher and Head of the National Group of the Republic of South Africa at the Flerov Laboratory of Nuclear Reactions, Joint Institute for Nuclear Research (JINR) in Dubna, Russia. He holds a PhD in Electrical Engineering, an MSc in Electronic Engineering, and a BEng in Mechatronics, all from Stellenbosch University.

With over a decade of expertise, Dr Rossouw specializes in advanced materials and surface science, particularly physical vapor deposition, thin-film engineering, and magnetron sputtering—applications integral to track-etched membranes in water treatment, energy, and biomedical technologies. He leads strategic R&D projects, oversees JINR–South Africa collaborations, supervises MSc and PhD students, and drives grant acquisition.

Dr Rossouw has authored 20 publications, which have garnered 254 citations and over 1,600 reads on ResearchGate, reflecting his active academic engagement. His research includes the development of electrospun PVDF-functionalized PET track-etched membranes for desalination, nanofiber adsorbents for metal recovery from spent lithium-ion batteries, and composite membranes fabricated via roll-to-roll Ti/TiO<sub>2</sub> magnetron sputtering.



**Leslie Felicia Petrik**, is Emeritus Professor, Department of Chemistry, University of the Western Cape (UWC), Bellville, Cape Town, South Africa, and Adjunct Professor, Department of Chemical Engineering, Cape Peninsula University of Technology, Bellville, Cape Town, South Africa. After obtaining her PhD in Chemistry in 2008 at the University of the Western Cape, she independently developed and led the Environmental and Nano Sciences research group, being principal investigator and grant holder of numerous local and international research agency projects with a focus on material science, nanotechnology, catalysis, and on environmental remediation, including beneficiation of industrial wastes and water treatment. Moreover, her scientific output, includes 5 granted patents; 11 book chapters; 248 international peer reviewed papers; numerous technical reports to industry and research agencies, and many conference presentations. She is considered to be amongst the top 3 % of scientists globally according to her last 6 years i10 Index and citations (AD Scientific index) with 10659 citations overall and an h-index of 57 and i-10 index of 183. Prof Petrik has received numerous awards such as the Water Legends Award of the Water Research Commission of South Africa, the Businesswomen of the Year Science and Technology Award, the National Science and Technology Forum NSTF-South32 award for her outstanding contribution to science, engineering, technology (SET) and innovation. She has supervised to completion and graduated 41 PhD, 72 MSc students and hosted 27 post-doctoral fellows



**Alexander Nikolaevich Nechaev** is Vice-Director of the Center of Applied Physics at the Flerov Laboratory of Nuclear Reactions, Joint Institute for Nuclear Research (JINR), Dubna, Russia. He obtained his PhD in Chemistry from the Institute of Physical Chemistry, Russian Academy of Sciences in 1995, specializing in colloid and membrane chemistry.

With over three decades of experience, Dr Nechaev has held senior research and academic positions at leading institutions in Russia and South Africa, including the Shubnikov Institute of Crystallography, the Kurnakov Institute of General and Inorganic Chemistry, and the University of the Western Cape, where he served as Extraordinary Professor. Since 2007, he has also been an invited expert of the International Atomic Energy Agency (IAEA) in the field of nuclear reactors and accelerator facilities for membrane production.

His research spans membrane and colloidal chemistry, nanomaterials, hydrogen technologies, and biomedical applications, with more than 80 Scopus-indexed publications (h-index 20) and over 140 total publications. Dr Nechaev's achievements have been recognized through awards such as the Gold Medal of the Russian Federation Exhibition of Achievements (2002) and the Bronze Award of the Russian National Foundation for Research in Nuclear Applied Physics (2003).



**Pavel Yurievich Apel** was graduated from the Leningrad Technological Institute in 1976. He has been pursuing his scientific career at the Flerov Laboratory of Nuclear Reactions in Dubna (Russia) where his activity is concerned with effects of accelerated heavy ions on polymers. At present he is the Head of Center of Applied Physics. In parallel, he was a Professor at the Dubna State University, where he gave lectures in 2008-2020. He published over 200 papers in peer-reviewed journals, some of which are recognized as significant contributions to the field, and co-authored 4 monographs. He was awarded the USSR Council of Minister's prize in 1989 and the Russian Federation Government prize in 2008 for the achievements in the field of science and technology. The main focus of his work is fabrication of micro- and nanostructures using the ion-track technique, including track-etched membranes and their application in academia and industry.

## 1 Introduction

Membranes created by ion track etching are distinguished by uniformly sized, engineered nanopores formed via energetic heavy particle irradiation and chemical etching [1]. Polyethylene terephthalate (PET) is commonly used due to its mechanical and chemical stability, yielding TeMs with precisely controlled pore diameters, densities, and geometries [2, 3]. These unique structural features give TeMs advantages over conventional membranes — notably, well-defined pore architecture and narrow pore size distribution — enabling predictable transport and filtration properties [4]. TeMs have found diverse applications, from biomedical uses (virus filtration, plasmapheresis) to environmental monitoring and ultra-fine filtration. In particular, they are employed for high-purity filtration of air and liquids (including drinking water purification), as templates for nanomaterial synthesis, and as model membranes for fundamental studies [5].

While pristine track-etched membranes (TeMs) have exceptional precision and well-defined pore structures, their surface properties do not meet requirements of many applications, which leads, for instance, to susceptibility to fouling by organic compounds during filtration [6, 7]. Recognizing these inherent limitations, researchers have actively pursued strategies to enhance membrane functionality and broaden their practical applications [5, 8]. Over the past decade, significant progress has been made by introducing functional surface modifications and developing composite fabrication techniques. By incorporating functional materials such as metal thin films, nanoparticles (NPs), and polymer nanofibers onto TeMs, membranes have gained valuable new attributes, including improved hydrophilicity, catalytic capabilities, selective permeability, and responsive behaviours. These enhanced membranes, known as composite track-etched membranes (CTeMs), represent an exciting and rapidly growing category of high-performance materials. CTeMs effectively combine the precise pore control of traditional TeMs with innovative surface chemistries and functionalities, enabling broader and more impactful real-world applications.

This review focuses on advances in functionalized TeMs achieved through the JINR–South Africa partnership, alongside relevant external developments, from 2007 onward. South African scientists have collaborated with FLNR (JINR) to access heavy ion irradiation facilities and expertise in track-etch technology. Through this partnership, a series of studies has produced composite and hybrid membranes tailored for water purification, catalysis, and sensing applications. We first outline the SA–FLNR collaborative framework and major co-authored works. We then discuss key advances in TeMs modification techniques (metal sputter-coating, chemical functionalization, nanofiber layering, etc.) and the resulting membrane performance improvements [3]. Next, we highlight how these functional membranes have been applied in areas such as water treatment (pollutant degradation, fouling mitigation), and chemical sensing (e.g. detecting trace contaminants). Finally, we identify gaps in the current reference set — for instance, applications like oil–water separation or emerging fabrication methods like stimuli-responsive grafting — and recommend recent high-quality references to bridge these gaps.

By drawing together results from both the SA–FLNR collaboration and complementary international studies, this article offers a clear overview of the state-of-the-art in functionalised track-etched membranes. It highlights how joint research has advanced the field, while also identifying promising directions for future development. The review focuses mainly on water purification and sensing applications, but also considers emerging opportunities in catalysis, environmental monitoring, and biomedical use. To achieve this, we combined a systematic review of published literature with an assessment of experimental approaches developed within the JINR–South Africa partnership [9–13]. This dual perspective — combining a structured literature survey with collaborative experimental insights — sets the stage for the Methodology section, where we outline the review process and inclusion criteria in detail.

## 2 Methodology

This article combines a systematic review of published literature with an overview of experimental approaches developed through the JINR–South Africa partnership.

The relevance of developments in the field of composite and hybrid nanomaterials is driven by the growing demand for high-performance filtration, separation, and adsorption technologies. The research of the team of authors focuses on the creation of track membranes (TeMs) with new functional properties by modifying the hydrophilic–hydrophobic balance of the surface, imparting photocatalytic activity, and creating specific selectivity. These properties are in demand in applications such as water desalination, rare earth extraction, radioactive contaminant purification, and rapid virus detection. TeMs modified with nanomaterials open up perspectives for innovative solutions in membrane technologies and medicine.

Our primary research goal is to enhance the performance and versatility of TeMs. Magnetron sputtering and electrospinning techniques provide a targeted and precisely controlled modification of the TeMs surface. Their use opens the way to the creation of composite and hybrid membranes with tailored functionalities, including increased durability, selective adsorption, and resistance to fouling, making them promising candidates for water purification, biotechnology, and medicine. Figure 1 summarises the concept and approaches developed in the articles to create new functional TeMs.

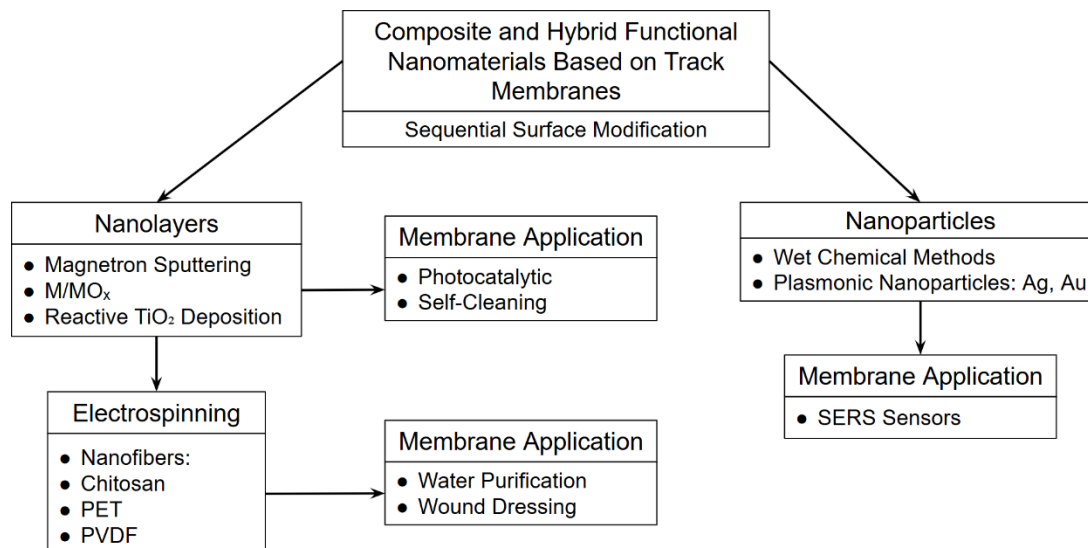


Figure 1. Conceptual schematic summarising functionalisation strategies for track-etched membranes (TeMs) — thin-film sputtering, chemical grafting/nanoparticle immobilisation, and nanofiber electrospinning — and their translation into key application domains

In addition to presenting the outcomes of our collaborative research, this paper follows the structure of a review article. Literature was systematically surveyed in Scopus, Web of Science, and Google Scholar using the keywords “track-etched membranes,” “functionalization,” “composite membranes,” “hybrid materials,” and “JINR South Africa collaboration.” Publications between 2007 and 2025 were prioritised to capture the full span of the partnership’s activities, with emphasis on peer-reviewed articles co-authored by South African and JINR researchers. To contextualise these works within global trends, additional high-quality international studies were included. Selection criteria excluded non-peer-reviewed reports, conference abstracts without full papers, and duplicated references. This methodological approach ensures that the review is both comprehensive and focused, while minimising redundancy and misaligned citations. Having established the review process, we next turn to the specific outputs of the JINR–South Africa partnership, beginning with an overview of its origins and representative collaborative works (Section 3).

### 3 South Africa — FLNR, JINR Collaboration Overview

#### 3.1 Origins and Framework

Cooperation between South African research institutions and JINR’s FLNR began in the mid-2000s under bilateral agreements to build capacity in nuclear science and materials research. A notable milestone was the 5th South African–JINR Symposium in 2007, where prospects for using FLNR’s heavy ion accelerators for materials applications (including membrane fabrication) were discussed [14]. These discussions laid the groundwork for joint projects leveraging FLNR’s heavy-ion track technology and South Africa’s applied chemistry and nanotechnology expertise. In practice, FLNR’s cyclotrons in Dubna irradiate polymer films (often PET) to produce latent tracks, which are then chemically etched to form membranes with prescribed pore sizes and densities [2]. South African students and researchers have actively participated in this process, obtaining TeMs samples for further modification and testing in local laboratories. This section highlights representative publications co-authored by SA and FLNR researchers, underscoring the collaborative achievements.



### 3.2 Metal Sputtering for Functional Coatings

One major collaborative thrust has been the deposition of metal/metal oxide thin films onto TeMs to alter surface properties. Rossouw et al. demonstrated this approach by planar magnetron sputtering of titanium (Ti) and titanium dioxide (TiO<sub>2</sub>) onto PET TeMs [14], see Fig 2.

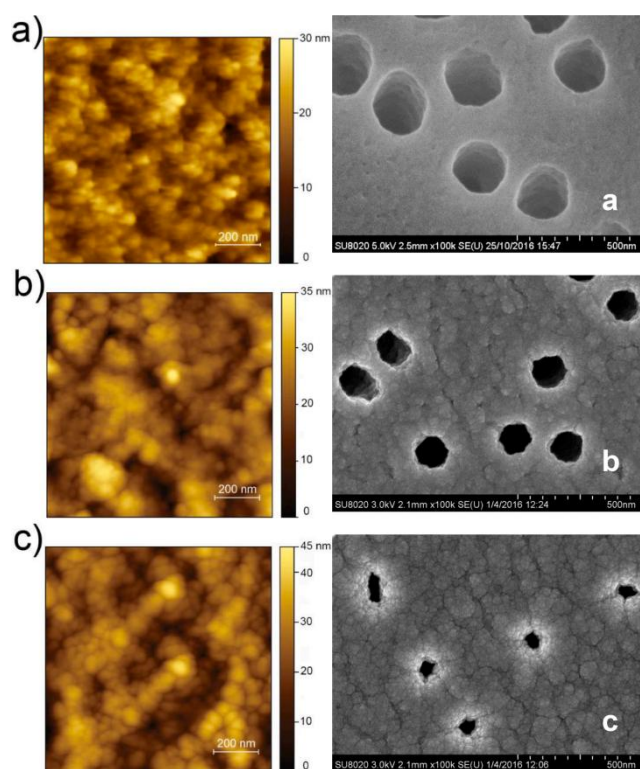


Figure 2 SEM and AFM images of PET track-etched membranes sputter-coated with titanium/titanium dioxide (Ti/TiO<sub>2</sub>). Coated samples show uniform pore-wall coverage while preserving circular geometry, confirming functionalisation without pore blockage.

(a) pristine TeMs, (b) Ti-coated TeMs, (c) TiO<sub>2</sub>-Ti-coated TeMs.

Reprinted from [15]. Copyright (2021) with permission from Elsevier

The Ti/TiO<sub>2</sub>-coated membranes exhibited dramatically improved hydrophilicity — water contact angle dropped from ~72° (untreated PET) to ~43–45° after coating — and acquired photocatalytic activity under UV light [15]. These hydrophilic, self-cleaning surfaces mitigate organic fouling, a key issue in filtration [16, 17]. The study, published in 2021, was co-authored by researchers from JINR and South Africa (including Stellenbosch engineers and University of Western Cape chemists), reflecting a true partnership [15].

Notably, the TeMs themselves were produced at FLNR and then modified via sputtering to create hybrid membranes with a durable TiO<sub>2</sub> active layer. This work established that industrial sputtering is a viable method to functionalize porous polymer supports without occluding their pores [18], and it inspired follow-up efforts to scale up the coating process (see Future Directions).

### 3.3 Electrospun Nanofiber–Track Membrane Composites

The partnership has also explored integrating TeMs with nanofibrous layers to create hierarchical composites. Pereao et al. fabricated composite membranes by electrospinning chitosan/polyethylene oxide (CS/PEO) nanofibers directly onto a Ti-sputter-coated PET track-etched membrane [19, 20], see Fig. 3.



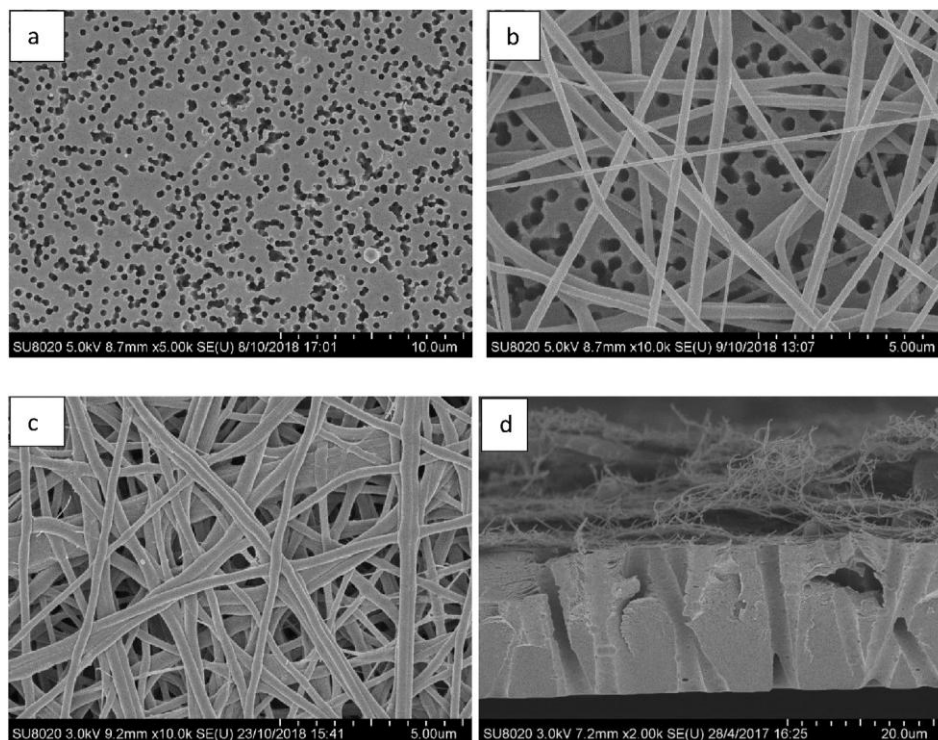


Figure 3 SEM micrographs of electrospun chitosan/polyethylene oxide (CS/PEO) nanofibers deposited on Ti-coated PET track-etched membranes. Cross-sectional images reveal hierarchical dual-scale porosity, with a nanofiber mat atop micron-scale track pores, enhancing adsorption, hydrophilicity, and mechanical stability. Reprinted from [19]. Copyright (2021) with permission from Elsevier

The Ti coating (deposited at FLNR) made the PET membrane electrically conductive and thus able to serve as the grounded collector for electrospinning. The resulting CS-nanofiber/Ti–PET composite exhibited a high surface area and new functionality: the chitosan nanofibers provide active adsorption sites and hydrophilicity, while the TeMs provide mechanical support and controlled microporosity. The authors demonstrated the composite's potential in water treatment, showing that it is stable in water (after crosslinking) and non-toxic to model aquatic organisms (*Daphnia magna*), indicating suitability for environmental use. They suggested such composites could be used as affinity membranes for capturing toxic heavy metals or organic pollutants from water [21]. This study [19] again involved JINR scientists (who provided irradiated PET films and technical expertise) and South African researchers who performed the electrospinning and application testing. It underscores a key collaborative achievement: combining two advanced fabrication techniques — ion track etching and electrospinning — to engineer a multifunctional membrane. Building on this, a 2025 follow-up by Bode-Aluko et al. extended the concept to nano-micro composite membranes by depositing different polymer nanofibers (polyamide-6 and polyacrylonitrile) onto track-etched PET. That study, supported by South Africa's DST and including an FLNR co-author (Nechaev), demonstrated effective removal of a model dye (Rhodamine 6G) in continuous filtration mode using the electrospun/track-etched membrane, outperforming standalone nanofiber or track-etched filters in dye rejection [21–23].

Taken together, these three approaches — thin-film sputtering, chemical grafting with nanoparticles, and nanofiber electrospinning — represent the main collaborative strategies of the SA–FLNR partnership. Each introduces distinct functionalities to track-etched membranes, ranging from improved hydrophilicity and photocatalysis to catalytic sensing and enhanced adsorption. This provides a cohesive framework for understanding the contribution of the partnership before situating it within the global context of membrane functionalization in Section 4.

In summary, the SA–FLNR partnership has yielded multiple novel composite membranes: metal-coated TeMs for anti-fouling and photocatalysis [15,18], ligand-functionalized TeMs for nanoparticle-based sensing [24], and nanofiber-coated TeMs for enhanced adsorption and filtration performance [19]. Each of these projects combined JINR's track-etch materials with South Africa's applied research strengths, resulting in co-authored publications in international journals. The next sections delve deeper into the technological advances and applications demonstrated in these works.

#### 4 Advances in Track-Etched Membrane Functionalization

To fully unlock TeMs' potential, researchers have developed various post-etch modification techniques. Here we detail the main approaches — physical deposition, chemical functionalization, and composite fabrication — highlighting how they improve membrane performance. Collaborative SA–FLNR studies serve as prime examples of each approach, and we compare them with external progress in the field.

##### 4.1 Metal/Metal Oxide Thin-Film Coatings

Depositing a thin inorganic film onto a polymer membrane can dramatically alter its surface characteristics without changing pore geometry too much. The Rossouw et al. study showed that a ~50–100 nm Ti/TiO<sub>2</sub> sputtered layer endows PET TeMs with hydrophilicity and photocatalytic ability [15, 25]. Before coating, PET is hydrophobic (contact angle ~72°) and prone to organic fouling; after coating with TiO<sub>2</sub>, the membrane surface became hydrophilic (contact angle ~45°) and could leverage TiO<sub>2</sub>'s well-known ability to generate reactive oxygen species under UV [15]. This means organic foulants can be more easily washed off or even degraded (self-cleaning membrane). The pores remained mostly open and circular post-sputtering [14, 26], indicating that planar magnetron sputtering — even in a roll-to-roll industrial setup — can uniformly coat the membrane without clogging (a crucial feasibility point). These advances illustrate that thin-film coatings (Ti, Cu, etc.) can introduce multiple functionalities — anti-fouling, photocatalysis, adsorption — to TeMs in a single modification step.

##### 4.2 Chemical Grafting and In-Pore Deposition

An alternative to physical coating is to chemically attach new functionalities, either by forming chemical bonds on the pore walls or by template depositing materials inside pores. The SA–FLNR example of DETA grafting followed by silver electroless deposition fits here: first, surface amine groups were grafted via aminolysis of PET (introducing –NH<sub>2</sub> sites), then Ag<sup>+</sup> ions were bound and reduced to form Ag nanoparticles on the membrane [24], see Fig 4. This two-step wet-chemical process preserved the pore structure while adding a robust functional layer (in this case, enabling SERS and antimicrobial potential). These approaches highlight the tunability of track-etched pores: by either covalently attaching functional molecules or growing nanostructures within the channels, one can create membranes that not only filter by size, but also carry out chemical transformations (catalysis) or selectively bind contaminants (adsorption).

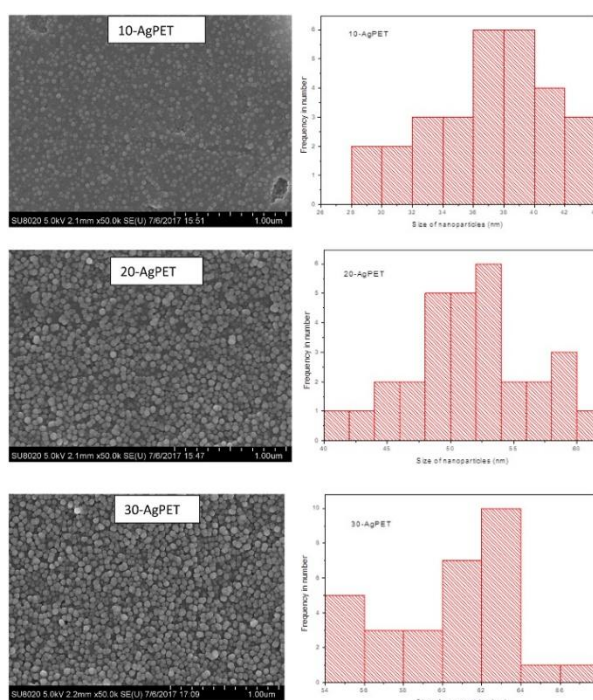


Figure 4. SEM images of silver-coated PET membranes prepared at 90 °C with 2 mL of 1 % trisodium citrate for immobilisation times of 10 min (10-AgPET), 20 min (20-AgPET), and 30 min (30-AgPET). Corresponding histograms show size distributions of silver nanoparticles for each sample, confirming growth in particle size with increased immobilisation time. Reprinted from [24]. Copyright (2021) with permission from Springer Nature

#### 4.3 Polymer Nanofiber Layering (Hybrid Membranes)

By combining TeMs with electrospun nanofibers, researchers can create multilayer or hierarchical membranes that synergistically exploit the features of each component. The collaborative works by Pereao and Bode-Aluko are instructive — they directly electrospun nanofibers onto track-etched supports [19, 21]. The electrospun layer (whether chitosan-based or synthetic polymer) adds a mesoporous, high-surface-area network atop the TeM's well-defined through-pores. This dual-scale porosity (nano-fiber interstices and micropores in TeMs) can enhance filtration: the nanofiber mat can capture fine particulates or adsorb dissolved pollutants, while the underlying TeMs provide mechanical strength and a guarantee of maximum pore size (preventing any large breakthrough particles). Indeed, Bode-Aluko et al. found that a PA6-nanofiber/PET-TeMs composite achieved higher dye removal efficiency in continuous flow than an electrospun nanofiber filter alone, owing to the composite's improved permeability and support of the nanofiber layer. Another benefit is versatility — different functional nanofibers can be chosen (chitosan for metal ion binding, PAN for solvent resistance, etc.) to tailor the membrane to target contaminants. Elsewhere, researchers have developed analogous hybrids, for example coating TeMs with a chitosan hydrogel to make a reactive adsorbent membrane [20]. The concept of composite membranes extends to inorganic hybrids too: one can deposit materials like graphene oxide or metal–organic frameworks (MOFs) onto TeMs to impart new functions (e.g., adsorptive or catalytic sites) [27]. In all cases, the track-etched membrane acts as a precision scaffold that can be “decorated” with a secondary phase, yielding a membrane with enhanced functionality while maintaining predictable flow paths, see Fig 5.

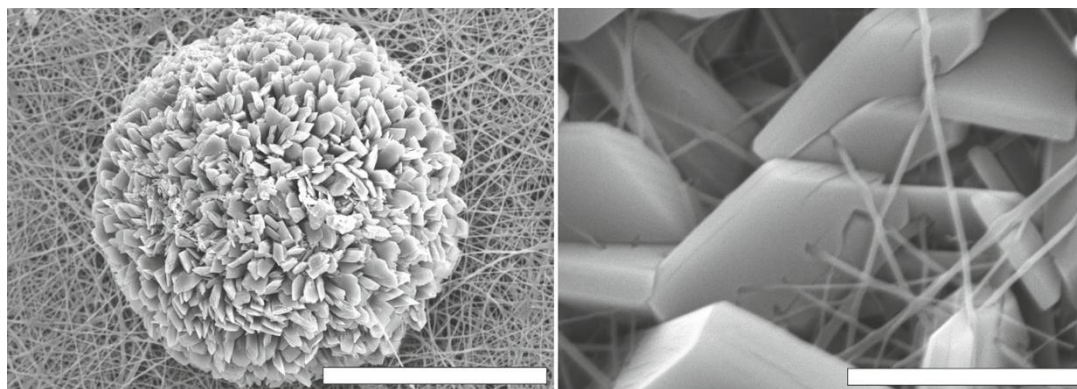


Figure 5. Surface micrographs of a TeMs + Chitosan + Ni-MOF sample at various magnifications; synthesis time: 24 h. Reprinted from [27]. Copyright (2024) with permission from Pleiades Publishing, Ltd.

Across these methods, a unifying theme is that functionalization does not sacrifice the unique order of track-etched pores. The JINR–SA studies carefully verified pore integrity via SEM/AFM and flow measurements after modifications [15, 18]. This is crucial: unlike many random-pore membranes, TeMs start with a well-characterized structure, and effective modifications must retain that structure (or modify it in a controlled way). The advancements above demonstrate that with the right techniques — whether physical vapor deposition, chemical grafting, or layer-by-layer assembly — one can introduce active functionality while preserving the engineered pore network of TeMs.

In summary, Section 4 illustrates that functionalization transforms TeMs from passive size-exclusion membranes into active, multifunctional materials. The SA–FLNR case studies stand as early demonstrations of this concept, while international work has expanded the field toward stimuli-responsive, MOF-integrated, and multi-scale hybrid membranes. This contextualisation strengthens the review by showing how local achievements connect with global research trajectories.

#### 5 Composite and Hybrid Membranes

Functionalized track-etched membranes are often described as composite or hybrid membranes, reflecting their multi-material makeup. In this section, we examine the properties these composites exhibit and how they translate into performance improvements. We draw examples from both the JINR–South Africa papers and external literature to illustrate key points.

### 5.1 Improved Hydrophilicity and Fouling Resistance

Many polymer membranes (PET, polycarbonate, etc.) are hydrophobic, causing hydrophobic organic foulants to adsorb during filtration. Coating the TeMs with a more hydrophilic layer (whether inorganic or polymer) can mitigate this. Rossouw et al. reported that TiO<sub>2</sub>-coated track membranes had significantly lower water contact angles and thus were less prone to fouling by organic matter [15]. Similarly, grafting hydrophilic polymers (like polyacrylic acid or polyvinylpyrrolidone) onto pore walls has been shown to create a hydration layer that resists protein or oil adsorption. In composite membranes from the collaboration, the inclusion of hydrophilic chitosan nanofibers rendered the surface much more wettable than bare PET [19, 20]. A practical outcome is extended membrane lifespan and flux: for instance, a TiO<sub>2</sub>-Ti coated PET TeMs exhibited self-cleaning under UV irradiation — organic foulants were photocatalytically broken down, restoring water flux. This attribute is highly valuable in water purification systems where fouling is a primary cause of performance decline.

### 5.2 Catalytic and Reactive Functions

Composites that incorporate catalytic nanomaterials enable the membrane to actively degrade pollutants. The silver-loaded TeMs (both in the SA-FLNR SERS study and the external photocatalysis study) exemplify this. Ndilowe et al. mainly leveraged Ag for sensing, but silver is also known for antimicrobial and catalytic properties; a silver-coated membrane can inactivate bacteria and even catalyze reactions like dye reduction. In the work by Mashentseva et al., Cu/CuO loaded membranes could catalytically hydrogenate nitroaromatic pollutants (using NaBH<sub>4</sub> as a reducing agent) as water passed through, effectively functioning as a reactor in addition to a filter [28]. The same membrane could adsorb arsenic ions, as CuO is a known arsenic sorbent — this dual functionality (adsorption + catalysis) is a clear advantage of hybridization. Another example is TiO<sub>2</sub> coatings: beyond fouling control, TiO<sub>2</sub> under UV can oxidize organic pollutants in situ (e.g. breaking down trace pharmaceuticals during filtration) [15]. Thus, functionalized TeMs can be designed as active membranes that not only sieve out contaminants by size, but chemically neutralize or transform them. This expands the role of membranes in water treatment from passive barriers to reactive interfaces.

### 5.3 Enhanced Selectivity and Sensitivity

By incorporating recognition elements, TeMs can achieve selectivity for certain molecules or improved sensitivity in detection. The uniform pores of a TeMs are ideal templates for creating sensing channels; for instance, coating conical track-etched nanopores with responsive polymer brushes yields a sensor that modulates ionic current in response to specific chemical stimuli (pH, metal ions, etc.) [20]. In the SA-FLNR references, the SERS membrane is a great illustration: the membrane acts as a sample pre-concentrator (trapping analyte molecules on its surface) and as a SERS-active sensor, allowing trace detection of acetaminophen [24]. The limit of detection achieved (sub ppm) is competitive with lab instrument methods, yet the approach is field-deployable by simply dipping the membrane in water and then performing Raman analysis. This shows how hybrid membranes can serve as self-contained sensor substrates. External studies have pursued biosensing: for example, Torati et al. fabricated an electrochemical sensor for DNA by depositing gold nanowire arrays in track-etched pores and functionalizing them with DNA probes [29]. The resulting device could selectively detect *Mycobacterium tuberculosis* DNA sequences at low concentrations — something a plain polymer membrane could never do. These cases underscore that by grafting biomolecules or nanosensors inside the well-defined pores, one can transform a TeMs into a highly sensitive and selective detection platform. The collaboration hasn't yet reported biosensing, but it has laid groundwork with the SERS chemical sensor and could extend to biosensors in future (indeed, the partnership's membrane was poised to detect other drugs and hormones in water [30]).

### 5.4 Mechanical Stability and Throughput

One often overlooked benefit of forming composites with TeMs is mechanical reinforcement and higher throughput. Electrospun nanofiber mats alone can be too fragile to use as standalone filters, especially at small fiber diameters. By spinning them onto a sturdy track-etched film (23 μm PET in Perea's case [19, 20]), the resulting laminate can withstand handling and pressurized flow. The TeM's regular pore structure can also reduce flow resistance compared to a thick nanofiber mat, giving a more predictable permeance. Bode-Aluko's 2025 results indicated that the PA6/PAN nanofiber coated TeMs maintained good permeability while achieving high dye removal, benefiting from the hierarchical porosity (nano and micro) [21]. In another external study, track-etched membranes were used as a support for a thin selective layer in a composite nanofiltration membrane, significantly increasing water flux due to the low tortuosity of straight-through

pores [31]. This concept is now being applied to develop thin-film nanocomposite (TFN) membranes where TeMs serve as support for ultra-thin selective coatings, marrying high flux of track pores with selectivity of the coating.

Taken together, these results demonstrate that composite and hybrid TeMs consistently outperform their single-component counterparts, whether by improving fouling resistance, catalytic activity, or mechanical durability. Importantly, they validate the principle that TeMs function not only as precision porous films, but also as scaffolds that can be adapted for diverse purposes by integrating nanomaterials and polymers. This forms a conceptual bridge between the materials-oriented innovations in Section 4 and their deployment in real-world scenarios, discussed in Section 6.

Collectively, these examples illustrate how composite/hybrid TeMs embody the adage “the whole is greater than the sum of its parts.” By carefully combining materials, one designs membranes that are multi-functional — they can filter, catalyze, sense, and self-clean in one system.

### *6 Applications in Water Purification and Sensing*

The ultimate test of these advanced membranes is in real-world applications. Two areas of particular interest — and relevance to both South Africa and JINR’s mission — are water purification (including treatment of wastewater or drinking water) and chemical sensing for environmental monitoring. The collaborative works have direct implications for these fields, as do several external studies we consider for context.

#### *6.1 Water Purification Applications*

Access to clean water is a critical issue, and membranes play a central role in filtration-based water treatment (microfiltration, ultrafiltration, etc.). Track-etched membranes, with pore sizes typically in the micro- to sub-micron range (0.1–1  $\mu\text{m}$  in many studies [15, 19]), are generally suited to microfiltration tasks like removing bacteria, protozoa, and particulate contaminants. However, by functionalizing TeMs, we can extend their utility to removing dissolved pollutants and even killing microbes, moving into realms usually served by adsorption media or chemical disinfectants.

Several of the reviewed membranes address organic pollutant removal. For instance, the  $\text{TiO}_2$ -modified PET TeMs can photocatalytically degrade organic molecules that foul the membrane surface [15, 32]. While Rossouw et al. focused on self-cleaning rather than bulk pollutant removal, the same principle could be applied to break down contaminants in the feed water (e.g., pesticide residues) as it passes through a  $\text{TiO}_2$ -coated membrane under UV illumination. In a South African context, where rural water may contain organic pollutants and limited infrastructure exists for advanced oxidation, such a membrane could provide a passive means of continuous water detoxification using sunlight. Expanding on photocatalysis, the silver microtubule PET membranes demonstrated complete decomposition of methylene blue dye under visible light [33], indicating that functional TeMs can harness even solar visible spectrum for water remediation. Dyes such as methylene blue or rhodamine are models for textile wastewater pollutants; the composite membranes loaded with Ag or CuO not only filtered these dyes but actively degraded them [28], achieving higher removal efficiency than size-exclusion alone.

Another pollutant class is heavy metals. While a plain PET membrane would not remove metal ions (they pass through the pores), a functionalized one can. The chitosan nanofiber composite is a prime example: chitosan’s amine and hydroxyl groups have strong affinity for metal cations (e.g.  $\text{Pb}^{2+}$ ,  $\text{Cd}^{2+}$ , [34, 35]). A CS-coated TeMs can thus serve as a binding membrane to strip metals from water. Perea et al. suggested their CS/PEO-Ti/PET membrane could target toxic metals [32, 36, 37], and indeed chitosan-based filters are known to chelate metals effectively. In external work, poly(acrylic acid)-grafted TeMs loaded with iron oxide NPs have been used to adsorb arsenic and chromium from wastewater, functioning as a hybrid ion-exchange membrane [38]. The Cu/CuO-TeMs by Mashentseva et al. similarly achieved As(III) removal to meet <0.05 mg/L levels, which is the WHO guideline for arsenic in drinking water [28]. These capabilities are especially relevant to regions facing heavy metal contamination (e.g., mining-impacted waters in Southern Africa). A track-etched membrane functionalized for metal uptake could be deployed as a point-of-use filter that not only sieves out sediment and microbes but also scavenges dissolved metals — a multifaceted approach to water purification. Moreover, the same principle of functionalizing nanofibers can be applied to selectively recover metals of value from mixed hydrometallurgical solutions [37, 39].

Antimicrobial activity is another key application. Waterborne pathogens are traditionally removed by microfiltration (for bacteria) and ultrafiltration (for viruses), which TeMs can handle due to precise pore control. Functionalisation, however, adds a kill mechanism. Silver-coated TeMs are intrinsically antimicrobial



because  $\text{Ag}^+$  ions and nanosilver disrupt microbial cell membranes. Thus, the AgNP-functionalised TeMs developed in the JINR–South Africa collaboration could serve dual purposes: SERS sensing (as shown) and disinfection. Embedding biocidal agents into track-etched filters is a viable strategy: water passing through is both physically filtered and exposed to antimicrobial surfaces [21, 22]. Some commercial TeMs (e.g., polycarbonate filters) are already used for microbial analysis, and coatings could convert them into active barriers that prevent downstream bacterial growth. While the reviewed works did not yet quantify pathogen kill, this represents a clear and practical extension — particularly relevant to South African water treatment challenges.

## 6.2 Sensing Applications

Environmental sensing, especially pollutant detection in water, is a crucial application of functionalised TeMs. The importance of developing effective methods for monitoring emerging contaminants in aquatic systems has been emphasised in several reports, including work commissioned by the Water Research Commission [30]. In this context, the JINR–South Africa collaboration provided a clear proof-of-concept with AgNP-coated membranes applied as Surface-Enhanced Raman Spectroscopy (SERS) substrates. In this demonstration, the system enabled detection of acetaminophen at concentrations as low as 0.15 mg/L, highlighting the potential of TeMs-based SERS platforms for trace pollutant monitoring [24]. Such devices integrate sampling and sensing in one step: analytes are concentrated during filtration and then identified using a portable Raman spectrometer, without complex sample preparation. This proof-of-concept illustrates how functionalised membranes could be developed into field-deployable kits for monitoring pharmaceuticals, pesticides, and other contaminants in water.

Beyond SERS, track-etched membranes can be incorporated into electrochemical sensors. For example, a conductive track-etched membrane (such as one sputter-coated with a thin metal film) can act as a working electrode with a well-defined porous structure. Researchers have used gold-coated TeMs to detect heavy metal ions via anodic stripping voltammetry, with the pores facilitating rapid diffusion of ions to the electrode surface. Another avenue is biosensing: functionalizing pores with aptamers or enzymes that produce a readable signal when a target analyte is present. A notable case, as referenced earlier, is the DNA-functionalized Silver or Au nanotube arrays for detecting specific DNA sequences (like pathogens) [24, 29, 40]. The uniform pore geometry of TeMs yields consistent sensor response across the membrane area, which is advantageous for reproducibility.

The South African context offers many relevant sensing targets: monitoring of emerging contaminants (pharmaceuticals, endocrine disruptors) in water bodies, detection of pathogens, and even security applications like detecting explosives or toxins. Functionalized TeMs can be tailored to these — for instance, a membrane with molecularly imprinted polymer within its pores could selectively bind a pesticide and include a reporter dye to signal its capture. The groundwork laid by the SERS membrane shows how to marry chemistry with the TeMs platform for sensing. Given that FLNR has expertise in radiation chemistry, one future collaboration could involve grafting radiolabelled or luminescent groups in pores to create scintillating membranes for radiation sensing or radiochemical detection.

These applications highlight the dual strengths of the JINR–South Africa work: addressing urgent South African water challenges while also contributing globally relevant sensing technologies. By linking membrane structure directly to pollutant removal or analyte detection, the partnership illustrates how collaborative science can translate fundamental modifications into practical outcomes. This prepares the ground for identifying gaps and outlining future research priorities in Section 7.

In summary, water purification and sensing are being redefined by these advanced membranes. Instead of using separate units for filtration, adsorption, and detection, multi-functional TeMs strive to do all simultaneously: filter out what you can, degrade or bind what you can't filter, and even indicate what contaminants were present. The JINR–South Africa partnership's prototypes — photocatalytic membranes, adsorptive nanofiber composites, and SERS membranes — embody this integration. In the next section, we discuss what gaps remain in the current repertoire of references and how further research (some already underway elsewhere) can fill those gaps, moving the technology closer to practical deployment.

## 7 Gaps and Future Directions

While the collection of references reviewed demonstrates significant progress, there are notable gaps and emerging opportunities in functionalized TeMs that have not yet been fully covered by the SA–FLNR works. Identifying these gaps is important to chart future collaboration efforts and to position the research



within global membrane science trends. Below, we outline key areas that warrant further exploration, along with suggested high-quality references that could guide these investigations:

### 7.1 Stimuli-Responsive “Smart” Membranes

None of the current SA–FLNR studies explicitly dealt with stimuli-responsive gating membranes. These are membranes that alter their permeability in response to environmental triggers (pH, temperature, light, etc.). Incorporating stimuli responsive polymer brushes or hydrogels into track-etched pores can create membranes that act as on-demand valves — for instance, open at high pH and closed at low pH, useful for controlled drug delivery or self-regulating filtration [11, 20]. Recent breakthroughs include optothermally responsive TeMs grafted with PNIPAM-metal nanocomposites that change flow in response to light, and block copolymer grafted TeMs that separate oil–water emulsions by switching hydrophilicity with pH [41, 42]. These “smart” membranes represent a cutting-edge direction that the collaboration could pursue. A 2023 study by Muslimova et al. reported a PET TeMs grafted via RAFT polymerization with a styrene/acrylic acid copolymer, achieving tunable wettability and successful oil-water separation [42]. Integrating similar stimuli-responsive layers in JINR-fabricated TeMs could lead to membranes that adapt to feed conditions (e.g., resisting fouling by switching to hydrophobic when oil is present, then to hydrophilic for cleaning).

### 7.2 Broader Application Spectrum

Beyond water pollutants and SERS sensing, track-etched membranes are also being explored for gas separation and biomedical applications. Gas separation is challenging due to the relatively large pore size of TeMs, but integrating ultra-thin selective coatings [43] could yield hybrid membranes suitable for vapor or gas filtration. In life sciences, TeMs are emerging as cell culture templates or scaffolds for tissue engineering, with their pores enabling nutrient flow and cell migration pathways [44]. They are also being investigated as artificial membranes for organ-on-chip devices [45].

Another gap relates to anti-biofouling and antimicrobial performance. While Section 6.2 highlighted the dual use of AgNP-coated membranes developed within the South Africa–FLNR partnership, future collaborative studies should directly test functionalised TeMs against bacteria and viruses under realistic conditions. Recent reports show, for instance, that copper nanoparticle-embedded polymer membranes achieve >99 % bacterial inactivation [46]. Incorporating such studies — alongside photocatalytic examples like visible-light active TiO<sub>2</sub> membranes inactivating *E. coli* [47] — would strengthen the case for JINR–South Africa membranes as comprehensive water treatment solutions.

### 7.3 Advanced Composite Architectures

To date, the composite membranes developed through the JINR–South Africa partnership predominantly integrate polymers, metals, and metal oxides. However, there remains an exciting gap in incorporating emerging nanomaterials, particularly two-dimensional (2D) materials (such as graphene and MXenes) and Metal–Organic Frameworks (MOFs) [48].

For instance, 2D nanosheets could be strategically coated onto TeMs to impart selective barrier properties for smaller contaminants or introduce conductive functionalities. MOFs, renowned for their porous crystalline structures, offer a promising avenue to add highly selective adsorption or catalytic sites to membranes. Recent research demonstrated functionalizing PET track-etched membranes with Ni-based MOFs using chitosan as a linker, significantly enhancing adsorption capacities for organic molecules [27]. Such hybrids, leveraging both macro-porosity of TeMs and nano-porosity of MOFs, represent an exciting advancement in multi-scale filtration technology. This type of integration is underrepresented in current collaboration literature, marking a logical next step for future collaborative studies.

### 7.4 Scale-Up and Practical Deployment

Beyond material composition innovations, scaling the fabrication of functionalized TeMs from laboratory to practical, real-world applications remains a critical challenge. The collaboration has begun addressing this with initiatives such as Rossouw’s pioneering work on roll-to-roll sputtering methods, explicitly aimed at achieving continuous, industrial-scale production of functionalized membranes [18]. However, practical scale-up strategies and methods remain largely underrepresented in the current body of references.

Future studies should prioritize pilot-scale demonstrations, including the production and field-testing of larger-scale (e.g., square-meter) rolls of functionalized track membranes. Such membranes could be evaluated in realistic operational environments, such as integrated water treatment modules or in sensor cartridge configurations for environmental monitoring. A pivotal reference in this context is [18] study on the industri-

al-scale production and integration of track membranes into practical devices, providing valuable engineering insights and guidance on large-scale manufacturing and handling.

Furthermore, addressing economic and lifecycle considerations, such as coating durability, membrane regeneration strategies, and fouling resistance under realistic water conditions, is essential yet currently missing from the collaboration's literature. Incorporating perspectives from environmental engineering literature, such as studies on long-term ultrafiltration membrane fouling by Lee et al. from 2017, will be crucial for ensuring the next generation of functional TeMs are both effective and practically viable [49].

### *7.5 Infrastructure Development*

Complementing material and process innovations, infrastructure enhancements are also central to advancing functionalized track-etched membrane research. In South Africa, iThemba LABS provides a unique national platform that supports both nuclear science and applied materials studies. Its cyclotron facilities, originally established for nuclear physics and medical isotope production, also offer ion-beam capabilities that can be adapted for track-etch membrane fabrication and modification. Beyond beamlines, iThemba LABS houses complementary facilities such as cleanrooms for sample preparation, thin-film deposition equipment, and advanced characterization instruments (SEM, RBS, PIXE), which are critical for developing and testing membrane materials.

Importantly, iThemba LABS is not only a research hub but also a training environment, where South African students and researchers gain hands-on experience with ion beam techniques and materials science applications. In this way, it complements JINR's infrastructure in Dubna, enabling a bilateral pathway where membranes can be fabricated, modified, and tested across both sites. Strengthening this integration provides opportunities to expand the collaborative outputs of JINR and South Africa, and lays the foundation for scaling laboratory innovations toward real-world applications.

### *7.6 Outlook*

The gaps we have identified also point to exciting opportunities for future work. Track-etched membranes are moving toward becoming smarter, easier to produce on a larger scale, and increasingly tailored for specific applications. By introducing responsive grafting methods [50], exploring the potential of new nanomaterials [50], and focusing on practical scale-up [27], the JINR–South Africa partnership can continue to play a leading role in this field. If these directions are pursued, functionalized membranes could take on a much wider range of challenges—from simple, self-cleaning water filters to compact “lab-on-membrane” systems for environmental monitoring—helping to push membrane technology into its next stage of development.

In sum, Section 7 highlights both the unmet challenges and promising opportunities that remain for functionalized TeMs. By identifying where the SA–FLNR partnership can contribute — such as in smart membranes, MOF and 2D hybrids, and pilot-scale roll-to-roll fabrication — the discussion provides a forward-looking framework that connects naturally to the overall conclusions in Section 8.

## *8 Conclusions*

In conclusion, the JINR–South Africa partnership has become a notable contributor to membrane science, marrying fundamental research (ion track physics, surface chemistry) with pressing applied needs (clean water and environmental sensing). The composite and hybrid TeMs developed under this collaboration illustrate the power of international cooperation in addressing multidisciplinary challenges. By continuing to fill knowledge gaps — adopting intelligent polymer grafts, exploring new composites like MOF@TeMs, and focusing on pilot-scale production — the partnership is poised to drive further innovations in functional membranes. These advanced membranes have the potential not only to improve water quality and analytical detection in South Africa and the Eurasian region, but also to serve as globally relevant solutions in the quest for sustainable and smart water treatment technologies.

The joint efforts of JINR's FLNR and South African researchers over the past ~15 years have significantly advanced the field of functionalized track-etched membranes. By uniting the precision of ion-track nanotechnology with innovative chemistry and nanomaterials engineering, this partnership has produced composite membranes that transcend the traditional role of passive filtration. These works represent a cycle of interconnected studies in which diverse methods for fabricating nanostructured track membranes were tested under real conditions and their efficiency confirmed, with results published in highly cited Russian and international journals.

Key outcomes include:

- Hydrophilic, antifouling membranes via metal oxide coatings, which maintain high flux and self-cleaning properties, showing promise for more sustainable water filtration;
- Catalytically active membranes that degrade organic pollutants or adsorb heavy metals during filtration, achieved by embedding nanoparticles or catalytic coatings on TeMs—merging separation and reaction in one step;
- Sensing membranes, such as the silver-coated SERS platform, capable of capturing and detecting contaminants in situ, introducing a new paradigm of “analytical membranes”;
- Hierarchical composite membranes combining nanofiber mats with track-etched films, which improve adsorption capacity and mechanical robustness by leveraging multi-scale porosity.

This review also related these achievements to global research trends, highlighting complementary studies (e.g., electroless deposition of metal microtubes, grafted responsive polymers) that broaden the implications of the collaborative works. While the references cover strong foundations in water-related applications and sensing, there is still scope to expand into smart membranes, advanced composite architectures (such as MOF@TeMs), and scaling techniques. Encouragingly, steps toward roll-to-roll modification already suggest translation to industry, while emerging studies on stimuli-responsive TeMs provide a blueprint for adaptive next-generation membranes.

In conclusion, the JINR–South Africa partnership has become a notable contributor to membrane science, marrying fundamental research with pressing applied needs in clean water and environmental sensing. By continuing to address these gaps and extending collaborative innovation, the partnership is well-positioned to drive future advances in functional membranes. These membranes have the potential not only to improve water quality and analytical detection in South Africa and the Eurasian region but also to contribute globally to sustainable and smart water treatment technologies.

Ultimately, the JINR–South Africa partnership serves as a model of how targeted international collaboration can transform niche nanomaterials research into technologies with broad societal relevance, bridging laboratory innovation with real-world impact.

#### *Author Information\**

*\*The authors' names are presented in the following order: First Name, Middle Name and Last Name*

**Arnoux Rossouw** (*corresponding author*) — PhD, Senior Researcher, Flerov Laboratory of Nuclear Reactions, Joint Institute for Nuclear Research, Dubna, Joliot-Curie street 6, 141980, Moscow region, Russia; e-mail: [rossouw@jinr.ru](mailto:rossouw@jinr.ru); <https://orcid.org/0000-0002-6793-5252>

**Leslie Felicia Petrik** — Emeritus Professor, Department of Chemistry, University of the Western Cape (UWC), Bellville, Cape Town, South Africa, and Adjunct Professor, Department of Chemical Engineering, Cape Peninsula University of Technology, 7535, Bellville, Cape Town, South Africa; e-mail: [lpetrik@uwc.ac.za](mailto:lpetrik@uwc.ac.za); <https://orcid.org/0000-0002-2049-1551>

**Alexander Nikolaevich Nechaev** — Candidate of Chemical Sciences, Deputy Head of Department, Flerov Laboratory of Nuclear Reactions, Joint Institute for Nuclear Research, Dubna, Joliot-Curie street 6, 141980, Moscow region, Russia; e-mail: [nechaeffalexander@gmail.com](mailto:nechaeffalexander@gmail.com); <https://orcid.org/0000-0002-5138-4265>

**Pavel Yurievich Apel** — Doctor of Chemical Sciences, Head of Department, Flerov Laboratory of Nuclear Reactions, Joint Institute for Nuclear Research, Dubna, Joliot-Curie street 6, 141980, Moscow region, Russia; e-mail: [apel@jinr.ru](mailto:apel@jinr.ru); <https://orcid.org/0000-0003-1259-163X>

#### *Author Contributions*

The manuscript was written through contributions of all authors. All authors have given approval to the final version of the manuscript. **CRedit**: **Arnoux Rossouw** conceptualization, investigation, data curation, formal analysis, funding acquisition, validation, writing-original draft, writing-review & editing; **Leslie Felicia Petrik** conceptualization, investigation, methodology, validation, writing-review & editing; **Alexander Nikolaevich Nechaev** conceptualization, investigation formal analysis, resources, supervision, writing-review & editing; **Pavel Yurievich Apel** conceptualization, methodology, validation, writing-review & editing.

### Conflicts of Interest

The authors declare no conflict of interest.

### Acknowledgements

The authors would like to thank the South Africa's National Research Foundation for supporting the long-lasting partnership between JINR and RSA universities.

### References

- 1 Fleischer, R. L., Price, P. B., & Walker, R. M. (1965). Tracks of Charged Particles in Solids. *Science*, 149(3682), 383–393. <https://doi.org/10.1126/science.149.3682.383>
- 2 Flerov, G.N., Apel', P.Y., Didyk, A.Y., Kuznetsov, V.I., Oganessian, R.T. (1989). Use of heavy-ion accelerators to produce nuclear membranes. *At Energy*, 67, 763–770. <https://doi.org/10.1007/BF01123341>
- 3 Apel, P. (2001). Track etching technique in membrane technology. *Radiat Meas*, 34, 559–566 [https://doi.org/10.1016/S1350-4487\(01\)00228-1/](https://doi.org/10.1016/S1350-4487(01)00228-1/)
- 4 Fischer, B.E., Spohr, R. (1983). Production and use of nuclear tracks: imprinting structure on solids. *Rev Mod Phys*, 55(4), 907–948. <https://doi.org/10.1103/RevModPhys.55.907>
- 5 Ma, T., Janot, J.M., Balme, S. (2020). Track-Etched Nanopore/Membrane: From Fundamental to Applications. *Small Meth*, 5, 2000366. <https://doi.org/10.1002/smt.202000366>
- 6 Apel, P. Yu. (2013). Track-Etching. *Encyclopedia of Membrane Science and Technology*, 1–25. Portico. <https://doi.org/10.1002/9781118522318.emst040>
- 7 Karl, D. M. (2007). Plastics-irradiated-etched: The Nuclepore® filter turns 45 years old. *Limnology and Oceanography Bulletin*, 16(3), 49–54. Portico. <https://doi.org/10.1002/lob.200716349>
- 8 Ulbricht, M. (2006) Advanced functional polymer membranes. *Polymer*, 47(7), 2217–62. <https://doi.org/10.1016/j.polymer.2006.01.084>
- 9 Ilić, R., Skvarč, J., Golovchenko, A.N. (2003) Nuclear tracks: Present and future perspectives. *Radiat Meas*, 36, 83–88. [https://doi.org/10.1016/S1350-4487\(03\)00247-6](https://doi.org/10.1016/S1350-4487(03)00247-6)
- 10 Arsalan, M., Akhtar, S., & Khan, M. E. (2024). Synthetic composite membranes and their manifold applications: A comprehensive review. *Journal of Polymer Science and Engineering*, 7(2), 8211. <https://doi.org/10.24294/jpse8211>
- 11 Mashentseva, A.A., Sutekin, D.S., Rakisheva, S.R., Barsbay, M. (2024) Composite Track-Etched Membranes: Synthesis and Multifaced Applications. *Polymers*, 16(18), 2616. <https://doi.org/10.3390/polym16182616>
- 12 Vo, T.S., Lwin, K.M. & Kim, K. (2024) Recent developments of nano-enhanced composite membranes designed for water/wastewater purification—a review. *Adv Compos Hybrid Mater*, 7, 127. <https://doi.org/10.1007/s42114-024-00923-5>
- 13 Green, L., Ojemaye, C., Petrik, L., Barnes, J., Solomon, N., Beukes, A., Farr, V., Zackon, M. (2025) Contaminant Denialism in Water Governance. *Water Resour Res*, 61(7) <https://doi.org/10.1029/2024WR037875>
- 14 Rossouw, A. (2022) Planar magnetron sputtering of Ti and TiO<sub>2</sub> for polyethylene terephthalate track-etched membrane surface modification. Stellenbosch, Stellenbosch University. Available from: <https://scholar.sun.ac.za/items/776099bb-a955-4e49-b5fe-3ee44cb35052>
- 15 Rossouw, A., Kristavchuk, O., Olejniczak, A., Bode-Aluko, C., Gorberg, B., Nechaev, A., Petrik, L., Perold, W., Apel, P.. (2021) Modification of polyethylene terephthalate track etched membranes by planar magnetron sputtered Ti/TiO<sub>2</sub> thin films. *Thin Solid Films*, 725, 138641. <https://doi.org/10.1016/j.tsf.2021.138641>
- 16 Artoshina, O. V., Milovich, F.O., Rossouw, A., Gorberg, B.L., Iskhakova, L.D., Ermakov, R.P., Semina, V.K., Kochnev, Yu.K., Nechaev, A.N., Apel, P.Yu. (2016) Structure and phase composition of thin TiO<sub>2</sub> films grown on the surface of metallized track-etched polyethylene terephthalate membranes by reactive magnetron sputtering. *Inorg Mater*, 52(9), 945–54. <https://doi.org/10.1134/S0020168516080021>
- 17 Artoshina, O.V., Rossouw, A., Semina, V.K., Nechaev, A.N., Apel, P.Yu. (2015). Structural and physicochemical properties of titanium dioxide thin films obtained by reactive magnetron sputtering, on the surface of track-etched membranes. *Petrol Chem*, 55(10), 759–68. <https://doi.org/10.1134/S0965544115100011>
- 18 Rossouw, A., Olejniczak, A., Olejniczak, K., Gorberg, B., Vinogradov, I., Kristavchuk, O., Nechaev, A., Petrik, L., Perold, W., Dmitriev, S. (2022). Ti and TiO<sub>2</sub> magnetron sputtering in roll-to-roll fabrication of hybrid membranes. *Surf Interf*, 31, 101975. <https://doi.org/10.1016/j.surf.2022.101975>
- 19 Perea, O., Uche, C., Bublikov, P.S., Bode-Aluko, C., Rossouw, A., Vinogradov, I.I., Nechaev, A.N., Opeolu, B., Petrik, L. (2021). Chitosan/PEO nanofibers electrospun on metallized track-etched membranes: fabrication and characterization. *Mater Today Chem*, 20, 100416. <https://doi.org/10.1016/j.mtchem.2020.100416>
- 20 Vinogradov, I.I., Petrik, L., Serpionov, G.V., Nechaev, A.N. (2021) Composite Membrane Based on Track-Etched Membrane and Chitosan Nanoscaffold. *Membr Membr Technol*, 3(6):400–10. <https://doi.org/10.1134/S2517751621060093>

- 21 Bode-Aluko, C.A., Pereao, O., Ameh, A.E., Omoniyi, E., Nechaev, A., Petrik, L. (2025). Removal of rhodamine 6G from aqueous solution in a continuous mode using nano-micro composite membranes. *Nano Trends*, 9, 100096. <https://doi.org/10.1016/j.nwnano.2025.100096>
- 22 Ademola Bode-Aluko, C., Pereao, O., Kyaw, H.H., Al-Naamani, L., Al-Abri, M.Z., Tay Zar Myint, M., Rossouw, A., Fato-ba, O., Petrik, L., Dobretsov, S. (2021). Photocatalytic and antifouling properties of electrospun TiO<sub>2</sub> polyacrylonitrile composite nanofibers under visible light. *Mater Sci Eng, B* 264, 114913. <https://doi.org/10.1016/j.mseb.2020.114913>
- 23 Zhang, L., Sun, F., Zuo, Y., Fan, C., Xu, S., Yang, S., Gu, F. (2014). Immobilisation of CdS nanoparticles on chitosan micro-spheres via a photochemical method with enhanced photocatalytic activity in the decolourisation of methyl orange. *Appl Catal B*, 156–157, 293–300. <https://doi.org/10.1016/j.apcatb.2014.03.015>
- 24 Ndilowe, G.M., Bode-Aluko, C.A., Chimponda, D., Kristavchuk, O., Kochnev, I., Nechaev, A., Petrik, L. (2021). Fabrication of silver-coated PET track-etched membrane as SERS platform for detection of acetaminophen. *Colloid Polym Sci*, 299(11), 1729–1741. <https://doi.org/10.1007/s00396-021-04900-y>
- 25 Rossouw, A., Artoshina, O. V., Nechaev, A. N., Apel, P. Yu., Petrik, L., Perold, W. J., & Pineda-Vargas, C. A. (2014). Stable Ion Beam Analysis (RBS and PIXE) Study of Photocatalytic Track-Etched Membranes. *Exotic Nuclei*, 591–596. [https://doi.org/10.1142/9789814632041\\_0065](https://doi.org/10.1142/9789814632041_0065)
- 26 Rossouw, A., Vinogradov, I.I., Serpionov, G.V., Gorberg, B.L., Molokanova, L.G., Nechaev, A.N. (2022). Composite Track Membrane Produced by Roll Technology of Magnetron Sputtering of Titanium Nanolayer. *Membr Membr Technol*, 4(3), 177–188. <https://doi.org/10.1134/S2517751622030039>
- 27 Ponomareva, O.Y., Drozhzhin, N.A., Vinogradov, I.I., Vershinina, T.N., Altynov, V.A., Zuba, I., Nechaev A.N., Pawlukojć, A. (2024) Metal–Organic Framework Based on Nickel, L-Tryptophan, and 1,2-Bis(4-Pyridyl)Ethylene, Consolidated on a Track-Etched Membrane. *Russian J Inorg Chem*, 69(6), 914–924. <https://doi.org/10.1134/S0036023624600667>
- 28 Mashentseva, A.A., Barsbay, M., Zdorovets, M. V., Zheltov, D.A., Güven, O. (2020). Cu/CuO Composite Track-Etched Membranes for Catalytic Decomposition of Nitrophenols and Removal of As(III). *Nanomaterials*, 10(8), 1552. <https://doi.org/10.3390/nano10081552>
- 29 Torati, S.R., Reddy, V., Yoon, S.S., Kim, C.G. (2016). Electrochemical biosensor for Mycobacterium tuberculosis DNA detection based on gold nanotubes array electrode platform. *Biosens Bioelectron*, 78, 483–488. <https://doi.org/10.1016/j.bios.2015.11.098>
- 30 Petrik, L.F., Fato-ba, O.O., Ndilowe, G.M., Omoniyi, E.O., Chimponda, D., Bode-Aluko, C.A. (2020). Emerging and Persistent Contaminants/Pathogens: Monitoring Methods Development. Water Research Commission, Pretoria. WRC Report. Available from: [www.wrc.org.za](http://www.wrc.org.za)
- 31 Bode-Aluko, C.A., Laatikainen, K., Pereao, O., Nechaev, A., Kochnev, I., Rossouw, A., Dobretsov, S., Branger, C., Sarbu, A., Leslie Petrik, L. (2019). Fabrication and characterisation of novel nanofiltration polymeric membrane. *Mater Today Commun*, 20, 100580. <https://doi.org/10.1016/j.mtcomm.2019.100580>
- 32 Pereao, O., Bode-Aluko, C., Laatikainen, K., Nechaev, A., Petrik, L. (2019). Morphology, Modification and Characterisation of Electrospun Polymer Nanofiber Adsorbent Material Used in Metal Ion Removal. *J Polym Environm*, 27(9), 1843–1860. <https://doi.org/10.1007/s10924-019-01497-w>
- 33 Mashentseva, A.A., Barsbay, M., Aimanova, N.A., Zdorovets, M.V. (2021). Application of Silver-Loaded Composite Track-Etched Membranes for Photocatalytic Decomposition of Methylene Blue under Visible Light. *Membranes*, 11, 60. <https://doi.org/10.3390/membranes11010060>
- 34 Nie, J., Wang, Z., Hu, Q. (2016). Chitosan Hydrogel Structure Modulated by Metal Ions. *Sci Rep*, 6, 36005. <https://doi.org/10.1038/srep36005>
- 35 Hsu, C.Y., Ajaj, Y., Mahmoud, Z.H., Kamil Ghadir, G., Khalid Alani, Z., Hussein, M.M., Hussein, S.A., Karim, M.M., Al-khalidi, A., Abbas, J.K., Kareem, A.H., Ehsan Kianfar. (2024). Adsorption of heavy metal ions use chitosan/graphene nanocomposites: A review study. *Results Chem*, 7, 101332. <https://doi.org/10.1016/j.rechem.2024.101332>
- 36 Pereao, O., Bode-Aluko, C., Fato-ba, O., Laatikainen, K., Petrik, L. (2018) Rare earth elements removal techniques from water/wastewater: a review. *Desalination Water Treat*, 130, 71–86. <https://doi.org/10.5004/dwt.2018.22844>
- 37 Tshisano, K., Mukaba, J.L., Pereao, O., Mouele, E.S.M., Rossouw, A., Drozhzhin, N., Nechaev, A.N., Tshentu, Z., Petrik, L., Bladergroen, B. (2025). Functionalized Polyethylene Terephthalate Nanofiber Adsorbents for Prospective Metal Recovery from Spent Lithium-Ion Batteries. *Water Air Soil Pollut*, 236(6), 1–15. <https://doi.org/10.1007/s11270-025-07992-2>
- 38 Fouda-Mbanga, B.G., Velepini, T., Pillay, K., Tywabi-Ngeva, Z. (2024). Heavy metals removals from wastewater and re-use of the metal loaded adsorbents in various applications: A review. *Hybrid Advances*, 6, 100193. <https://doi.org/10.1016/j.hybadv.2024.100193>
- 39 Kravets, L.I., Yarmolenko, M.A., Rogachev, A.V., Gainutdinov, R.V., Altynov, V.A., Lizunov, N.E. (2022). Formation of Hydrophobic and Superhydrophobic Coatings on Track-Etched Membrane Surfaces to Create Composite Membranes for Water Desalination. *Colloid J*, 84(4), 427–444. <https://doi.org/10.1134/S1061933X22040081>
- 40 Mashentseva, A., Borgekov, D., Kislitsin, S., Zdorovets, M., Migunova, A. (2015). Comparative catalytic activity of PET track-etched membranes with embedded silver and gold nanotubes. *Nucl Instrum Methods Phys Res B*, 365, 70–74. <https://doi.org/10.1016/j.nimb.2015.07.063>
- 41 Li, P.F., Xie, R., Jiang, J.C., Meng, T., Yang, M., Ju, X.J., Yang, L., Chu, L.-Y. (2009). Thermo-responsive gating membranes with controllable length and density of poly(N-isopropylacrylamide) chains grafted by ATRP method. *J Membr Sci*, 337(1–2), 310–317. <https://doi.org/10.1016/j.memsci.2009.04.010>

- 42 Muslimova, I.B., Zhatkanbayeva, Z.K., Omertasov, D.D., Melnikova, G.B., Yeszhanov, A.B., Güven, O., Chizhik, S.A., Zdorovets, M.V. and Korolkov, I.V. (2023). Stimuli-Responsive Track-Etched Membranes for Separation of Water–Oil Emulsions. *Membranes*, 13(5), 523. <https://doi.org/10.3390/membranes13050523>
- 43 Adeniyi, O.R. (2015). Swift heavy ion irradiation of polyester and polyolefin polymeric film for gas separation application. University of the Western Cape. Available from: <https://hdl.handle.net/10566/14679>
- 44 George, J.H., Nagel, D., Waller, S., Hill, E., Parri, H.R., Coleman, M.D., Cui, Z., Ye, H. (2018). A closer look at neuron interaction with track-etched microporous membranes. *Sci Rep*, 8, 15552. <https://doi.org/10.1038/s41598-018-33710-6>
- 45 Markov, P.A., Vinogradov, I.I., Kostromina, E., Eremin, P.S., Gilmudinova, I.R., Kudryashova, I.S., Greben, A., Rachin, A.P., Nechaev, A.N. (2022). A wound dressing based on a track-etched membrane modified by a biopolymer nanoframe: physico-chemical and biological characteristics. *Eur Polym J*, 181, 111709. <https://doi.org/10.1016/j.eurpolymj.2022.111709>
- 46 Salah, I., Allan, E., Nair, S.P., Parkin, I.P. (2024) Antibacterial performance of a copper nanoparticle thin film. *Nano Select*, 5(9), 2300134. <https://doi.org/10.1002/nano.202300134>
- 47 Malunga, S.M., Chaukura, N., Mbiriri, C.I., Gwenzi, W., Moyo, M., Kuvarega, A.T. (2022). Visible light photodegradation of methyl orange and *Escherichia coli* O157:H7 in wastewater. *S Afr J Sci*, 118(1–2), 10938. <https://doi.org/10.17159/sajs.2022/10938>
- 48 Omertassov, D.D., Shakayeva, A.K., Zhatkanbayeva, Z.K., Shakirzyanov, R.I., Zdorovets, M.V., Güven, O., Korolkov, I.V. (2025). HKUST-1 Synthesis in PET Track-Etched Membranes via Conversion of Deposited Cu for Carbon Dioxide Capture. *ACS Omega*, 10, 30271. <https://doi.org/10.1021/acsomega.5c01493>
- 49 Lee, D., Lee, Y., Choi, S.S., Lee, S.H., Kim, K.W., Lee, Y. (2019). Effect of membrane property and feed water organic matter quality on long-term performance of the gravity-driven membrane filtration process. *Envir Sci Pollut Res*, 26(2), 1152–1162. <https://doi.org/10.1007/s11356-017-9627-8>
- 50 Apel, P.Y., Bobreshova, O.V., Volkov, A.V., Volkov, V.V., Nikonenko, V.V., Stenina, I.A., Filippov, A.N., Yampolskii, Yu. P., Yaroslavlsev, A.B. (2019). Prospects of Membrane Science Development. *Membr Membr Technol*, 2019 1(2), 45–63. <https://doi.org/10.1134/S2517751619020021>



## MODIFICATION AND DEVELOPMENT OF NEW TYPES OF TEMs








### Article

Received: 27 May 2025 | Revised: 5 September 2025 |

Accepted: 9 September 2025 | Published online: 21 September 2025

UDC 66.081.6-278

<https://doi.org/10.31489/2959-0663/3-25-9>

Angelina V. Kryukova-Seliverstova<sup>1</sup>, Oleg L. Orelovich<sup>2</sup>, Vladimir A. Altynov<sup>2</sup>,  
Alexander V. Akimov<sup>3</sup>, Alexander S. Shmakov<sup>3</sup>, Daria V. Nikolskaya<sup>2</sup>,  
Nikita S. Kirilkin<sup>2</sup>, Uliana V. Pinaeva<sup>2\*</sup>

<sup>1</sup>Dubna State University, Dubna, Russia;

<sup>2</sup>Flerov Laboratory of Nuclear Reactions, Joint Institute for Nuclear Research, Dubna, Russia;

<sup>3</sup>Federal Research Center of Problems of Chemical Physics and Medicinal Chemistry RAS, Chernogolovka, Russia

(\*Corresponding author's e-mail: [pinaeva@jinr.ru](mailto:pinaeva@jinr.ru))

### Radiation Grafting of PVDF Track-Etched Membranes: A Study for Nanoscale Pore Functionalization

Functionalization of nanoporous membranes poses a substantial challenge in the development of advanced materials for selective transport applications. The primary objective of this study is to optimize the grafting process to ensure the functionalization is localized onto nanopore walls. Poly(vinylidene fluoride) (PVDF) foils were irradiated with Xe ions (1.2 MeV/u) followed by subsequent etching under optimized conditions to create nanoporous membranes. Radiation grafting of acrylic acid (AA) monomer was performed through the residual radical sites in post-etched pore walls of ion-irradiated PVDF. Radical concentrations after irradiation were quantified using EPR spectroscopy. Examination of reaction parameters including inhibitor concentration, temperature, monomer concentration, and reaction kinetics was conducted to achieve selective grafting within the nanopores. FT-IR and XPS analyses confirmed the successful covalent attachment of poly(acrylic acid) (PAA) to the PVDF TMs. Structural transformations of the PVDF matrix throughout the functionalization process were revealed by DSC analysis. The versatility of the approach was further demonstrated by grafting of pH-responsive poly(4-vinylpyridine), enabling modulation of nanopore surface charge, as evidenced by zeta-potential measurements. The spatial localization of the grafted polymer was confirmed by confocal fluorescence microscopy, demonstrating the potential for creating advanced functional membranes for separation and sensing applications.

**Keywords:** swift heavy ions, track-etched membranes, polyvinylidene fluoride, radiation grafting, acrylic acid, nanoporous membranes, pore functionalization, ion-irradiated

### Introduction

Radiation-induced grafting offers a versatile approach for tailoring polymer properties by creating active sites for monomer polymerization using ionizing radiation. Its adaptability to various polymers, monomers, and reaction conditions, through methods like direct, pre-irradiation, or peroxidation grafting, allows for tailoring of functionalities, such as hydrophilicity or chemical reactivity, onto surfaces or within the bulk material without requiring any contaminating reagents [1].

Poly(vinylidene fluoride) (PVDF) is a fluoropolymer that has garnered significant attention due to its excellent mechanical strength, thermal stability, chemical resistance, and electroactive properties [2]. The development of nanostructured and functionalized PVDF materials is particularly important as it strengthens these inherent properties while introducing new functionalities [3]. For instance, creating nanoporous PVDF membranes through swift heavy ion (SHI) irradiation followed by chemical etching allows for precise tuning

of pore size and geometry [4]. Subsequent functionalization of these nanopores through grafting imparts customized surface chemistries, enhancing performance in applications requiring high selectivity and controlled transport, such as advanced sensors, responsive biomedical implants, and proton-exchange membranes [5, 6].

Radiation grafting of vinyl monomers onto fluoropolymers has been extensively explored since Chapiro's seminal works in the 60s [7, 8]. Studies on radiation grafting of hydrophilic monomers, including acrylic acid (AA), onto polytetrafluoroethylene (PTFE) films to create permselective membranes, highlighted the challenges in controlling homopolymerization and the importance of solvent selection [9]. Ellinghorst et al. [10] described radiation-initiated grafting on PVDF films with AA, emphasizing the importance of achieving "grafting through" for homogeneous membrane properties. More recent studies by Betz, Clochard, Mazzei, and colleagues [11–14] have focused on grafting of styrene and (meth)acrylates onto PVDF, using electron-beam irradiated foils and SHI-etched tracks in PVDF. These works have investigated the influence of monomer concentration, inhibitor presence, and the role of water in achieving surface or grafting through. Mazzei et al. [15] and Cuscito et al. [16] specifically reported on AA grafting onto etched ion tracks in PVDF, demonstrating that residual active sites within the pores can successfully initiate graft polymerization reaction. The method was later enhanced by Barsbay et al. [17], employing RAFT-mediated radical polymerization to graft poly(acrylic acid) (PAA) into the nanochannel walls of track-etched PVDF for the controlled adjustment of nanopore size. Although these studies successfully demonstrated the feasibility of pore grafting approach, a comprehensive optimization of key radiation grafting parameters is still needed for further development of functional membranes.

The present study aims to investigate the radiation-induced graft polymerization process of AA monomer within the nanopores of PVDF track-etched membranes (TMs), built upon the established methodology of initiation through the residual active sites. Radical concentration after irradiation with xenon ion beam was quantified using EPR spectroscopy. A refined chemical etching protocol is reported, achieving a substantial decrease in oxidizer utilization. The effects of key variables on the grafting yield were examined, including inhibitor concentration, monomer concentration, temperature, and reaction kinetics. Covalent attachment of PAA to PVDF TMs was confirmed through FT-IR and XPS analyses, while enhanced hydrophilicity was verified by contact angle measurements. DSC analysis was employed to follow structural changes in PVDF throughout the functionalized membrane fabrication process. Most crucially, localized grafting within nanopores was demonstrated through zeta-potential measurements and confocal fluorescence microscopy. It is anticipated that this work will stimulate further research, thereby providing the basis for the design of advanced materials for use in energy, biomedical, and separation technologies.

## Experimental

### Materials

A polyvinylidene fluoride (PVDF) film with a thickness of 9  $\mu\text{m}$  was procured from Kureha Chemical Industries Co. Ltd. (Japan). The film exhibited a crystallinity degree of approximately 40 %, as measured by X-ray diffraction (XRD), with the dominant crystalline phase identified as the  $\alpha$ -phase and a minor contribution from the  $\beta$ -phase, as confirmed by Fourier-transform infrared (FT-IR) spectroscopy. Functionalized PVDF track-etched membranes (TMs) were synthesized using the following reagents: potassium hydroxide (KOH), potassium permanganate ( $\text{KMnO}_4$ ), sodium metabisulfite ( $\text{Na}_2\text{S}_2\text{O}_5$ ), acrylic acid (AA) monomer, and Mohr's salt ( $(\text{NH}_4)_2\text{Fe}(\text{SO}_4)_2 \cdot 6\text{H}_2\text{O}$ ). To emphasize the localized grafting through zeta-potential assessment, 4-vinylpyridine (4VP) radiation grafting was performed. For photoluminescence (PL) measurements, carboxylic acid activation of PVDF TMs was done to couple ethylenediamine (EDA) using 1-ethyl-3-(3-dimethylaminopropyl)carbodiimide (EDC) and N-hydroxysuccinimide (NHS) prior to grafting with PAA. All chemicals were purchased from Thermo Scientific (USA) and Chemreaktivsnab (Russia), and used as received. Deionized water (Milli-Q, resistivity  $\geq 18 \text{ M}\Omega \cdot \text{cm}$ ) was used for preparing all aqueous solutions.

### Swift Heavy Ion (SHI) Irradiation

PVDF foils were irradiated with  $^{132}\text{Xe}^{26+}$  ions (1.2 MeV/u) under vacuum using the IC-100 cyclotron at the Flerov Laboratory of Nuclear Reactions, Joint Institute for Nuclear Research (Dubna, Russia). The ion beam was oriented perpendicular to the film surface. The ion fluence, which is related to the resulting track density in the irradiated samples, varied from  $10^7$  to  $10^{10}$  ions/ $\text{cm}^2$ . The electronic stopping power ( $\Delta E_e/\Delta x$ ) estimation was made with the SRIM-2013. The average electronic energy loss for xenon ions (160 MeV) traversing the PVDF target with a density of  $1.78 \text{ g/cm}^3$  was determined to be approximately  $77.3 \text{ MeV} \cdot \text{cm}^2/\text{mg}$ , which is well above the registration threshold for fluoropolymers [18]. To mitigate post-

irradiation oxidative degradation, all irradiated samples were stored in hermetically sealed containers under a dry nitrogen atmosphere at  $-24\text{ }^{\circ}\text{C}$  until further use.

#### *Chemical Etching of Ion Tracks*

Chemical etching was performed to remove SHI-degraded material and to transform latent tracks into cylindrical through-nanopores. The process was conducted in an aqueous solution containing 10 M KOH and 0.1 M  $\text{KMnO}_4$  at  $65\text{ }^{\circ}\text{C}$  for 30 minutes (unless stated otherwise). The diameter of the resulting pores was  $45\pm 5\text{ nm}$  as determined by Scanning electron microscopy (SEM). To eliminate residual of  $\text{KMnO}_4$ , the track-etched membranes (TMs) were treated with an aqueous solution of  $\text{Na}_2\text{S}_2\text{O}_5$  (7.5 % w/v), thoroughly rinsed with deionized water, air-dried at room temperature, and weighted.

#### *Radiation Grafting of Acrylic Acid to PVDF TMs*

Radiation grafting reaction of acrylic acid (AA) was performed *via* a pre-irradiation method, initiated by residual trapped radicals remained in PVDF matrix after chemical etching. Most of the grafting experiments were performed on PVDF foils irradiated at the fluence of  $10^{10}\text{ cm}^{-2}$  (unless stated otherwise). Experimental data is presented as the mean value with error bars representing the standard deviation from at least three independent replicate experiments ( $n \geq 3$ ). Freshly etched TMs were immersed into custom-made glass Schlenk tubes containing an AA monomer solution (with or without Mohr's salt to suppress homopolymerization). In grafting experiments involving the use of Mohr's salt, the latter was grinded in fine powder and was first dissolved in water followed by the addition of AA monomer to yield the needed monomer solution concentration. The monomer solution was purged with argon for 20 minutes to remove dissolved oxygen. The tubes were then hermetically sealed and placed in a thermostated water bath at  $60\text{ }^{\circ}\text{C}$  for predetermined reaction times. After polymerization, grafted samples were thoroughly rinsed with deionized water, extracted in a Soxhlet apparatus with  $\sim 200\text{ mL}$  of boiling water for 12 hours, dried to constant weight, and weighed. The gravimetric grafting yield (GY) was calculated using equation

$$GY = \frac{m_f - m_0}{m_0} \times 100\%,$$

where  $m_0$  and  $m_f$  represent the masses of dry membranes before and after grafting, respectively.

#### *Characterization of PAA-g-PVDF TMs*

Radiation grafting of AA to PVDF TMs was monitored by Fourier-Transform Infrared spectroscopy (FT-IR) and X-ray Photoelectron Spectroscopy (XPS). FT-IR spectra were registered in attenuated total reflectance (ATR) and transmission modes on a Nicolet spectrometer (Thermo Scientific) with 32 scans and a resolution of  $1\text{ cm}^{-1}$ . XPS spectra were acquired using a Thermo Scientific K-Alpha spectrometer with monochromatic Al  $\text{K}\alpha$  X-rays ( $1486.6\text{ eV}$ ,  $12\text{ kV}$ ,  $3\text{ mA}$ ). Binding energies were calibrated against the C 1s peak ( $284.8\text{ eV}$ ). Survey scans ( $100\text{ eV}$  pass energy,  $0.5\text{ eV}$  step) and high-resolution spectra ( $20\text{ eV}$  pass energy,  $0.05\text{ eV}$  step) were collected and processed using the Advantage software.

Surface morphology and pore diameters were assessed by Field Emission Scanning Electron Microscopy (FESEM) on a HITACHI SU8020 instrument. Prior to imaging, samples were coated with a  $5\text{ nm}$  platinum/palladium layer using a Quorum Q150R magnetron sputtering machine to enhance the sample conductivity. Experimental data is provided as mean values with standard deviations determined from at least 30 pores.

Electron Paramagnetic Resonance (EPR) spectra of Xe-irradiated PVDF foils were recorded using a Bruker ElexSys II E500 X-band spectrometer ( $9.5\text{ GHz}$ ). Samples ( $3\text{--}5\text{ mg}$ ,  $\sim 7\times 30\text{ mm}$ ) were rolled into tubes, sealed in quartz ampoules under argon, and immediately cooled in a liquid nitrogen cryostat. Spectra were acquired between  $100\text{--}300\text{ K}$  with a microwave power of  $6.325\text{ mW}$  ( $15\text{ dB}$  attenuation),  $100\text{ kHz}$  modulation frequency, and  $1\text{ Gauss}$  modulation amplitude.

Photoluminescence (PL) measurements were performed on Rhodamine 6G-adsorbed PAA-g-PVDF TMs using a confocal microscope Ntegra Spectra NT-MDT equipped with a  $473\text{ nm}$  laser ( $0.2\text{ mW}$ ) and a  $100\times$  objective lens. Scans were recorded over a  $10\times 10\text{ }\mu\text{m}^2$  area with number of points of 50 along X and Y axes. Optical images were captured through a camera integrated into the transmission optical path.

Differential scanning calorimetry (DSC) measurements were performed using a Mettler Toledo DSC 3 instrument with aluminum crucibles under dynamic heating conditions from  $-50$  to  $200\text{ }^{\circ}\text{C}$  at a rate of  $10\text{ }^{\circ}\text{C}/\text{min}$  under nitrogen flow ( $10\text{ mL}/\text{min}$ ).

Contact angle ( $\theta$ ) measurements were conducted using a KRÜSS DSA100 Easy Drop system and Drop Shape Analysis software. Five 3  $\mu\text{L}$  droplets of Milli-Q water were deposited on each sample, and  $\theta$  values were averaged. All values represent the mean of at least ten independent measurements ( $n = 10$ ).

The membrane zeta-potentials ( $\zeta$ ) before and after radiation grafting of PVDF TMs were assessed through the measurements of streaming potential using a custom-made flow cell. The membrane sample (25 mm in diameter) was clamped between the two cell compartments with Ag/AgCl electrodes positioned on either side of the membrane, ensuring a leak-free seal for the pressure-driven flow. The measurements were carried out in a 0.01 M KCl at pH 3, 5, 6.5, and 8 under applied pressures 0–1 bar and confirmed by three consecutive runs. The  $\zeta$ -potentials ( $V$ ) were calculated using the Helmholtz–Smoluchowski equation:

$$\zeta = \frac{k \times \eta}{\varepsilon \times \varepsilon_0} \times \frac{\Delta E}{\Delta P},$$

where  $k$  is the electrolyte specific conductivity ( $\text{Ohm}^{-1} \cdot \text{m}^{-1}$ ),  $\eta$  is the electrolyte dynamic viscosity ( $\text{Pa} \cdot \text{s}$ );  $\varepsilon_0$  and  $\varepsilon$  are the dielectric permittivity of vacuum ( $8.854 \times 10^{-12} \text{ C} \cdot \text{V}^{-1} \cdot \text{m}^{-1}$ ) and the relative permittivity of electrolyte (dimensionless), respectively,  $\Delta E/\Delta P$  is the streaming potential-to-pressure gradient ratio ( $\text{V}/\text{Pa}$ ).

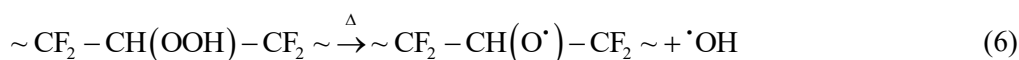
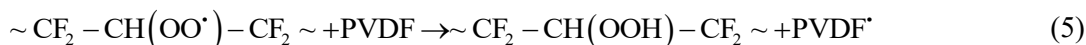
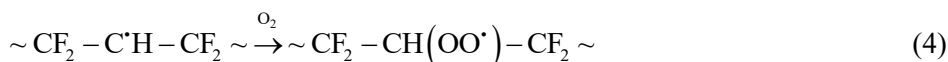
### Results and Discussion

#### SHI-Induced Changes and Generation of Initiators for Graft Polymerization in PVDF

At the ion energy used in this work (1.2 MeV/u), swift heavy ions (SHIs) lose their energy by means of electronic loss processes, but the damage is limited to the ion path. This distinguishes SHI irradiation from electron-beam or  $\gamma$ -rays, where the energy is “homogeneously” distributed. Energy absorption causes excitation and ionization of electrons in the outer shells of atoms, resulting in chemical bond scissions all along the projectile ion pathways. As a primary effect, alkyl in-chain (eq. 1 and 2) and end-chain radicals (eq. 3) are formed



As a result of contact with oxygen, some of the alkyl radicals can undergo oxidation to form peroxy radicals (eq. 4). These peroxy radicals can further form hydroperoxides upon H-abstraction from the PVDF backbone (eq. 5). The hydroperoxides thermally decompose into alkoxy and hydroxyl radicals (eq. 6)



In addition to oxidation, further radical reactions will define the final structure of SHI-irradiated PVDF. These include dehydrofluorination and disproportionation accompanied by the formation of  $\text{C}=\text{C}$  bonds, recombination to form cross-links in the polymer and gas molecules ( $\text{H}_2$ ,  $\text{F}_2$ , and  $\text{HF}$ ), H-abstraction, *etc.* Indeed, FT-IR confirmed the appearance of vinylidene groups  $-\text{FC}=\text{CH}_2$  and  $-\text{HC}=\text{CF}_2$  ( $1755 \text{ cm}^{-1}$ ) [19] which were assumed to be a result of main-chain breakage, and  $-\text{FC}=\text{CH}-$  ( $1713 \text{ cm}^{-1}$ ) as a result of C–H scission (*dehydrofluorination*). UV-vis. spectroscopy (not shown) revealed that isolated dienes (absorption maxima at 220 nm) are formed in predominant amounts as a result of radiolysis of PVDF under these irradiation conditions, while the rate of formation of trienes and polyenes is about two and three times slower, respectively.

EPR spectroscopy results for samples irradiated at ion fluences ranging from  $10^9$  to  $3 \times 10^{10}$  ions/ $\text{cm}^2$  revealed a significant number of radical species centered on the  $g$ -factor  $g_e$  corresponding to a mixture of polyradicals (Fig. 1 (a)). This is in accordance with observations reported in the literature [20].

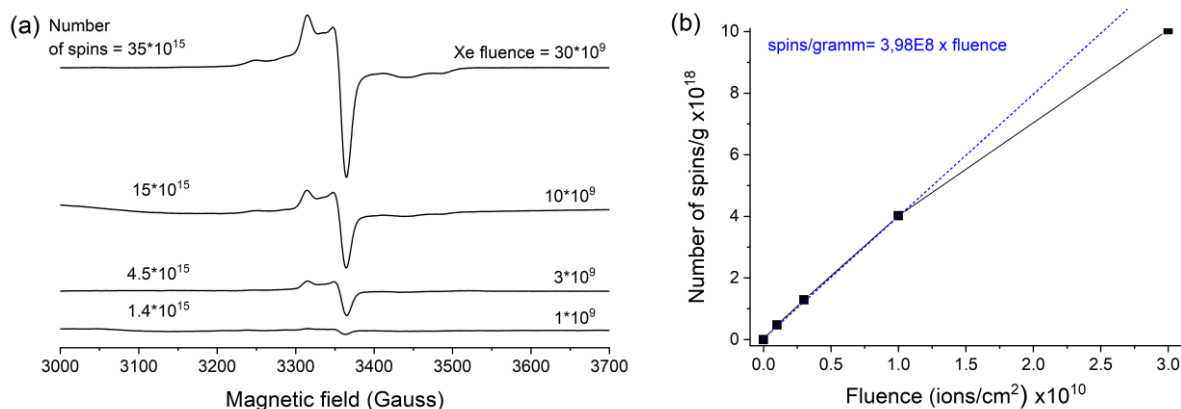


Figure 1. (a) EPR spectra of PVDF foils irradiated with Xe (1.2 MeV/u) at fluences from  $10^9$  to  $3 \times 10^{10}$  ions/cm<sup>2</sup> and (b) their corresponding number of radicals normalized by weight. All spectra were recorded at 200 K

Figure 1 (b) shows the dependence of the total number of radicals on ion fluence. Up to the fluence of  $10^{10}$  ions/cm<sup>2</sup>, a linear dependence is observed, followed by a deviation at higher fluences. Given the sample weight, polymer density and film thickness, the radical yield was found to be approximately equal to  $6 \times 10^5$  radicals per Xe ion. Spectral analysis allowed the identification of three types of radicals. These were: peroxy ( $-\text{CH}_2-\text{CFOO}^{\bullet}-\text{CH}_2-$ ), exhibiting the largest amplitude and accounting for approximately half of the total radical population; polyenyl ( $-\text{CH}=\text{C}^{\bullet}-\text{CH}_2-$ ) detected upon annealing (at room temperature under Ar atmosphere) as the number of peroxide radicals decreases; and alkyl in-chain/end-chain with single or double C-C/C=C bonds, exhibiting a broad, poorly structured spectrum, which constitute the remaining half of the total radical population [21–23]. An unexpected finding was the significant presence of peroxy radicals despite all the precautions taken to minimize the irradiated foil exposure to air. A possible explanation is the high amount of pre-adsorbed oxygen present in the foil prior to irradiation, which immediately reacts with the newly formed radical species.

These combined radiation-induced effects, including unsaturations as well as a free volume formed upon gas molecule production, make the latent tracks susceptible to chemical attack, allowing transformation into a porous structure.

#### *Chemical Etching of Xe-Irradiated PVDF Foils*

In this work, chemical etching of Xe-irradiated PVDF foils was carried out in a concentrated potassium hydroxide solution (10 M) in the presence of potassium permanganate as an oxidizing agent at 65 °C. Pioneering works conducted in the 1980s by Tretyakova and Shirkova on etching of heavy ion tracks in various fluoropolymers demonstrated that PVDF could be effectively etched using an excess of potassium permanganate under alkaline conditions [18, 24]. Grasselli and Betz [25] studied the effect of KOH concentration on the etching process. Their work, conducted in the presence of 0.25 M  $\text{KMnO}_4$ , demonstrated that high alkali concentration (9 M KOH) was essential for achieving well-defined porous structures. Additionally, it was demonstrated that etching temperatures between 55 and 65 °C were optimal for producing cylindrical pores. In contrast, higher temperatures (>85 °C) resulted in conical-shaped pores and lower temperatures (<50 °C) significantly slowed the chemical attack. For this reason the etching temperature in the current study was maintained in the range 60–65 °C.

The etching process was postulated to involve two consecutive steps [25]. The first step is an initial dehydrofluorination of the polymer structure induced by the alkaline environment, leading to the formation of C=C double bonds. The second step is the subsequent oxidative degradation of these double bonds by permanganate; this results in soluble low molecular weight compounds that are removed from the track regions. Indeed, due to the high electronegativity of fluorine, which “pulls” electron density away from neighboring carbon atoms, a high concentration of alkali catalyzes the dehydrofluorination of PVDF, resulting in the formation of  $-\text{CH}=\text{CF}-$ . In concentrated alkali,  $\text{KMnO}_4$  acts as a strong oxidizing agent capable of breaking C=C bonds and oxidizing them to carboxylic acid salts (for primary and secondary carbons). A double bond at a carbon in the tertiary position (for instance, in cross-linked track halo) oxidizes to ketones and carboxylic acid salts.

In this work, an attempt was made to lower the potassium permanganate concentration while retaining the same track etching efficiency, thereby optimizing the process from both technical and economic perspectives. Figure 2 (a) illustrates the effect of  $\text{KMnO}_4$  concentration in 10 M KOH aqueous solution on track etching rate.

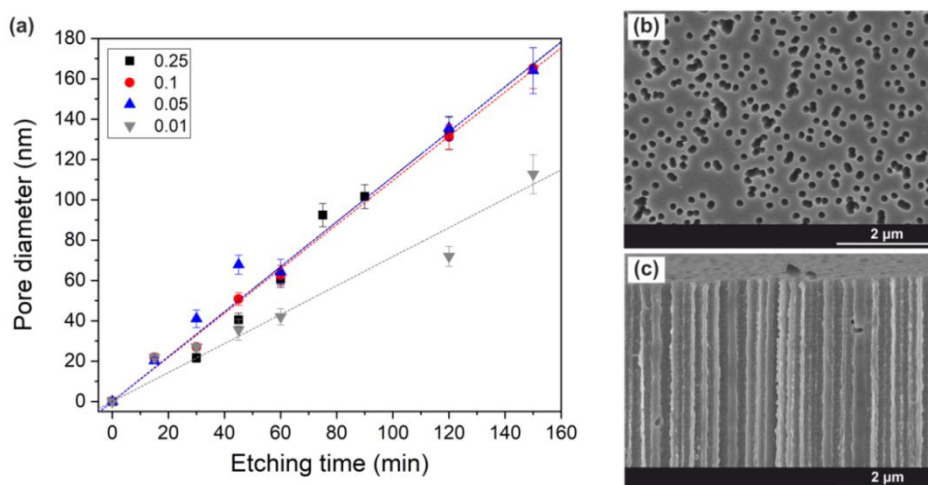


Figure 2. (a) Track etching rate of Xe-irradiated PVDF films as a function of  $\text{KMnO}_4$  concentration in 10 M KOH aqueous solution. SEM images of (b) surface and (c) cross-sectional views of the sample etched in 0.05 M  $\text{KMnO}_4$  (10 M KOH) at 63.5 °C for 120 min. Ion fluence:  $10^9$  ions/cm<sup>2</sup>

Prior to foil immersion in the etching solutions, they were pre-heated to correspond to the set etching temperature, ensuring consistent treatment conditions (63.5 °C). The track etching rate decreased from 1.1 nm/min to 0.7 nm/min when the  $\text{KMnO}_4$  concentration was reduced from 0.25 to 0.01 M, respectively. However, varying the permanganate concentration within the range of 0.25–0.05 M did not cause any significant difference. Notably, the best linear fit correlation was found for 0.1 M  $\text{KMnO}_4$ , indicating optimal process stability and reproducibility. Consequently, this concentration was selected for the fabrication of TMs in subsequent experiments.

Figures 2 (b) and (c) present SEM images of irradiated PVDF films etched in 10 M KOH with 0.05 M  $\text{KMnO}_4$ . The cross-sectional view clearly demonstrates the formation of through cylindrical channels under these etching conditions. These results confirm that the permanganate concentration can be reduced fivefold without sacrificing pore quality and presents a direct optimization of the process established in [25]. Beyond the evident economic and environmental benefits, the reduction of oxidizer concentrations can mitigate non-selective background oxidation, potentially affecting the membrane surface chemistry.

#### *Radiation Grafting of AA Within Nanopores of PVDF TMs*

Radiation-induced graft polymerization of AA onto etched tracks was carried out through pre-irradiation method. More specifically, a polymer substrate was irradiated under inert atmosphere and grafting reaction was initiated by radicals remained in the post-etched tracks. As seen from EPR results, the initiators of grafting include a mixture of alkyl radicals and their oxidized species. In earlier work [26] it was demonstrated that the integral amount of radicals trapped within PVDF etched tracks decays exponentially with etch time. The reason for such a decrease is that the longer the etching process, the larger the pores are formed, the less trapped radicals in track wall are remained. Grafting yield (GY), calculated as a weight of the grafted polymer over a weight of substrate (expressed in wt.%), for the studied allyl monomer rises as pore size enlarges up to the etch time of 35 min. This is followed by a decrease as the etch time exceeds 40 min. A 60 % radical consumption seen for TMs with a given pore size was accompanied with graft polymerization. Although, the first reports on AA grafting in heavy ion tracks were made about twenty years ago [27, 15], the understanding of effects affecting on grafting process of AA is still far from being complete. The following subsections will focus on key graft polymerization parameters, such as the effect of inhibitor, monomer concentration, reaction temperature, and time.



### Effect of Homopolymerization Inhibitor

The radiation grafting procedure involved immersing freshly etched nanoporous PVDF track-etched membranes (TMs) in aqueous solutions of acrylic acid (AA) monomer, followed by degassing and thermostating at 60 °C. Elevated temperature enhances the mobility of trapped radicals, improving their accessibility to the monomer. Simultaneously, it facilitates monomer diffusion toward active sites. However, these conditions also promote thermal homopolymerization of AA in solution, even when the monomer retains its standard stabilizer (MeHQ). Homopolymerization increases solution viscosity, limiting monomer availability and access to active sites within the nanopores. AA, like other acrylates, undergoes chain transfer reactions and exhibits fast polymerization kinetics, making GY control difficult.

To mitigate homopolymerization and slow down AA reactivity, ammonium ferrous sulfate (Mohr's salt) was employed. To emphasize the inhibition effect of Mohr's salt, a monomer concentration of 75 vol.% in water was chosen. This concentration was selected because the grafting rate is the fastest under such conditions and accompanied by a drastic expansion in the sample volume. Figure 3 illustrates the effect of Mohr's salt concentration on GY. The addition of the smallest quantity of Mohr's salt (0.05 %) caused a sharp decline in GY, reducing it by ca. 19 wt.% compared to inhibitor-free conditions (150 wt.%). Further increase in inhibitor concentration (0.1–0.5 %) resulted in a plateau, where GY remained largely unaffected by the additional inhibitor concentration increase. Mohr's salt acts as a radical scavenger through an electron transfer from  $\text{Fe}^{2+}$  to free radicals ( $\text{Fe}^{2+} + \text{R}^{\bullet} \rightarrow \text{Fe}^{3+} + \text{R}^{-}$ ), terminating both homopolymerization in the bulk solution and graft initiation at accessible radical sites. The drastic GY reduction at 0.05 % suggests efficient quenching of free radicals in the bulk solution and those in close proximity to the nanopore surface. The subsequent plateau reflects the radicals that remain shielded within the nanopore interior. There, steric hindrance and restricted diffusion limit  $\text{Fe}^{2+}$  penetration, thereby preserving grafting activity. This spatial heterogeneity in radical accessibility, with surface radicals being quenched while pore-confined radicals remain active, could explain the observed GY leveling-off at higher inhibitor concentrations.

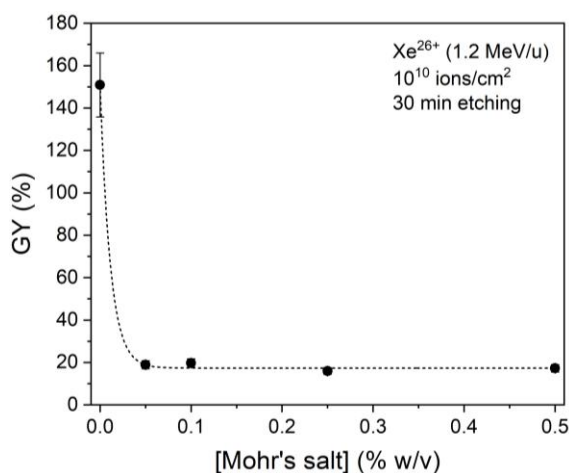


Figure 3. Dependence of the grafting yield (GY) on the Mohr's salt concentration (0–0.5 % w/v) in 75 vol.% AA aqueous solutions. Reaction conditions: 60 °C, 30 min

### Effect of Temperature and Monomer Concentration

The effect of reaction temperature on AA grafting was investigated at 55, 60, 65, and 70 °C. Higher temperatures typically enhance monomer diffusion and radical mobility within the polymer matrix, thereby accelerating grafting kinetics. However, the results revealed an optimal temperature range rather than a monotonic increase. GYs were comparable at 55 and 60 °C, representing the highest efficiency. Increasing the temperature to 65 °C resulted in a moderate decrease, and further elevation to 70 °C produced the lowest GY (not shown). Such temperature-dependent behavior indicates that excessive heating promotes competing processes. These include radical recombination (termination reactions) and thermal homopolymerization in solution, which reduce the availability of both radicals and monomer for grafting. Consequently, 60 °C was identified as the optimal temperature, providing an effective balance between enhanced diffusion kinetics and minimized side reactions. This is consistent with the range reported in [10] for AA grafting onto PVDF films.

Figure 4 (a) illustrates the effect of AA concentration (10–100 vol.% in water) on grafting efficiency, examined at 60 °C in the presence of 0.25 % Mohr's salt over 30 minutes reaction time. GY increased steadily with AA concentration up to 50 vol.%, followed by a significant enhancement at 75 vol.%, before declining at 100 vol.%. The observed trend with the maximum GY of ~22 % aligns with the behavior reported for electron-beam grafted PVDF films [12] and reflects the dual role of water in the grafting system.

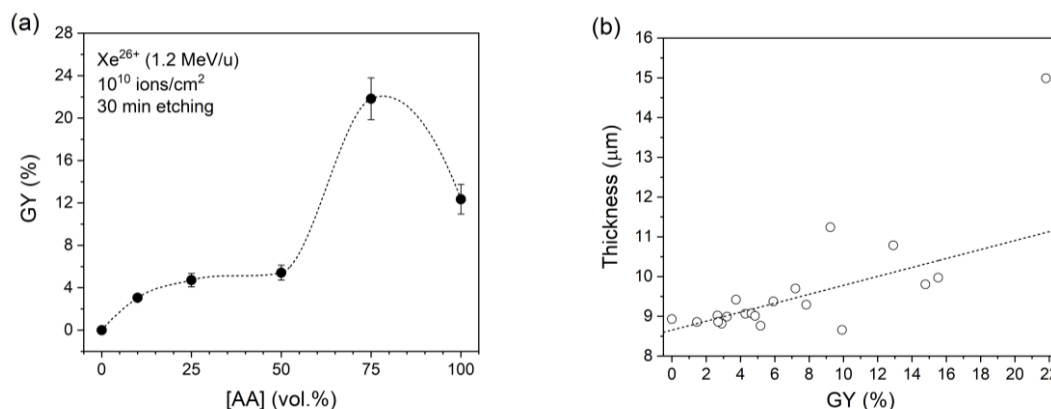


Figure 4. (a) Dependence of the grafting yield (GY) on the AA concentration in water. (b) Variation of sample average thickness as a function of GY. Mohr's salt concentration is 0.25 % w/v. Reaction conditions: 60 °C, 30 min

It serves not only as a solvent that facilitates monomer diffusion through the developing grafted polymer layer but also acts as a plasticizer for the PVDF, enhancing polymer chain mobility and accessibility of radical sites. Indeed, PVDF is a semi-crystalline polymer, and radicals generated during SHI irradiation can be localized in amorphous, crystalline or at the boundaries of crystalline/amorphous zones. The latter ones are expected to exhibit longer life-times, with their role in initiating graft polymerization being more significant than the radicals in amorphous zones. For continuous grafting, the monomer diffusion rate needs to be higher than the radical life-time. Furthermore, the monomer concentration must exceed its consumption during initiation and propagation. These factors, coupled with the enhanced swelling of PVDF in concentrated AA solutions (75 and 100 vol.%) [27], explain the observed grafting behavior. The decrease in GY at 100 vol.% AA aligns with literature reports indicating that PAA exhibits poor solubility in its monomer, leading to predominantly surface grafting rather than polymerization in bulk [10, 27].

Figure 4 (b) shows the correlation between GY and grafted membrane thickness. A GY of ~15 % from 100 vol.% AA results in approximately a 10 % thickness increase compared to the unmodified TM. In contrast, a GY of ~22 % from 75 vol.% AA led to about 60 % thickness expansion. This confirms that optimal water content is essential for achieving efficient pore-confined grafting. Based on these findings, pure AA is more suitable for achieving pore surface-localized functionalization. Diluted monomer solutions ( $\leq 50$  vol.%) promote pore wall grafting. Meanwhile, higher monomer concentrations (51 to 99 vol.%) enhance bulk graft polymerization throughout the pore walls, spreading into the bulk membrane structure.

#### Kinetics of Grafting

Figure 5 exhibits the grafting kinetics of AA to PVDF TMs in 50 and 75 vol.% AA solutions containing 0.25 % Mohr's salt at 60 °C. As shown, the GY progresses through two distinct phases: (I) a rapid increase with a maximum at 30–45 min, followed by (II) a gradual decline and asymptotic saturation at longer reaction times. This behavior persisted across monomer concentrations and was initially attributed to diffusion-controlled inhibitor effects. However, identical behavior was observed in diluted AA solutions ( $\leq 50$  vol.%) without any Mohr's salt.

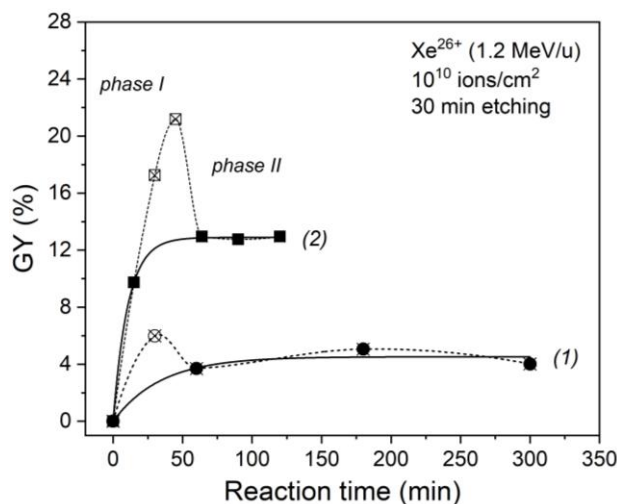


Figure 5. Grafting kinetics of AA to PVDF TMs at 60 °C. AA concentration is 50 (1) and 75 vol.% (2). Mohr's salt concentration is 0.25 % w/v. The spline connection of the experimental data highlights the behavior

During phase I, grafting acceleration arises from synergistic factors: (i) abundant radicals at pore surfaces initiate polymerization, (ii) unhindered AA diffusion into nanopores of water-plasticized PVDF, and (iii) hydrogen bonding between carboxyl groups of grafted PAA chains and incoming AA monomers, which locally enriches monomer concentration near reactive sites. These effects collectively maximize grafting efficiency during the initial stage. Subsequently, the observed decline (phase II) reflects both radical decay due to temperature-mediated recombination and consumption through grafting reactions. The apparent  $GY_{max}$  (empty crossed symbols) may be attributed to methodological artifacts: thermal polymerization of residual AA (diffused into PAA-g-PVDF) during post-grafting Soxhlet extraction in boiling water, inflating early GY measurements. This hypothesis was confirmed by using a more optimal washing procedure on grafted membranes. They were first soaked in water at room temperature for 12 hours, followed by extraction in boiling water. At longer reaction times, residual monomer diminishes. This leaves covalently grafted PAA as the primary contributor to the asymptotic plateau, which reflects a dynamic equilibrium between reduced grafting due to diffusion barriers and extractable homopolymer formation. The consistent behavior in inhibitor-free solutions confirms that pore confinement and post-processing artifacts are the primary drivers of the observed kinetic profile.

#### Characterization of PAA Nanopore-Grafted PVDF TMs

Figure 6 illustrates the FT-IR spectra of PVDF TMs before and after being grafted with PAA resulting in a GY of 22 %. The spectrum of pristine membrane (dashed line) includes: a doublet at 2985 and 3025  $\text{cm}^{-1}$  corresponding to *sym* and *asym* stretching vibrations of  $\text{CH}_2$ ; the bands at 1453, 1424, 1403, and 1385  $\text{cm}^{-1}$  assigned to  $\nu(\text{CH}_2)$  and  $\nu(\text{C}-\text{C})$  vibrations; the intense bands at 1211 and 1183  $\text{cm}^{-1}$  attributed to  $\nu(\text{CF}_2)$  vibration; the absorption bands in the 1000–500  $\text{cm}^{-1}$  range correspond to characteristic PVDF skeletal vibrations. Radiation grafting of PAA to PVDF TMs, conducted in 75 vol.% AA and 0.25 % w/v Mohr's salt at 60 °C, results in the appearance of a new absorption bands. These include a strong peak at  $\sim 1710 \text{ cm}^{-1}$ , assigned to  $\text{C}=\text{O}$  stretching vibration in associated carboxyl groups (hydrogen-bonded) with a shoulder at  $\sim 1750 \text{ cm}^{-1}$  corresponding to free carboxyl groups. The broad band in the 3500–2500  $\text{cm}^{-1}$  range, associated with  $\nu(\text{OH})$ , is usually too weak in dried samples and superimposed with  $\nu(\text{CH}_2)$  of PVDF. The low-intensity band at 1558  $\text{cm}^{-1}$  is attributed to asymmetric vibration of carboxylate groups. This arises from partial dissociation of AA units under neutral pH conditions during grafting in aqueous media. Notably, treatment in dilute alkaline solutions transforms the dominant 1710  $\text{cm}^{-1}$  (protonated carboxyl) into the 1558  $\text{cm}^{-1}$  band (deprotonated carboxylate), and *vice versa*, confirming the pH-responsive behavior of grafted PAA.

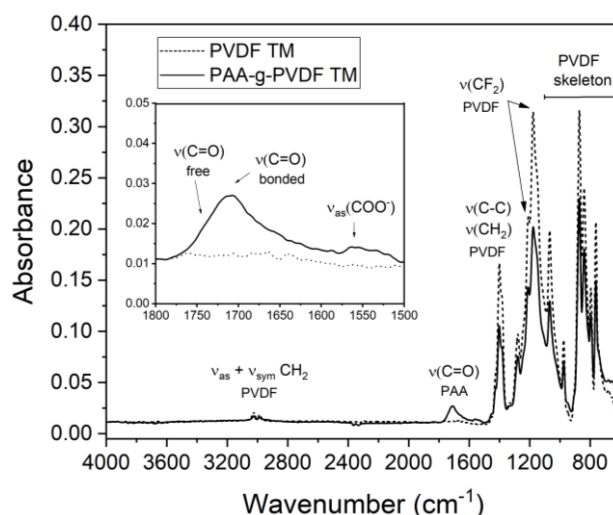


Figure 6. FT-IR spectra in ATR mode of PVDF TMs before and after PAA grafting (GY = 22 %). AA concentration: 75 vol.%. Mohr's salt concentration: 0.25 % w/v. Reaction conditions: 60 °C, 30 min

Surface chemical composition of samples grafted at various AA concentrations was analyzed by XPS. Figure 7 (a) shows a survey spectrum of non-modified PVDF TM, exhibiting characteristic F1s and C1s peaks with an F/C ratio of approximately 0.8. This reduced ratio (compared to pristine PVDF foil, F/C = 1.0) is attributed to radiation-induced dehydrofluorination during irradiation and latent track etching. Chemical etching selectively removes degraded polymer fragments from the latent tracks resulting in fluorine depletion overall the surface. After grafting in 75 % AA (Figure 7 (b)), XPS revealed a substantial increase in the O/F ratio from 0.1 to 0.6, demonstrating significant surface coverage by the grafted PAA layer.

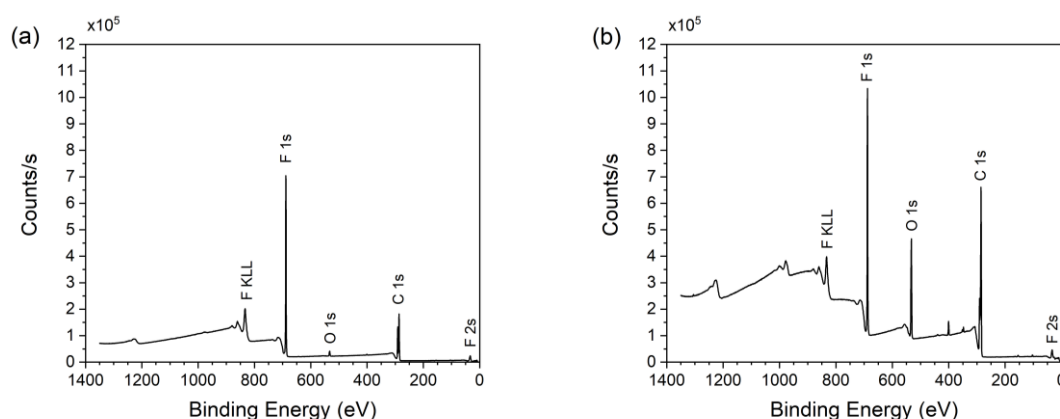


Figure 7. XPS survey spectra of PVDF TMs (a) before and (b) after PAA grafting (GY = 22 %). AA concentration: 75 vol.%. Mohr's salt concentration: 0.25 % w/v. Reaction conditions: 60 °C, 30 min

Table 1 summarizes atomic percentages for the PVDF TMs before and after PAA grafting depending on the monomer concentration and their GYs. When water was present in reaction solutions, the F/C ratio decreased progressively with increasing AA concentration, reaching a minimum at 75 vol.% AA. This indicates enhanced bulk functionalization, where growing PAA chains diffuse beyond nanopore confinement under optimal swelling conditions. This finding is consistent with the maximal membrane thickness expansion observed in Figure 4 (b).

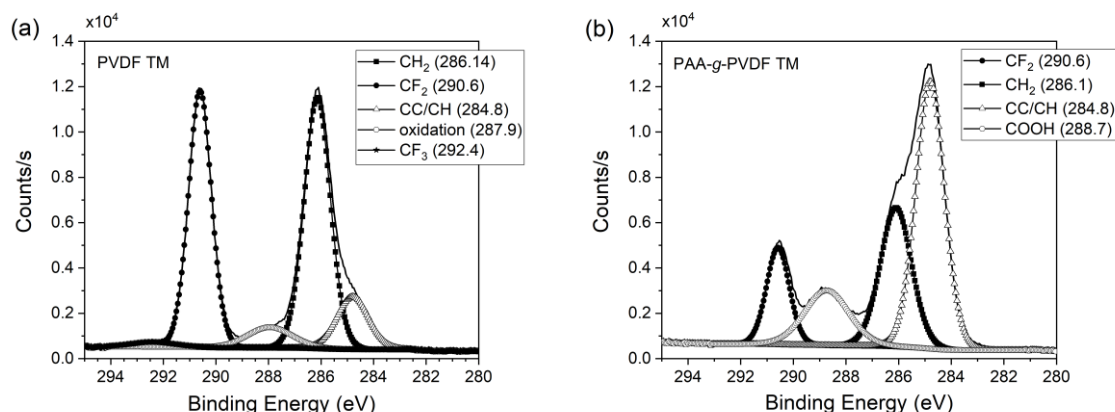


Figure 8. XPS C1s deconvoluted spectra of PVDF TMs (a) before and (b) after PAA grafting (GY = 22 %).

Table 1

Atomic composition of PAA-g-PVDF TMs

Sample	C1s (at.%)	F1s (at.%)	O1s (at.%)	F/C	O/F	GY (%)
PVDF TM	53.1	43.4	2.31	0.8	0.1	0
PAA-grafted PVDF TMs at varied [AA]						
10 vol.%	55.1	32.3	4.0	0.6	0.1	3.2
25 vol.%	56.2	38.5	4.0	0.7	0.1	4.3
50 vol.%	55.4	39.3	4.0	0.7	0.1	5.9
75 vol.%	62.7	21.4	12.4	0.3	0.6	21.8
100 vol.%	54.0	42.0	3.0	0.8	0.1	14.8

C1s regional spectra (Figure 8 (a)) for most grafted samples resembled pristine PVDF, confirming limited surface modification. In contrast, the sample grafted in 75 vol.% AA (Figure 8 (b)) showed pronounced carboxyl signatures (O–C=O at 288.7 eV). PVDF TMs grafted in 100 vol.% AA retained an F/C ratio identical to unmodified TMs, confirming strictly localized (nanopore-surface-only) modification. These results align with reported studies of PAA grafting onto electron-beam-irradiated PVDF foils [12].

Figure 9 depicts DSC curves revealing structural changes in PVDF foils induced by sequential processing, with key parameters summarized in Table 2. The pristine PVDF exhibits a characteristic endothermic melting peak,  $T_m$ , at 175.7 °C with an enthalpy of 49.0 J/g. Given the enthalpy of melting for fully crystalline PVDF ( $\Delta H_{100\%} = 104.7$  J/g) [28], the crystallinity degree,  $\chi_c$ , found as  $\Delta H_m / \Delta H_{100\%} \times 100\%$  is estimated to be 46.8 %. Irradiation slightly reduces crystallinity while increasing the melting temperature ( $T_m$ ) from 175.7 to 178.3 °C. This  $T_m$  increase is a due to radiation-induced cross-linking, restricting chain mobility and suppressing relaxation processes [29, 30]. Subsequent chemical etching restored  $T_m$  to 175.8 °C, confirming the selective removal of the radiation-damaged polymer from the latent tracks. After PAA grafting,  $T_m$  shifts to 177.6 °C. This shift is possibly due to two factors: (i) constrained PVDF chain mobility from interfacial PAA, and (ii) temperature-mediated radical recombination, inducing cross-links during graft polymerization. The observed reduction in  $\chi_c$  with increasing GY is a well-documented phenomenon. Our results, showing a drop from 46.4 % to 30.6 %, align with the trends reported for other grafted systems, such as methyl methacrylate- and styrene-grafted PVDF [11, 31]. Such a behavior evidences the disruption of crystallites by the growing polymer grafts, initiated at the crystalline/amorphous boundaries. The consistency of this effect across different monomers and grafting methods confirms that the structural consequences of grafting are universal, thereby validating our findings. Additional transitions were observed. An exothermic transition near –40 °C (close to  $T_g$  of PVDF) points out nanoscale phase separation between flexible PVDF domains and glassy PAA ( $T_g \approx 100$  °C). A broad endotherm at approximately 60 °C reflects dehydration of PAA-grafted samples.



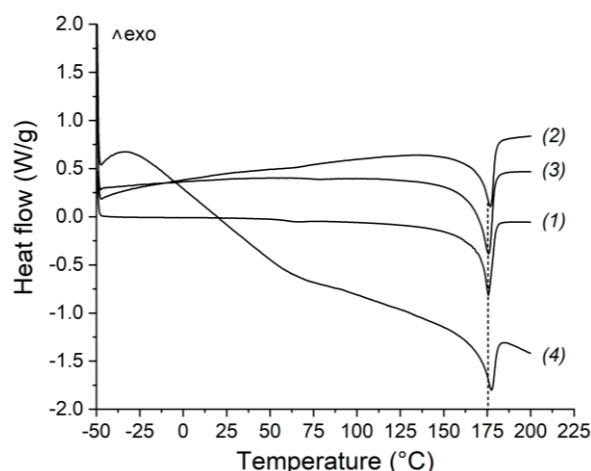


Figure 9. DSC curves for pristine PVDF (1), Xe-irradiated PVDF (2), PVDF TM (3), and PAA-g-PVDF TM (GY = 22 %) (4). AA concentration: 75 vol.%. Mohr's salt concentration: 0.25 % w/v. Reaction conditions: 60 °C, 30 min

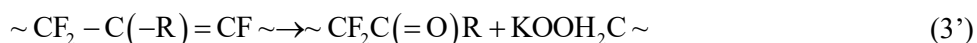
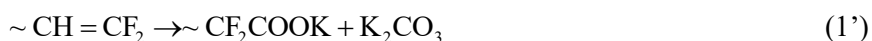
Table 2

**Melting temperature ( $T_m$ ), enthalpy of melting ( $\Delta H_m$ ), and crystallinity degree ( $\chi_c$ ) derived from DSC for pristine, Xe-irradiated, etched and AA-grafted PVDF TMs**

Sample	$T_m$ (°C)	$\Delta H_m$ (J/g)	$\chi_c$ (%)
PVDF	175.7	49.0	46.8
PVDF-Xe	178.3	48.5	46.3
PVDF TM	175.8	48.6	46.4
PAA-g-PVDF TM	177.6	32.0	30.6

Contact angle measurements confirm the progressive modification of the surface across different processing stages. Pristine PVDF foil exhibited a contact angle of  $80 \pm 5^\circ$ . Etched membranes showed significant hydrophilization, reducing the contact angle to  $65 \pm 2^\circ$ , attributed to carboxyl group formation. Following PAA grafting, contact angles modestly decreased across all AA concentrations, reaching  $57 \pm 6^\circ$  for membranes grafted in 100 vol.% AA. Despite PAA's inherent hydrophilicity, this relatively small reduction confirms that wetting is primarily governed by nanometer-scale pore openings rather than bulk or surface functionalization.

Zeta-potential measurements provide valuable insights into the surface chemistry and nanoscale functionalization of PVDF TMs. As seen in figure 10, unmodified PVDF TMs exhibit a pH-independent negative charge ( $\zeta \approx -20$  mV across pH 3–8). This can be attributed to carboxylic acid groups (fluorinated and not) and ketones formed upon oxidative cleavage of C=C in various positions:



To demonstrate the versatility of the pore-confined grafting approach beyond PAA, poly(4-vinylpyridine) (P4VP), a cation-exchange polymer exhibiting pH-dependent charge behavior, was grafted to PVDF TMs. Its inverse charge modulation verifies that the interfacial properties are governed solely by the grafted polymer. Upon P4VP grafting, the charge behavior changes dramatically. Below pH 5.2, protonation causes a strong positive potential ( $\zeta \approx +20$  mV at pH 3). Above pH 5.2, deprotonation restores a negative charge ( $\zeta \approx -20$  mV at pH 8). The isoelectric point (IEP) of 5.2 found for the P4VP-g-PVDF TMs is consistent with the dissociation constant of pure P4VP [32]. The complete counterbalancing of the negative membrane charge emphasizes a uniform and continuous grafted P4VP layer that governs the interfacial behavior without interference from the substrate. This ability to precisely engineer the surface charge of the nanopores is crucial for advanced applications such as charge-selective separation, nanofluidic devices, and sensors.

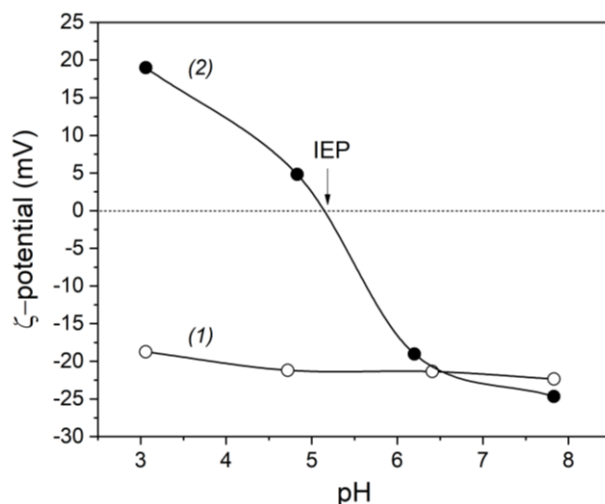


Figure 10. Zeta-potential of PVDF TMs before (1) and after (2) grafting with P4VP (GY = 1.6 %, fluence of  $10^9$  ions/cm<sup>2</sup>) as a function of pH

Confocal laser fluorescence microscopy was employed to visualize the location of grafted polymer. This was achieved by detecting Rhodamine 6G (Rh6G), a fluorescent agent that binds to carboxylic acid groups of the grafted PAA chains. To distinguish between grafted PAA and carboxyl groups introduced by PVDF oxidation during chemical etching, a control experiment was performed. Prior to grafting, freshly prepared membranes were treated with EDC/NHS (2:1 molar ratio) in 0.1 M acetate buffer (pH 5.0), followed by coupling with ethylenediamine (EDA) in PBS (pH 7.4). These carboxyl-deactivated samples were then subjected to PAA in 100 vol.% AA to ensure grafting occurred exclusively from pore surfaces. Figure 11 presents the photoluminescence surface mapping of PAA-g-PVDF TMs before and after Rh6G sorption.

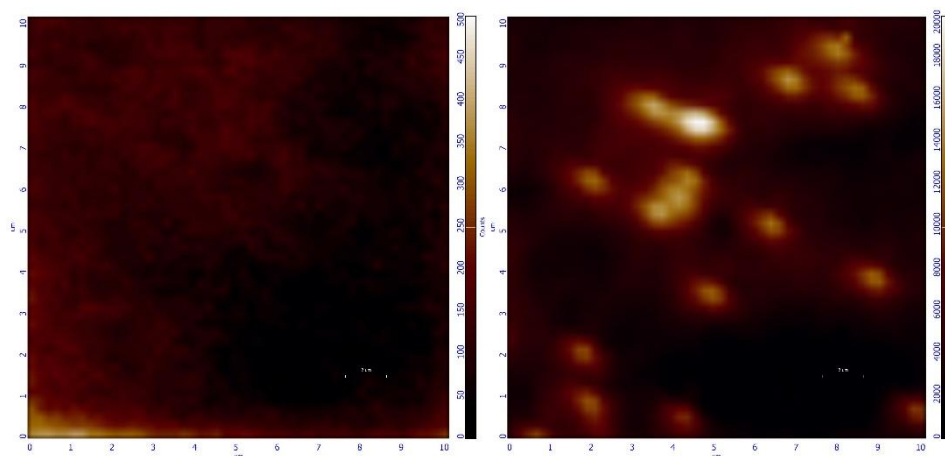


Figure 11. Photoluminescence surface mapping of PAA-g-PVDF TMs before (left) and after (right) sorption of Rhodamine 6G. Grafting was performed in 100 vol.% AA onto PVDF TMs with the fluence of  $10^7$  ions/cm<sup>2</sup>.

Intensity scales: 0–500 and 0–20,000 counts for left and right images, respectively. Scale bars: 2  $\mu$ m

Although PVDF exhibits intrinsic luminescence and Rh6G adsorbs nonspecifically on membrane surface, both contributing to background luminescence, the intense pore-localized signal contrasts sharply with the surrounding matrix. This spatial contrast, combined with pore density matching the ion fluence, clearly confirms nanopore-confined grafting.

### Conclusions

Pore-localized functionalization of nanoporous PVDF TMs has been achieved through radiation-induced graft polymerization of AA monomer. Cylindrical through nanopores were produced by irradiation with energetic xenon ions under optimized alkaline oxidative etching, retaining residual radical sites along the ion tracks. These radical sites eliminate the need for external initiators or activation, enabling direct initi-

ation of polymerization reaction exclusively within the nanopores. Grafting efficiency was demonstrated through optimization of inhibitor concentration, monomer concentration, reaction temperature and time.

FT-IR and XPS analyses revealed a covalent attachment of PAA to PVDF TMs while its efficiency towards bulk *versus* surface modification is mainly governed by the monomer/solvent ratio. When growing PAA chains can diffuse beyond the etched track confinement under optimal polymer substrate swelling conditions, a significant decrease in the crystallinity of the grafted samples was observed by DSC. This was attributed to the crystallite disruption by PAA grafts initiated at crystalline/amorphous boundaries. Furthermore, the assessment of zeta-potentials provided a valuable insight into the surface chemistry and confirmed a continuous pore functionalization resulted in a complete counterbalancing of the negatively charged pore walls when cation-exchange P4VP chains are grafted. Confocal fluorescence microscopy enabled the visualization of PAA-grafted nanopores by detecting the luminescence of Rhodamine 6G adsorbed onto the carboxyl groups, illustrating that the grafted polymer is confined to the pore interiors.

The presented findings illustrate the potential of radiation-induced grafting as a powerful technique for tailoring the surface chemistry of nanoporous membranes at the nanoscale. This approach offers a platform for creating nanoporous membranes with tunable characteristics for energy, biomedical, and separation applications, opening new possibilities for spatially-controlled functionality in advanced materials.

### *Funding*

This work was supported by Sistema Public Joint Stock Financial Corporation (grant No. 801/39-24) and JINR-SA Project JINR23030981618 (grant No. 1004). The EPR studies were conducted within the framework of State Assignment No. 124013100858-3.

### *Author Information\**

*\*The authors' names are presented in the following order: First Name, Middle Name and Last Name*

**Angelina Viktorovna Kryukova-Seliverstova** — Master student, Department of Nanotechnology and New Materials, Dubna State University, Universitetskaya Street, 141980, Dubna, Russia; e-mail: [angelina3082001@gmail.com](mailto:angelina3082001@gmail.com)

**Oleg Leonidovich Orelovich** — Head of Electron Microscopy Group, Flerov Laboratory of Nuclear Reactions, Joint Institute for Nuclear Research, Joliot-Curie Street, 141980, Dubna, Russia; e-mail: [orel@jinr.ru](mailto:orel@jinr.ru); <https://orcid.org/0000-0002-8786-1828>

**Vladimir Alekseevich Altynov** — Research Scientist, Flerov Laboratory of Nuclear Reactions, Joint Institute for Nuclear Research, Joliot-Curie Street, 141980, Dubna, Russia; e-mail: [altynov@jinr.ru](mailto:altynov@jinr.ru); <https://orcid.org/0000-0001-6247-8884>

**Alexander Vladimirovich Akimov** — Leading Researcher, Laboratory for Physical Methods of Functional Materials Research, Federal Research Center of Problems of Chemical Physics and Medicinal Chemistry RAS, Academician Semenov Avenue, 142432, Chernogolovka, Russia; e-mail: [shura@icp.ac.ru](mailto:shura@icp.ac.ru); <https://orcid.org/0000-0001-6159-439X>

**Alexander Sergeevich Shmakov** — Research Assistant, Laboratory for Physical Methods of Functional Materials Research, Federal Research Center of Problems of Chemical Physics and Medicinal Chemistry RAS, Academician Semenov Avenue, 142432, Chernogolovka, Russia; e-mail: [shmakovchem@mail.ru](mailto:shmakovchem@mail.ru); <https://orcid.org/0009-0009-8084-0088>

**Daria Vladimirovna Nikolskaya** — Process Engineer, Flerov Laboratory of Nuclear Reactions, Joint Institute for Nuclear Research, Joliot-Curie Street, 141980, Dubna, Russia; e-mail: [nikolskaya@jinr.ru](mailto:nikolskaya@jinr.ru); <https://orcid.org/0009-0004-2181-1002>

**Nikita Sergeevich Kirilkin** — Junior Research Scientist, Flerov Laboratory of Nuclear Reactions, Joint Institute for Nuclear Research, Joliot-Curie Street, 141980, Dubna, Russia; e-mail: [kirilkin@jinr.ru](mailto:kirilkin@jinr.ru); <https://orcid.org/0000-0003-3782-0515>

**Uliana Vladimirovna Pinaeva** (*corresponding author*) — Research Scientist, Flerov Laboratory of Nuclear Reactions, Joint Institute for Nuclear Research, Joliot-Curie Street, 141980, Dubna, Russia; e-mail: [pinaeva@jinr.ru](mailto:pinaeva@jinr.ru); <https://orcid.org/0000-0003-1724-6149>

### Author Contributions

The manuscript was prepared with contributions from all authors, and all authors have approved the final version for submission. **CRedit**: **Angelina Viktorovna Kryukova-Seliverstova** investigation, formal analysis, visualization, writing — original draft; **Oleg Leonidovich Orelovich** investigation, formal analysis; **Vladimir Alekseevich Altynov** — investigation, formal analysis; **Alexander Vladimirovich Akimov** conceptualization, methodology, formal analysis; **Alexander Sergeevich Shmakov** investigation, writing — original draft; **Daria Vladimirovna Nikolskaya** investigation, resources; **Nikita Sergeevich Kirilkin** investigation, formal analysis; **Uliana Vladimirovna Pinaeva** conceptualization, methodology, investigation, formal analysis, writing — review & editing, supervision.

### Acknowledgments

Authors gratefully acknowledge Oleg M. Ivanov for performing the irradiation of PVDF foils and for his insightful contributions to discussions during this research.

### Conflicts of Interest

The authors declare no conflict of interest.

### References

- 1 Nasef, M. M., & Güven, O. (2012). Radiation-grafted copolymers for separation and purification purposes: Status, challenges and future directions. *Progress in Polymer Science*, 37(12), 1597–1656. <https://doi.org/10.1016/j.progpolymsci.2012.07.004>
- 2 Saxena, P., & Shukla, P. (2021). A comprehensive review on fundamental properties and applications of poly (vinylidene fluoride)(PVDF). *Advanced Composites and Hybrid Materials*, 4(1), 8–26. <https://doi.org/10.1007/s42114-021-00217-0>
- 3 Costa, C. M., Cardoso, V. F., Pedro, M., Correia, D. M., Gonçalves, R., Costa, P., Correia, V., Ribeiro, C., Fernandes, M. M., Martins, P. M., & Lanceros-Méndez, S. (2023). Smart and multifunctional materials based on electroactive poly (vinylidene fluoride): recent advances and opportunities in sensors, actuators, energy, environmental, and biomedical applications. *Chemical reviews*, 123(19), 11392–11487. <https://doi.org/10.1021/acs.chemrev.3c00196>
- 4 Apel, P. Y. (2019). Fabrication of functional micro-and nanoporous materials from polymers modified by swift heavy ions. *Radiation Physics and Chemistry*, 159, 25–24. <https://doi.org/10.1016/j.radphyschem.2019.01.0>
- 5 Ma, T., Janot, J. M., Balme, S. (2020). Track-etched nanopore/membrane: from fundamental to applications. *Small Methods*, 4(9), 2000366. <https://doi.org/10.1002/smt.202000366>
- 6 Barsbay, M., & Güven, O. (2014). Grafting in confined spaces: Functionalization of nanochannels of track-etched membranes. *Radiation Physics and Chemistry*, 105, 26–30. <https://doi.org/10.1016/j.radphyschem.2014.05.018>
- 7 Chapiro, A. (1959). Préparation des copolymères greffés du polytétrafluoroéthylène (Teflon) par voie radiochimique. *Journal of Polymer Science*, 34(127), 481–501. <https://doi.org/10.1002/pol.1959.1203412735>
- 8 Dargaville, T. R., George, G. A., Hill, D. J. T., & Whittaker, A. K. (2003). High energy radiation grafting of fluoropolymers. *Progress in Polymer Science*, 28(9), 1355–1376. [https://doi.org/10.1016/s0079-6700\(03\)00047-9](https://doi.org/10.1016/s0079-6700(03)00047-9)
- 9 Chapiro, A. (1977). Radiation induced grafting. *Radiation Physics and Chemistry*, 9(1-3), 55–67. [https://doi.org/10.1016/0146-5724\(77\)90072-3](https://doi.org/10.1016/0146-5724(77)90072-3)
- 10 Ellinghorst, G., Niemöller, A., & Vierkotten, D. (1983). Radiation initiated grafting of polymer films — an alternative technique to prepare membranes for various separation problems. *Radiation Physics and Chemistry*, 22(3-5), 635–642. [https://doi.org/10.1016/0146-5724\(83\)90073-0](https://doi.org/10.1016/0146-5724(83)90073-0)
- 11 Betz, N. (1995). Ion track grafting. *Nuclear Instruments and Methods in Physics Research Section B Beam Interactions with Materials and Atoms*, 105(1-4), 55–62. [https://doi.org/10.1016/0168-583x\(95\)00911-6](https://doi.org/10.1016/0168-583x(95)00911-6)
- 12 Clochard, M.-C., Bégué, J.-P., Lafon, A., Caldemaison, D., Bittencourt, C., Pireaux, J. J., & Betz, N. (2004). Tailoring bulk and surface grafting of poly(acrylic acid) in electron-irradiated PVDF. *Polymer*, 45(26), 8683–8694. <https://doi.org/10.1016/j.polymer.2004.10.052>
- 13 Mazzei, R., Bermúdez, G. G., Betz, N., & Cabanillas, E. (2004). Swift heavy ion induced graft polymerization in track etched membranes' submicroscopic pores. *Nuclear Instruments and Methods in Physics Research Section B: Beam Interactions with Materials and Atoms*, 226(4), 575–584. <https://doi.org/10.1016/j.nimb.2004.08.001>
- 14 Mazzei, R., García Bermúdez, G., Camporotondi, D. E., Arbeitman, C., del Grosso, M. F., & Behar, M. (2012). New membranes obtained by grafted irradiated PVDF foils. *Nuclear Instruments and Methods in Physics Research Section B: Beam Interactions with Materials and Atoms*, 287, 26–30. <https://doi.org/10.1016/j.nimb.2012.05.040>
- 15 Mazzei, R., Betz, N., Bermúdez, G. G., Massa, G., & Smolko, E. (2005). Submicroscopic pores grafted using the residual sites produced by swift heavy ions. *Nuclear Instruments and Methods in Physics Research Section B: Beam Interactions with Materials and Atoms*, 236(1-4), 407–412. <https://doi.org/10.1016/j.nimb.2005.04.007>

- 16 Cuscito, O., Clochard, M. -C., Esnouf, S., Betz, N., & Lairez, D. (2007). Nanoporous  $\beta$ -PVDF membranes with selectively functionalized pores. *Nuclear Instruments and Methods in Physics Research Section B: Beam Interactions with Materials and Atoms*, 265(1), 309–313. <https://doi.org/10.1016/j.nimb.2007.08.089>
- 17 Barsbay, M., Güven, O., Bessbousse, H., Wade, T., Beuneu, F., & Clochard, M. -C. (2013). Nanopore size tuning of polymeric membranes using the RAFT-mediated radical polymerization. *Journal of Membrane Science*, 445, 135–145. <https://doi.org/10.1016/j.memsci.2013.05.029>
- 18 Tretyakova, S. P., Shirkova, V. V., Khitrova, N. B., & Borcea, C. (1986). Polyvinylidenefluoride (PVF) as a charged particle detector. *Nucl. Tracks Radiat. Meas.*, 12.
- 19 Balanzat, E., Bouffard, S., A. Le Moël, & Betz, N. (1994). Physico-chemical modifications induced in polymers by swift heavy ions. *Nuclear Instruments and Methods in Physics Research Section B Beam Interactions with Materials and Atoms*, 91(1-4), 140–145. [https://doi.org/10.1016/0168-583x\(94\)96204-9](https://doi.org/10.1016/0168-583x(94)96204-9)
- 20 Bogar, M. S., Beuermann, S., Dmitrieva, E., Drache, M., Gohs, U., Kunz, U., Lemmermann, T., Rosenkranz, M., Stehle, M., & Zschech, C. (2021). Quantitative EPR study of poly(vinylidene fluoride) activated by electron beam treatment. *Radiation Physics and Chemistry*, 184, 109421. <https://doi.org/10.1016/j.radphyschem.2021.109421>
- 21 Komaki, Y., Ishikawa, N., Morishita, N., & Takamura, S. (1996). Radicals in heavy ion-irradiated polyvinylidene fluoride. *Radiation Measurements*, 26(1), 123–129. [https://doi.org/10.1016/1350-4487\(95\)00286-3](https://doi.org/10.1016/1350-4487(95)00286-3)
- 22 Betz, N., Petersohn, E., & Le Moël, A. (1996). Free radicals in swift heavy ion irradiated fluoropolymers: An electron spin resonance study. *Radiation Physics and Chemistry*, 47(3), 411–414. [https://doi.org/10.1016/0969-806x\(95\)00127-j](https://doi.org/10.1016/0969-806x(95)00127-j)
- 23 Goslar, J., Hilczer, & B., Smogór, H. (2005). ESR studies of fast electron irradiated ferroelectric poly (vinylidene fluoride). *Acta Physica Polonica A*, 108(1), 89–94.
- 24 Tretyakova, S. P., & Jolos, L. V. (1978). Heavy ion particle track detector of fluoropolymers. *Prib. Tekh. Eksp.*, 1, 36–41.
- 25 Grasselli, M., & Betz, N. (2005). Making porous membranes by chemical etching of heavy-ion tracks in  $\beta$ -PVDF films. *Nuclear Instruments and Methods in Physics Research Section B: Beam Interactions with Materials and Atoms*, 236(1-4), 501–507. <https://doi.org/10.1016/j.nimb.2005.04.027>
- 26 Pinaeva, U., Dietz, T. C., Sheikhy, M. -Al., Balanzat, E., Castellino, M., Wade, T. L., & Clochard, M. -C. (2019). Bis[2-(methacryloyloxy)ethyl] phosphate radiografted into track-etched PVDF for uranium (VI) determination by means of cathodic stripping voltammetry. *Reactive and Functional Polymers*, 142, 77–86. <https://doi.org/10.1016/j.reactfunctpolym.2019.06.006>
- 27 Betz, N., Begue, J., Goncalves, M., K. Gionnet, G. Délérís, & A. Le Moël. (2003). Functionalisation of PAA radiation grafted PVDF. *Nuclear Instruments and Methods in Physics Research Section B: Beam Interactions with Materials and Atoms*, 208, 434–441. [https://doi.org/10.1016/s0168-583x\(03\)00900-5](https://doi.org/10.1016/s0168-583x(03)00900-5)
- 28 Zhou, Z., Li, W., He, T., Qian, L., Tan, G., & Ning, C. (2016). Polarization of an electroactive functional film on titanium for inducing osteogenic differentiation. *Scientific Reports*, 6(1). <https://doi.org/10.1038/srep35512>
- 29 Volgina, E., Pinaeva, U., Temnov, D., Ivanov, O., Mitrofanov, S., & Nechaev, A. (2025). Relaxation processes in swift heavy ion irradiated poly(vinylidene fluoride) films. *Radiation Physics and Chemistry*, 230, 112593. <https://doi.org/10.1016/j.radphyschem.2025.112593>
- 30 Betz, N., Petersohn, E., & Le Moël, A. (1996). Swift heavy ions effects in fluoropolymers: radicals and crosslinking. *Nuclear Instruments and Methods in Physics Research Section B: Beam Interactions with Materials and Atoms*, 116(1-4), 207–211. [https://doi.org/10.1016/0168-583x\(96\)00125-5](https://doi.org/10.1016/0168-583x(96)00125-5)
- 31 Percolla, R., Musumeci, P., Calcagno, L., Foti, G., & Ciavola, G. (1995). Grafting of styrene in polyvinylidene fluoride by high energy ion irradiation. *Nuclear Instruments and Methods in Physics Research Section B: Beam Interactions with Materials and Atoms*, 105(1-4), 181–185. [https://doi.org/10.1016/0168-583x\(95\)00636-2](https://doi.org/10.1016/0168-583x(95)00636-2)
- 32 Wang, H., Lee, I. H., & Yan, M. (2012). A general method to determine ionization constants of responsive polymer thin films. *Journal of Colloid and Interface Science*, 365(1), 178–183. <https://doi.org/10.1016/j.jcis.2011.08.081>



Arman B. Yeszhanov\* , Ilya V. Korolkov , Maxim V. Zdorovets 

*Institute of Nuclear Physics, Almaty, Kazakhstan*

(\*Corresponding author's e-mail: [a.yeszhanov@inp.kz](mailto:a.yeszhanov@inp.kz))

## Graft Polymerization of Octadecyl Acrylate on PET Track-Etched Membranes for Direct Contact Membrane Distillation

Water purification is a critical environmental and social issue of our era. The contamination of water sources by industrial waste, agricultural chemicals, household debris, and plastic pollution significantly degrades the quality of available freshwater. This poses substantial threats to human health and ecosystems. While water is plentiful on Earth, only a limited amount is freshwater that people can safely consume. Population growth, urbanization, and climate change are further exacerbating this scarcity, especially in arid regions. This study examines the membrane distillation process employing ion-track membranes. Hydrophobic poly(ethylene terephthalate) ion-track membranes with increased pore diameters were synthesized via UV-induced graft polymerization of octadecyl acrylate on the membrane surface. Hydrophobic properties were assessed through water contact angle measurements. Fourier transform infrared spectroscopy analyzed functional groups while scanning electron microscopy examined surface morphology. The hydrophobic membranes were subsequently evaluated for desalination performance using direct contact membrane distillation method with saline solutions of varying concentrations. The effect of pore size and feed salt concentration on permeate flux and salt rejection efficiency was systematically examined. Membranes with a contact angle of  $95 \pm 3^\circ$  were tested in saline solutions with concentrations from 7.5 to 30 g/L.

**Keywords:** ion-track membranes, polymerization, membrane distillation, desalination, poly(ethylene terephthalate), salt rejection, water flux, water treatment

### Introduction

The advancement of urbanization, together with rising population numbers and heightened industrial water usage, along with the escalating consequences of global climate change such as desertification and the reduction of freshwater sources may intensify the difficulties in maintaining dependable access to clean drinking water [1]. While approximately 70 % of the Earth's surface is covered by water, only about 2.5 % of it is fresh. Most of this fresh water is found in rivers, lakes, and groundwater. However, these resources are not always available or sufficient to meet the needs of the population [2, 3].

Industrial wastewater pollution is also one of the main threats to the environment and human health. Production processes in various industries are accompanied by the formation of significant amounts of waste that are discharged into water bodies. Without proper treatment, these effluents contain many toxic substances, which leads to the degradation of ecosystems, deterioration of water quality, and an increase in diseases. The shortage of fresh water resources and the problem of wastewater treatment highlight the urgent need to study innovative methods for the production of clean water on a large scale [4–9].

There is increasing focus on developing new, promising water purification methods that are more compact, cost-effective, and easier to operate than traditional techniques. Membrane separation processes, in particular, are gaining attention in the field of both natural and wastewater treatment [10–13]. Among the well-established methods, such as direct and reverse osmosis, as well as micro and ultrafiltration, the membrane distillation process is promising due to its energy efficiency, high degree of purification and flexibility in application. One of the main advantages of this process is its ability to operate at low temperatures, which makes it attractive for the use of low-potential or renewable energy sources. Membrane distillation does not require high pressure, which simplifies the design of the equipment and reduces operating costs [14–19].

In the membrane distillation (MD) process, the membrane plays a vital role as a selective barrier, preventing the passage of undesirable materials from the feed while allowing water vapor to pass through to the permeate side. MD membrane should meet specific requirements: high hydrophobicity and porosity, durability to sustain long-term operation.



Polymers predominantly utilized in the synthesis of membranes for membrane distillation (MD) applications include polytetrafluoroethylene (PTFE), polydimethylsiloxane (PDMS), polystyrene (PS), and poly(vinylidene fluoride) (PVDF). However, they have several disadvantages that can limit their performance and practicality for example thermal degradation, expensiveness of material, weak productivity. Therefore, the investigation of new types of membranes for MD is an urgent task [20–26].

One of the emerging types of membranes that have been successfully implemented in the MD process are ion-track membranes (TeMs) [27–32]. TeMs exhibit a range of advantageous physicochemical properties, including uniform pore morphology with controllable areal pore density, a narrowly dispersed pore size distribution characterized by low structural tortuosity, and reduced membrane thickness conducive to efficient mass transport. Currently, polymer matrices for the production of track-etched membranes are made from films of polycarbonate (PC), poly(ethyleneterephthalate) (PET), polyimide (PI), polypropylene and fluorinated polymers.

The use of PET TeMs in membrane distillation is appealing due to their unique properties. However, PET TeMs have low hydrophobic properties, which may limit their effective use in the MD process. Various surface modification methods are employed to improve hydrophobic properties. The simplest approaches to enhancing membrane hydrophobicity, such as graft polymerization, primarily involve depositing functional groups onto the membrane surface.

In our previous studies [27–32], PET TeMs were modified through ultraviolet (UV) initiated graft polymerization using different monomers and effectively applied in water desalination via membrane distillation. This study focuses on the fabrication of hydrophobic PET TeMs with large pore sizes by grafting octadecyl acrylate (OA) and their application in desalination processes.

## Experimental

### Chemical Substances

Hostaphan® brand PET film manufactured by Mitsubishi Polyester Film (Germany) with a nominal thickness of 12 µm was used. Sodium hydroxide (NaOH), benzophenone (C<sub>13</sub>H<sub>10</sub>O), N,N-dimethylformamide (C<sub>3</sub>H<sub>7</sub>NO), ethyl alcohol (C<sub>2</sub>H<sub>5</sub>OH), isoproryl alcohol (C<sub>3</sub>H<sub>8</sub>O), octadecyl acrylate (C<sub>21</sub>H<sub>40</sub>O<sub>2</sub>, 97 %), sodium chloride (NaCl) were purchased from Sigma-Aldrich. Octadecyl acrylate was subjected to separation using a column packed with alumina. All experiments were conducted using deionized water with a resistivity of 18.2 MΩ·cm at 25 °C.

### Photoinitiated Graft Polymerization of Octadecyl Acrylate

PET films samples (12 µm) were irradiated in a DC-60 (Astana branch of Institute of Nuclear Physics, Kazakhstan) heavy ion accelerator with a pore fluence of  $1 \cdot 10^6$  ion/cm<sup>2</sup>. The chemical etching procedure was carried out according to the parameters established in previous studies [27–31].

The experimental procedure entailed the submersion of samples in a solution comprising octadecyl acrylate and isopropyl alcohol. The concentrations of the solution varied from 5 % to 30 %, with the incorporation of 0.0016 M benzophenone initiator. Dual-sided graft polymerization was performed under an OSRAM Ultra Vitalux E27 UV lamp (UVA: 315–400 nm, 13.6 W; UVB: 280–315 nm, 3.0 W), with distance from the UV lamp of 10 cm, with a total reaction time limited to 60 minutes. After the grafting process, the samples underwent washing, drying, and gravimetric analysis to quantify the grafting degree by the equation:

$$\omega = \frac{(m_2 - m_1)}{m_1} \cdot 100 \%, \quad (1)$$

where  $m_1$  is the weight of the membrane before grafting,  $m_2$  is the weight of the membrane after grafting.

### Membrane Property Characterization Methods

InfraLUM FT-08 was used to analyze the functional groups present on the membrane surface. Data were recorded at 25°C. The Fourier transform infrared spectroscopy (FTIR) analysis was performed with a spectral resolution of 2 cm<sup>-1</sup>, averaging 32 scans per sample, over a wavenumber range of 4000–400 cm<sup>-1</sup>.

Hitachi TM 3030 scanning electron microscope was employed for the pore diameters evaluation.

The membrane pore size was also determined by the gas permeability method at a pressure of 20 kPa.

Quantitative assessment of the wetting properties of surfaces was carried out by measuring contact angles. The surface hydrophobicity was evaluated via static sessile drop method (on five random zones of sam-

ples) using Digital Microscope (Micron-400, China). The captured contact angle images were analyzed using the ImageJ software.

#### Testing of Hydrophobic PET TeMs in Membrane Distillation

Membrane distillation (MD) experiments were carried out using a DCMD setup, with the system specifications detailed in our earlier studies [32]. The membrane was installed in a specially designed experimental cell for conducting the membrane distillation (MD) process. The flow rates on both sides were regulated and sustained using a peristaltic pump. A consistent temperature difference of  $70 \pm 5$  °C was maintained throughout the experiment. Permeate flux was calculated by weighing the amount of permeate collected. The experiments were conducted using saline solutions with varying NaCl concentrations. Salt rejection was determined using a HI2030-01 salinity meter.

The pure water permeation flux was calculated using the formula [32]:

$$Q = \frac{m}{S \cdot t}, \quad (2)$$

where  $Q$  is a pure water permeation flux ( $\text{kg}/\text{m}^2 \cdot \text{h}$ );  $m$  is an amount of permeate mass (kg);  $t$  is a time interval (hr);  $S$  is a membrane area ( $\text{m}^2$ ).

The standard deviation (SD) was calculated using the formula:

$$s = \sqrt{\frac{1}{n-1} \sum_{i=1}^n (x_i - \bar{x})^2}, \quad (3)$$

where  $s$  is a standard deviation;  $n$  is a number of replicates;  $x_i$  is an individual measurement values,  $\bar{x}$  is an average value.

#### Results and Discussion

The modification outline of PET TeMs is presented in Figure 1. UV-photoinitiated graft polymerization is an efficient and environmentally friendly method for modifying polymer materials, which uses ultraviolet radiation to initiate the grafting of monomers onto the polymer surface. Figure 1a illustrates the UV-photoinitiated graft polymerization process, which begins with the activation of a photoinitiator. Upon absorption of UV light, the photoinitiator enters an excited state which, which leads to the formation of free radicals. Figure 1b shows the interaction of radicals with monomer molecules, initiating their polymerization and forming grafted polymer chains on the surface of the base material. Key features of this method include a high reaction rate at room temperature, no need for heating or high pressure, which prevents thermal degradation of the polymer and preserves its original physical and chemical properties. UV-induced graft polymerization is a resource-efficient technique characterized by low energy consumption and the absence of toxic solvent usage, making it an environmentally friendly method [33].

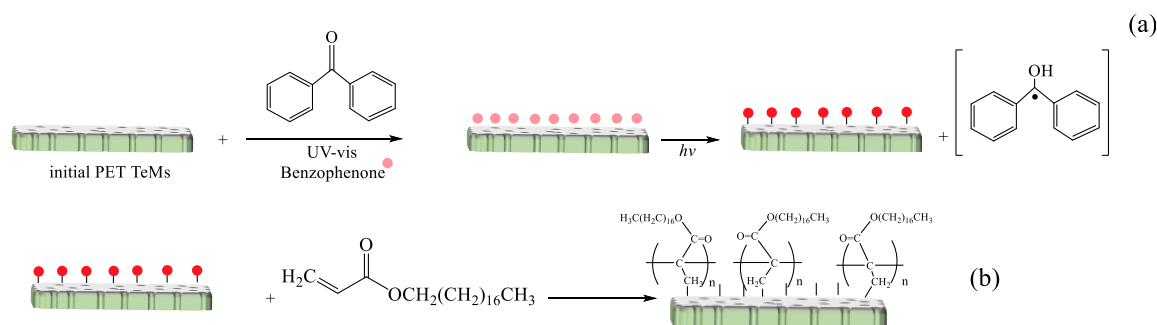


Figure 1. Scheme of UV-photoinitiated graft polymerization of octadecyl acrylate

Figure 2 shows the FTIR spectra for the identification of functional groups before and after modification with octadecyl acrylate. The characteristic absorption bands of unmodified PET TeMs have been previously reported [29–31]. Upon grafting with OA, new absorption peaks appeared at approximately  $\sim 2920$   $\text{cm}^{-1}$  and  $2850$   $\text{cm}^{-1}$ , corresponding to the C–H stretching vibrations. The intensity of these peaks increases with increasing OA concentration.

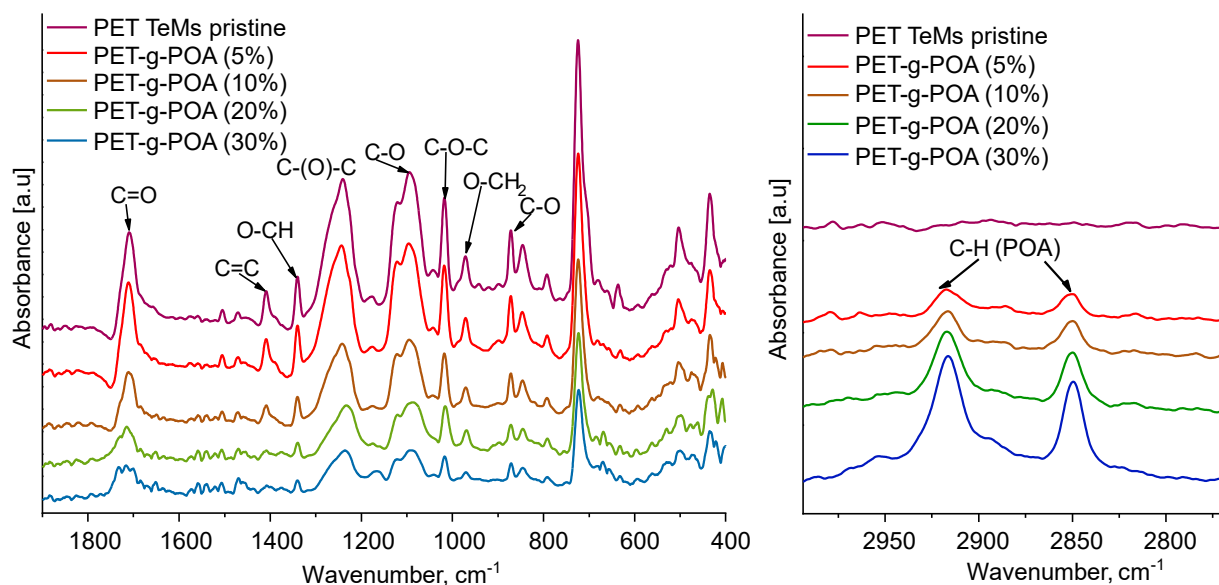


Figure 2. FTIR spectra comparison of pristine and poly(octadecyl acrylate)-grafted PET ion-track membranes over selected spectral ranges

Figure 3 demonstrates the effect of monomer concentration and irradiation time on the grafting degree. It was demonstrated that the optimal reaction condition is an OA concentration of 10 % (the degree of grafting is 3.39 %). However, it is also important to note that increasing the concentration of OA leads to changes in the morphology of the membrane surface, leading to pore overgrowth. Thus, at a concentration of octadecyl acrylate of 20 %, the grafting degree was 5.29 %, and at 30 % — 9.17 %. Figure 3b demonstrates that the grafting degree increases with irradiation time. The optimal duration for maintaining the pore structure is 60 minutes, while extending the irradiation time further results in surface degradation of the PET TeMs.

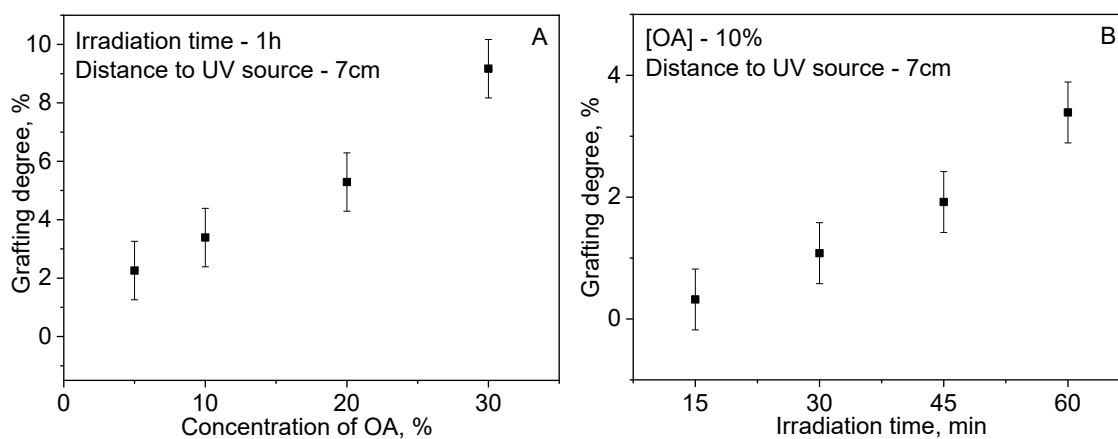


Figure 3. The effect of concentration OA and irradiation time on the grafting degree

The surface morphology of pristine and modified PET TeMs was analyzed using scanning electron microscopy (SEM). The results of the pore diameter values are presented in Table 1. SEM images of the initial and modified membranes are shown in Figure 4. SEM images demonstrate that increasing the concentration of octadecyl acrylate leads to a gradual decrease in the membrane pore size. Thus, at a concentration of 10 %, the pore size decreased from  $920 \pm 10$  nm to  $754 \pm 8$  nm with a grafting degree of 3.39 %.

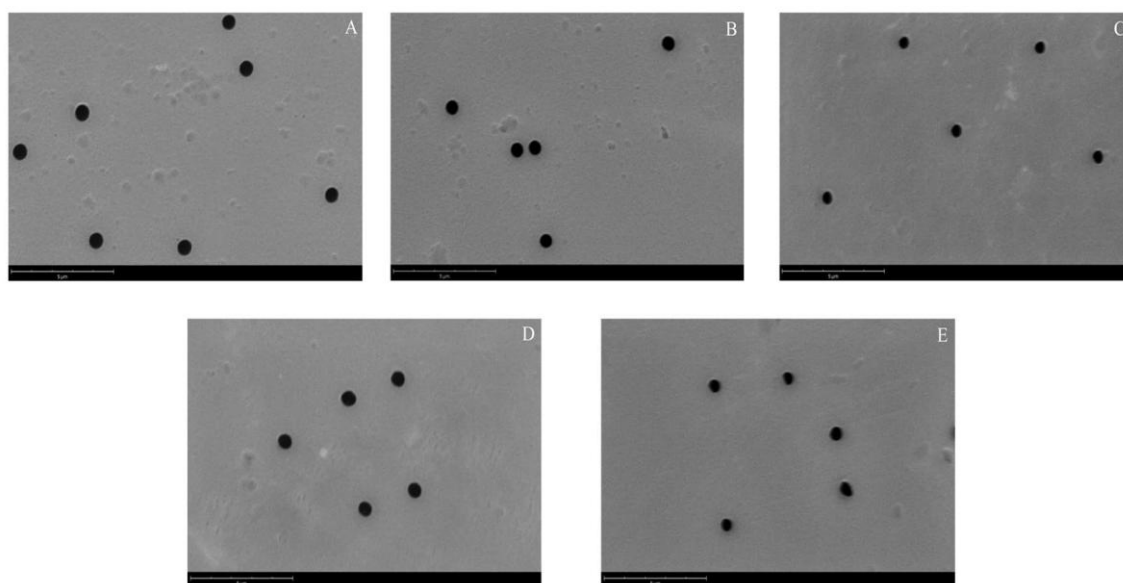


Figure 4. SEM images of pristine PET TeMs (a) and PET TeMs-g-POA (5 %) (b); (10 %) (c); (20 %) (d); 30 % (e)

Table 1

Characteristics of PET TeMs before and after OA modification

Sample	Concentration of OA, %	Graft yield, %	Effective pore size, nm	Pore size (SEM analysis), nm	Contact angle, °	Liquid Entry Pressure, MPa
PET TeMs	—	—	900±14	~920±10	~50-55	—
PET TeMs-g-POA	5	2.26	760±9	796±13	83°±3	0.15
	10	3.39	720±6	754±8	95°±3	≥0.34
	20	5.29	649±8	674±10	86°±4	≥0.39
	30	9.17	630±4	662±7	77°±2	≥0.5

Water contact angle (CA) measurements were employed to evaluate the hydrophobic properties. Figure 5 shows the CA values recorded at various locations on the PET TeMs before and after graft polymerization with octadecyl acrylate. The maximum contact angle is obtained at a 10 % concentration of octadecyl acrylate. A further increase in concentration reduces the value of the CA.

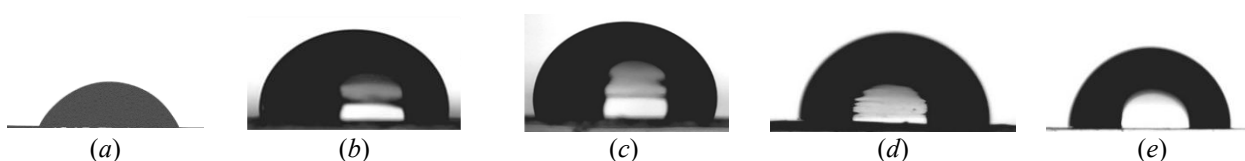


Figure 5. CA of the pristine PET TeMs (a), modified with OA (5 %) (b); (10 %) (c); (20 %) (d); 30 % (e)

#### Efficiency of Modified PET Ion-Track Membranes in Membrane Distillation Processes

Modified ion-track membranes (10 % of OA) pore sizes of  $700 \pm 25$  nm and  $980 \pm 20$  nm were evaluated in DCMD experiments using model saline solutions with NaCl concentrations of 7.5, 15, and 30 g/L. The experimental setup followed the procedure detailed in our previous publication [32]. The effect of membrane pore size and salt concentration on productivity and salt rejection was analyzed, with the corresponding results summarized in Table 2 and illustrated in Figure 6.

Table 2

## Membrane distillation of saline solutions using PET TeMs-g-POA

	PET TeMs-g-POA with pore diameter of 725 nm	PET TeMs-g-POA with pore diameter of 1000 nm
NaCl 7.5 g/L	Degree of salt rejection — 96.16 % Water flow — 1.64 kg/m <sup>2</sup> h	Degree of salt rejection — 81.37 % Water flow — 1.58 kg/m <sup>2</sup> h
NaCl 15 g/L	Degree of salt rejection — 97.24 % Water flow — 1.42 kg/m <sup>2</sup> h	Degree of salt rejection — 80.52 % Water flow — 1.28 kg/m <sup>2</sup> h
NaCl 30 g/L	Degree of salt rejection — 96.12 % Water flow — 0.98 kg/m <sup>2</sup> h	Degree of salt rejection — 70.38 % Water flow — 0.97 kg/m <sup>2</sup> h

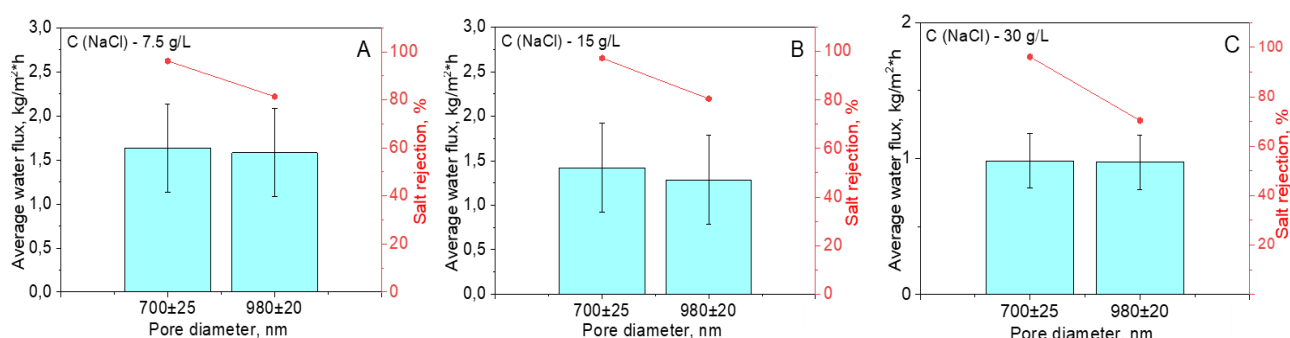


Figure 6. Productivity and salt rejection performance in DCMD experiments

Table 2 and Figure 6 illustrate the decreasing trend in water flux as the salt concentration increases, highlighting the adverse effect of salinity on membrane performance. Permeate flux of  $1.64 \pm 1$ ,  $0.98 \pm 1$  was measured for membranes with pore diameters of  $700 \pm 25$  nm using 7.5 and 30 g/L NaCl feed, respectively. In comparison, membranes with pore diameters of  $980 \pm 20$  nm exhibited a water flux of  $1.58 \text{ kg/m}^2 \cdot \text{h}$  at 7.5 g/L and  $0.9713 \text{ kg/m}^2 \cdot \text{h}$  at 30 g/L, indicating a similar trend of decreasing productivity with increasing salt concentration. At a concentration of 15 g/L, the salt rejection rate was 97.24 % for membranes with  $700 \pm 25$  nm pores and 80.52 % for those with  $980 \pm 20$  nm pores.

Table 3 summarizes the characteristics and performance metrics of PET TeMs modified via various methods for application in MD.

Table 3

## Relationship between pore size, LEP values and contact angle in PET TeMs modified by various methods, and their performance in membrane distillation process

Modification methods	Pore size, nm	Contact angle, °	Water flux, kg/m <sup>2</sup> ·h	Salt rejection, %	LEP, MPa	Reference
UV-graft polymerization of TEVS and VIM	$200 \pm 18$	105	0.088 — for 30 g/L NaCl	95.2	>0.430	[30]
UV-graft polymerization of styrene	$220 \pm 15$	99	0.2193 — for 30 g/L NaCl	97.5	0.340	[31]
Immobilization of silica nanoparticles	$263 \pm 5$	132	6.5 — for 30 g/L NaCl	98	0.430	[29]
UV-graft polymerization of lauryl methacrylate	724	94	1.88 — for 7.5 g/L NaCl	91.39	0.340	[32]
Electrospun PVDF nano-fibers	300–5000	~140	4.68–6.78 —for 26.5 g/L NaCl	99.97	/	[34]
Electrospun PVC nano-fibers	$1159 \pm 27$ — $2494 \pm 81$	~155	13.61 — for 15 g/L NaCl	97.15	/	[35]

As can be seen in Table 3, surface modification by immobilization of silica nanoparticles resulted in the high degree of hydrophobization, achieving a contact angle of 132° and a water flux of 6.5 kg/m<sup>2</sup>h when treating a 30 g/L NaCl solution [29]. However, this method presents certain limitations, including high labor intensity and the gradual degradation of the nanoparticle layer during prolonged operation. One of the key challenges in membrane hydrophobization remains the development of methods capable of effectively treating membranes with large pore diameters, as these are directly correlated with higher productivity rates. Such modifications must maintain a high level of salt rejection to ensure the feasibility of MD processes under real-world conditions.

Among the studied approaches, hybrid membranes fabricated by electrospinning on the surface of TeMs poly(vinylidene fluoride) (PVDF) and poly(vinyl chloride) (PVC) nanofibers demonstrated outstanding performance in terms of both water flux and salt rejection. PVDF-based membranes showed water flux values ranging from 4.68 to 6.78 kg/m<sup>2</sup>h with nearly complete salt rejection (99.97 %) for a 26.5 g/L NaCl solution [34], while PET TeMs-PVC nanofibers reached a flux of 13.61 kg/m<sup>2</sup>h and 97.15 % salt rejection at 15 g/L NaCl concentration [35]. UV-induced graft polymerization of lauryl methacrylate (LMA) [32] enabling moderate hydrophobization (contact angle of 94°) and flux values of 1.88 kg/m<sup>2</sup>h with salt rejection above 91 % for PET TeMs with ~720 nm pores.

In the present study, UV-initiated graft polymerization of octadecyl acrylate (OA) onto PET TeMs was carried out under optimized conditions (10 wt% OA, UV exposure 60 min, 10 cm from UV lamp). This method provided effective hydrophobization of membranes with large pore diameters (725 and 1000 nm), achieving salt rejections of 96.16 % and 81.37 %, respectively, for a 7.5 g/L NaCl solution. Although hybrid PET TeMs demonstrate higher water flux in membrane distillation, their multilayered structure remains a critical disadvantage. Over time, this layered architecture may degrade. In contrast, the formation of covalent bonds during photoinitiated graft polymerization can overcome this disadvantage by ensuring strong interfacial adhesion between the functional layer and the membrane surface. Compared to lauryl methacrylate (LMA), octadecyl acrylate (OA) demonstrated superior salt rejection performance, particularly for PET TeMs with larger pore diameters. This enhancement can be attributed to the longer alkyl chain of OA, which forms a more densely packed and hydrophobic surface layer.

### Conclusions

The present study successfully accomplished a chemical modification of PET TeMs by octadecyl acrylate (OA). Hydrophobic PET TeMs were obtained by photoinitiated graft polymerization with controlled variation of monomer concentration and irradiation duration to optimize surface functionalization. The combined application of FTIR spectroscopy, SEM analysis, and contact angle measurements allowed a thorough assessment of the samples chemical composition, surface structure, and wettability properties. Grafting of OA at optimal conditions (concentration of OA — 10 %, time — 60 min, distance from UV-lamp 10 cm) led to an increase in the contact angle to 95 °C. In membrane distillation (MD) tests, these hydrophobic PET TeMs exhibited a productivity of 1.64 kg/m<sup>2</sup>h and a purification rate of 96.16 % with a membrane pore diameter of 725 nm, while membranes with a pore diameter of 1000 nm at the same NaCl concentration (7.5 g/L) showed a lower productivity of 1.58 kg/m<sup>2</sup> h and a purification rate of 81.37 %.

### Funding

This study was supported by the Ministry of Science and Higher Education of the Republic of Kazakhstan under grant numbers BR28713053 and AP14869096.

### Author Information\*

\*The authors' names are presented in the following order: First Name, Middle Name and Last Name

**Arman Bakhytzhonovich Yezhanov** (*corresponding author*) — Master of Chemical Sciences, Junior Scientific Researcher, Astana Branch, Institute of Nuclear Physics of the Republic of Kazakhstan, Abylai-khan street 2/1, 010000, Astana, Kazakhstan; e-mail: [a.yezhanov@inp.kz](mailto:a.yezhanov@inp.kz); <https://orcid.org/0000-0002-1328-8678>

**Ilya Vladimirovich Korolkov** — PhD, Associated Professor, Senior Researcher, Astana branch, Institute of Nuclear Physics of the Republic of Kazakhstan, Abylai-khan street 2/1, 010000, Astana, Kazakhstan; e-mail: [i.korolkov@inp.kz](mailto:i.korolkov@inp.kz); <https://orcid.org/0000-0002-0766-2803>



**Maxim Vladimirovich Zdorovets** — Candidate of Physical and Mathematical Science, Professor, Director, Astana Branch, Institute of Nuclear Physics of the Republic of Kazakhstan, Abylai-khan street 2/1, 010000, Astana, Kazakhstan; e-mail: [mzdorovets@inp.kz](mailto:mzdorovets@inp.kz); <https://orcid.org/0000-0003-2992-1375>

#### Author Contributions

The manuscript was prepared with contributions from all authors, and all authors have approved the final version for submission. **CRedit**: **Arman Bakhytzhonovich Yeszhanov** — investigation, writing-original draft, data curation, visualization; **Ilya Vladimirovich Korolkov** — supervision, writing-review & editing, project administration; **Maxim Vladimirovich Zdorovets** — financial support acquisition, data management.






#### Conflicts of Interest

The authors declare that they have no financial or personal conflicts of interest that could have affected the results reported in this study.

#### References

- 1 Shalaby, S. M., Zayed, M. E., Hammad, F. A., Menesy, A. S., & Elbar, A. R. A. (2024). Recent advances in membrane distillation hybrids for energy-efficient process configurations: Technology categorization, operational parameters identification, and energy recovery strategies. *Process Safety and Environmental Protection*, 190, 817–838. <https://doi.org/10.1016/J.PSEP.2024.07.098>
- 2 Wang, Y., Liu, X., Ge, J., Li, J., & Jin, Y. (2023). Distillation performance in a novel minichannel membrane distillation device. *Chemical Engineering Journal*, 462, 142335. <https://doi.org/10.1016/J.CEJ.2023.142335>
- 3 Khalifa, A., Etman, A., El-Adawy, M., Alawad, S. M., & Nemitallah, M. A. (2025). Development of membrane distillation powered by engine exhaust for water desalination. *Applied Thermal Engineering*, 258, 124839. <https://doi.org/10.1016/J.APPLTHERMALENG.2024.124839>
- 4 Khalifa, A., Kotb, M., & M. Alawad, S. (2025). Energy-efficient and cost-effective water desalination using membrane distillation with air-cooled dehumidifier bank. *Energy Conversion and Management: X*, 25, 100844. <https://doi.org/10.1016/J.ECMX.2024.100844>
- 5 AlMehri, M., Shaheen, A., Ghazal, A., Almarzooqi, N., Raza, A., Zhang, T., & AlMarzooqi, F. (2024). Photothermal ZrN composite membranes for solar-driven water distillation. *Journal of Environmental Chemical Engineering*, 12(5), 113763. <https://doi.org/10.1016/J.JECE.2024.113763>
- 6 Shaikh, J. S., Aswalekar, U., Ismail, S., & Akhade, A. (2024). The potential of integrating solar-powered membrane distillation with a humidification–dehumidification system to recover potable water from textile wastewater. *Chemical Engineering and Processing — Process Intensification*, 205, 110036. <https://doi.org/10.1016/J.CEP.2024.110036>
- 7 Tian, M., Yin, Y., Zhang, Y., & Han, L. (2025). Membrane distillation goes green: Advancements in green membrane preparation and renewable energy utilization. *Desalination*, 597, 118344. <https://doi.org/10.1016/J.DESAL.2024.118344>
- 8 Zhang, N., Zhang, J., Gao, C., Yuan, S., & Wang, Z. (2025). Emerging advanced membranes for removal of volatile organic compounds during membrane distillation. *Desalination*, 597, 118372. <https://doi.org/10.1016/J.DESAL.2024.118372>
- 9 Abejón, R., Romero, J., & Quijada-Maldonado, E. (2024). Potential of membrane distillation for water recovery and reuse in water stress scenarios: Perspective from a bibliometric analysis. *Desalination*, 591, 117989. <https://doi.org/10.1016/J.DESAL.2024.117989>
- 10 Ahmadi, H., Ziapour, B. M., Ghaebi, H., & Nematollahzadeh, A. (2024). Optimization of vacuum membrane distillation and advanced design of compact solar water heaters with heat recovery. *Journal of Water Process Engineering*, 67, 106212. <https://doi.org/10.1016/J.JWPE.2024.106212>
- 11 Park, H. J., Park, H., Kim, J., Lee, K., Naddeo, V., & Choo, K. H. (2024). Enhancing sustainability: Upcycled membrane distillation for water and nutrient recovery from anaerobic membrane bioreactor effluent. *Chemical Engineering Journal*, 498, 155267. <https://doi.org/10.1016/J.CEJ.2024.155267>
- 12 Pawar, R., & Vidic, R. D. (2024). Impact of surfactants used in oil and gas extraction on produced water treatment by membrane distillation. *Desalination*, 586, 117906. <https://doi.org/10.1016/J.DESAL.2024.117906>
- 13 Zhang, R., Chen, Y., Wang, H., Duan, X., & Ren, Y. (2024). A Janus membrane with silica nanoparticles interlayer for treating coal mine water via membrane distillation. *Separation and Purification Technology*, 350, 127995. <https://doi.org/10.1016/J.SEPPUR.2024.127995>
- 14 Maliwan, T., & Hu, J. (2025). Release of microplastics from polymeric ultrafiltration membrane system for drinking water treatment under different operating conditions. *Water Research*, 274, 123047. <https://doi.org/10.1016/J.WATRES.2024.123047>
- 15 Park, Y., Choi, Y., Choi, J., Ju, J., Kim, B., & Lee, S. (2020). Effect of vibration on fouling propensity of hollow fiber membranes in microfiltration and membrane distillation. *Desalination and Water Treatment*, 192, 11–18. <https://doi.org/10.5004/DWT.2020.25151>

- 16 Ortega-Bravo, J. C., Guzman, C., Iturra, N., & Rubilar, M. (2023). Forward osmosis, reverse osmosis, and distillation membranes evaluation for ethanol extraction in osmotic and thermic equilibrium. *Journal of Membrane Science*, 669, 121292. <https://doi.org/10.1016/J.MEMSCI.2022.121292>
- 17 Ali, A. S., & Bounahmidi, T. (2024). Coupling of photovoltaic thermal with hybrid forward osmosis-membrane distillation: Energy and water production dynamic analysis. *Journal of Water Process Engineering*, 64, 105710. <https://doi.org/10.1016/J.JWPE.2024.105710>
- 18 Otávio Rosa e Silva, G., Rodrigues dos Santos, C., Souza Casella, G., Pinheiro Drumond, G., & Cristina Santos Amaral, M. (2025). Membrane fouling in integrated forward osmosis and membrane distillation systems — A review. *Separation and Purification Technology*, 356, 129955. <https://doi.org/10.1016/J.SEPPUR.2024.129955>
- 19 Wang, L., Sun, X., Gao, F., Yang, Y., & Song, R. (2024). Solar membrane distillation: An emerging technology for reverse osmosis concentrated brine treatment. *Desalination*, 592, 118124. <https://doi.org/10.1016/J.DESAL.2024.118124>
- 20 Li, X., García-Payo, M. C., Khayet, M., Wang, M., & Wang, X. (2017). Superhydrophobic polysulfone/polydimethylsiloxane electrospun nanofibrous membranes for water desalination by direct contact membrane distillation. *Journal of Membrane Science*, 542, 308–319. <https://doi.org/10.1016/J.MEMSCI.2017.08.011>
- 21 Bahrami Eynolghasi, M., Mohammadi, T., & Tofighy, M. A. (2022). Fabrication of polystyrene (PS)/cyclohexanol-based carbon nanotubes (CNTs) mixed matrix membranes for vacuum membrane distillation application. *Journal of Environmental Chemical Engineering*, 10(4), 108175. <https://doi.org/10.1016/J.JECE.2022.108175>
- 22 Omar, N. M. A., Othman, M. H. D., Tai, Z. S., Kurniawan, T. A., Puteh, M. H., Jaafar, J., Rahman, M. A., Bakar, S. A., & Abdullah, H. (2024). A review of superhydrophobic and omniphobic membranes as innovative solutions for enhancing water desalination performance through membrane distillation. *Surfaces and Interfaces*, 46, 104035. <https://doi.org/10.1016/J.SURFIN.2024.104035>
- 23 Jilagam, N. K., Vaghela, G., Chakraborty, T., Guo, J., Farid, M. U., Jeong, S., Shon, H. K., An, A. K., & Deka, B. J. (2024). Frontier of metal-organic framework nanofillers for pre-eminent membrane distillation applications. *Desalination*, 592, 118127. <https://doi.org/10.1016/J.DESAL.2024.118127>
- 24 Nthunya, L. N., Chong, K. C., Lai, S. O., Lau, W. J., López-Maldonado, E. A., Camacho, L. M., Shirazi, M. M. A., Ali, A., Mamba, B. B., Osial, M., Pietrzyk-Thel, P., Pregowska, A., & Mahlangu, O. T. (2024). Progress in membrane distillation processes for dye wastewater treatment: A review. *Chemosphere*, 360, 142347. <https://doi.org/10.1016/J.CHEMOSPHERE.2024.142347>
- 25 Jawed, A. S., Nassar, L., Hegab, H. M., van der Merwe, R., Al Marzooqi, F., Banat, F., & Hasan, S. W. (2024). Recent developments in solar-powered membrane distillation for sustainable desalination. *Heliyon*, 10(11), e31656. <https://doi.org/10.1016/J.HELİYON.2024.E31656>
- 26 Guo, Q., Liu, Y., Li, T., Gao, L., Yin, S., Li, S., & Zhang, L. (2024). Enhancement and optimization of membrane distillation processes: A systematic review of influential mechanisms, optimization and applications. *Desalination*, 586, 117862. <https://doi.org/10.1016/J.DESAL.2024.117862>
- 27 Shakayeva, A. K., Yeszhanov, A. B., Borissenko, A. N., Kassymzhanov, M. T., Zhumazhanova, A. T., Khlebnikov, N. A., Nurkassimov, A. K., Zdorovets, M. V., Güven, O., & Korolkov, I. V. (2024). Surface Modification of Polyethylene Terephthalate Track-Etched Membranes by 2,2,3,3,4,4,5,5,6,6,7,7-Dodecafluoroheptyl Acrylate for Application in Water Desalination by Direct Contact Membrane Distillation. *Membranes*, 14(7). <https://doi.org/10.3390/membranes14070145>
- 28 Yeszhanov, A. B., Korolkov, I. V., Dosmagambetova, S. S., Zdorovets, M. V., & Güven, O. (2021). Recent Progress in the Membrane Distillation and Impact of Track-Etched Membranes. *Polymers*, 13(15). <https://doi.org/10.3390/polym13152520>
- 29 Korolkov, I. V., Kuandykova, A., Yeszhanov, A. B., Güven, O., Gorin, Y. G., & Zdorovets, M. V. (2020). Modification of PET Ion-Track Membranes by Silica Nanoparticles for Direct Contact Membrane Distillation of Salt Solutions. *Membranes*, 10(11), 1–15. <https://doi.org/10.3390/MEMBRANES10110322>
- 30 Korolkov, I. V., Gorin, Y. G., Yeszhanov, A. B., Kozlovskiy, A. L., & Zdorovets, M. V. (2018). Preparation of PET track-etched membranes for membrane distillation by photo-induced graft polymerization. *Materials Chemistry and Physics*, 205, 55–63. <https://doi.org/10.1016/J.MATCHEMPHYS.2017.11.006>
- 31 Korolkov, I. V., Yeszhanov, A. B., Zdorovets, M. V., Gorin, Y. G., Güven, O., Dosmagambetova, S. S., Khlebnikov, N. A., Serkov, K. V., Krasnopyorova, M. V., Milts, O. S., & Zheltov, D. A. (2019). Modification of PET ion track membranes for membrane distillation of low-level liquid radioactive wastes and salt solutions. *Separation and Purification Technology*, 227, 115694. <https://doi.org/10.1016/J.SEPPUR.2019.115694>
- 32 Yeszhanov, A. B., Korolkov, I. V., Güven, O., Melnikova, G. B., Dosmagambetova, S. S., Borissenko, A. N., Nurkassimov, A. K., Kassymzhanov, M. T., & Zdorovets, M. V. (2024). Effect of hydrophobized PET TeMs membrane pore-size on saline water treatment by direct contact membrane distillation. *RSC Advances*, 14(6), 4034–4042. <https://doi.org/10.1039/D3RA07475G>
- 33 Deng, J., Wang, L., Liu, L., & Yang, W. (2009). Developments and new applications of UV-induced surface graft polymerizations. *Progress in Polymer Science*, 34(2), 156–193. <https://doi.org/10.1016/J.PROGPOLYMSCI.2008.06.002>
- 34 Kravets, L., Vinogradov, I., Rossouw, A., Gorberg, B., Nechaev, A., & Apel, P. (2025). Functionalization of PET track-etched membranes with electrospun PVDF nanofibers for hybrid membranes fabrication in water desalination. *Separation and Purification Technology*, 371(March), 133395. <https://doi.org/10.1016/j.seppur.2025.133395>
- 35 Yeszhanov, A. B., Shakayeva, A. Kh., Zdorovets, M. V., Borgekov, D. B., Kozlovskiy, A. L., Kharkin, P. V., Zheltov, D. A., Krasnopyorova, M. V., Güven, O., & Korolkov, I. V. (2025). Hybrid Membranes Based on Track-Etched Membranes and Nanofiber Layer for Water–Oil Separation and Membrane Distillation of Low-Level Liquid Radioactive Wastes and Salt Solutions. *Membranes*, 15(7), 202. <https://doi.org/10.3390/membranes15070202>

Maria A. Ponomar<sup>1</sup>, Veronika V. Sarapulova<sup>1\*</sup>, Vera V. Guliaeva<sup>1</sup>,  
Pavel Yu. Apel<sup>2</sup>, Natalia D. Pismenskaya<sup>1</sup>

<sup>1</sup>Kuban State University, Krasnodar, Russia;

<sup>2</sup>Joint Institute for Nuclear Research, Dubna, Moscow region, Russia

(\*Corresponding author's e-mail: [vsarapulova@gmail.com](mailto:vsarapulova@gmail.com))

## Transport Properties of Cation-Exchange Membranes Obtained by Pore Filling of Track-Etched Membranes with Perfluorosulfonic Acid Polymer

In this paper the correlation between the structural characteristics and transport properties of pore-filling membranes formed by embedding an ion-conducting polymer into track-etched substrates was studied. Cation-exchange membranes were fabricated by filling the pores of track-etched membranes with a perfluorosulfonic acid polymer (trade mark LF-4SC). The resulting membranes differed in the volume fraction of the ion-conducting polymer and in the presence or absence of a surface LF-4SC layer. SEM and ATR-FTIR spectroscopy were employed to characterize the chemical composition and structure of the membranes. A comparative analysis of ion-exchange capacity and water uptake was carried out. Concentration dependences of specific electrical conductivity and diffusion permeability in NaCl solutions were obtained. The effects of pore filling degree and LF-4SC layer thickness on osmotic transport, diffusion permeability, and selectivity were analyzed. The electrical resistance of the prepared membranes was found to be comparable to that of the commercial MF-4SC membrane, produced from the same perfluorosulfonic acid polymer, despite a significant fraction of the polymer in the new membranes not participating in counterion transport. The observed structure–property relationships were interpreted within the framework of the two-phase microheterogeneous model, providing insight into the functional behavior of the composite membranes.

**Keywords:** cation-exchange membranes, track-etched membranes, pore-filling membranes, perfluorosulfonic, electrical conductivity, osmotic flux, diffusion permeability, true transport numbers

### 1. Introduction

The growing demand for ion-exchange membranes (IEMs) and proton-exchange membranes (PEMs), driven by expanding application areas, has stimulated exponential research efforts. Beyond dialysis and electrodialysis, IEMs and PEMs are now used in a wide range of technologies, including membrane bioreactors, hydrogen production electrolyzers, low-temperature fuel cells, flow batteries, and membrane capacitive deionization, etc. Meeting these diverse requirements demands a careful balance between high transport performance and cost control. Consequently, understanding the relationship between membrane structure and transport properties is essential to address this challenge [1, 2]. The microheterogeneous model, originally formulated by N.P. Gnusin et al. [3, 4] and later refined [5–7], provides a valuable framework for predicting the transport characteristics of ion-exchange membranes. Based on effective medium theory [8], this model describes a swollen IEM (or PEM) as a multiphase system, in which membrane properties are determined by the intrinsic features and spatial organization of the constituent phases. In the simplest case, a membrane is considered as a two-phase system. The first phase, known as the “gel phase”, includes the inert binder, reinforcing fabric and the polymer matrix carrying fixed groups, as well as a charged solution of mobile counterions (and, to a lesser extent, coions) that neutralize the charge of the fixed groups. The second phase is an electroneutral solution, identical to the external equilibrium solution, which fills the intergel space, including structural defects and the central regions of meso- and macropores of the IEM (PEM). The microheterogeneous model is mainly employed to interpret the concentration-dependent behavior of several key membrane properties, such as specific electrical conductivity [9–13], diffusion permeability [14–16], and sorption capacity [13, 17–19]. It is also used to determine the volume fractions of the gel phase ( $f_2$ ) and intergel space ( $f_1$ ), the coefficient  $\alpha$  reflecting the spatial arrangement of the phases, and to estimate counterion and coion diffusion coefficients within the membrane [11, 20]. Most studies applying this model have focused on (1) homogeneous membranes with a uniform nanostructure, (2) quasi-homogeneous composite membranes, or

(3) heterogeneous membranes [21, 22]. Type (1) includes monopolymer or interpolymer membranes, for example, Nafion 117 (DuPont, USA) and CJMA-4 (Hefei Chemjoy Polymer Material Co, China). Quasi-homogeneous (2) composite membranes, such as CSE, ASE (Astom, Japan), consist of an ion-exchange material containing granules of inert binder (40–60 nm). Heterogeneous membranes (3), for example, Ralex AMH PES (Mega, Czech Republic) and MK-40 (Shchekinoazot, Russia), contain ion-exchange resin granules (5–50  $\mu\text{m}$ ) dispersed in an inert binder. Most of these membranes include a reinforcing fabric with a fiber diameter of 30–55  $\mu\text{m}$  [23, 24]. Recently, a new class of quasi-homogeneous membranes, known as pore-filling membranes (PFMs), has been developed. Functional PFMs are attracting increasing attention because their production costs are comparable to those of heterogeneous membranes. This advantage arises from a simpler fabrication process, the use of inexpensive substrates, and lower consumption of pore-filling electrolyte. At the same time, PFMs demonstrate excellent electrochemical characteristics and physicochemical properties similar to those of homogeneous membranes [25–27]. PFMs are typically prepared either by casting an ion-exchange polymer dispersion onto a porous substrate or by soaking the substrate in an ion-exchange polyelectrolyte [22]. Depending on pore orientation within the substrate, PFMs can be classified as isotropic, anisotropic, or asymmetric [28, 29]. Figure 1 illustrates examples of such substrates and a schematic of pores filled with ion-exchange material.

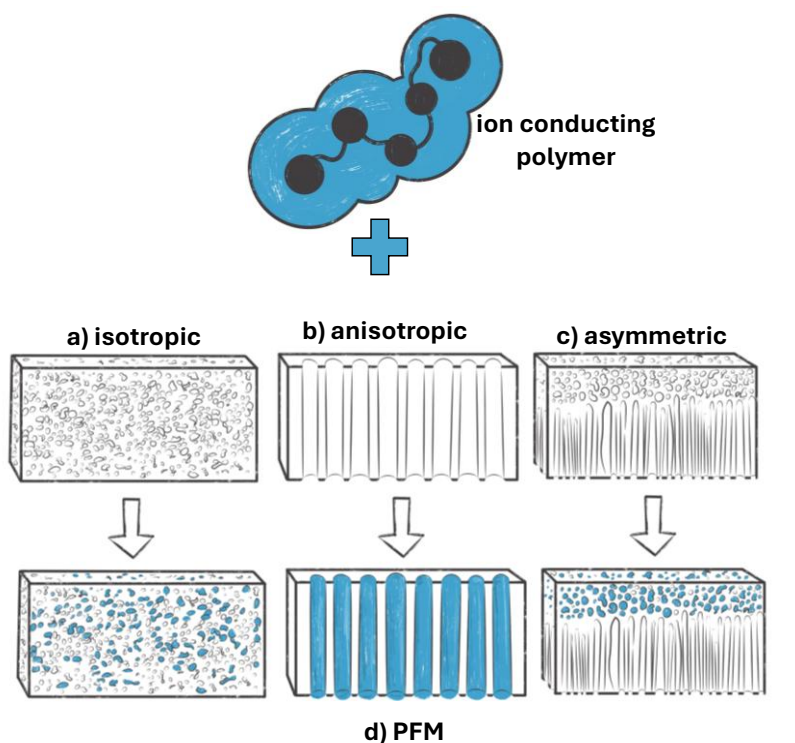


Figure 1. Representative cross-sections of isotropic (a), anisotropic (b), and asymmetric (c) substrates, and PFM (d) derived from them

In fact, PFMs combine the advantages of homogeneous ion-exchange films and porous membranes, while their unique structure helps overcome traditional challenges such as the compromise between thickness and mechanical stability, as well as high ion-exchange capacity and water uptake [30]. The morphology of the porous substrate provides high mechanical stability even for relatively thin PFMs and suppresses undesirable excessive swelling of polyelectrolytes in the membrane pores when humidity, temperature, or external solution concentration changes [31]. A substantial reduction in the number of dead-end pores, compared to membranes of previous generations, ensures high conductivity of PFMs [32]. A dispersion of perfluorosulfonic acid (PFSA) polymer in various solvents [28, 33–36] and 2-acrylamido-2-methyl-1-propanesulfonic acid (AMPS) [37, 38] are often used as cation-exchange pore-filling agents. Literature sources have also reported the possibility of producing environmentally friendly pore filling membranes [27, 39, 40]. In addition, the pore-filling method is the most common approach for preparing so-called “stimuli-responsive” or “smart” membranes [40–44]. Such membranes not only exhibit good selectivity but may also

possess a range of additional functions. For example, R. Xie et al. fabricated thermo-sensitive membranes by grafting poly(N-isopropylacrylamide) (PNIPAM) onto the surfaces and into the pores of polycarbonate track-etched (PCTE) membranes via plasma-graft pore-filling polymerization [44]. R. Childs et al. [43] prepared pH-sensitive pore-filled membranes by incorporating a cross-linked poly(4-vinylpyridine) gel as the pore-filling electrolyte into a porous polyethylene host membrane; in this case, the pure-water permeability of the resulting membrane was reversibly controlled by pH. Commercial examples of PFMs include membranes from Fujifilm Manufacturing B.V. (The Netherlands), which use a nonwoven polyolefin porous substrate made of polyolefin fibers [45], as well as the Nafion™ XL membrane by Ion Power Inc. (USA), which employs a woven microporous substrate made of expanded polytetrafluoroethylene [33].

Anisotropic materials, in particular track-etched membranes (TMs), show considerable promise as PFM substrates due to their ordered, parallel and through pores oriented perpendicular to the membrane surface plane, as well as their regular pore geometry with a narrow pore size distribution (Fig. 1b). Several studies [46, 47] have demonstrated that PFMs with TM substrates exhibit enhanced electrical conductivity compared to conventional IEMs (PEMs), which is attributed to the reduced tortuosity of the counterion transport pathways. Moreover, the low thickness and high mechanical strength of TMs indicate the potential for reduced surface resistance in TM-based PFMs. Despite the growing number of publications on PFMs with TM substrates [28, 34, 48–50], a significant gap remains in the literature regarding the relationship between structure and transport characteristics of these membranes, particularly when analyzed using modern modeling approaches such as the microheterogeneous model.

This study aims to elucidate the relationship between structure and transport properties of pore-filling membranes prepared by incorporating an ion-conducting polymer into track-etched substrates. The specific objectives are: (i) experimental determination of key structural parameters; (ii) measurement of specific electrical conductivity, diffusion permeability, and counterion/coion transport numbers; and (iii) interpretation of the structure–transport property relationship using the two-phase microheterogeneous model.

## 2. Experimental

### 2.1 Membranes

Track-etched membranes with different pore diameters and pore densities were used to fabricate cation-exchange PFMs (Table 1). The TMs were produced at the Flerov Laboratory of Nuclear Reactions, Joint Institute for Nuclear Research (Dubna, Russia) from polyethylene terephthalate films (Hostaphan RNK, Mitsubishi Polyester Films, Japan). The methodology and details of the TM fabrication process are reported elsewhere [51]. The structural, transport, and electrochemical properties of TM 24 and TM 543 have been described previously [52]. A dispersion of LF-4SC (OJSC Plastpolymer, Russia) in the H<sup>+</sup> form (10 % in isopropyl alcohol, equivalent weight — average weight of the polymer per functional group — 980 g mol<sup>−1</sup>) was used as a cation-exchange filler. LF-4SC is obtained by radical copolymerization of tetrafluoroethylene and fluorovinyl ether with a fluorosulfone group [53].

Table 1

Some characteristics of TM used as anisotropic substrates for PFMs fabrication

Parameter	TM-24	TM-543	TM-120
Matrix material	polyethylene terephthalate		
Fixed groups	-COOH, -OH		
<sup>1</sup> Pore diameter, $d_p$ , nm	1340 ± 10	580 ± 5	140 ± 3
<sup>1</sup> Surface pore density, $N \times 10^7$ cm <sup>−2</sup>	1	7	89
<sup>2</sup> Surface porosity, $\varepsilon$ %	12 ± 1	19 ± 1	14 ± 1
<sup>1</sup> — the number of tracks (pores) per unit area was estimated using SEM images;			
<sup>2</sup> — total pore area normalized per unit area of the membrane surface; estimated using the equation $\varepsilon = (1/4)\pi Nd_p^2$ [54].			

All TM substrates were initially weighed in an air-dry state and subsequently cleaned by sequential washing with isopropanol (C<sub>3</sub>H<sub>8</sub>O, 99.9 %, Sigma-Aldrich) and deionized water (conductivity = 5.28 ± 0.01 μS cm<sup>−1</sup>, pH = 4.86 ± 0.01 at 25 °C) prior to any modification.

A track-etched membrane was mounted in a filter holder (vacuum filtration device, Fig. S1, Supplementary Materials) on top of a 1 cm thick silicone rubber band with ~5 μm diameter holes. Ten milliliters of LF-4SC solution (PFSA concentration of 5.0, 2.5, or 1.5 wt %) were applied onto the upper surface of the TM



(Surface 1), and the system was hermetically sealed. Air beneath the membrane was evacuated using a vacuum pump until the first drops of the pore-filling solution appeared at the lower surface of the TM (Surface 2). The sample was then carefully removed and dried in a vacuum oven at 80 °C for 3 hours. This procedure was repeated twice. The resulting membranes were designated PF-Y\_X, where Y denotes the track-etched membrane number (Table 1) and X corresponds to the LF-4SC mass concentration in the pore-filling solution.

The commercial homogeneous cation-exchange membrane MF-4SC (OJSC Plastpolymer, Russia) was investigated as a reference for comparative analysis. The membrane MF-4SC (an analogue of Nafion-117) is prepared by solution casting of LF-4SC in the lithium form (10 wt% in dimethylformamide solution).

For conditioning of PFSA-based CEMs, oxidative-thermal pretreatment is commonly employed [47, 55], which removes residual unreacted monomers and leads to pore expansion. In order to avoid possible deformation of the substrate, a standard salt pretreatment [21] was applied to both experimental and commercial membranes in this study.

## 2.2 Experimental Methods for Membrane Characterization

**Morphology of membrane surfaces and cross-sections.** The morphology of the membrane surfaces and cross-sections of dry samples was examined after transport characterization using a JEOL JSM-7500F scanning electron microscope (SEM) (JEOL Ltd., Japan). To improve conductivity and enhance image quality, the samples were coated with a thin (about 5 nm) layer of silver nanoparticles. The surface porosity was determined as the ratio of the pore outlet area to the unit area of the TM.

**The chemical composition of the surface of air-dried samples** was analyzed by energy-dispersive X-ray spectroscopy coupled with SEM, as well as by attenuated total reflectance Fourier-transform infrared (ATR-FTIR) spectroscopy using a Vertex70 spectrometer (Bruker Optics, Germany) in the range of 4000–500 cm<sup>-1</sup>. The IR spectra were processed using OPUS<sup>TM</sup> software.

**Membrane thickness** was measured at least 20 times at different points across each air-dried sample using a Micron MKC-25 digital micrometer (Micron, China). The average thickness and measurement error were then calculated.

**Perfluorosulfonic acid polymer content in PF-Y\_X.** The amount of cation-exchange material in the fabricated membranes ( $\Delta m$ , g cm<sup>-2</sup>) was calculated as:

$$\Delta m = \frac{m_0 - m_1}{S_0} \times 100 \%, \quad (1)$$

where  $m_0$  is the weight of the dry track-etched substrate membrane, g;  $m_1$  is the weight of the dry PF-Y\_X membrane, g; and  $S_0$  is the membrane area, cm<sup>2</sup>.

**Water uptake.** All membranes were pre-equilibrated in deionized water. The sample was then removed, and excess surface moisture was carefully blotted with filter paper. Subsequently, the sample was placed in an MB25 moisture content analyzer (Ohaus Co., USA). The mass of the swollen sample,  $m_{sw}$ , was measured at a temperature of 25 °C. Water was evaporated at 100 °C until a constant mass of the dry sample,  $m_{dry}$ , was achieved. The water uptake of the membrane,  $W$  (%), was calculated as:

$$W = \frac{m_{sw} - m_{dry}}{m_{dry}} \times 100 \%. \quad (2)$$

**The total ion-exchange capacity ( $Q$ )** of both strongly acidic cation-exchange membranes and weakly acidic track-etched membranes was determined using the static method [19, 52]. A membrane sample of known dry mass ( $m_{dry}$ ), converted to the H<sup>+</sup> form, was immersed for 24 h with periodic shaking in either 100 mL of 0.1 M sodium hydroxide (for membranes with strongly acidic groups) or 20 mL of 0.01 M sodium acetate (for membranes with weakly acidic groups). The resulting solutions (with the membranes still immersed) were then potentiometrically titrated with 0.1 M HCl solution (strongly acidic fixed groups) or 0.01 M NaOH solution (weakly acidic fixed groups) using an EasyPlusTitrators autotitrator (METTLER TOLEDO, Switzerland). Titration data were recorded via computer output.

The ion-exchange capacity of the dry membrane (strongly acidic fixed groups),  $Q$  (mmol g<sup>-1</sup>) was determined using the formula:

$$Q = \frac{100 - kV}{10 \cdot m_{dry}}, \quad (3)$$

where  $V$  is the volume of hydrochloric acid solution used for titration;  $k$  is a coefficient equal to the ratio of the working solution volume to the aliquot volume.



The calculation of the ion-exchange capacity of the dry membrane (weakly acidic fixed groups) in mmol g<sup>-1</sup> was carried out according to the equation:

$$Q = \frac{(V_T C_T)}{m_{dry}}, \quad (4)$$

where  $V_T$  is the volume of titrant (NaOH) corresponding to the inflection point of the potentiometric titration curve.

**Specific electrical conductivity** was measured by the difference method [56] using a clip cell and a GW Instek LCR-76002 RLC immittance analyzer (GW Instek, China) in NaCl solutions of 0.1, 0.2, 0.3, 0.4, and 0.5 M.

**Diffusion permeability.** Integral diffusion permeability coefficients were determined in a two-chamber flow cell according to the procedure described in [19]. The membrane separated compartment I (initially deionized water) and compartment II (NaCl solution: 0.1, 0.2, 0.3, 0.4, 0.5 M). The NaCl concentration in compartment I ( $C_I$ ) was calculated from electrical conductivity and pH using Kirchhoff's law and the second Gluckauf approximation. The electrolyte diffusion flux density through the membranes was determined as

$$J_{dif} = \frac{1}{S} \frac{d(C_I V_I)}{dt}, \text{ where } V_I \text{ is the volume of water in compartment I and } S \text{ is the active membrane area.}$$

**Osmotic permeability** [57] was estimated in conjunction with diffusion permeability by measuring water transfer from compartment I (deionized water) to compartment II (NaCl solution) over 3 hours. The water flux density,  $J_w$  [mol s<sup>-1</sup> m<sup>-2</sup>], was then calculated using the formula:

$$J_w = \frac{\rho(V_0 - V_t)}{MtS}, \quad (5)$$

where  $V$  is the volume of water in compartment I (cm<sup>3</sup>),  $\rho$  is the density of distilled water (considered equal to 1.0 g cm<sup>-3</sup>);  $M$  is the molar mass of water (18 g mol<sup>-1</sup>),  $S$  is the active area of the swollen membrane (m<sup>2</sup>);  $t$  is the experiment duration (s). Index 0 denotes the volume in compartment I before the start of the experiment.

Experiments were conducted at 25.0 ± 0.5 °C.

### 3. Results and Discussion

#### 3.1 Microstructure and Chemical Composition of the Studied Membranes

##### SEM Images of Dry Samples

Figures 2 and 3 present the surface and cross-section images of both the TM substrates and the resulting PF-Y\_X samples.

As seen in Figure 2 and Figure 3, the pore outlets are randomly distributed across the surface of the TM substrates, which is typical of such membranes [58]. SEM cross-sectional images reveal predominantly cylindrical pores (> 0.5 μm) oriented perpendicular to the surface plane. It has been reported [47] that smaller pores exhibit less regular geometries.

Figure 2 and Figure 3 also demonstrate that, in PF-Y\_1.5 samples prepared with a pore-filling solution containing 1.5 wt % LF-4SC, the ion-conducting polymer occupies the pores of the TM substrate to a greater extent compared to other cases. The cross-sectional images of PF-Y\_1.5 (Fig. 2 b, e, h) clearly show penetration of the LF-4SC polymer into the TM substrate from Surface I, onto which the solution was applied during fabrication. The polymer penetration depth increases in the order PF-120\_1.5 < PF-543\_1.5 < PF-24\_1.5, correlating with the increasing pore diameter of the TM substrate.

When the concentration of LF-4SC in the pore-filling solution was increased, a distinct polymer surface layer formed (as illustrated in Fig. 2 c, f, i). This layer was primarily observed on Surface I, the surface onto which the pore-filling solution had been applied. By contrast, Surface II, which faced the vacuum chamber during the membrane fabrication process, showed only negligible polymer deposition. For example, in the PF-120\_X membrane (Fig. 3), Surface I appeared practically homogeneous, whereas the morphology of Surface II remained similar to that of the original TM-120 substrate (Fig. 2c). The thickness of the LF-4SC layer increased in the order PF-24\_5 < PF-543\_5 < PF-120\_5 (Fig. 3, Table 3), indicating an inverse correlation between the thickness of the polymer layer and the pore diameter of the TM substrate.

For comparison, the homogeneous MF-4SC membrane exhibited a uniform surface and bulk structure [59].

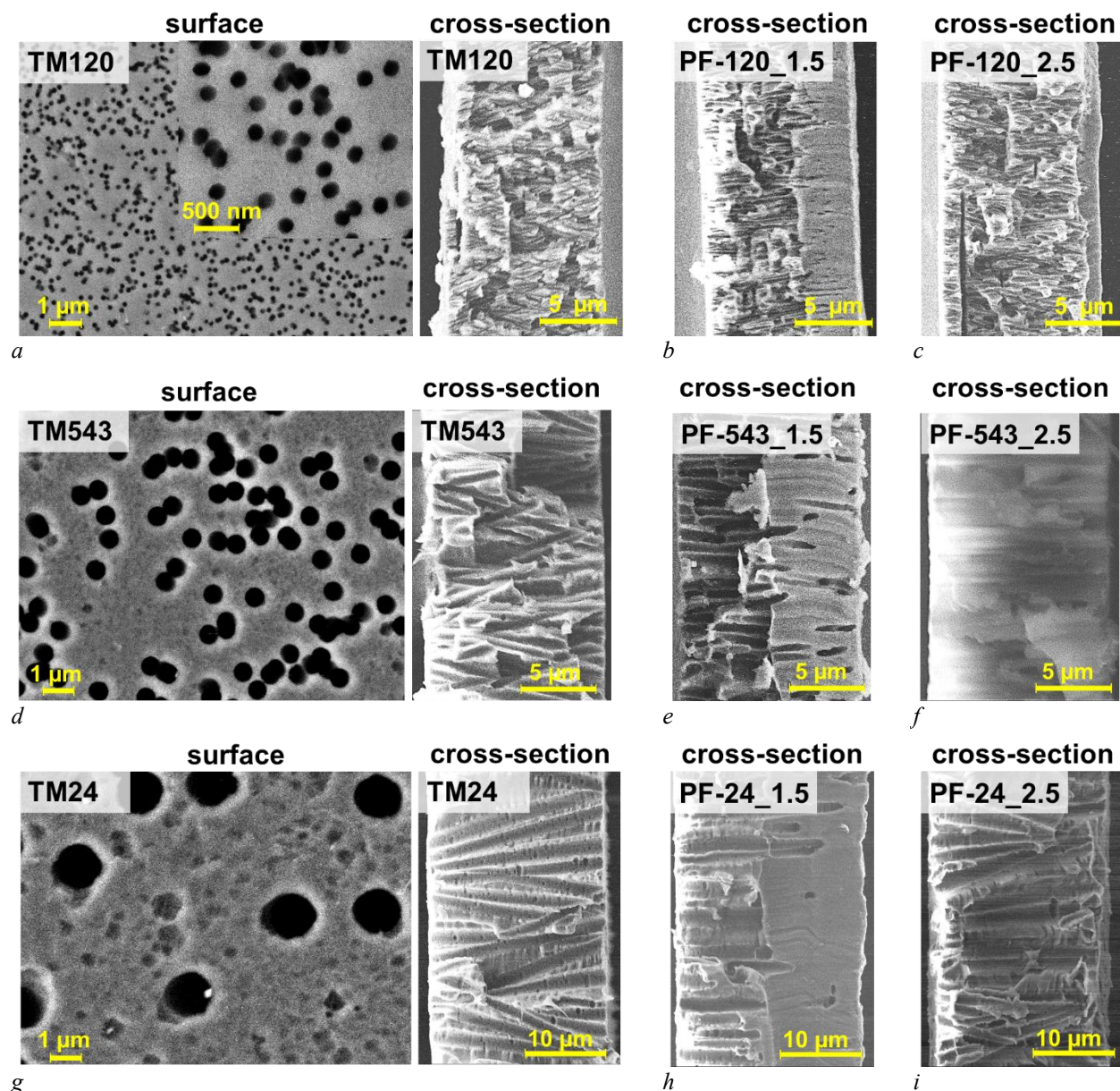


Figure 2. SEM images of the surfaces and cross-sections of the TM substrates (a, d, g), as well as cross-sections of the experimental samples PF-Y\_1.5 (b, e, h) and PF-Y\_2.5 (c, f, i)

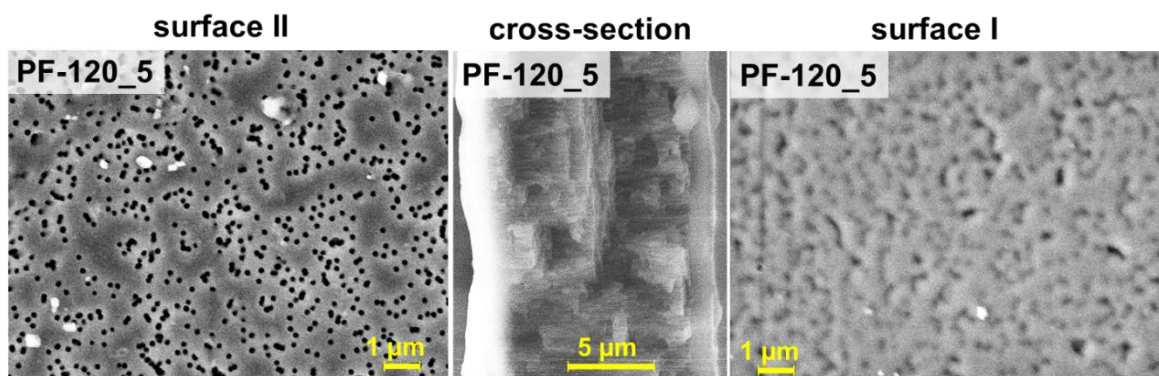


Figure 3. SEM images of the surfaces and cross-section of the experimental sample PF-120\_5. Further details are provided in the text

### 3.2 Results of ATIR Spectroscopy and Energy-Dispersive X-Ray Spectroscopy

The data obtained from scanning electron microscopy are consistent with the compositional analysis provided by energy-dispersive X-ray (EDX) spectroscopy (Fig. S2, Supplementary Materials), as detailed in Table 2. The EDX results show that on Surface I the fluorine content (originating from the LF-4SC polymer) increases both with higher LF-4SC concentration in the pore-filling solution and with decreasing pore diameter of the substrate surface. In contrast, at Surface II, a higher fluorine content was detected in sample PF-543-2.5 than in PF-120-5.0, suggesting a different trend.

Table 2

Carbon, oxygen and fluorine content (atomic %) on the membrane surface and cross-section

Membrane	$^2\Delta m_{dry}$ , $\text{mg}\cdot\text{cm}^{-2}$	Surface I			Cross-section (near surface II)		
		C	O	F	C	O	F
TM-Y	—	88	12	—	88	12	—
PF-543 2.5	0.26	55	23	22	63	23	14
PF-120 5.0	0.27	40	2	58	76	21	3

<sup>1</sup>Reproducibility of three measurements is  $\pm 2\%$ .  
<sup>2</sup>Membrane mass gain after modification.

Figure 4 shows the IR spectra of the LF-4SC film, the TM-120 track membrane, and the PF-120\_5 sample.

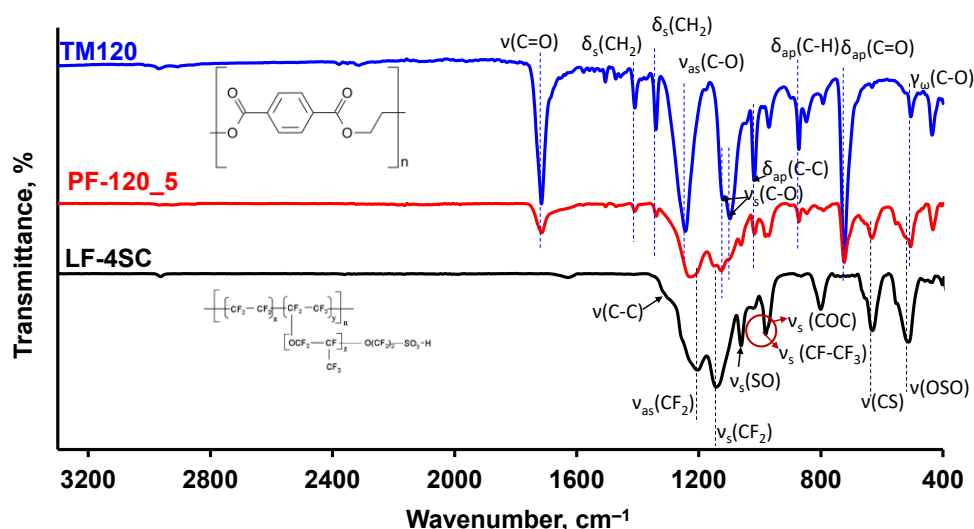


Figure 4. IR spectra of the TM-120 substrate surface, PF-120\_5.0 sample cross-section, and LF-4SC film (cast from isopropyl alcohol)

The IR spectrum of the TM-120 substrate exhibits characteristic bands of polyethylene terephthalate [60, 61]: C=O (stretching vibrations of carbonyl groups,  $1715\text{ cm}^{-1}$ ), C–O (stretching vibrations in ester groups,  $1243\text{ cm}^{-1}$ ), C–O–C (stretching vibrations in ethers,  $1097\text{ cm}^{-1}$  and  $1120\text{ cm}^{-1}$ ), CH<sub>2</sub>- (symmetrical bending vibrations of methylene groups in the plane of H atoms,  $1410\text{ cm}^{-1}$  and  $1340\text{ cm}^{-1}$ ), C–C (bending vibrations of the benzene ring in the plane of the ring,  $1018\text{ cm}^{-1}$ ), C–H (bending vibrations of the benzene ring perpendicular to the plane of the ring,  $872\text{ cm}^{-1}$ ), C=O (bending vibrations of the carbonyl group in the plane of the C atoms,  $723\text{ cm}^{-1}$ ).

The IR spectrum of the LF-4SC layer is characterized by asymmetric and symmetric stretching vibrations of the CF<sub>2</sub> groups at  $1143$  and  $1203\text{ cm}^{-1}$ , as well as strong stretching of the –SO<sub>2</sub>F side chain at  $1205\text{ cm}^{-1}$  and medium-intensity stretching of the C–O–C group at  $989\text{ cm}^{-1}$ , which are characteristic of perfluorsulfonic acid [62, 63]. The IR spectrum of the PF-120\_5 sample cross-section is a superposition of the spectra of TM-120 and the LF-4SC film. For PF-120\_5, a pronounced decrease in the intensity of the peaks characterizing polyethylene terephthalate is observed, while broad intense peaks appear at  $507\text{ cm}^{-1}$ ,

632  $\text{cm}^{-1}$ , along with a weak band at 1060  $\text{cm}^{-1}$ , corresponding to symmetric and asymmetric vibrations of sulfo-groups [63].

### 3.3 Equilibrium and Transport Characteristics of Membranes

Table 3 provides a summary of the key characteristics of the studied membranes. Figure 5 compares area resistance, osmotic water flux ( $J_w$ ), and NaCl diffusion flux ( $J_s$ ) for the track-etched membranes and the resulting ion-exchange membranes (PF-Y\_X), with MF-4SC included as a reference. The performance of the PF-Y\_X membranes is largely governed by the properties of the TM substrates employed in their fabrication (Tables 1, 3).

Table 3

Some characteristics of the membranes under study

Membrane	$\Delta m_{dry}$ , $\text{mg cm}^{-2}$	$d_{sw}$ , $\mu\text{m}$	$d_{dry}$ , $\mu\text{m}$	$\Delta d_{dry}$ , $\mu\text{m}$	$Q$ , $\text{mmol g}^{-1}_{dry}$	$\Delta Q/\varepsilon$ , $\text{mmol g}^{-1}_{dry}$	$W$ , %	$\Delta W/\varepsilon$ , %
<b>MF-4SC</b>	–	195±2	177±3		0.84	–	24.0	–
<b>TM 24</b>	–	21±1			0.01	–	2.5	–
PF-24 1.5	0.05	23.4	21.0	0.2	0.02	0.09	3.1	5.2
PF-24 2.5	0.06	23.8	22.8	0.8	0.03	0.18	3.4	7.6
PF-24 5	0.17	23.8	23.0	1.0	0.05	0.37	5.0	20.8
<b>TM 543</b>	–	11±1			0.02	–	3.9	–
PF-543 1.5	0.06	12.8	11.7	0.7	0.04	0.08	8.3	23.0
PF-543 2.5	0.26	18.4	15.7	4.7	0.20	0.93	9.5	29.6
PF-543 5	0.45	20.8	19.0	8.0	0.35	1.71	23.4	102.4
<b>TM 120</b>	–	10±1			0.05	–	2	–
PF-120 1.5	0.08	14.7	12.8	2.8	0.09	0.31	8.3	45.2
PF-120 2.5	0.12	19.4	16.3	6.3	0.11	0.47	6.1	29.0
PF-120 5	0.27	20.6	18.7	9.5	0.27	1.61	14.9	91.9
Error		±0.05	±0.3		±0.01		±1.0	

Literature [6, 64, 65] reports the formation of a “loose” or “gel layer” on the TM pore walls, containing –OH and –COOH groups. This nanometer-thick layer is generated during heavy ion bombardment followed by chemical etching, as a result of incomplete polymer degradation. The gel layer, typically a few nanometers thick, exhibits ion-exchange characteristics and is capable of swelling in aqueous environments. Polytetrafluoroethylene track-etched membranes have shown surface charge densities ranging from 0.1 to 1 elementary charge per  $\text{nm}^2$ , as determined by various methods [6, 64, 65]. Consequently, the ion-exchange capacity of the TMs increases in the following order: TM 24 < TM 543 < TM 120, which correlates with a decreasing pore diameter and increasing pore density (Tables 1 and 3), thereby enhancing the relative contribution of the “gel layer”.

The water uptake of TMs depends not only on the degree of hydration of the fixed groups within the gel layer, but also on the amount of free water in the membranes, which is determined by the value of the volume porosity (here assumed to be equivalent to the surface porosity; Table 1). Accordingly, water uptake increases in the order TM 120 ≈ TM 24 < TM 543.

The adopted pore-filling strategy for producing PF-Y\_X membranes leads to a systematic increase in several key properties with increasing LF-4SC concentration in the impregnating solution. Specifically, increases are observed in the specific mass of the ion-conducting polymer, membrane thickness, ion-exchange capacity, and water uptake (Table 3). The difference in thickness, measured in the dry state, between the PF-Y\_X membranes and their corresponding TM substrates allows estimation of the thickness of the LF-4SC layer formed on the surface of these experimental membranes. The lowest values of this parameter ( $\Delta d$ ) are observed for PF-Y\_1.5 samples (prepared with the 1.5 wt% LF-4SC solution), whereas the highest are found for PF-543\_5.0 and PF-120\_5.0.

When the ion-conducting polymer is predominantly located within the pores of the PF-Y\_X samples, the resulting increase in ion-exchange capacity and water uptake, normalized to the porosity of the TM substrate, shows a relatively weak dependence on the LF-4SC concentration used for pore filling. In contrast, the formation of an LF-4SC film on the surface of the PF-Y\_5 samples (fabricated with the highest LF-4SC concentration) leads to a sharp and significant increase in the measured values of ion-exchange capacity ( $\Delta Q/\varepsilon$ )



and water uptake ( $\Delta W/\varepsilon$ ), as summarized in Table 3. Moreover, when the ion-conducting polymer is primarily located within the pores of the membranes, the rigid and inflexible structure of the TM substrate restricts the swelling of the PF-Y\_X samples. However, the particular type of TM substrate used does not appear to exert any significant effect on the degree of swelling exhibited by the LF-4SC surface layer of these membranes.

The observed differences in the extent to which the pores are filled with the ion-exchange material, coupled with the presence of layers of ion-conducting polymer on the surface of certain PF-Y\_X samples, give rise to a complex and intricate relationship between the underlying structural parameters of the TM substrate, the concentration of LF-4SC used in the pore filling solution, and the resulting transport characteristics of the fabricated experimental membranes (Fig. 5).

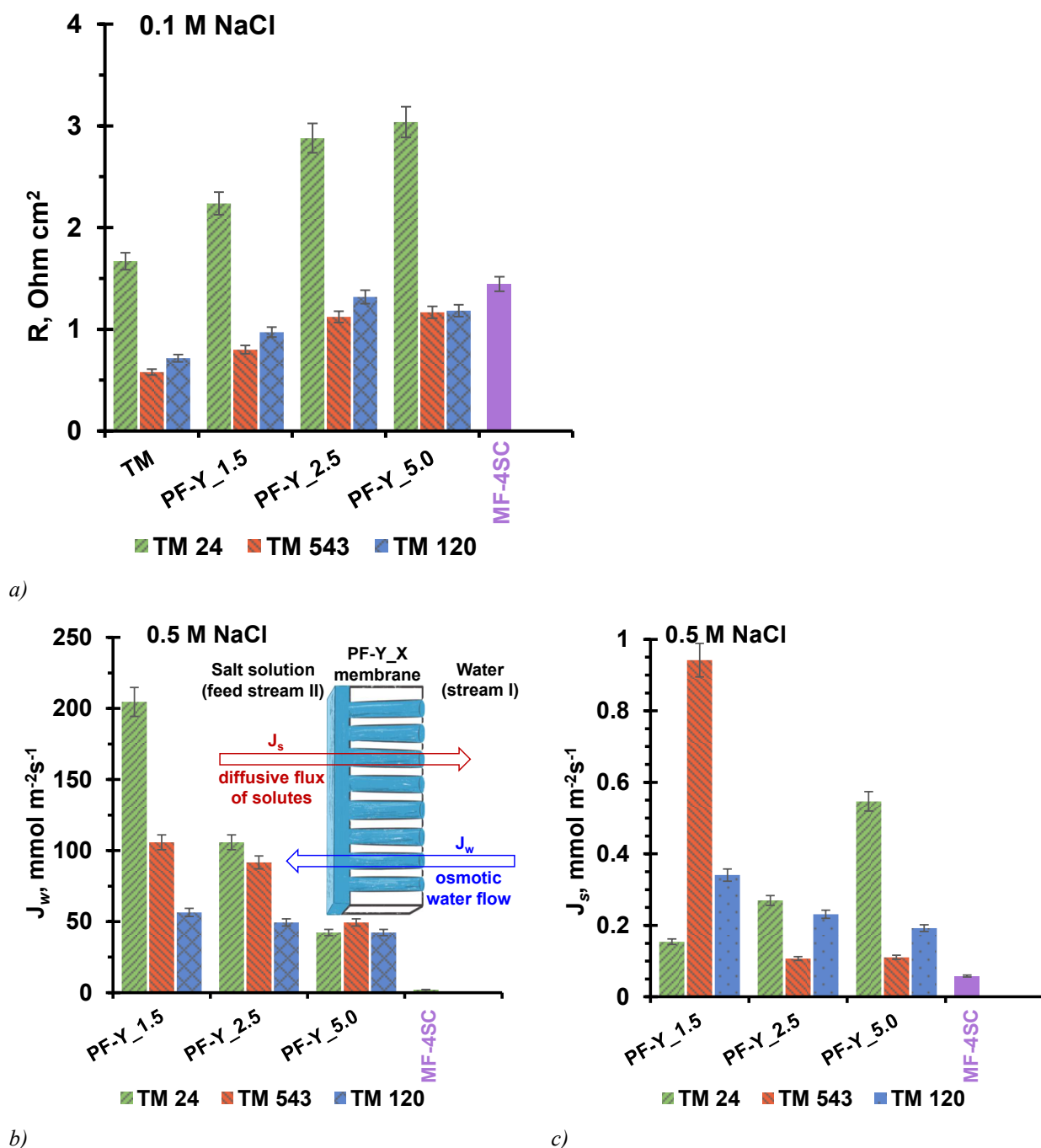


Figure 5. Area resistance (a), densities of the osmotic water flux  $J_w$  (b) and electrolyte diffusion flux across the membrane  $J_s$  (NaCl) (c) of the TM substrates and ion-exchange membranes (PF-Y\_X).

The characteristics of the MF-4SC membrane are given for comparison

The PF-Y\_X membranes exhibit higher area resistance compared to the TM substrates (Fig. 5a), as expected [2]. This effect arises because the ion-exchange material replaces the 0.1 M NaCl solution (90.9 Ohm cm<sup>2</sup>) within the TM pores, the resistance of which is approximately 1.4 times lower than that of LF-4SC. Furthermore, the LF-4SC film itself adds to the resistance of the PF-Y\_X membranes, with the contribution increasing proportionally to its thickness.



Figure 6. Schematic illustration of the PF-Y\_X sample, consisting of a layer of LF-4SC ion-conducting material and a track membrane with straight pores filled with the same ion-conducting material

In line with the concepts outlined in studies [47, 66], the resistance of the PF-Y\_X samples, schematically illustrated in Figure 6, can be regarded as the sum of the resistances of the LF-4SC layer and the track-etched membrane, the pores of which are filled with the same ion-exchange material:

$$R_{PF-Y_X} = R_{FL} + R_{PFL} \quad (6)$$

Hereafter, the following indices are used: PF-Y\_X — a sample of the PFM membrane; FL — the film layer of the LF-4SC polymer on the PFM surface; PFL (pore-filled layer) — the TM with pores filled with the LF-4SC polymer. The resistance of LF-4SC film can be easily estimated using the following formula:

$$R_{FL} = \frac{d_{FL}}{\kappa_{FL}^*}, \quad (7)$$

where  $\kappa_{FL}^*$  is equal to specific electrical conductivity of the LF-4SC. Then:

$$R_{PFL}^{exp} = R_{PF-Y_X}^{exp} - \frac{d_{FL}}{\kappa_{FL}^*} \quad (8)$$

The index *exp* denotes the resistance found experimentally.

The resistance of an ideal PFL layer can be estimated under the following assumptions: all pores of the track membrane are straight, and the LF-4SC polymer completely and defect-free fills these pores (Fig. 6). In this case, the PFL can be considered as a parallel circuit consisting of alternating components of the dielectric material of the TM and the ion-exchange material. Accordingly, the resistance of the PFL layer is determined as:

$$\frac{1}{R_{PFL}} = \frac{1}{R_{TM}} + \frac{1}{R_F} \quad (9)$$

Here  $R_{TM}$  denotes the resistance of the material from which the track-etched membranes are made. As a first approximation, we may assume that  $R_{TM} \rightarrow \infty$ . Then  $R_{PFL} = R_F$ , where  $R_F$  is the resistance of the LF-4SC polymer, completely filling the pores:

$$R_{PFL} = R_F = \frac{d_{PFL}}{\varepsilon \kappa_{FL}^*}, \quad (10)$$

where  $\varepsilon$  is the volume fraction of pores in the PFL layer, which is equal to the volumetric porosity of the TM. To estimate the value of  $R_{PFL}^{exp}$ , we use equation (10), substituting  $\varepsilon^{exp}$  in place of  $\varepsilon$ . The parameter  $\varepsilon^{exp}$  accounts for the incomplete filling of TM pores with the LF-4SC polymer. The coefficient  $\gamma$  is determined as follows:



$$\gamma(\%) = 100 \frac{R_{PFL}^{exp} - R_{PFL}}{R_{PFL}} = 100 \frac{\varepsilon - \varepsilon^{exp}}{\varepsilon^{exp}}, \quad (11)$$

allows estimation of the proportion of TM pores that are not filled with the LF-4SC polymer.

The estimated  $\gamma$  values, calculated using formula (11), are presented in Figure 7. These values correlate well with the SEM morphological observations, indicating that a decrease in TM pore diameter and an increase in LF-4SC concentration in the pore-filling solution both enhance the fraction of pore volume left unoccupied by the LF-4SC polymer. Notably, despite this incomplete filling, the  $R$  values measured for the PF-543\_X and PF-120\_X samples are comparable to those obtained for the MF-4SC membrane (Fig. 5a). This result, favorable for electromembrane applications, is primarily attributed to the markedly reduced thickness of PFMs relative to conventional membranes.

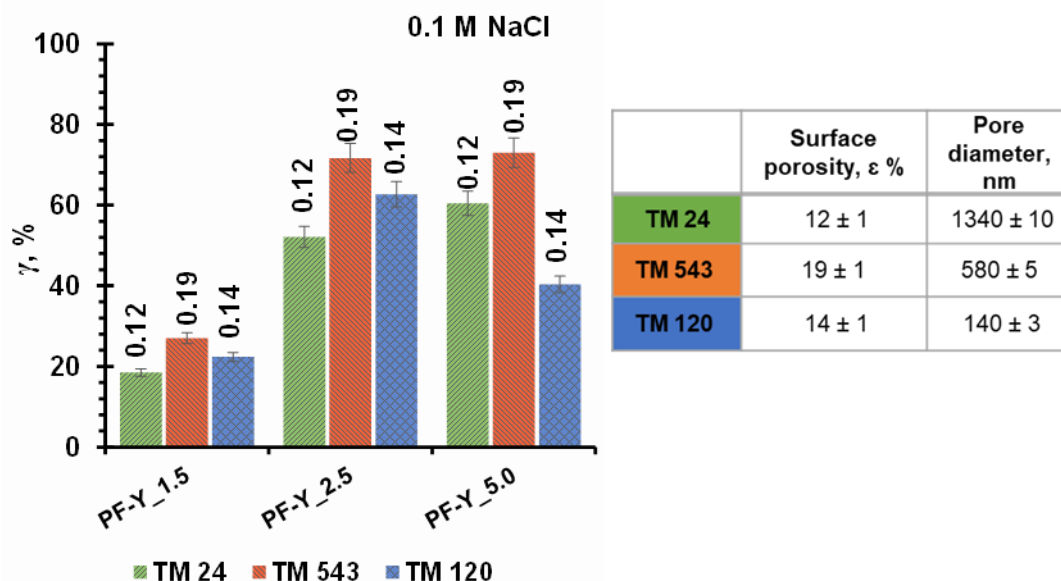


Figure 7. Proportion of PF-Y\_X pores not filled with LF-4SC ion-conducting polymer. The surface porosity (assumed to be equal to the volume porosity) for each TM is provided in the table

Due to the fact that the thickness of the electrical double layer formed on the pore walls is two orders of magnitude smaller than the pore diameter (Table 1) [6], water transport through the TM membrane can occur even under a small pressure difference. In contrast, the PF-Y\_X samples lose this ability because of pore filling (Fig. 3c). Moreover, the measured values of  $J_w$  (osmotic water flux) decrease with increasing LF-4SC concentration in the pore-filling solution and with increasing thickness of the LF-4SC layer formed on the PF-Y\_X surface. Despite this decrease in  $J_w$ , the resulting values still significantly exceed those that are measured for the MF-4SC membrane. The comparatively high  $J_w$  values can be attributed to non-uniform pore filling with the ion-exchange material, a defect that is most apparent in the PF-24\_1.5 sample, but is also present in all of the obtained samples (as can be seen in Fig. 5). The presence of the LF-4SC layer as a continuous film on the surface of the PF-Y\_5.0 samples further reduces water flux density. However, these values still remain elevated, primarily because the thickness of this surface film is much smaller than the total thickness of the MF-4SC membrane (Table 3).

The electrolyte diffusion flux through the PF-Y\_X experimental membranes is generally higher than that measured for the commercial MF-4SC membrane (Fig. 3d). Notably, for the PF-24\_X samples, the flux increases with increasing LF-4SC concentration, whereas for the PF-543\_X and PF-120\_X samples, the flow decreases with increasing LF-4SC concentration in the pore-filling solution. The largest reductions in diffusion flux, relative to the MF-4SC membrane, are observed for PF-543\_2.5 and PF-543\_5.0.

The differences in how the TM pore morphology and LF-4SC concentration affect the osmotic and diffusion permeability of the membranes are presumably attributed to the PF-Y\_X fabrication process. Due to the amphiphilic nature of the PFSA polymer, it readily forms micelles in polar solvents such as water and isopropyl alcohol [67, 68], which prevents complete, void-free filling of the substrate pores. The effect of polymer aggregation is further enhanced by decreasing the substrate pore size [28, 69] and increasing the

polyelectrolyte concentration in the pore filling solution, which increases its viscosity. Consequently, for each substrate with a specific pore diameter, there exists an optimal polymer concentration that leads to the formation of nanovoids [70]. The presence of these nanovoids introduces a complex influence on both the osmotic pressure (which should be applied to the concentrated solution to prevent the solvent from transferring across the membrane) and the diffusion of electrolyte through the membrane [35, 71]. It is noteworthy that the osmotic and diffusion flows across the membrane are oppositely directed (insertion in Fig. 5b), hence a high osmotic flux can effectively hinder electrolyte diffusion across the membrane.

Considering all the data, the PF-120\_5 and PF-543\_5 samples emerge as the most suitable for providing an optimized balance between transport characteristics, mechanical strength, minimal membrane thickness, and efficient use of ion-exchange material.

### 3.4 Structural and Transport Parameters of the Studied Membranes

The two-phase microheterogeneous model [4] provides a deeper understanding of the structure-property relationship in PF-120\_5 and PF-543\_5 membranes. Using this model, the structural and transport parameters of these membranes, along with those of MF-4SC, were determined from the concentration dependence of their specific conductivity (Fig. 8a, b) and diffusion permeability (Fig. 8c) in NaCl solutions.

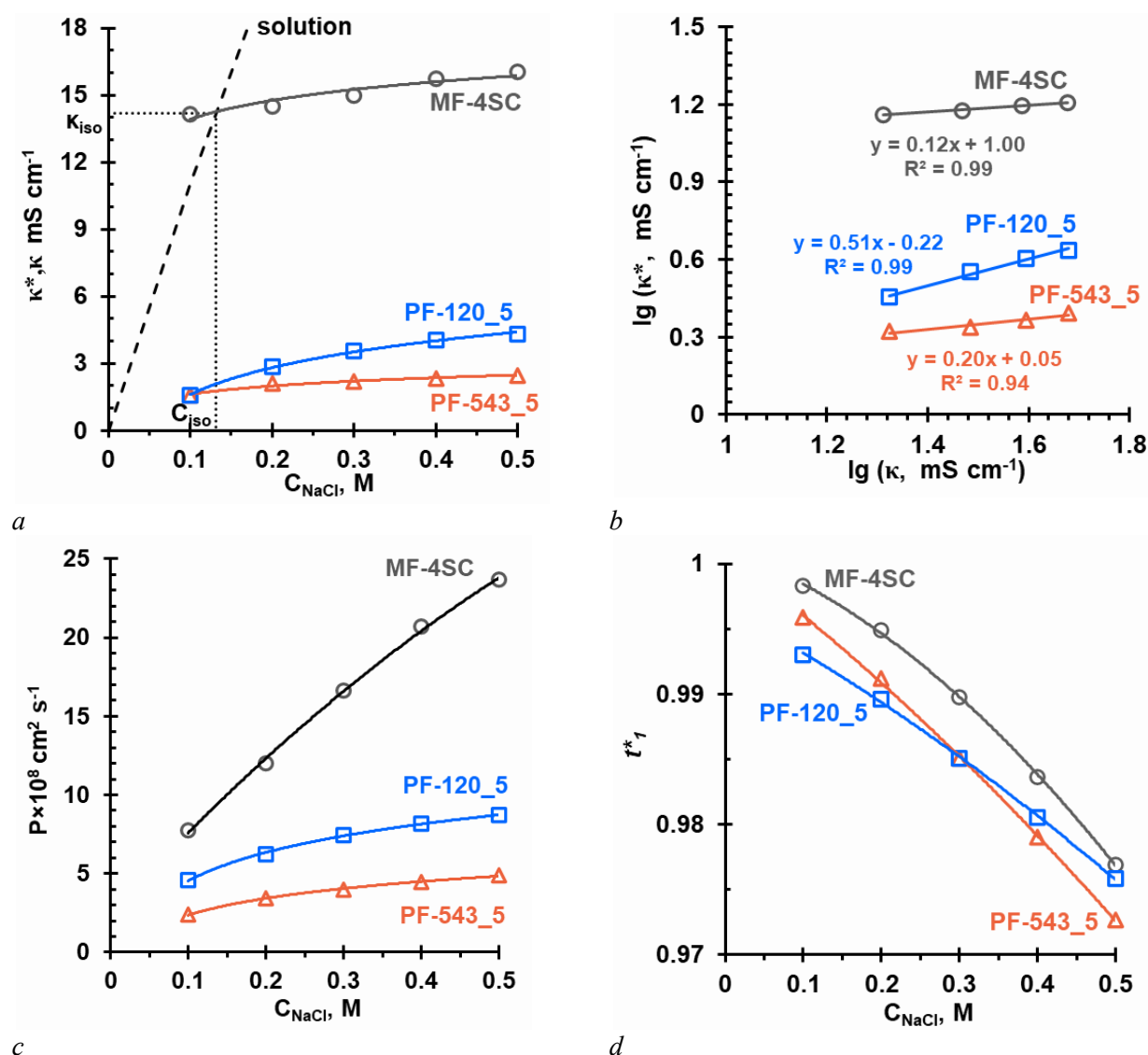


Figure 8. Concentration dependences of specific electrical conductivity  $\kappa^*$  (a), integral coefficient of diffusion permeability  $P$  (c) and counterion transport numbers  $t_1^*$  (d) of the studied membranes in NaCl solution.

Figure (b) demonstrates the procedure for determining the parameter  $f_2$ . The numbers near the curves correspond to the membrane designations (Table 3). The dotted line in Fig. (a) corresponds to the concentration dependence of the solution's electrical conductivity

Table 5 presents values of the structural parameter ( $\alpha$ ), characterizing gel phase/intergel space arrangement), intergel space volume fraction ( $f_2$ ), ion-exchange capacity ( $\bar{Q}$ ) and counterion diffusion coefficient ( $\bar{D}_1$ ) in the gel phase, as obtained from the microheterogeneous model. Figure 8b illustrates the  $f_2$  determination from the slope of membrane electrical conductivity versus NaCl solutions concentration curves (logarithmic coordinates). Details on determining other parameters are provided in [19, 72].

Table 5

**Structural and transport parameters of the studied membranes in NaCl solution, determined using a microheterogeneous model**

Membrane	$f_2$	$\alpha$	$\bar{Q}$ , mmol cm <sup>-3</sup> <sub>sw</sub>	$\bar{D}_1 \times 10^6$ , cm <sup>2</sup> s <sup>-1</sup>
MF-4SC	0.12±0.02	0.35±0.02	1.1±0.1	2.9±0.2
PF-543_5	0.20±0.02	0.27±0.02	0.5±0.1	0.6±0.2
PF-120_5	0.51±0.02	0.09±0.02	0.7±0.1	0.2±0.2

Prior to discussing the data obtained, it should be noted that the studied MF-4SC membrane apparently exhibits lower crystallinity compared to similar membranes reported in [73–75]. This follows from the higher water uptake, specific electrical conductivity, volume fraction of intergel spaces, and the value of the diffusion permeability coefficient of MF-4SC (Figure 8, Table 5), which may result from differences in solvent removal (annealing) conditions during commercial membrane production, as well as variations in pre-treatment procedures.

The specific electrical conductivity of the membranes is primarily governed by counterion transport. For the experimental PF-543\_5 and PF-120\_5 membranes, as well as for the commercial MF-4SC membrane, specific conductivity increases with increasing concentration of the external solution. This behavior is typical of most ion-exchange membranes in strong electrolyte solutions and has been extensively discussed in the literature [24]. Within the studied range of NaCl concentrations, the conductivity of the PF-543\_5 and PF-120\_5 samples is nearly an order of magnitude lower than that of the commercial MF-4SC membrane (Fig. 8a). This reduction, discussed in Section 3.2, is mainly attributed to the low volume fraction of pores in the track-etched membranes and the incomplete filling of these pores with the LF-4SC polymer. Based on the derived  $f_2$  values (Table 5), the PF-120\_5 sample appears to contain a greater number of voids filled with the external solution than the PF-543\_5 sample. As mentioned in Section 3.1, this difference arises from the partial aggregation of the LF-4SC polymer due to its high concentration in the pore-filling solution [28, 69]. However, it is important to note that, only in the case of the MF-4SC membrane, the studied concentration range satisfies the condition  $0.1C_{iso} < C < 10C_{iso}$ , where  $C_{iso}$  represents the concentration of isoelectric conductivity of the gel phase and the intergel space. This condition is required for the simplified equation  $\kappa^* = \bar{\kappa}^{f_1} \kappa^{f_2}$  to be applicable (the derivation of this equation is provided in the S3, Supplementary materials). Consequently, the  $f_2$  values that were determined for the PF-120\_5 and PF-543\_5 samples may be overestimated [24].

Parameter  $\alpha$  (characterizing gel/intergel phase arrangement) increases in the sequence: PF-120\_5 < PF-543\_5 < MF-4SC (Table 5). This trend suggests a gradual transition from a predominantly parallel arrangement of these phases in PF-120\_5 to a more balanced combination of parallel and sequential contacts in MF-4SC. The primary determinant of the  $\alpha$  values appears to be the morphology of the LF-4SC polymer within the pores rather than the thickness of the LF-4SC layer on the surface of the TM substrates (Table 3). Considering the inherent measurement uncertainties, the studied membranes exhibit a clear inverse relationship between  $\alpha$  and  $f_2$  (Fig. 9), a behavior commonly observed in many commercial membranes [4, 76, 77].

The ion exchange capacity of the gel phase ( $\bar{Q} = Q / f_1$ ) of the PF-120\_5.0 and PF-545\_5.0 samples is the same, taking into account the measurement error, and is almost three times lower compared to the same parameter for the commercial MF-4SC membrane. These data also indirectly indicate incomplete filling of the PFL pores with the LF-4SC ion-conducting polymer.

The diffusion coefficient of counterions in the membrane ( $\bar{D}_1 \times 10^6$ ) decreases in the sequence MF-4SC > PF-543\_5 > PF-543\_5, reflecting the increasing pore-filling defects in the PFL layer of the experimental samples.

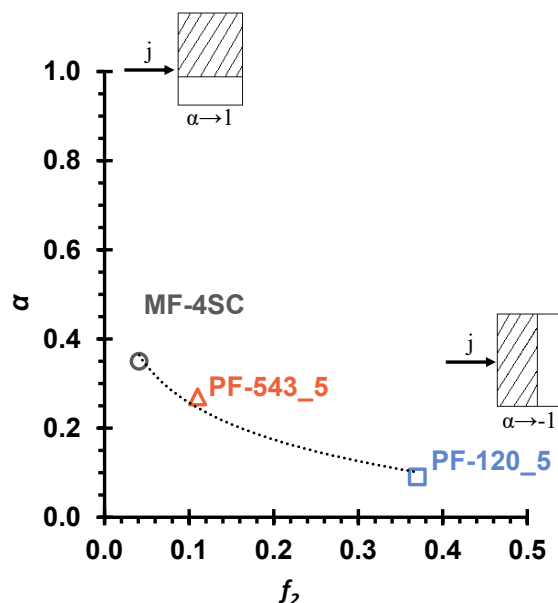


Figure 9. Dependence of the parameter  $\alpha$  on the parameter  $f_2$  of the studied membranes in a NaCl solution

The diffusion permeability of membranes is primarily governed by coion transport, effectively representing the non-selective transport of electrolyte through the ion-exchange membrane. Consistent with observations for many other ion-exchange membranes [24], the diffusion permeability of MF-4SC, PF-120\_5.0, and PF-545\_5.0 increases with increasing concentration of the external solution (Fig. 8c), a phenomenon attributed to the reduced effectiveness of the Donnan (electrostatic) exclusion of coions from the gel phase of the membrane [78]. Somewhat unexpectedly, the slope of these dependencies decreases in the order MF-4SC > PF-120\_5.0 > PF-545\_5.0. The concentration of coions within the gel phase is, to a first approximation, inversely proportional to the concentration of fixed ions, i.e., the ion-exchange capacity of the gel phase ( $\bar{Q} = Q / f_1$ ). The higher the density of the fixed groups, the stronger the Donnan exclusion of coions from the gel phase. Consequently, it might be expected that the diffusion permeability of the membrane would decrease with increasing  $\bar{Q}$  and with decreasing  $f_2$ , as the Donnan exclusion of coions is not effective within the intergel space. On the other hand, if the intergel solution forms a continuous pathway for coion transport, the values of  $P$  can be relatively high. This case is most likely to occur with a predominantly parallel arrangement of the  $f_1$  and  $f_2$  phases, which corresponds to  $\alpha \rightarrow -1$ . However, it appears that the primary factor contributing to the reduced diffusion permeability coefficient of the membranes is not these effects but rather the low overall pore content within the PFL structure, which restricts the available pathways for coion transport.

The transport numbers of coions,  $t_A$  and counterions ( $t_1^* = 1 - t_A$ ) were calculated using the equations proposed in [72] (derivation provided in S3, Supplementary Materials) and the experimental concentration dependences of the specific electrical conductivity and diffusion permeability of the studied membranes (Fig. 8). It is known [72] that, to a first approximation, the transport number of counterions determines the membrane selectivity. Its value is proportional to the conductivity and inversely proportional to the diffusion permeability of the membrane. The calculated values (Fig. 8d) indicate that, within the studied NaCl concentration range, the selectivity of the experimental PF-120\_5 and PF-543\_5 membranes approaches that of the commercial MF-4SC membrane. As mentioned earlier, the higher  $t_1^*$  values of the MF-4SC membrane compared to the PF-Y\_5.0 membranes are due to the higher  $\bar{Q}$  values and the absence of areas of the TM pores not filled with LF-4SC polymer.

Furthermore, physicochemical properties of the fabricated PF-543\_5 membrane were evaluated, and a comparison was made with commercially available cation-exchange membranes [38, 79, 80] as well as previously reported laboratory-prepared pore-filling membranes [37–39, 79–82] in terms of key properties, including thickness, IEC, transport number, electrical resistance, and water uptake (Table S1). The values of the “true” ( $t_1^*$ ) transport number of PF-543\_5 membrane prepared in the present study were comparable to

previously reported apparent ( $t_{app}^*$ ) counterion transport numbers determined using the potentiometric method [24, 37]. The resistance of PF-543\_5 was lower than that of commercial ion-exchange membranes but generally higher than that of PFMs prepared on the basis of an isotropic substrate. The water uptake of the prepared membrane was lower than that of the compared membranes. Both of these factors can be explained by the low porosity of the original track membrane.

#### 4. Conclusions

It is demonstrated that pore filling of the track-etched membrane with the PFSA polymer LF-4SC is an effective approach for producing thin cation-exchange membranes. The best-performing membranes obtained in this study exhibit electrical resistance and selectivity comparable to the commercial MF-4SC membrane, with the added advantage of reduced swelling upon dilution of the external electrolyte solution. However, these same samples show higher osmotic and diffusion fluxes compared to MF-4SC. These performance differences arise from incomplete filling of the track-etched membrane pores with the ion-conducting material, as well as from the formation of the LF-4SC layer on one of the PF-Y\_X membrane surfaces. These undesirable trends observed for the transport characteristics of the experimental samples become more pronounced with increasing concentration of LF-4SC (from 1.5 wt % to 5 wt %) in the pore-filling solution and with decreasing pore diameter of the track-etched membranes.

Modeling the PF-Y\_X membranes as track-etched membranes with straight pores filled with an ion-conducting polymer, overlaid with a surface layer of the same polymer, allows quantifying the contribution of pore-filling defects to the overall resistance of the samples. Furthermore, analysis of the concentration-dependent data for specific electrical conductivity and integral diffusion permeability coefficients of the PF-Y\_X samples using a microheterogeneous model demonstrates that, when these pore-filling defects are taken into account, the fabricated membranes exhibit the same fundamental behaviors characteristic of most commercial ion-exchange membranes.

The set of determined transport characteristics for the PF-543\_5 sample ( $R$  0.89 Ohm·cm<sup>2</sup>,  $J_w$  49.4 mmol m<sup>-2</sup> s<sup>-1</sup>,  $J_s$  0.11 mmol m<sup>-2</sup> s<sup>-1</sup>,  $t_1^* = 0.97$  in 0.5M NaCl) indicates its potential suitability for use in electrodialyzer-concentrators and other electromembrane modules.

#### Supporting Information

The Supporting Information is available free at <https://ejc.buketov.edu.kz/index.php/ejc/article/view/309/279>

#### Funding

The study was carried out with financial support from the Russian Science Foundation, project No. 23-79-01261, <https://rscf.ru/project/23-79-01261/>

#### Author Information\*

\*The authors' names are presented in the following order: First Name, Middle Name and Last Name

**Maria Alekseevna Ponomar** — Postgraduate Student, Junior Research Fellow, Kuban State University, 149 Stavropolskaya St., 350040, Krasnodar, Russia; e-mail: [ponomar.marie@yandex.ru](mailto:ponomar.marie@yandex.ru); <https://orcid.org/0000-0001-9139-4954>

**Veronika Vladimirovna Sarapulova** (*corresponding author*) — PhD in Electrochemistry, Senior Researcher, Kuban State University, Stavropolskaya St., 149, 350040, Krasnodar, Russia; e-mail: [vsarapulova@gmail.com](mailto:vsarapulova@gmail.com); <https://orcid.org/0000-0002-7902-6662>

**Vera Vladimirovna Guliaeva** — Master's Student, Laboratory Assistant, Kuban State University, Stavropolskaya St., 149, 350040, Krasnodar, Russia; e-mail: [vera\\_gulyaeva\\_2002@mail.ru](mailto:vera_gulyaeva_2002@mail.ru); <https://orcid.org/0009-0002-9370-9432>

**Pavel Yuryevich Apel** — Doctor of Sciences, Professor, Flerov Laboratory of Nuclear Reactions, Joint Institute for Nuclear Research, 141980, Dubna, Moscow Region, Russia; e-mail: [apel@jinr.ru](mailto:apel@jinr.ru); <https://orcid.org/0000-0003-1259-163X>

**Natalia Dmitrievna Pismenskaya** — Doctor of Sciences, Professor, Kuban State University, Stavropolskaya St., 149, 350040, Krasnodar, Russia; e-mail: [n\\_pismen@mail.ru](mailto:n_pismen@mail.ru); <https://orcid.org/0000-0001-5736-0136>



### Author Contributions

The manuscript was written through contributions of all authors. All authors have given approval to the final version of the manuscript. **CReditT: Maria Alekseevna Ponomar** investigation, data curation, methodology; **Veronika Vladimirovna Sarapulova** conceptualization, data curation, writing-original draft, writing-review & editing, funding acquisition; **Vera Vladimirovna Guliaeva** investigation, data curation, formal analysis; **Pavel Yuryevich Apel** methodology, resources, writing-review & editing; **Natalia Dmitrievna Pismenskaya** supervision, validation, writing-original draft, writing-review & editing.

### Acknowledgments

The work was carried out using the equipment of the Scientific and Educational Center “Diagnostics of the Structure and Properties of Nanomaterials”, Kuban State University Collective Use Center. <https://ckp-nano.kubsu.ru/>

### Conflicts of Interest

The authors declare no conflict of interest.

### References

- 1 Nikonenko, V., Nebavsky, A., Mareev, S., Kovalenko, A., Urtenov, M., & Pourcelly, G. (2018). Modelling of ion transport in electromembrane systems: impacts of membrane bulk and surface heterogeneity. *Applied Sciences*, 9(1), 25. <https://doi.org/10.3390/app9010025>
- 2 Stenina, I., Golubenko, D., Nikonenko, V., & Yaroslavl'tsev, A. (2020). Selectivity of transport processes in ion-exchange membranes: relationship with the structure and methods for its improvement. *International Journal of Molecular Sciences*, 21(15), 5517. <https://doi.org/10.3390/ijms21155517>
- 3 Gnusin, N. P., Berezina, N. P., Kononenko, N. A., & Dyomina, O. A. (2004). Transport structural parameters to characterize ion exchange membranes. *Journal of Membrane Science*, 243(1–2), 301–310. <https://doi.org/10.1016/j.memsci.2004.06.033>
- 4 Zabolotsky, V. I., & Nikonenko, V. V. (1993). Effect of structural membrane inhomogeneity on transport properties. *Journal of Membrane Science*, 79(2–3), 181–198. [https://doi.org/10.1016/0376-7388\(93\)85115-D](https://doi.org/10.1016/0376-7388(93)85115-D)
- 5 Nichka, V. S., Mareev, S. A., Porozhnyy, M. V., Shkirkaya, S. A., Safronova, E. Yu., Pismenskaya, N. D., & Nikonenko, V. V. (2019). Modified microheterogeneous model for describing electrical conductivity of membranes in dilute electrolyte solutions. *Membranes and Membrane Technologies*, 1(3), 190–199. <https://doi.org/10.1134/S2517751619030028>
- 6 Nichka, V. S., Mareev, S. A., Apel, P. Yu., Sabbatovskiy, K. G., Sobolev, V. D., & Nikonenko, V. V. (2022). Modeling the conductivity and diffusion permeability of a track-etched membrane taking into account a loose layer. *Membranes*, 12(12), 1283. <https://doi.org/10.3390/membranes12121283>
- 7 Porozhnyy, M., Huguet, P., Cretin, M., Safronova, E., & Nikonenko, V. (2016). Mathematical modeling of transport properties of proton-exchange membranes containing immobilized nanoparticles. *International Journal of Hydrogen Energy*, 41(34), 15605–15614. <https://doi.org/10.1016/j.ijhydene.2016.06.057>
- 8 Choy, T. C. (2015). *Effective Medium Theory: Principles and Applications*. Oxford University Press.
- 9 Sedkaoui, Y., Szymczyk, A., Lounici, H., & Arous, O. (2016). A new lateral method for characterizing the electrical conductivity of ion-exchange membranes. *Journal of Membrane Science*, 507, 34–42. <https://doi.org/10.1016/j.memsci.2016.02.003>
- 10 Vyas, P. V., Ray, P., Adhikary, S. K., Shah, B. G., & Rangarajan, R. (2003). Studies of the effect of variation of blend ratio on permselectivity and heterogeneity of ion-exchange membranes. *Journal of Colloid and Interface Science*, 257, 127–134. [https://doi.org/10.1016/S0021-9797\(02\)00025-5](https://doi.org/10.1016/S0021-9797(02)00025-5)
- 11 Davydov, D., Nosova, E., Loza, S., Achoh, A., Korzhov, A., Sharafan, M., & Melnikov, S. (2021). Use of the microheterogeneous model to assess the applicability of ion-exchange membranes in the process of generating electricity from a concentration gradient. *Membranes*, 11(6), 406. <https://doi.org/10.3390/membranes11060406>
- 12 Gohil, G. (2004). Comparative studies on electrochemical characterization of homogeneous type of ion-exchange membranes. *Journal of Membrane Science*, 240(1–2), 211–219. <https://doi.org/10.1016/j.memsci.2004.04.022>
- 13 Le, X. T., Bui, T. H., Viel, P., Berthelot, T., & Palacin, S. (2009). On the structure–properties relationship of the AMV anion exchange membrane. *Journal of Membrane Science*, 340(1–2), 133–140. <https://doi.org/10.1016/j.memsci.2009.05.025>
- 14 Loza, N. V., & Kutenko, N. A. (2024). Effect of Nature and Charge of Counterions and Co-Ions on Electротransport Properties of Heterogeneous Anion Exchange Membranes. *Membranes and Membrane Technologies*, 6(3), 193–204. <https://doi.org/10.1134/S2517751624600274>
- 15 Novikova, S. A., Volodina, E. I., Pis'menskaya, N. D., Veresov, A. G., Stenina, I. A., & Yaroslavl'tsev, A. B. (2005). Ionic transport in cation-exchange membranes MK-40 modified with zirconium phosphate. *Russian Journal of Electrochemistry*, 41(10), 1070–1076. <https://doi.org/10.1007/s11175-005-0183-z>

- 16 Zabolotskii, V. I., Loza, S. A., & Sharafan, M. V. (2005). Physicochemical properties of profiled heterogeneous ion-exchange membranes. *Russian Journal of Electrochemistry*, 41(10), 1053–1060. <https://doi.org/10.1007/s11175-005-0180-2>
- 17 Tuan, L. X., Verbanck, M., Buess-Herman, C., & Hurwitz, H. D. (2006). Properties of CMV cation exchange membranes in sulfuric acid media. *Journal of Membrane Science*, 284(1–2), 67–78. <https://doi.org/10.1016/j.memsci.2006.06.036>
- 18 Iddya, A., Zarzycki, P., Kingsbury, R., Khor, C. M., Ma, S., Wang, J., Wheeldon, I., Ren, Z. J., Hoek, E. M. V., & Jassby, D. (2022). A reverse-selective ion exchange membrane for the selective transport of phosphates via an outer-sphere complexation–diffusion pathway. *Nature Nanotechnology*, 17(11), 1222–1228. <https://doi.org/10.1038/s41565-022-01209-x>
- 19 Pismenskaya, N. D., Nevakshenova, E. E., & Nikonenko, V. V. (2018). Using a single set of structural and kinetic parameters of the microheterogeneous model to describe the sorption and kinetic properties of ion-exchange membranes. *Petroleum Chemistry*, 58(6), 465–473. <https://doi.org/10.1134/S0965544118060087>
- 20 Salmeron-Sanchez, I., Asenjo-Pascual, J., Avilés-Moreno, J. R., & Ocón, P. (2022). Microstructural description of ion exchange membranes: The effect of PPy-based modification. *Journal of Membrane Science*, 659, 120771. <https://doi.org/10.1016/j.memsci.2022.120771>
- 21 Berezina, N. P., Kononenko, N. A., Dyomina, O. A., & Gnusin, N. P. (2008). Characterization of ion-exchange membrane materials: Properties vs structure. *Advances in Colloid and Interface Science*, 139(1–2), 3–28. <https://doi.org/10.1016/j.cis.2008.01.002>
- 22 Xu, T., & Wang, Y. (2024). *Ion Exchange Membranes: Design, Preparation, and Applications*. Wiley-VCH GmbH.
- 23 Stránská, E., & Neděla, D. (2018). Reinforcing fabrics as the mechanical support of ion exchange membranes. *Journal of Industrial Textiles*, 48(2), 432–447. <https://doi.org/10.1177/1528083717732075>
- 24 Sarapulova, V., Pismenskaya, N., Titorova, V., Sharafan, M., Wang, Y., Xu, T., Zhang, Y., & Nikonenko, V. (2021). Transport characteristics of CJMAED™ homogeneous anion exchange membranes in sodium chloride and sodium sulfate solutions. *International Journal of Molecular Sciences*, 22(3), 1415. <https://doi.org/10.3390/ijms22031415>
- 25 Eti, M., Hidayati Othman, N., Guuml; ler, E., & Kabay, N. (2021). Ion exchange membranes for reverse electrodialysis RED) applications—Recent developments. *Journal of Membrane Science and Research*, 7(4). <https://doi.org/10.22079/jmsr.2021.534937.1482>
- 26 Niccolai, F., Guazzelli, E., El Koura, Z., Pucher, I., & Martinelli, E. (2025). A critical update on the design of dense ion-conducting membranes for redox flow batteries. *Advanced Sustainable Systems*, 9(2), 2400661. <https://doi.org/10.1002/adsu.202400661>
- 27 Yang, S., Choi, Y. -W., Choi, J., Jeong, N., Kim, H., Jeong, H., Byeon, S. Y., Yoon, H., & Kim, Y. H. (2019). Green fabrication of pore-filling anion exchange membranes using R2R processing. *Journal of Membrane Science*, 584, 181–190. <https://doi.org/10.1016/j.memsci.2019.04.075>
- 28 Gloukhovski, R., Freger, V., & Tsur, Y. (2018). Understanding methods of preparation and characterization of pore-filling polymer composites for proton exchange membranes: A beginner's guide. *Reviews in Chemical Engineering*, 34(4), 455–479. <https://doi.org/10.1515/revce-2016-0065>
- 29 Fan, H., Xu, Y., Zhao, F., Chen, Q. -B., Wang, D., & Wang, J. (2023). A novel porous asymmetric cation exchange membrane with thin selective layer for efficient electrodialysis desalination. *Chemical Engineering Journal*, 472, 144856. <https://doi.org/10.1016/j.cej.2023.144856>
- 30 Wu, J., Dai, Q., Zhang, H., & Li, X. (2020). Recent development in composite membranes for flow batteries. *ChemSusChem*, 13(15), 3805–3819. <https://doi.org/10.1002/cssc.202000633>
- 31 Chavan, V., Agarwal, C., Adya, V. C., & Pandey, A. K. (2018). Hybrid organic-inorganic anion-exchange pore-filled membranes for the recovery of nitric acid from highly acidic aqueous waste streams. *Water Research*, 133, 87–98. <https://doi.org/10.1016/j.watres.2018.01.023>
- 32 Kim, D.-H., Seo, S.-J., Lee, M.-J., Park, J.-S., Moon, S.-H., Kang, Y. S., Choi, Y.-W., & Kang, M.-S. (2014). Pore-filled anion-exchange membranes for non-aqueous redox flow batteries with dual-metal-complex redox shuttles. *Journal of Membrane Science*, 454, 44–50. <https://doi.org/10.1016/j.memsci.2013.11.051>
- 33 Shi, S., Weber, A. Z., & Kusoglu, A. (2016). Structure/property relationship of Nafion XL composite membranes. *Journal of Membrane Science*, 516, 123–134. <https://doi.org/10.1016/j.memsci.2016.06.004>
- 34 Dalal, U., Kapoor, M., & Verma, A. (2023). Low-cost pore-filled PVDF–Nafion composite membrane for the vanadium redox flow battery. *Energy & Fuels*, 37(17), 13457–13466. <https://doi.org/10.1021/acs.energyfuels.3c01932>
- 35 Fang, Y., & Leddy, J. (1995). Surface diffusion in microstructured, ion-exchange matrixes: Nafion/Neutron Track-Etched Polycarbonate Membrane composites. *The Journal of Physical Chemistry*, 99(16), 6064–6073. <https://doi.org/10.1021/j100016a049>
- 36 Kang, S. E., & Lee, C. H. (2015). Perfluorinated sulfonic acid ionomer-PTFE pore-filling membranes for polymer electrolyte membrane fuel cells. *Membrane Journal*, 25(2), 171–179. [https://doi.org/10.14579/MEMBRANE\\_JOURNAL.2015.25.2.171](https://doi.org/10.14579/MEMBRANE_JOURNAL.2015.25.2.171)
- 37 Cha, J.-E., Seo, M. H., Choi, Y.-W., & Kim, W. B. (2021). A practical approach to measuring the ion-transport number of cation-exchange membranes: Effects of junction potential and analyte concentration. *Journal of Membrane Science*, 635, 119471. <https://doi.org/10.1016/j.memsci.2021.119471>
- 38 Yang, S., Choi, Y.-W., Choi, J., Jeong, N., Kim, H., Nam, J.-Y., & Jeong, H. (2019). R2R fabrication of pore-filling cation-exchange membranes via one-time impregnation and their application in reverse electrodialysis. *ACS Sustainable Chemistry & Engineering*, accsuschemeng.9b01450. <https://doi.org/10.1021/acssuschemeng.9b01450>






- 39 Wang, B., Yan, J., Wang, H., Li, R., Fu, R., Jiang, C., Nikonenko, V., Pismenskaya, N., Wang, Y., & Xu, T. (2024). Solvent-free fabrication of pore-filling cation-exchange membranes for highly efficient desalination. *Chemical Engineering Science*, 287, 119782. <https://doi.org/10.1016/j.ces.2024.119782>
- 40 Wang, M., An, Q.-F., Wu, L.-G., Mo, J.-X., & Gao, C.-J. (2007). Preparation of pH-responsive phenolphthalein poly(ether sulfone) membrane by redox-graft pore-filling polymerization technique. *Journal of Membrane Science*, 287(2), 257–263. <https://doi.org/10.1016/j.memsci.2006.10.049>
- 41 Hu, K., & Dickson, J. M. (2007). Development and characterization of poly(vinylidene fluoride)–poly(acrylic acid) pore-filled pH-sensitive membranes. *Journal of Membrane Science*, 301(1–2), 19–28. <https://doi.org/10.1016/j.memsci.2007.05.031>
- 42 Hu, K., & Dickson, J. M. (2008). Modelling of the pore structure variation with pH for pore-filled pH-sensitive poly(vinylidene fluoride)–poly(acrylic acid) membranes. *Journal of Membrane Science*, 321(2), 162–171. <https://doi.org/10.1016/j.memsci.2008.04.046>
- 43 Mika, A. M., Childs, R. F., & Dickson, J. M. (2002). Salt separation and hydrodynamic permeability of a porous membrane filled with pH-sensitive gel. *Journal of Membrane Science*, 206(1–2), 19–30. [https://doi.org/10.1016/S0376-7388\(01\)00474-4](https://doi.org/10.1016/S0376-7388(01)00474-4)
- 44 Xie, R., Chu, L.-Y., Chen, W.-M., Xiao, W., Wang, H.-D., & Qu, J.-B. (2005). Characterization of microstructure of poly(N-isopropylacrylamide)-grafted polycarbonate track-etched membranes prepared by plasma-graft pore-filling polymerization. *Journal of Membrane Science*, 258(1–2), 157–166. <https://doi.org/10.1016/j.memsci.2005.03.012>
- 45 Zou, Z., Wu, L., Luo, T., Yan, Z., & Wang, X. (2021). Assessment of anion exchange membrane selectivity with ionic membrane conductivity, revised with Manning's theory or the Kohlrausch's law. *Journal of Membrane Science*, 635, 119496. <https://doi.org/10.1016/j.memsci.2021.119496>
- 46 Golubenko, D. V., Yurova, P. A., Desyatov, A. V., Stenina, I. A., Kosarev, S. A., & Yaroslavl'tsev, A. B. (2022). Pore filled ion-conducting materials based on track-etched membranes and sulfonated polystyrene. *Membranes and Membrane Technologies*, 4(6), 398–403. <https://doi.org/10.1134/S2517751622060026>
- 47 Gloukhovski, R., Tsur, Y., & Freger, V. (2017). A Nafion-filled polycarbonate track-etched composite membrane with enhanced selectivity for direct methanol fuel cells. *Fuel Cells*, 17(1), 56–66. <https://doi.org/10.1002/fuce.201600154>
- 48 Parmanbek, N., Sütėkin, D. S., Barsbay, M., Mashentseva, A. A., Zheltov, D. A., Aimanova, N. A., Jakupova, Z. Ye., & Zdorovets, M. V. (2022). Hybrid PET track-etched membranes grafted by well-defined poly(2-(dimethylamino)ethyl methacrylate) brushes and loaded with silver nanoparticles for the removal of As(III). *Polymers*, 14(19), 4026. <https://doi.org/10.3390/polym14194026>
- 49 Korolkov, I. V., Yeszhanov, A. B., Shakayeva, A. Kh., Shlimas, D. I., Zhumazhanova, A., & Zdorovets, M. V. (2022). Photo-induced graft (co)polymerization of glycidyl methacrylate and acrylonitrile on PET ion-track membranes for electrochemical detection of uranyl ions. *Colloids and Surfaces A: Physicochemical and Engineering Aspects*, 648, 129086. <https://doi.org/10.1016/j.colsurfa.2022.129086>
- 50 Meyer, N., Arroyo, N., Janot, J. -M., Lepoitevin, M., Stevenson, A., Nemeir, I. A., Perrier, V., Bougard, D., Belondrade, M., Cot, D., Bentin, J., Picaud, F., Torrent, J., & Balme, S. (2021). Detection of amyloid- $\beta$  fibrils using track-etched nanopores: effect of geometry and crowding. *ACS Sensors*, 6(10), 3733–3743. <https://doi.org/10.1021/acssensors.1c01523>
- 51 Hoek, E. M. V., & Tarabara, V. V. (2013). *Encyclopedia of Membrane Science and Technology*. Wiley. <https://doi.org/10.1002/9781118522318>
- 52 Sarapulova, V. V., Pasechnaya, E. L., Titorova, V. D., Pismenskaya, N. D., Apel, P. Yu., & Nikonenko, V. V. (2020). Electrochemical properties of ultrafiltration and nanofiltration membranes in solutions of sodium and calcium chloride. *Membranes and Membrane Technologies*, 2(5), 332–350. <https://doi.org/10.1134/S2517751620050066>
- 53 Yaroslavcev, A. B., & Nikonenko, V. V. (2009). Ionoobmennye membrannye materialy: svoystva, mo-difikaciya i prakticheskoe primeneniye [Ion-exchange membrane materials: properties, modification and practical application]. *Rossiiskie Nanotekhnologii — Russian Nanotechnologies*, 4(3–4), 33–53 [in Russian].
- 54 Apel, P. Yu., & Dmitriev, S. N. (2004). Optimizaciya formy por trekovyh membrane [Optimization of the pore shape of track membranes]. *Seriya. Kriticheskie Tekhnologii. Membrany — Series. Critical Technologies. Membranes*, 3(23), 32–37 [in Russian].
- 55 Berezina, N. P., Timofeev, S. V., Rolle, A. L., Fedorovich, N. V., & Dyuran-Vidal', S. (2002). Elektrotransportnye i strukturnye svoystva perflorirovannyh membran Nafion-117 i MF-4SK [Electrotransport and structural properties of perfluorinated membranes Nafion-117 and MF-4SK]. *Elektrokhimiya — Electrochemistry*, 38(8), 1009–1015 [in Russian].
- 56 Karpenko, L. V., Demina, O. A., Dvorkina, G. A., Parshikov, S. B., Larshe, K., Okler, B., & Berezina, N. P. (2001). Sravnitel'noe izuchenie metodov opredeleniya udel'noj elektroprovodnosti ionoob-mennyh membrane [Comparative study of methods for determining the specific conductivity of ion-exchange membranes]. *Elektrokhimiya — Electrochemistry*, 37(3), 328–335 [in Russian].
- 57 Galama, A. H., Saakes, M., Bruning, H., Rijnaarts, H. H. M., & Post, J. W. (2014). Seawater predesalination with electrodi-alysis. *Desalination*, 342, 61–69. <https://doi.org/10.1016/j.desal.2013.07.012>
- 58 Gumirova, V. N., Razumovskaya, I. V., Apel, P. Yu., Bedin, S. A., & Bazhenov, S. L., Abdura-shidova, G. S. (2013). Metody opredeleniya raspredeleniya por po poverhnosti trekovyh membrane [Methods for determining the distribution of pores on the surface of track membranes]. *Prepodavatel' XXI Vek — Teacher XXI Century*, 2 [in Russian].
- 59 Sanchez, C., Espinos, F. J., Barjola, A., Escorihuela, J., & Compañ, V. (2022). Hydrogen production from methanol–water solution and pure water electrolysis using nanocomposite perfluorinated sulfocationic membranes modified by polyaniline. *Polymers*, 14(21), 4500. <https://doi.org/10.3390/polym14214500>

- 60 Kravec, L. I., Yarmolenko, M. A., Rogachev, A. A., Gajnutdinov, R. V., Altynov, V. A., & Lizunov, N. E. (2021). Formirovanie na poverhnosti trekovykh membrangidrofobnykh pokrytiy metodom el-ektronno-luchevogo dispergirvaniya polivinilhlorida v vakuume [Formation of hydrophobic membrane coatings on the surface of track films using the method of electron beam dispersion of polyvinyl chloride in a vacuum]. *Nanoindustriya Rossii — Nanoindustry of Russia*, 14(6s), 44–54 [in Russian]. <https://doi.org/10.22184/1993-8578.2021.14.6s.44.54>
- 61 Djebara, M., Stoquert, J. P., Abdesselam, M., Muller, D., & Chami, A. C. (2012). FTIR analysis of polyethylene terephthalate irradiated by MeV He<sup>+</sup>. *Nuclear Instruments and Methods in Physics Research Section B: Beam Interactions with Materials and Atoms*, 274, 70–77. <https://doi.org/10.1016/j.nimb.2011.11.022>
- 62 Liang, Z., Chen, W., Liu, J., Wang, S., Zhou, Z., Li, W., Sun, G., & Xin, Q. (2004). FT-IR study of the microstructure of Nafion® membrane. *Journal of Membrane Science*, 233(1–2), 39–44. <https://doi.org/10.1016/j.memsci.2003.12.008>
- 63 Kinumoto, T., Inaba, M., Nakayama, Y., Ogata, K., Umebayashi, R., Tasaka, A., Iriyama, Y., Abe, T., & Ogumi, Z. (2006). Durability of perfluorinated ionomer membrane against hydrogen peroxide. *Journal of Power Sources*, 158(2), 1222–1228. <https://doi.org/10.1016/j.jpowsour.2005.10.043>
- 64 Déjardin, P., Vasina, E. N., Berezkin, V. V., Sobolev, V. D., & Volkov, V. I. (2005). Streaming potential in cylindrical pores of poly(ethylene terephthalate) track-etched membranes: variation of apparent  $\zeta$  potential with pore radius. *Langmuir*, 21(10), 4680–4685. <https://doi.org/10.1021/la046913e>
- 65 Apel, P. Yu., Blonskaya, I. V., Ivanov, O. M., Kristavchuk, O. V., Lizunov, N. E., Nechaev, A. N., Orelovich, O. L., Polezhaeva, O. A., & Dmitriev, S. N. (2020). Creation of ion-selective membranes from polyethylene terephthalate films irradiated with heavy ions: critical parameters of the process. *Membranes and Membrane Technologies*, 2(2), 98–108. <https://doi.org/10.1134/S251775162002002X>
- 66 Yaroslavtsev, A. B. (2012). Ion conductivity of composite materials on the base of solid electrolytes and ion-exchange membranes. *Inorganic Materials*, 48(13), 1193–1209. <https://doi.org/10.1134/S0020168512130055>
- 67 Ma, C.-H., Yu, T. L., Lin, H.-L., Huang, Y.-T., Chen, Y.-L., Jeng, U.-S., Lai, Y.-H., & Sun, Y.-S. (2009). Morphology and properties of Nafion membranes prepared by solution casting. *Polymer*, 50(7), 1764–1777. <https://doi.org/10.1016/j.polymer.2009.01.060>
- 68 Safronova, E. Yu., Voropaeva, D. Yu., Safronov, D. V., Stretton, N., Parshina, A. V., & Yaroslavtsev, A. B. (2022). Correlation between Nafion morphology in various dispersion liquids and properties of the cast membranes. *Membranes*, 13(1), 13. <https://doi.org/10.3390/membranes13010013>
- 69 Kim, R., Kim, H. G., Doo, G., Choi, C., Kim, S., Lee, J.-H., Heo, J., Jung, H.-Y., & Kim, H.-T. (2017). Ultrathin Nafion-filled porous membrane for zinc/bromine redox flow batteries. *Scientific Reports*, 7(1), 10503. <https://doi.org/10.1038/s41598-017-10850-9>
- 70 Khandavalli, S., Park, J. H., Winter, H. H., Myers, D. J., Ulsh, M., & Mauger, S. A. (2023). Viscoelasticity enhancement and shear thickening of perfluorinated sulfonic acid ionomer dispersions in water–alcohol solvent mixtures. *Macromolecules*, 56(17), 6988–7005. <https://doi.org/10.1021/acs.macromol.3c00383>
- 71 Yamauchi, Y., Blonskaya, I. V., & Apel, P. Yu. (2019). Osmos v otricatel'no zaryazhennykh nanoka-pil-lyarah i ego usilenie anionnym poverhnostno-aktivnym veshchestvom [Osmosis in negatively charged nanocapillaries and its enhancement by cationic surfactant]. *Kolloidnyy Zhurnal — Colloid Journal*, 81(1), 125–136 [in Russian]. <https://doi.org/10.1134/S0023291219010166>
- 72 Larchet, C., Dammak, L., Auclair, B., Parchikov, S., & Nikonenko, V. (2004). A simplified procedure for ion-exchange membrane characterisation. *New Journal of Chemistry*, 28(10), 1260. <https://doi.org/10.1039/b316725a>
- 73 Kusoglu, A., & Weber, A. Z. (2017). New insights into perfluorinated sulfonic-acid ionomers. *Chemical Reviews*, 117(3), 987–1104. <https://doi.org/10.1021/acs.chemrev.6b00159>
- 74 Yin, C., Wang, Z., Luo, Y., Li, J., Zhou, Y., Zhang, X., Zhang, H., Fang, P., & He, C. (2018). Thermal annealing on free volumes, crystallinity and proton conductivity of Nafion membranes. *Journal of Physics and Chemistry of Solids*, 120, 71–78. <https://doi.org/10.1016/j.jpcs.2018.04.028>
- 75 Kamel, M. S. A., Mohamed, H. F. M., Abdel-Hamed, M. O., & Abdel-Hady, E. E. (2019). Characterization and evaluation of Nafion HP JP as proton exchange membrane: Transport properties, nanostructure, morphology, and cell performance. *Journal of Solid State Electrochemistry*, 23(9), 2639–2656. <https://doi.org/10.1007/s10008-019-04366-7>
- 76 Salmeron-Sanchez, I., Asenjo-Pascual, J., Avilés-Moreno, J. R., Pérez-Flores, J. C., Mauleón, P., & Ocón, P. (2022). Chemical physics insight of PPy-based modified ion exchange membranes: A fundamental approach. *Journal of Membrane Science*, 643, 120020. <https://doi.org/10.1016/j.memsci.2021.120020>
- 77 Falina, I. V., Demina, O. A., Kononenko, N. A., & Annikova, L. A. (2017). Influence of inert components on the formation of conducting channels in ion-exchange membranes. *Journal of Solid State Electrochemistry*, 21(3), 767–775. <https://doi.org/10.1007/s10008-016-3415-0>
- 78 Luo, T., Abdu, S., & Wessling, M. (2018). Selectivity of ion exchange membranes: A review. *Journal of Membrane Science*, 555, 429–454. <https://doi.org/10.1016/j.memsci.2018.03.051>
- 79 Kim, D.-H., Choi, Y.-E., Park, J.-S., & Kang, M.-S. (2019). Capacitive deionization employing pore-filled cation-exchange membranes for energy-efficient removal of multivalent cations. *Electrochimica Acta*, 295, 164–172. <https://doi.org/10.1016/j.electacta.2018.10.124>
- 80 Kim, D.-H., & Kang, M.-S. (2018). Water electrolysis using pore-filled proton-exchange membranes for hydrogen water production. *Chemistry Letters*, 47(10), 1265–1268. <https://doi.org/10.1246/cl.180560>

81 Akter, M., & Park, J. -S. (2023). Fouling and mitigation behavior of foulants on ion exchange membranes with surface property in reverse electrodialysis. *Membranes*, 13(1), 106. <https://doi.org/10.3390/membranes13010106>

82 Fan, H., Xu, Y., Zhao, F., Chen, Q. -B., Wang, D., & Wang, J. (2023). A novel porous asymmetric cation exchange membrane with thin selective layer for efficient electrodialysis desalination. *Chemical Engineering Journal*, 472, 144856. <https://doi.org/10.1016/j.cej.2023.144856>



Aigerim Kh. Shakayeva<sup>1, 2\*</sup> , Dias D. Omertasov<sup>1,2</sup>, Zh K. Zhatkanbayeva<sup>2</sup> ,  
Ainash T. Zhumazhanova<sup>1</sup> , Maxim V. Zdorovets<sup>1, 2</sup> , Ilya V. Korolkov<sup>1,2</sup> 

<sup>1</sup> Institute of Nuclear Physics, Almaty, Kazakhstan;

<sup>2</sup>L.N. Gumilyov Eurasian National University, Astana, Kazakhstan

(\*Corresponding author's e-mail: [shakayeva19@gmail.com](mailto:shakayeva19@gmail.com))

## Graft Polymerization of Allylamine for the Modification of PET Track-Etched Membrane

Track-etched membranes (TMs), characterized by their precisely controlled pore size, geometry, and distribution, offer a promising platform for the development of advanced membrane systems and serve as model membranes for testing and optimizing surface modification techniques. This study presents a perspective modification of poly(ethylene terephthalate) track-etched membranes (PET TM) based on photo-induced graft polymerization of allylamine (AlAm) to introduce primary amine groups on the membrane surface. The polymerization process was optimized by evaluating key parameters, including reaction time, monomer concentration, solvent, and distance from UV-lamp. Optimal conditions for photoinduced graft polymerization were found: grafting time 60 minutes, AlAm monomer concentration 50 %, 2-propanol as a solvent and distance to UV lamp 10 cm. These parameters allowed effective modification of the polymer while maintaining the integrity of the membrane porous structure. The modified membranes were characterized using SEM-EDX, ATR FTIR, and UV-spectroscopy. The results demonstrate the successful fabrication of membranes with a high amino group content (up to  $10.6 \pm 0.3 \mu\text{mol/g}$ ) while preserving their porous structure. This functionalization enhances the practical potential for the environment and biomedical fields.

**Keywords:** track-etched membrane, poly(ethylene terephthalate), allylamine, photoinduced graft polymerization, modification, polymeric membranes, porous structure, surface functionalization, UV irradiation

### Introduction

Track-etched membranes (TM) are a unique class of polymeric membranes obtained through heavy-ion irradiation of polymer films, followed by chemical etching of the ion tracks to create well-defined pores [1, 2]. This fabrication process allows precise control over pore size, shape, and density, enabling the development of membranes with tailored properties for specific applications [3]. Several polymers, such as poly(ethylene terephthalate) (PET), polycarbonate (PC), polyimide (PI), polypropylene (PP) and poly(vinylidene fluoride) (PVDF) are widely used for ion-tracking technology. Poly(ethylene terephthalate) has been found to have a number of applications in the form of functionalized TM owing to its chemical stability, mechanical strength, and thermal stability [4]. PET TM are widely used in medical and analytical applications, including drug purification, virus filtration, and plasma separation [5–8]. TM are also used for quality control of food and water, air and liquid filtration for environments, drinking water purification systems, and analytical monitoring of various substances [9–14].

Most polymeric materials have a pristine surface with low surface energies. Thus, the control of chemistry at polymer surfaces has become increasingly important for at least the major way of applications [15, 16]. The use of chemical and physical modification is one of the most effective approaches to improve membrane properties. Various surface modification techniques have been applied to enhance the functionality of TM, including radiation, chemical, photochemical, and plasma — induced initiation techniques and physical or chemical adsorption [17–20]. These methods are therefore usually employed to obtain TM with specific properties, such as adhesiveness, wettability, biocompatibility, and antifouling, to carry out their intended tasks. The UV-induced surface graft polymerization has several advantages over other surface modification techniques. These advantages include a rapid reaction rate, low processing cost, simple experimental setup, and high potential for industrial scalability. One significant benefit is that the grafted polymer chains are confined to a thin surface layer, which minimizes alteration to the bulk properties of the material. This

makes photo-induced grafting a powerful tool for precisely tuning surface characteristics without compromising the structural integrity of the substrate [21].

In our study, we presented the modification of PET TM with allylamines (AlAm) using photo-induced graft polymerization. The AlAm is an attractive category of amines with its molecular structure consisting of highly dense primary amines at the side chain [22]. Additionally, AlAm is a suitable binding material in supported amine systems due to cohesive forces between the chains and adhesive forces with the supports [23, 24]. The allyl group is used for the modification of the molecule onto various templates, including polymers and inorganic supports [25]. In addition, the allyl group allows for efficient participation in radical polymerization, while the introduced amine groups can serve as reactive sites for further chemical functionalization or biomolecule immobilization. Functionalized AlAm systems have been developed to address, among other things, issues related to oxidative and thermal stability in CO<sub>2</sub> capture processes [26].

### *Experimental*

#### *Reagents*

Allylamine (98 %), benzophenone (BP) (97 %), N, N-dimethylformamide (99.9 %), sodium hydroxide (98 %), acetic acid (99.5 %), ethanol (98 %), 2-propanol (99.8 %) were produced from Sigma-Aldrich. To eliminate stabilizers, AlAm underwent purification via aluminum oxide packed chromatographic columns. The deionized water utilized in experimental procedures was purified through an “Aquilon-D301” purification system, ensuring a resistivity level of 18.2 MΩ.

#### *Preparation and Modification of Track-Etched Membrane*

For all measurements, PET TM with a thickness of 12 μm, pore density of  $1 \cdot 10^6$  pore/cm<sup>2</sup>, and an effective pore diameter of ~250 nm was used. The membranes were fabricated by irradiating a PET film with <sup>84</sup>Kr<sup>15+</sup> ions accelerated to an average energy of ~1.75 MeV/nucleon using a DC-60 ion accelerator (Institute of Nuclear Physics of Kazakhstan), followed by chemical treatment in 2.2M NaOH solution at 85 °C. The samples were rinsed with 5 % acetic acid and DI water and stored in air at room temperature.

The 5×5 cm TM was immersed in a 5 % solution of BP in DMF for 24 hours. Following this treatment, the membranes were rinsed with ethanol and subsequently air-dried. The quantitative determination of BP adsorbed on the surface of PET TM was performed using a spectrophotometric assay. The samples with adsorbed BP were briefly washed with ethanol at room temperature, dried, and then immersed in pure ethanol at 40 °C to desorb loosely bound BP from the membrane surface. The amount of released BP was subsequently measured by UV–vis spectroscopy at 253 nm. The PET TM was placed in a solution containing AlAm. Chloroform, 2-propanol, acetonitrile, and deionized water were used as solvents. To eliminate dissolved oxygen, the reaction mixture was purged with Ar. The photo-induced graft polymerization was conducted under irradiation using an OSRAM Ultra Vitalux E27 lamp (UVA: 315–400 nm, 13.6 W; UVB: 280–315 nm, 3.0 W) for different durations.

#### *Characterization of the Morphological and Chemical Properties*

The chemical structure of the membrane was investigated through the Fourier Transform Infrared Spectroscopy (FTIR) technique using InfraLUM FT-08. The FTIR spectra were recorded in the range of 400–4000 cm<sup>−1</sup>, with a resolution of 1 cm<sup>−1</sup> and an average number of 20 scans, by using an attenuated total reflectance (ATR) module. The ATR-FTIR analyses were performed on both sides of the membranes.

The change of morphology and pore size after modification was evaluated by scanning electron microscopy (SEM). Before the analyses, a 10 nm thick layer of gold was applied on the surface. The pore size determination was performed using the Phenom Image Viewer program. The elemental composition of the sample was studied by using the energy-dispersive X-ray spectroscopy (EDX) system Bruker Xflash MIN SVE at an accelerating voltage of 15 kV. The results of the analysis are presented as averages based on three data points.

The number of available amino end-groups was quantified using 500 μmol/L acid orange (AO) solution (in HCl, pH=3). Samples of modified PET TM of 1 cm<sup>2</sup> in size were immersed in AO. The adsorption of AO on the membrane surface is carried out for 12 hours. After the samples were removed, it was washed twice in a HCl (pH=3) solution, and dried. The AO was desorbed in 5 ml of NaOH solution (pH=12) for 15 min on a shaker. The concentration of the amino group was determined on UV-vis — spectrophotometer SPECORD-250 at a wavelength of 495 nm according to the calibration curve.

## Results and Discussion

Photo-induced graft polymerization is typically carried out by the pre-immobilization of a photoinitiator onto the surface of the membrane to be modified. In this approach, BP is one of the most commonly used photoinitiators [27]. The grafting process was carried out in two stages: in the first stage, the covalent immobilization of the sensitizer BP onto the surface of the PET TM was performed. In principle, upon UV irradiation, BP molecules are first excited to a singlet state, followed by a transition to a triplet state via intersystem crossing [28]. Studies have shown that triplet-state BP and its derivatives can abstract hydrogen atoms from nearby polymer substrates, leading to the formation of surface-bound radicals ( $R^\bullet$ ) that are capable of initiating graft polymerization. The resulting benzopinacol radicals (BP-OH $^\bullet$ ) are comparatively less reactive and do not readily participate in free radical polymerization. Instead, they tend to terminate the reaction through radical coupling, rather than propagating the polymer chains [21]. In the second stage, the graft polymerization was conducted in the presence of an AlAm monomer solution. The PET TM surface was modified by scheme presented in Figure 1.

The interaction of BP with the polymer surface occurs through electrostatic and van der Waals forces, and is influenced by the hydrophilic–hydrophobic balance and the crystalline–amorphous characteristics of the polymer. A hydrophilic polymer such as PET can form more ordered and stronger bonds with BP. When BP was dissolved in alcohol, the maximum adsorbed concentration on the membrane surface did not exceed 19  $\mu\text{mol/g}$ . The low concentration is associated with the leaching of adsorbed BP [29]. The dissolution of BP in DMF resulted in an adsorbed BP concentration of 580  $\mu\text{mol/g}$  on the membrane surface [14]. The increase in adsorbed initiator concentration results from BP molecules in DMF permeating the template and forming additional active centers [30]. An increase in the concentration of the photoinitiator of PET TM leads to more efficient AlAm grafting.

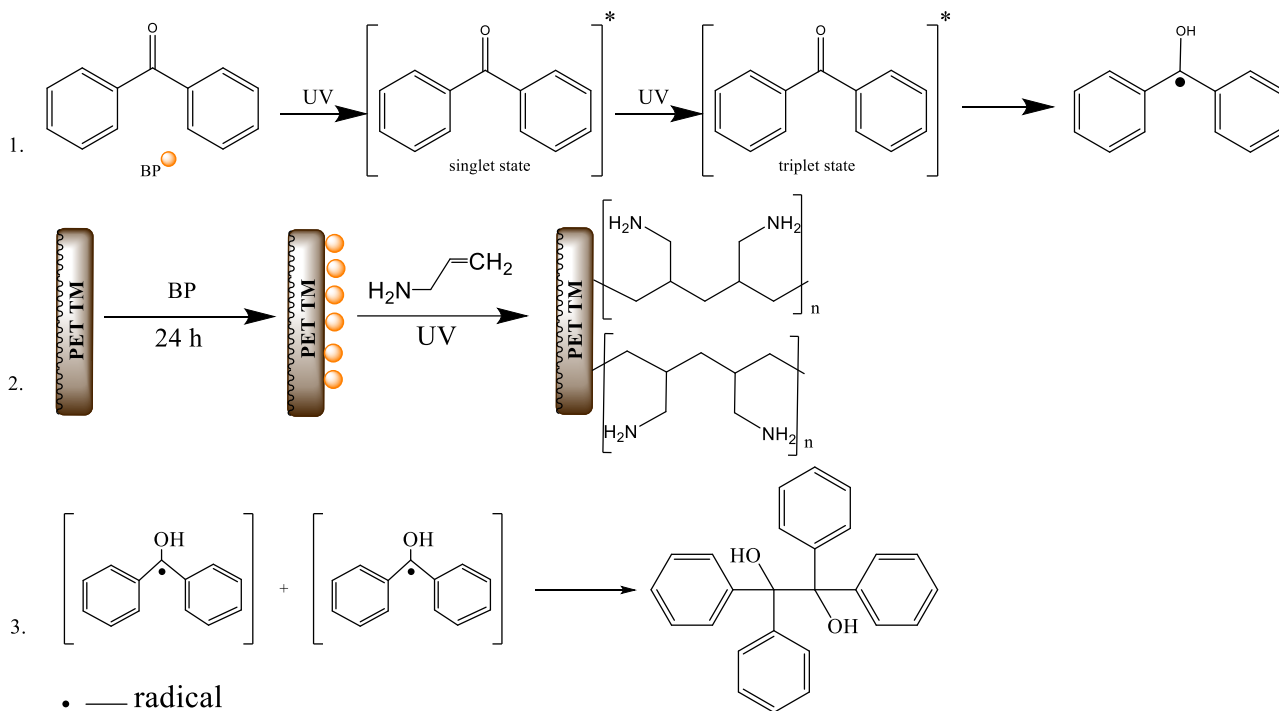


Figure 1. Scheme of modification of PET TM

The polymerization process was impacted by monomer concentration, solvent, irradiation dose, and polymerization time. Firstly, a series of experiments was conducted to determine the optimal solvent for graft polymerization. Allylamine is highly soluble in water, alcohols, and nonpolar solvents. When the reaction was conducted in deionized water, chloroform, and acetonitrile, it led to the decomposition of the sample. The degradation was attributed to the pH level (10–11) of the reaction mixture, where a polymer PET degradation occurs. Additionally, chloroform has a low boiling point, and it easily evaporates from the reaction mixture. The 2-propanol was found to provide a more stable environment, minimizing polymer degradation of the sample.

The distance from UV-irradiation affected the polymerization process, an increase in this distance leads to a reduction in the irradiation dose. The optimal distance from UV-lamp was determined at 10 cm. A reduction to 7 cm adversely affected the membrane quality. The PET TM became brittle and prone to breakage. On the other hand, an increase in the distance to 15 cm resulted in a significantly lower polymerization of AlAm.

The photo-induced graft polymerization was carried out at a range of monomer concentration from 10 % to 50 %. After each experiment, the concentration of amino groups in the PET TM was analyzed. Table 1 shows the variation of the content of amino-groups at different parameters.

According to the data presented in Table 1, an increasing trend in AlAm concentration from 10 % to 50 % leads to an increase in the amino group concentration ( $10.6 \pm 0.31 \mu\text{mol/g}$ ). This suggests that higher monomer content enhances amine group concentration. However, reducing the reaction time from 60 to 45- or 30 min results in a decrease in amino group concentration, indicating that a longer reaction time is necessary for effective polymerization. Further increase in monomer concentration and polymerization time can lead to sample degradation due to increased pH, making membrane removal difficult. This suggests that in order to achieve a high level of amino group functionalization without compromising membrane integrity, an optimal balance between monomer concentration and reaction time is critical.

Table 1

**Results of elemental analysis, pore size, and concentration of amino group for PET TM under various parameters of graft polymerization**

No	Concentration of AlAm, %	<i>t</i> , min	Concentration of amino group, $\mu\text{mol/g}$	Pore size (from SEM analysis), nm	Concentration of N (from EDX analysis), %
1	—	—	—	$322 \pm 21$	—
2	10	60	$5.7 \pm 0.6$	$305 \pm 18$	$2.7 \pm 0.1$
3	30	60	$6.6 \pm 0.1$	$269 \pm 25$	$8.9 \pm 2.2$
4	50	60	$10.6 \pm 0.3$	$267 \pm 22$	$9.2 \pm 0.7$
5	50	45	$9.6 \pm 0.3$	$303 \pm 18$	$8.5 \pm 0.1$
6	50	30	$5.8 \pm 0.3$	$304 \pm 19$	$2.2 \pm 0.1$

The ATR FTIR spectra of the pristine and modified PET TM are presented in Figure 2. The adsorption bands at  $3100\text{--}2800 \text{ cm}^{-1}$  have been attributed to aromatic and aliphatic  $\text{C-H}$  bonds stretching,  $1719 \text{ cm}^{-1}$  to the ester carbonyl bond,  $1240 \text{ cm}^{-1}$  to the ester group stretching [17]. After polymerization FTIR spectra shows the appearance of a small peak at  $3365 \text{ cm}^{-1}$  corresponding to the  $\text{N-H}_2$  stretching vibration [18]. The intensity of this peak increases slightly with increasing monomer concentration.

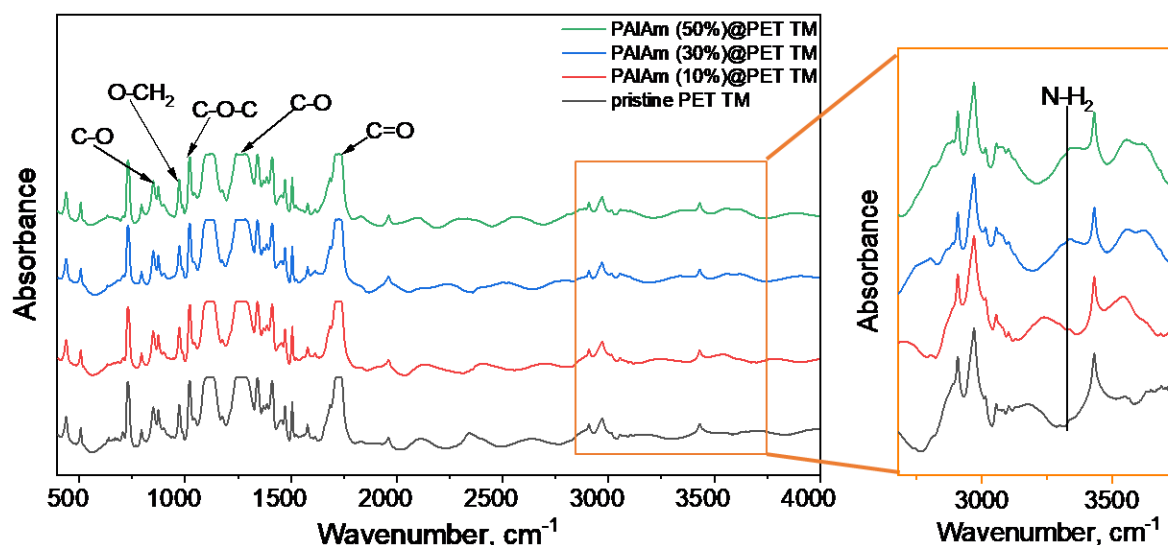


Figure 2. ATR FTIR spectra of the PET TM without and with layer modification

The morphological differences of the functionalized membranes were examined using SEM, with the corresponding results presented in Figure 3. The microphotographs illustrate that the pores of pristine PET

TM are distinctly visible with well-defined edges. After modification with increasing monomer concentration from 10 % to 50 % the pore size slightly decreased from  $305 \pm 5$  nm to  $267 \pm 3$  nm. Although, according to the obtained EDX analysis results (Table 1), an increase in AlAm concentration leads to a gradual growth of the N content from  $2.7 \pm 0.1$  % to  $9.2 \pm 0.7$  %.

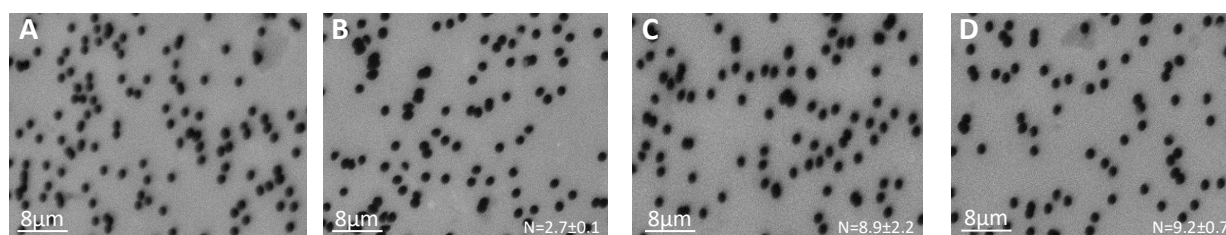


Figure 3. SEM images of pristine PET TM (A) and AlAm functionalized membranes at different concentrations: 10 % (B), 30 % (C), and 50 % (D)

The grafting of AlAm in different polymerization times in the PET TM surface gave rise to the appearance of a new peak in the FTIR spectra related to the AlAm structure, such as at  $3365 \text{ cm}^{-1}$ , which has been attributed to amino group stretching. Figure 4 shows ATR FTIR spectra of pristine and modified membranes in different polymerization times.

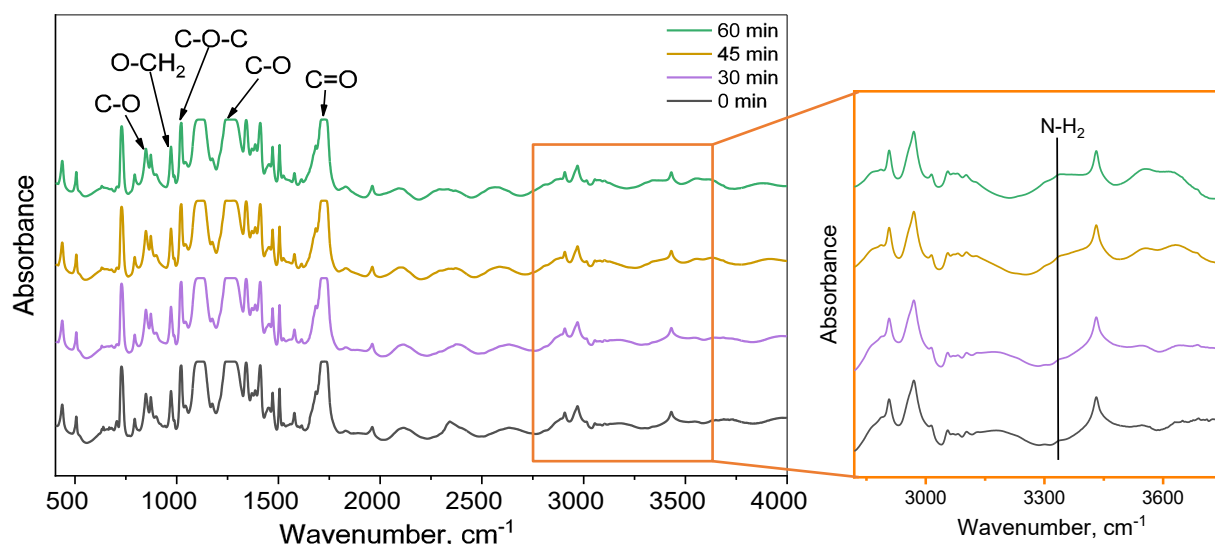


Figure 4. ATR FTIR spectra of pristine and AlAm functionalized membranes at various graft polymerization times

The impact of grafting time on the morphology of TM is illustrated in Figure 5, showing differences between the unmodified and AlAm functionalized surface. The SEM images reveal a smooth surface and a small reduction in the pore size of the TM, which indicates the formation of an AlAm polymer layer. As shown in Table 1, an increase in nitrogen concentration and amino groups is observed with longer polymerization times. At a grafting time of 30 minutes, the nitrogen concentration reached  $2.21 \pm 0.05$  %, while the amino group content, as determined by UV-spectroscopy, was  $5.80 \pm 0.27 \text{ μmol/g}$ .

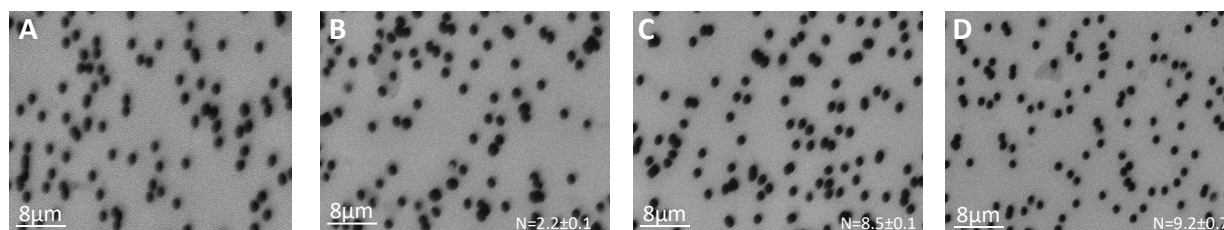


Figure 5. Microphotographs of pristine PET TM (A) and PAIAm modified PET TM at various grafting times: 30 min (B), 45 min (C) and 60 min (D)



Experimental findings indicate that the most efficient photo-induced graft polymerization of AlAm occurs under a monomer concentration of 50 %, a distance from the UV-lamp of 10 cm, and a reaction time of 60 min. The formation of a polymer layer on the PET TM surface is supported by evidence from SEM micrographs, EDX, and FTIR spectroscopy. The photo-induced graft polymerization of AlAm in TM offers an approach for introducing primary amine groups on the membrane surface and significantly enhancing its functionality. The amine groups increase surface hydrophilicity, allowing for reversible interactions with gases like CO<sub>2</sub> through carbamate formation, and providing reactive sites for further chemical modification or biomolecule immobilization. The next stage of this research, the transport properties, such as gas and water permeability, will be investigated to evaluate the performance of the modified TM in practical applications. Additionally, due to the high content of amino groups on the surface of PET TM, this modification can be utilized as a template for the synthesis of MOFs and for the development of adsorbents for carbon dioxide capture and removal of different water pollutants.

### Conclusions

In conclusion, the results confirm that PET TM can be effectively modified by photo-induced AlAm graft polymerization, leading to a marked increase in the concentration of surface amino functionalities. The optimal parameters for the photo-induced graft polymerization of AlAm were determined as a UV lamp distance of 10 cm, an AlAm concentration of 50 %, and a grafting time of 60 min, ensuring the preservation of the porous membrane structure, as confirmed by SEM-EDX, ATR FTIR, and UV spectroscopy. The modification enhances the chemical functionality of PET TM, offering opportunities for a variety of applications. These modified membranes can be utilized for CO<sub>2</sub> separation and capture, water purification and electrochemical and biosensing technology.

### Funding

The work was funded by the Ministry of Science and Higher Education of the Republic of Kazakhstan (grant No AP19676702).

### Author Information\*

*\*The authors' names are presented in the following order: First Name, Middle Name and Last Name*

**Aigerim Khairatovna Shakayeva** (*corresponding author*) — PhD Student, L.N. Gumilyov Eurasian National University, Satbaev str. 2, 010000, Astana, Kazakhstan; Engineer, Astana branch of the Institute of Nuclear Physics of the Republic of Kazakhstan, Abylay khana 2/1, 010000, Astana, Kazakhstan; e-mail: [shakayeva19@gmail.com](mailto:shakayeva19@gmail.com); <https://orcid.org/0000-0001-5731-1115>

**Dias Dumanuli Omertasov** — Master Student, L.N. Gumilyov Eurasian National University, Satbaev str. 2, 010000, Astana, Kazakhstan; e-mail: [dias2101@mail.ru](mailto:dias2101@mail.ru)

**Zhanna Kalanbekovna Zhatkanbayeva** — Candidate of Chemical Sciences, Associated Professor, Department of Chemistry, L.N. Gumilyov Eurasian National University, Satbaev str. 2, 010000, Astana, Kazakhstan; e-mail: [zhanna01011973@mail.ru](mailto:zhanna01011973@mail.ru), <https://orcid.org/0000-0001-6584-2565>

**Ainash Turlybekovna Zhumazhanova** — PhD, Engineer, Astana branch of the Institute of Nuclear Physics of the Republic of Kazakhstan, Abylay khan 2/1, 010000, Astana, Kazakhstan; e-mail: [ainash.zhumazhanova@gmail.com](mailto:ainash.zhumazhanova@gmail.com); <https://orcid.org/0000-0002-5483-9552>

**Maxim Vladimirovich Zdorovets** — Candidate of Physical and Mathematical Science, Professor. Director, Astana branch of the Institute of Nuclear Physics of the Republic of Kazakhstan, Abylay khan 2/1, 010000, Astana, Kazakhstan; e-mail: [mzdorovets@inp.kz](mailto:mzdorovets@inp.kz); <https://orcid.org/0000-0003-2992-1375>

**Ilya Vladimirovich Korolkov** — PhD, Associated Professor, Senior researcher, Astana branch of the Institute of Nuclear Physics of the Republic of Kazakhstan, Abylay khan 2/1, 010000, Astana, Kazakhstan; e-mail: [i.korolkov@inp.kz](mailto:i.korolkov@inp.kz); <https://orcid.org/0000-0002-0766-2803>

### Author Contributions

All authors contributed to the preparation of the manuscript. All authors approved the final version of the manuscript. **CRedit**: **Aigerim Khairatovna Shakayeva** investigation, writing — original draft, data cu-

ration, visualization; **Dias Dumanuli Omertasov** — investigation; **Zhanna Kalanbekovna Zhatkanbayeva** — supervision; **Ainash Turlybekovna Zhumazhanova** investigation, data curation; **Maxim Vladimirovich Zdorovets** — supervision, data curation; **Ilya Vladimirovich Korolkov** conceptualization, supervision, writing review and editing, project administration, funding acquisition.

### Acknowledgments

The work was carried out with the financial support of the Ministry of Science and Higher Education of the Republic of Kazakhstan (grant No AP19676702).

### Conflicts of Interest

The authors declare that they have no known competing financial interests or personal relationships that could have appeared to influence the work reported in this paper.

### References

- 1 Rossouw, A., Nechaev, A., & Apel, P. (2021). Modification of polyethylene terephthalate track etched membranes by planar magnetron sputtered Ti/TiO<sub>2</sub> thin films. *Thin Solid Films*, 725(138641), 1–9. <https://doi.org/10.1016/j.tsf.2021.138641>
- 2 Apel, P. (2001). Track etching technique in membrane technology. *Radiation Measurements*, 34(43), 559–566. [https://doi.org/10.1016/S1350-4487\(01\)00228-1](https://doi.org/10.1016/S1350-4487(01)00228-1)
- 3 Apel, P. Y., Bashevoy, V. V., & Trautmann, C. (2016). Shedding light on the mechanism of asymmetric track etching: an interplay between latent track structure, etchant diffusion and osmotic flow. *Physical Chemistry Chemical Physics*, 18(6), 25421–25433. <https://doi.org/10.1039/C6CP05465J>
- 4 Kaya, D., & Keçeci, K. (2020). Review—Track-Etched Nanoporous Polymer Membranes as Sensors: A Review. *Journal of The Electrochemical Society*, 167(3), 037543. <https://doi.org/10.1149/1945-7111/AB67A7>
- 5 Vinogradov, I. I., Drozhzhin, N. A., Kravets, L. I., Rossouw, A., Vershinina, T. N., & Nechaev, A. N. (2024). Formation of Hybrid Membranes for Water Desalination by Membrane Distillation. *Colloid Journal*, 86(5), 667–679. <https://doi.org/10.1134/S1061933X24600519>
- 6 Zhdanov, G., Nyhrikova, E., Meshcheryakova, N., & Kristavchuk, O. (2022). A Combination of Membrane Filtration and Raman-Active DNA Ligand Greatly Enhances Sensitivity of SERS-Based Aptasensors for Influenza A Virus. *Frontiers in Chemistry*, 10(June), 1–14. <https://doi.org/10.3389/fchem.2022.937180>
- 7 Ulbricht, M., Matuschewski, H., Oechel, A., & Hicke, H. (1996). Photo-induced graft polymerization surface modifications for the preparation of hydrophilic and low-protein-adsorbing ultrafiltration membranes. *Journal of Membrane Science*, 115, 31–47.
- 8 Markov, P. A., Vinogradov, I. I., Kostromina, E., Eremin, P. S., Gilmudinova, I. R., Kudryashova, I. S., Greben, A., Rachin, A. P., & Nechaev, A. N. (2022). A wound dressing based on a track-etched membrane modified by a biopolymer nanoframe: physicochemical and biological characteristics. *European Polymer Journal*, 181(November), 111709. <https://doi.org/10.1016/j.eurpolymj.2022.111709>
- 9 Vinogradov, I. I., Andreev, E. V., Yushin, N. S., Sokhatskii, A. S., Altynov, V. A., & Gustova, M. V. (2023). A Hybrid Membrane for the Simultaneous Selective Sorption of Cesium in the Ionic and Colloid Forms. *Theoretical Foundations of Chemical Engineering*, 57(4), 549–562. <https://doi.org/10.1134/S0040579523040498>
- 10 Perea, O., Uche, C., Bublikov, P. S., Bode-aluko, C., Rossouw, A., & Vinogradov, I. I. (2021). Chitosan / PEO nanofibers electrospun on metallized track-etched membranes: fabrication and characterization. *Materials Today Chemistry*, 20, 100416. <https://doi.org/10.1016/j.mtchem.2020.100416>
- 11 Perea, O., Omoniyi, Laatikainen, K., Bode-aluko, C., Kochnev, I., Fatoba, O., Nechaev, A. N., & Petrik, L. (2020). Adsorption of Ce<sup>3+</sup> and Nd<sup>3+</sup> by diglycolic acid functionalised electrospun polystyrene nanofiber from aqueous solution. *Separation and Purification Technology*, 233 (September 2019), 116059. <https://doi.org/10.1016/j.seppur.2019.116059>
- 12 Omertasov, D. D., Shakayeva, A. K., Zhatkanbayeva, Z. K., Shakirzyanov, R. I., Zdorovets, M. V., Güven, O., & Korolkov, I. V. (2025). HKUST-1 Synthesis in PET Track-Etched Membranes via Conversion of Deposited Cu for Carbon Dioxide Capture. *ACS Omega*, 10, 30271. [https://doi.org/10.1021/ACSOMEGA.5C01493/ASSET/IMAGES/LARGE/AO5C01493\\_0011.JPEG](https://doi.org/10.1021/ACSOMEGA.5C01493/ASSET/IMAGES/LARGE/AO5C01493_0011.JPEG)
- 13 Muslimova, I. B., Zhumanazar, N., Melnikova, G. B., Yeszhanov, A. B., Zhatkanbayeva, Z. K., Chizhik, S. A., Zdorovets, M. V., Güven, O., & Korolkov, I. V. (2024). Preparation and application of stimuli-responsive PET TeMs: RAFT graft block copolymerisation of styrene and acrylic acid for the separation of water–oil emulsions. *RSC Advances*, 14(20), 14425–14437. <https://doi.org/10.1039/D4RA02117G>
- 14 Shakayeva, Aigerim Kh, Yeszhanov, A. B., Borissenko, A. N., Kassymzhanov, M. T., Zhumazhanova, A. T., Khlebnikov, N. A., Nurkassimov, A. K., Zdorovets, M. V., Güven, O., & Korolkov, I. V. (2024). Surface Modification of Polyethylene Terephthalate Track-Etched Membranes by 2,2,3,3,4,4,5,5,6,6,7,7-Dodecafluoroheptyl Acrylate for Application in Water Desalination by Direct Contact Membrane Distillation. *Membranes*, 14(7), 145. <https://doi.org/10.3390/MEMBRANES14070145/S1>
- 15 Ryntz, R. A. (1994). Coating adhesion to low surface free energy substrates. *Progress in Organic Coatings*, 25(1), 73–83. [https://doi.org/10.1016/0300-9440\(94\)00503-6](https://doi.org/10.1016/0300-9440(94)00503-6)

- 16 Noeske, M., Degenhardt, J., Strudthoff, S., & Lommatzsch, U. (2004). Plasma jet treatment of five polymers at atmospheric pressure: Surface modifications and the relevance for adhesion. *International Journal of Adhesion and Adhesives*, 24(2), 171–177. <https://doi.org/10.1016/J.IJADHADH.2003.09.006>
- 17 Gupta, B., Plummer, C., Bisson, I., Frey, P., & Hilborn, J. (2002). Plasma-induced graft polymerization of acrylic acid onto poly(ethylene terephthalate) films: Characterization and human smooth muscle cell growth on grafted films. *Biomaterials*, 23(3), 863–871. [https://doi.org/10.1016/S0142-9612\(01\)00195-8](https://doi.org/10.1016/S0142-9612(01)00195-8)
- 18 Soto Espinoza, S. L., Arbeitman, C. R., Clochard, M. C., & Grasselli, M. (2014). Functionalization of nanochannels by radio-induced grafting polymerization on PET track-etched membranes. *Radiation Physics and Chemistry*, 94(1), 72–75. <https://doi.org/10.1016/J.RADPHYSHEM.2013.05.043>
- 19 Ulbricht, M. (1996). Photograft-polymer-modified microporous membranes with environment-sensitive permeabilities. *Reactive and Functional Polymers*, 31(2), 165–177. [https://doi.org/10.1016/1381-5148\(96\)00055-7](https://doi.org/10.1016/1381-5148(96)00055-7)
- 20 Wu, G., Li, Y., Han, M., & Liu, X. (2006). Novel thermo-sensitive membranes prepared by rapid bulk photo-grafting polymerization of N,N-diethylacrylamide onto the microfiltration membranes Nylon. *Journal of Membrane Science*, 283(1–2), 13–20. <https://doi.org/10.1016/J.MEMSCI.2006.05.017>
- 21 Deng, J., Wang, L., Liu, L., & Yang, W. (2009). Developments and new applications of UV-induced surface graft polymerizations. *Progress in Polymer Science*, 34(2), 156–193. <https://doi.org/10.1016/j.progpolymsci.2008.06.002>
- 22 Cai, Y., Wang, Z., Yi, C., Bai, Y., Wang, J., & Wang, S. (2008). Gas transport property of polyallylamine–poly(vinyl alcohol)/polysulfone composite membranes. *Journal of Membrane Science*, 310(1–2), 184–196. <https://doi.org/10.1016/J.MEMSCI.2007.10.052>
- 23 Klinthong, W., Huang, C. H., & Tan, C. S. (2014). Polyallylamine and NaOH as a novel binder to pelletize amine-functionalized mesoporous silicas for CO<sub>2</sub> capture. *Microporous and Mesoporous Materials*, 197, 278–287. <https://doi.org/10.1016/J.MICROMESO.2014.06.030>
- 24 Alkhabbaz, M. A., Khunsupat, R., & Jones, C. W. (2014). Guanidinylated poly(allylamine) supported on mesoporous silica for CO<sub>2</sub> capture from flue gas. *Fuel*, 121, 79–85. <https://doi.org/10.1016/J.FUEL.2013.12.018>
- 25 Shiue, A., Chin, K. Y., Yin, M. J., Cheng, C. Y., Chang, S. M., & Leggett, G. (2023). Poly(allylamine)–based amine blends for separation of carbon dioxide in the indoor environment. *Optik*, 284. <https://doi.org/10.1016/j.ijleo.2023.170973>
- 26 Mathai, A., & Karanikolos, G. N. (2020). CO<sub>2</sub> capture adsorbents functionalized by amine — bearing polymers : A review. *International Journal of Greenhouse Gas Control*, 96 (September 2019), 103005. <https://doi.org/10.1016/j.ijggc.2020.103005>
- 27 Hong, K. H., Liu, N., & Sun, G. (2009). UV-induced graft polymerization of acrylamide on cellulose by using immobilized benzophenone as a photo-initiator. *European Polymer Journal*, 45(8), 2443–2449. <https://doi.org/10.1016/J.EURPOLYMJ.2009.04.026>
- 28 Ruckert, D., & Geuskens, G. (1996). Surface modification of polymers—IV. Grafting of acrylamide via an unexpected mechanism using a water soluble photo-initiator. *European Polymer Journal*, 32(2), 201–208. [https://doi.org/10.1016/0014-3057\(95\)00136-0](https://doi.org/10.1016/0014-3057(95)00136-0)
- 29 Korolkov, I. V., Mashentseva, A. A., Güven, O., & Taltenov, A. A. (2015). UV-induced graft polymerization of acrylic acid in the sub-micronchannels of oxidized PET track-etched membrane. *Nuclear Instruments and Methods in Physics Research, Section B: Beam Interactions with Materials and Atoms*, 365, 419–423. <https://doi.org/10.1016/j.nimb.2015.07.057>
- 30 Liu, S., Chen, H., Zhang, Y., Sun, K., Xu, Y., Morlet-Savary, F., Graff, B., Noirbent, G., Pigot, C., Brunel, D., Nechab, M., Gigmes, D., Xiao, P., Dumur, F., & Lalevée, J. (2020). Monocomponent photoinitiators based on benzophenone-carbazole structure for LED photoinitiating systems and application on 3D printing. *Polymers*, 12(6). <https://doi.org/10.3390/polym12061394>

## PROSPECTIVE APPLICATIONS OF TEMs

### Article

Received: 20 May 2025 | Revised: 27 August 2025 |

Accepted: 4 September 2025 | Published online: 21 September 2025

UDC 544.42+519.242.7

<https://doi.org/10.31489/2959-0663/3-25-4>

Alexandr V. Mitrofanov<sup>1</sup>, Pavel Yu. Apel<sup>2</sup>, Oleg M. Ivanov<sup>2</sup>, Fedor A. Pudonin<sup>1\*</sup>

<sup>1</sup>*Lebedev Physical Institute, Russian Academy of Sciences, Moscow, Russia;*

<sup>2</sup>*Joint Institute for Nuclear Research, Dubna, Moscow region, Russia*

(\*Corresponding author's e-mail: [pudoninfa@lebedev.ru](mailto:pudoninfa@lebedev.ru))

### A New Application of Track-Etched Membranes in X-Ray and Vacuum Ultraviolet Optics

Due to their unique structure properties, track-etched membranes are widely used in scientific and engineering practice to solve specific tasks and perform certain functions. Typical examples are diffraction filters, supports for thin-film X-ray filters and collimators in solar X-ray radiometers. In this paper new non-trivial application of track-etched membranes in optical instruments exploited in vacuum is suggested. Metal-coated track-etched membranes with modified architecture of pore channels can be used as air inlet/outlet elements that block the stray optical radiation within the inner space of the instruments. The membrane consists of two arrays of opaque channels intersecting at a certain angle inside its volume. Both surfaces are coated with light-absorbing and reflective layers of aluminum, which allows background optical radiation to be suppressed by several orders of magnitude. Residual air can pass through the membrane, which reduces the mechanical load on the sensitive elements of the device during fluctuations in external pressure. The developed "black" membranes are promising for use in various X-ray optical devices, including those for space purposes.

**Keywords:** accelerated ions, track-etched membranes, pore channels, X-ray optics, solar astronomy, air inlet/outlet, stray optical radiation, thin-film X-ray filters, solar X-ray radiometers

### Introduction

Irradiation of polymers with high energy heavy ions is widely used for nanostructuring of polymers, including production of the so-called track-etched membranes (TEMs) [1, 2]. Membranes of this kind have straight pore channels the shape and the size of which can be varied at will. The main characteristics of TEMs — thickness, pore density and pore diameter — can be precisely controlled. Due to the unique properties, TEMs occupy many special niches in academia and modern technologies.

The design of X-ray telescopes and solar radiometers often includes a means that provides the effective absorption of background electromagnetic radiation in a wide wavelength range from X-rays to near infrared radiation and, at the same time, serves as air inlet and outlet which allows for fast pumping of inner vacuum space of the instrument. In some cases the means should protect detectors also from electrons and ions. Due to the elimination of atmospheric air from the apparatus, the gas dynamic load on the delicate parts such as thin-film X-ray filters under harsh conditions during the launching into Earth orbit is mitigated [3]. Quite often, relatively massive mechanical devices are used, made of blackened metal, and containing arrays of channels in the form of a multi-pass labyrinth. The channels provide a high flowrate of the residual gas and guarantee the fast vacuumation of the apparatus. Another existing approach is the LIGA technology allowing fabrication of thin plates with narrow channels [4, 5].

In the 1970-s and 1980-s, track-etched membranes were reported to be used as the key component of multi-layer thermal insulation [6, 7]. The idea was based on the fact that metallized TMs with submicron and micron pore channels constitute thin-film optical filters and, at the same time, are gas-permeable. This paper presents further development of the bifunctional filter, based on the ideas introduced in Refs [6, 7]. To this end, the morphology of pore space in polyethylene terephthalate track-etched membranes was modified such that to prevent direct propagation of optical radiation through the pore channels. In addition, the membranes were coated with light-reflecting and light-absorbing layers. Physical characteristics of the obtained structures are discussed.

Diffraction filters based on a metal-coated conventional track-etched membrane has been developed and described in previous publications [12]. The membrane having straight pore channels successfully blocked relatively long wave radiation but was not opaque to short wave lengths. In contrast, in the present paper we propose a distinctly different architecture of the membrane, namely the structure with labyrinth channels. This imparts the membrane a new functionality. To the best of our knowledge, such approach has not been reported previously.

### Experimental

Polyethylene terephthalate (PETP) films with the thickness of 19 and 23  $\mu\text{m}$  were irradiated with accelerated xenon ions on the IC100 cyclotron of the Flerov Laboratory of Nuclear Reactions (JINR, Dubna) [8]. The ions impinged onto the film subsequently from both sides at angles of 20 or 45° relative to normal to the surface. (Fig. 1). The ion-irradiated films were treated with soft ultraviolet radiation in order to sensitize the ion tracks and etched chemically thus forming two arrays of mutually intersecting pore channels (Fig. 1). The range of Xe ions with the energy of 160 MeV in PETP was 20–21  $\mu\text{m}$  [9]. Therefore, the etched out straight pore channels did not penetrate the whole film thickness. However, the channels were connected to each other in the membrane depth, thus making possible the flow of air through the membranes.

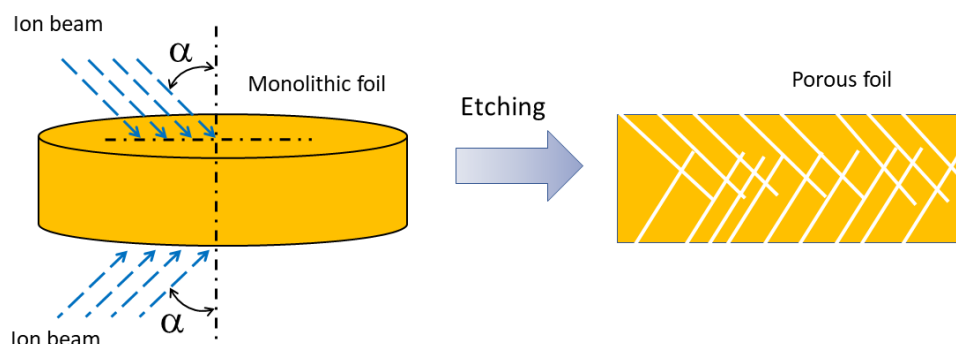


Figure 1. The principle of fabrication of a track-etched membrane having no straight through pore channels

Chemical etching was performed under mild conditions (sodium hydroxide concentration of 1 mol/L, temperature of 60 °C) in order to provide a high track-to-bulk etch rate ratio and obtain the cylindrical pore channels. The scanning electron microscope SU8020 (Hitachi, Japan) was employed to image the membrane samples in the secondary electron mode. The fracturing technique was used for cross-section imaging. Prior to fracturing, the samples were embrittled using a controllable photo-oxidation process, most comprehensively described in Ref. [10]. The specimens were sputter-coated with a thin Pt-Pd layer. The air flowrate was measured on 1  $\text{cm}^2$  area of the fabricated membranes using spherical float flowmeters (Gilmont Instruments).

### Results and Discussion

#### Membrane Morphology

The geometry shown in Figure 1 represents two arrays of parallel pore channels tilted at the angle  $\alpha$  relative to normal, with the surface pore density  $n$  in each array. The ions impinged the foil surface from both sides so that their trajectories cross at an angle of  $2\pi - 2\alpha$  in the side projection. After etching, the pore channels that belong to one array may intersect with the channels of the second array. In order to provide high air flowrate through the membrane, the conditions for multiple pore channel intersections have to be fulfilled.



In the case shown in Figure 1 the mean number of channel intersections (per one channel)  $N$  can be found using the following formula [11]:

$$N = 4 n d H \tan \alpha, \quad (1)$$

where  $H$  is the thickness of the layer with intersections (see Fig. 2),  $d$  is the channel diameter. Examples of the morphology of membranes obtained under such conditions are illustrated by the scanning electron microscope (SEM) images in Figure 2. Structural parameters of the membranes are shown in Table 1.

Table 1

Structural parameters and airflow rates of track membranes used to fabricate the air inlet/outlet device

Membrane	Thickness, $\mu\text{m}$	Pore density in each array $n$ , $\text{cm}^{-2}$	Tilt angle $\alpha$ , $^\circ$	Pore diameter $d$ , $\mu\text{m}$	Mean number of channel intersections $N$	Typical airflow at $\Delta P = 0.01$ MPa, $\text{cm}^3 \text{ cm}^{-2} \text{ min}^{-1}$
A	19	$2 \times 10^9$	45	0.05	28	12
B	23	$6 \times 10^7$	20	0.35	5	100
C	23	$1 \times 10^8$	45	0.60	26	800

As can be seen in the microphotographs, the thickness of the layer within which the channels intersect one another is approximately 7, 17 and 11  $\mu\text{m}$  in membranes A, B and C, respectively. Using the known structure characteristics (Table 1) and formula (1) we can estimate the mean number of channel intersections. This quantity is approximately 28, 5 and 26 for membranes A, B, and C, respectively. In all three cases the number of intersections is large enough to guarantee that practically all channels of one array are connected with channels of the second array [11]. Accordingly, the membranes exhibited a substantial permeability for air in the tests performed under a small differential pressure  $\Delta P = 0.01$  MPa. By varying the channel density, channel diameter and the number of channel intersections, the permeability of the porous foils can be adjusted in accordance with specific requirements.

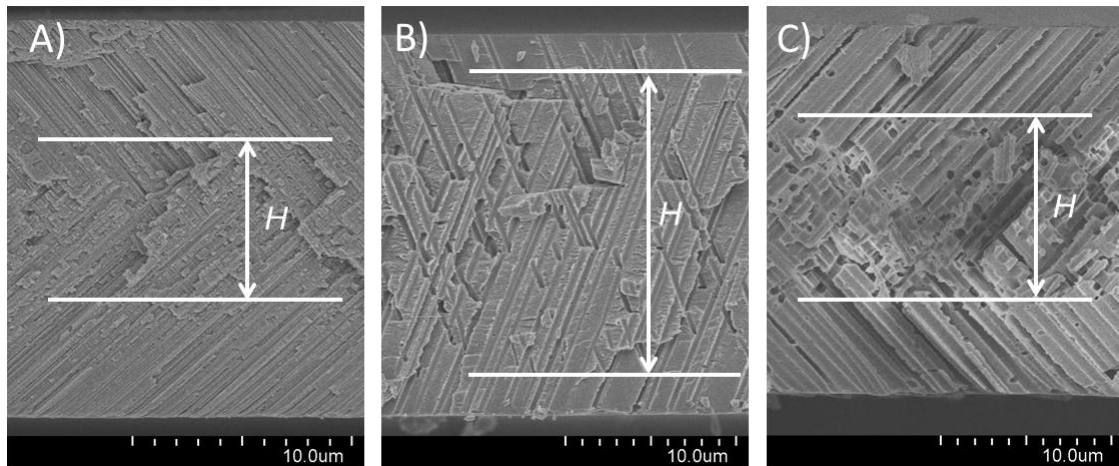


Figure 2. SEM micrographs of track-etched membranes with mutually intersecting arrays of tilted channels.  $H$  is the thickness of the layer where the channels intersect. See text for further details

In order to exclude the possibility of formation of straight through channels in the membrane, the thickness  $H$  should be markedly smaller than the total film thickness. On the other hand, the value of  $H$  should be large enough to obtain a satisfactory number of pore intersections. The examples presented in Figure 2 have been fabricated following this principle.

The number of channel intersections linearly depends on the quantities  $n$ ,  $d$ , and  $H$ . The effect of angle  $\alpha$  is non-linear in the range of practical interest,  $\alpha \in [10 \text{ to } 60^\circ]$ . Increasing the number of intersections at the expense of an increase in  $n$  and  $d$  has a limitation caused by the fact that the volume porosity  $P$  of the membrane matrix in two outer layers

$$P = n \pi d^2 / 4 \cos \alpha \quad (2)$$

should not exceed 0.2–0.3 (for simplicity, here we neglect the effect of pore overlaps). The gas permeability of a membrane is proportional to the fourth and third power of  $d$  at small and large Knudsen numbers, respectively. Therefore, a structure with larger pore diameters is favored with regard to the necessity of fast elimination of residual air. At the same time, the relatively large pore diameter, on the order of 1  $\mu\text{m}$ , is acceptable because of a strong suppression of electromagnetic radiation by the mechanism of diffraction filtering [12].

#### *Light Absorbing Coating*

Absorption of background radiation in different spectral ranges is governed by different mechanisms and caused by different reasons. To make the membranes non-transparent, a two-layer coating was deposited onto the surface of a porous membrane. Aluminum was RF-sputtered in argon plasma using the triode-type sputtering unit Sputron-2 (Balzers). The first layer 100 nm thick (so-called black Al [13]) was deposited at a relatively high pressure of residual gas ( $\sim 10^{-4}$  mbar). Then the vacuum chamber was pumped down to  $\sim 5\text{--}7 \times 10^{-6}$  mbar and the second aluminum layer was deposited in an atmosphere of pure argon until the layer thickness reached 80–100 nm. The procedure was performed on both sides of the membrane; the total thickness of metal was ca. 200 nm on each side.

#### *Optical Properties*

The walls of pore channels were partially covered by the metal, which ensured formation of efficient absorbing optical wedge in the visible range of electromagnetic spectrum [12, 14]. Stray radiation in the red and near infrared ranges was cut by the metal-coated track-etched membrane by the mechanism of diffraction filtering [14, 15]. The specific geometry of the channels array in the membranes excluded the direct penetration of optical radiation. The considerable roughness of the channel walls additionally favored the losses of radiation due to its scattering during the transport through the channel.

The developed “black membrane” possesses two key parameters. The one is the gas flowrate through the membranes at a certain differential pressure and the other one is the optical transmittance. In contrast to the former parameter, which can be easily measured in a wide range, the estimation of the optical transmittance is not a trivial task. In the X-ray region, numerical modeling of distribution of the field amplitude inside micrometer-sized cylindrical pores in polymer track membranes is possible. The refractive index of the polymer matrix is close to 1 (with small real and imaginary additives) in this case, and the calculation of transport of radiation through the pore channels can be performed using a 3D parabolic equation [12, 16]. However, there are no suitable models for the visible and ultraviolet spectrum range and the non-uniform porous bodies. Direct experimental estimate of the optical properties of the black membrane is also not easy because of the necessity to measure light intensities that differ by many orders of magnitude. Our experiments have shown that ordinary track membranes with pores of 0.7–0.9  $\mu\text{m}$  in diameter covered by Al layers on both sides provide attenuation of optical radiation by 5–6 orders of magnitude. The measurements have been performed using a filament of incandescent lamp and a set of neutral density filters. In the case of the back membranes with non-through crossing pores the measurement of attenuation is beyond the capabilities of this method. Based on a rough extrapolation, suppression of optical radiation by 10–12 orders of magnitude seems to be plausible.

#### *Conclusions*

We suggested a new non-trivial application of track-etched membranes. A structurally modified TM can act as an air inlet and outlet in the optical instruments exploited in vacuum. The membrane contains two arrays of non-through channels that intersect each other in the membrane bulk under a certain angle. Both sides of the membrane are coated with light-absorbing and light-reflecting aluminum layers, which ensures the suppression of background optical radiation by several orders of magnitude. At the same time the residual air can pass through the membrane, which reduces the mechanical load on the delicate parts of the instrument when external pressure changes. The developed “black” membranes can be employed when designing various X ray optical instruments, including those that are exploited in space.

### Author Information\*

\*The authors' names are presented in the following order: First Name, Middle Name and Last Name

**Alexandr Victorovich Mitrofanov** — Candidate of Physical and Mathematical Sciences, Leading Researcher, P.N. Lebedev Physical Institute, Leninsky Prospekt, 53, 119991, Moscow, Russia; e-mail: [mitrofanovav@lebedev.ru](mailto:mitrofanovav@lebedev.ru)

**Pavel Yurievich Apel** — Doctor of Chemical Sciences, Head of Department, Flerov Laboratory of Nuclear Reactions, Joint Institute for Nuclear Research, Joliot-Curie street 6, 141980, Dubna, Moscow region, Russia; e-mail: [apel@jinr.ru](mailto:apel@jinr.ru); <https://orcid.org/0000-0003-1259-163X>

**Oleg Mikhailovich Ivanov** — Head of Group, Flerov Laboratory of Nuclear Reactions, Joint Institute for Nuclear Research, Joliot-Curie street 6, 141980, Dubna, Moscow region, Russia; e-mail: [ivom@jinr.ru](mailto:ivom@jinr.ru)

**Fedor Alekseevich Pudonin** (*corresponding author*) — Doctor of Physical and Mathematical Sciences, Principal Researcher, Head of Department, P.N. Lebedev Physical Institute, Leninsky Prospekt, 53, 119991, Moscow, Russia; e-mail: [pudoninfa@lebedev.ru](mailto:pudoninfa@lebedev.ru); <https://orcid.org/0000-0002-3849-3096>

### Author Contributions

The manuscript was written through contributions of all authors. All authors have given approval to the final version of the manuscript. **CRedit**: **Alexandr Victorovich Mitrofanov** conceptualization, data curation, investigation, methodology, validation, writing-review & editing; **Pavel Yurievich Apel** conceptualization, formal analysis, validation, writing-original draft, writing-review & editing; **Oleg Mikhailovich Ivanov** investigation, writing-original draft; **Fedor Alekseevich Pudonin** investigation, technology, data curation, formal analysis, writing-review & editing.

### Acknowledgments

The authors would like to thank O.L. Orelovitch and O.A. Polezhaeva for technical assistance.

### Conflicts of Interest

The authors declare no conflict of interest.

### References

- 1 Fischer, B.E., & Spohr, R. (1983). Production and use of nuclear tracks: imprinting structure on solids. *Rev. Mod. Phys.*, 55, 907–948. <https://doi.org/10.1103/RevModPhys.55.907>
- 2 Apel, P. (2003). Swift heavy ion effects in polymers: Industrial applications. *Nucl. Instrum. Meth. in Phys. Res., Section B*, 208, 11–20. [https://doi.org/10.1016/S0168-583X\(03\)00634-7](https://doi.org/10.1016/S0168-583X(03)00634-7)
- 3 Mitrofanov, A. V., Apel, P. Y., Ivanov, O. M., Nazmov, V. P., & Pudonin, F. A. (2010). Light traps based on micro- and nanostructures. In *X-Ray Optics–2010: Proceedings of the Conference* (Chernogolovka, Russia, September 20–23, 2010, pp. 145–146) [in Russian].
- 4 Malek, C. K., & Saile, V. (2004). Applications of LIGA technology to precision manufacturing of high-aspect-ratio micro-components and -systems: a review. *Microelectronics Journal*, 35(2), 131–143. <https://doi.org/10.1016/j.mejo.2003.10.003>
- 5 Menz, W., Mohr, J., & Paul, O. (2001). *Microsystem technology*. Wiley-VCH.
- 6 Flerov, G. N., & Barashenkov, V. S. (1975). Practical applications of heavy ion beams. *Soviet Physics Uspekhi*, 17(5), 783–793. <https://doi.org/10.1070/pu1975v017n05abeh004371>
- 7 Flerov, G. N., Kuznetsov, V. I., Verkin, B. I., Mikhalechenko, R. S., & Pershin, N. P. (1982). Thermophysical and gas-dynamic properties of screen-vacuum thermal insulations on the basis of polynuclear filters. In *Proceedings of the 4th Meeting on the Application of Novel Nuclear Physics Methods for Solving Scientific, Technical and National Economic Tasks* (JINR Communication P18-82-117, pp. 150–153). Dubna: Joint Institute for Nuclear Research [in Russian].
- 8 Gikal, B. N., Dmitriev, S. N., Gul'bekyan, G. G., Apel', P. Yu., Bashevoi, V. V., Bogomolov, S. L., Borisov, O. N., Buzmakov, V. A., Ivanenko, I. A., Ivanov, O. M., Kazarinov, N. Yu., Kolesov, I. V., Mironov, V. I., Papash, A. I., Pashchenko, S. V., Skuratov, V. A., Tikhomirov, A. V., Khabarov, M. V., Cherevatenko, A. P., & Yazvitskii, N. Yu. (2008). IC-100 accelerator complex for scientific and applied research. *Physics of Particles and Nuclei Letters*, 5(1), 33–48. <https://doi.org/10.1134/s1547477108010068>
- 9 Biersack, J. P., & Ziegler, J. F. (1982). The Stopping and Range of Ions in Solids. *Ion Implantation Techniques*, 122–156. [https://doi.org/10.1007/978-3-642-68779-2\\_5](https://doi.org/10.1007/978-3-642-68779-2_5) Free SRIM software is available from the website: <http://www.srim.org>

- 10 Blonskaya, I. V., Kirilkin, N. S., Kristavchuk, O. V., Lizunov, N. E., Mityukhin, S. A., Orelovich, O. L., Polezhaeva, O. A., & Apel, P. Y. (2023). Visualization and characterization of ion latent tracks in semicrystalline polymers by FESEM. *Nuclear Instruments and Methods in Physics Research Section B: Beam Interactions with Materials and Atoms*, 542, 66–73. <https://doi.org/10.1016/j.nimb.2023.06.009>
- 11 Apel, P. Y. (2025). Intersections of pore channels in track-etched polymer templates and membranes. *Materials Chemistry and Physics*, 339, 130681. <https://doi.org/10.1016/j.matchemphys.2025.130681>
- 12 Mitrofanov, A. V., & Apel, P. Yu. (2009). X-ray diffraction filters based on track membranes. *Bulletin of the Russian Academy of Sciences: Physics*, 73(1), 57–61. <https://doi.org/10.3103/s106287380901016x>
- 13 More-Chevalier, J., Novotný, M., Hruška, P., Fekete, L., Fitl, P., Bulíř, J., Pokorný, P., Volfová, L., Havlová, Š., Vondráček, M., & Lančok, J. (2020). Fabrication of black aluminium thin films by magnetron sputtering. *RSC Advances*, 10(35), 20765–20771. <https://doi.org/10.1039/d0ra00866d>
- 14 Mitrofanov, A. V., Apel, P. Yu., Blonskaya, I. V., & Orelovitch, O. L. (2006). Diffraction filters based on polyimide and poly(ethylene naphthalate) track membranes. *Technical Physics*, 51(9). <https://doi.org/10.1134/s1063784206090209>
- 15 Kravets, V. G., Schedin, F., & Grigorenko, A. N. (2009). Almost Complete Absorption of Light in Nanostructured Metallic Coatings: Blackbody Behavior. *PIERS Online*, 5(4), 397–400. <https://doi.org/10.2529/piers090219104337>
- 16 Mitrofanov, A.V., Feshchenko, R.M. (2023). On the numerical modeling of track-etched membranes used as collimators of the X-ray radiation. *Zhurnal Tekhnicheskoy Fiziki*, 93(7), 948–952. <https://doi.org/10.21883/jtf.2023.07.55751.55-23>

Maksim V. Balyasin<sup>1</sup>, Genrikh V. Serpionov<sup>2\*</sup>, Mikhail E. Krashennnikov<sup>1</sup>,  
Alexey V. Lyundup<sup>1</sup>, Alexander N. Nechaev<sup>2</sup>

<sup>1</sup>*Peoples' Friendship University of Russia named after Patrice Lumumba, Moscow, Russia;*

<sup>2</sup>*Joint Institute for Nuclear Research, Dubna, Moscow region, Russia*

(\*Corresponding author-mail: [genrihserpionov@gmail.com](mailto:genrihserpionov@gmail.com))

## Biological Compatibility of Polyethylene Terephthalate Track Membranes: Growth, Proliferation, and Viability of Cells in Culture Systems

This study evaluated the biocompatibility of polyethylene terephthalate track membranes (PET TMs) obtained by heavy ion irradiation followed by chemical etching, with respect to cell growth, proliferation, and viability in culture systems. Physical parameters of the PET TMs were determined, including Young's modulus, ultimate tensile strength, and contact angle. Cytotoxicity of PET TMs was studied on three cell cultures: the epithelial line MCF7 (adenocarcinoma), fibroblast-like mouse line 3T3, and a primary culture of mesenchymal stromal cells (MSCs) isolated from rabbit bone marrow. Cytotoxicity was assessed using two methods: extraction from the material and the direct contact method in accordance with the Interstate Standard ISO 10993-5:2011, IDT. The results demonstrated that neither PET TM extracts nor direct contact samples significantly affected cell growth. The proliferation rate of MCF7 cells was 0.01531 1/h for the extract and 0.01568 1/h for direct contact, which did not differ statistically from the control group (0.01877 1/h,  $p = 0.138$ ). Microscopic analysis confirmed the preservation of cellular morphology: MCF7 cells retained cuboidal morphology, while 3T3 cells exhibited a spindle-shaped morphology. Real-time cell analysis (RTCA) revealed no significant effect of the tested samples on the cellular index ( $C_i$ ), further supporting the absence of a cytotoxic effect. Visual observations of cell cultures after incubation with the studied samples also did not reveal cell confluence and morphology changes. These findings provide important evidence for the safety of PET TMs in biomedical research and cell culture systems, recommending them for further research in tissue engineering and regenerative medicine.

**Keywords:** heavy ion irradiation, chemical etching, track-etched membrane, polyethylene terephthalate, regenerative medicine, cytotoxicity, cell culturing, tissue engineering

### Introduction

Track membranes (TMs) are thin polymer films (5–30  $\mu\text{m}$  in thickness) with a pore system of strictly defined geometry. They are obtained by irradiating the polymer film with heavy ions followed by chemical etching to form nano- and micropores [1]. The most widely used TMs are made of polyethylene terephthalate (PET) and polycarbonate (PC). TMs have broad applications in medicine and biochemistry [2], including biological and chemical sensing [3–5], water purification [6, 7], electrophoresis [8], plasmapheresis [9], and numerous other technological and biomedical processes. In addition, TMs are employed in cell cultivation systems, particularly in Transwell systems [10–12]. Transwell systems (TS) are containers for cell cultivation that enable the creation of bi- or multilayer cellular models [13] with static or dynamic movement of the culture medium. They typically consist of two chambers: an apical chamber with a semipermeable membrane installed at the bottom and a basolateral chamber. These systems are widely used for two-dimensional (2D) and three-dimensional (3D) cell cultivation. In 2D culturing, membranes provide a flat surface that allows studying cell adhesion, proliferation, and morphology. In the case of 3D culturing, TMs support multilayer co-cultivation of different cell types, with distinct cell populations adhering to each side of the membrane as well as to the bottom of the basolateral chamber. This setup mimics tissue–tissue interactions *in vivo*, which is particularly important for tissue engineering and regenerative medicine, studies of pathological processes such as carcinogenesis, investigations of specific cell functions, and the analysis of tissue barrier properties [13–16].

Numerous studies have utilized TS to develop *in vitro* models of the intestinal epithelial barrier, enabling the investigation of absorption [17], interactions with pathogenic microorganisms [18], drug screening [19], and evaluation of drug-induced toxicity [20]. TS have also been applied to generate artificial blood-



brain barrier models for studying immune cell migration into the CNS, a key feature of multiple sclerosis pathogenesis [21, 22]. Furthermore, these systems have been used to investigate the function of brain endothelial cells by co-cultivating endothelial cells with astrocytes or pericytes [23, 24].

Transwell analysis is traditionally used to assess the migratory and invasive activity of tumor cells. Li et al. (2018) used TS for tumor cells' migratory study. It was demonstrated that depletion of the active pool of Prdx1 protein reduced the invasive and migratory capacity of colorectal cancer cells, whereas increased Prdx1 expression produced the opposite effect [25]. Using TS, Zhao et al. (2022) showed that miR-29b-3p microRNA exerted an inhibitory effect on the proliferation, invasion, and migration of 22Rv1 prostate cancer cells [26]. TS have also been applied to investigate the impact of ICOS gene expression on the invasive potential of hepatocellular carcinoma cells [27]. The inhibitory role of secretory cGMP-dependent protein kinase type II (PKG II) in the migration, invasion, and proliferation of gastric cancer cells was likewise demonstrated using TS [28]. Furthermore, Jeon et al. (2016) employed TS to study the influence of mitochondria on invasion and migration in drug-resistant lung adenocarcinoma cells [29].

TS have been applied to study amyloidogenesis, prion transfer between cells, and the processes of amyloid absorption by macrophages in the presence of various amyloid neurodegenerative diseases [30–33]. In addition, TM-based systems have been used to investigate the effect of the spatial organization of the cell culture of fibroblast-like cells and dermal fibroblasts on the level of expression of bone remodeling markers [34] and the level of fibroblast migration [35].

Track-etched membranes have also been employed in the development of “organ-on-a-chip” systems. Organs on chips (organ chips) are microfluidic cell culturing devices containing continuously perfused hollow microchannels populated with living cells. This design enables simulation of physiological processes at the tissue and organ levels, offering a potential alternative to animal experiments in the future [36]. Furthermore, track membranes are integral components of multi-chamber microfluidic devices [37, 38].

The quantitative method of transepithelial/transendothelial electrical resistance (TEER) is widely used for measuring the integrity of tight junction dynamics in cell culture models of endothelial and epithelial monolayers. TEER values serve as reliable indicators of the integrity of cellular barriers prior to evaluating the transport of drugs or chemicals. TEER measurements can be performed in real time without damaging the cells. A classic TEER setup consists of a cell monolayer cultured on a semipermeable filter insert, which separates the system into apical (upper) and basolateral (lower) compartments. For electrical measurements, two electrodes are used: one placed in the upper compartment and the other in the lower one, separated by a cell monolayer. In these devices, TMs serve as substrates for cell growth, forming a monolayer through which electrical resistance is measured. They provide a controlled porous structure that promotes cell adhesion, growth, and differentiation [38, 39].

Despite the widespread use of TS for culturing various cell lines and microfluidic devices equipped with TMs, there is limited information in the literature regarding the influence of TM chemical composition on cell growth and proliferation, as well as on their potential cytotoxicity.

Several studies have examined the toxicity of bisphenol A, a monomer unit of polycarbonate membranes, and the degree of its extraction from the polymer [40–44]. These findings are relevant for evaluating the toxicity of polycarbonate films, as they undergo alkaline hydrolysis and are exposed to aqueous environments during cell cultivation. In contrast, no studies have directly assessed the cytotoxicity of PET TMs. Nevertheless, some reports indicate that PET, in the form of nano- and microgranules, can exhibit toxic effects [45, 46].

Therefore, the present study aims to investigate the impact of the chemical composition of PET TMs on cell growth, proliferation, and viability, with a particular focus on evaluating potential cytotoxicity. The results obtained in this study may be utilized to assess the feasibility of applying PET TMs in regenerative medicine, particularly as a component of implantable biological capsules carrying living cells.

## *Experimental*

### *Preparation of TMs for Working with Cell Cultures*

To fabricate TMs with cylindrical pores, a high-quality polyester polyethylene terephthalate film was used (“PJSC Chemical Plant, Vladimir, Russia, premium grade, State standard No. 24234-80) with a thickness of 11  $\mu\text{m}$ . The film was irradiated with accelerated heavy ions using an IC 100 cyclotron. The irradiated samples were then subjected to ultraviolet (UV) sensitization followed by chemical etching. Detailed production conditions and membrane characteristics are described by Apel et al. (2021) [47]. Final-

ly, the resulting membranes were sterilized by autoclaving at a temperature of 121 °C and a pressure of 1 atm for 60 minutes.

#### *Measurement of the mechanical characteristics of TMs*

The tensile mechanical properties of the investigated films were measured at room temperature using a Shimadzu AGS-X testing machine equipped with a 50 N load cell. Rectangular samples with a width of 10 mm and a gauge length of 35 mm were stretched at a rate of 1 mm/min. The sample thickness was measured by a Mitutoyo Iitematic vl-50 thickness tester (measuring force 0.01 N). The stress and strain parameters were calculated using the Trapezium X software.

#### *Hydrophilic-Hydrophobic Properties of TMs*

The degree of hydrophilicity of the polyester films and TMs was determined by measuring the contact angle of wetting with water ( $\theta^\circ$ ) using the “sitting drop” method on a DSA-100 device (KRÜSS, Germany).

#### *Scanning Electron Microscopy (SEM)*

A high-resolution scanning electron microscope, FESEM SU-8020 (Hitachi, Tokyo, Japan), was used for morphological analysis of the surface, as well as the number and diameter of pores in PET TMs. The examination was conducted in the secondary electron (SE) registration mode at an accelerating voltage of 3 kV with a magnification of  $5 \times 10^4$  times. Prior to examination, a 15 nm layer of platinum-palladium alloy was deposited onto the samples by magnetron sputtering using a Quorum Q150T S system.

#### *Cell Cultures*

The cell cultures were provided by the leading researcher M.E. Krashennnikov (Research and Educational Center “Cell Technologies”, Peoples’ Friendship University of Russia named after Patrice Lumumba, Moscow, Russia). Linear cell cultures and primary cell culture were selected for the work: MCF7 — a line of human epithelial cells (adenocarcinoma); 3T3 — a line of mouse embryonic immortalized fibroblasts; MSC — mesenchymal stromal cells isolated from rabbit bone marrow. Multipotent cells with the ability to differentiate in the adipo-, osteo- and chondrogenic direction, as well as the ability to actively proliferate. They have a fibroblast-like, spindle-shaped morphology. All cells were tested for the absence of mycoplasma contamination prior to experiments using a chemiluminescent detection system (Servicebio, China). Rabbit MSCs were maintained in T75 culture flasks (Sarstedt, Germany) in DMEM/F12 medium (Himedia, India) supplemented with L-glutamine, 10 % FBS (Himedia, India), insulin 1.6 µg/ml (PanEco, Russia), FGF2 — 4 ng/ml (FGF2, Israel), dexamethasone 2 nM (Russia), penicillin-streptomycin (PanEco, Russia), passaged every 3 days 1/5 no more than 5 passages, under conditions of +37 °C, high humidity and an atmosphere of 5 % CO<sub>2</sub>.

MCF7 and 3T3 cell cultures were maintained in T75 culture flasks (Sarstedt, Germany) in DMEM/F12 culture medium (Himedia, India) supplemented with L-glutamine, 10 % FBS (Himedia, India), and penicillin-streptomycin (PanEco, Russia), passaged every 3 days 1/10, under conditions of +37 °C, high humidity and 5 % CO<sub>2</sub> atmosphere.

#### *Cytotoxicity*

Cytotoxicity testing was performed in accordance with the Interstate Standard ISO 10993-5-2011, “medical devices. evaluation of the biological effect of medical devices”. Part 5. Cytotoxicity studies: *in vitro* methods” [48]. In accordance with the Interstate Standard, the studies were performed on: 1) an extract from the material; 2) on the material itself (direct contact method). Phosphate buffered saline (PBS) with normal pH (7.2) and physiological osmolality was selected as the eluent. In the control group, a 1:1 mixture of PBS and culture medium was applied. In the extract group, the extract was added in a 1:1 PBS solution with the culture medium. In the direct contact group, PET TMs were placed directly into the culture, with a 1:1 PBS-to-culture medium mixture added. Two methods, described below, were employed to assess cytotoxicity.

#### *Extract Preparation*

Extracts were prepared under conditions of 121 °C and 1 atm for 1 hour. PET TM samples at  $1.6 \pm 0.2$  mg/cm<sup>2</sup> were immersed in sterile phosphate-buffered saline (PBS, pH 7.2; PanEco, Russia). The final material-to-solution ratio was  $1.6 \pm 0.2$  mg/ml.

### Preparation of Test Samples

Metal punches with a diameter of 10 mm and an area of 0.79 cm<sup>2</sup> were used to prepare PET TM samples for direct contact. The material was cut on a silicone substrate and subsequently sterilized in PBS under the specified conditions in a volume of 1 cm<sup>2</sup> per 1 ml of solution.

### Cytotoxicity (Imaging)

Imaging was chosen as the primary method for assessing cytotoxicity, using automated inverted microscopy with photo and video recording under continuous culture conditions (37 °C, 5 % CO<sub>2</sub>, and high humidity). MCF7 and 3T3 cell cultures were seeded into 24-well plates (10,000 cells/cm<sup>2</sup>; well surface area = 2 cm<sup>2</sup>) according to Table 1. After 24 h, the test samples were introduced, and cultivation was continued for an additional 3 days. The criterion for cytotoxicity was a significant difference in confluency (a characteristic of the area occupied by the cell culture during cultivation) at the end of the experiment (a difference of more than 20 % confluency) for samples with a weak cytotoxic effect or a visible change in morphology for samples with a pronounced cytotoxic effect (growth arrest, cell death, balling and detachment).

### Real-Time Cellular Cytotoxicity Assay (RTCA)

The real-time cellular assay (RTCA) is a non-invasive method based on continuous measurement of cellular impedance. This approach employs gold microelectrodes embedded in the bottom of a microtiter plate well to monitor resistance to electron flow in a conductive solution. When adherent cells attach to the electrodes, they impede the flow of current, which is quantified by the dimensionless parameter Cell Index ( $C_i$ ), where  $C_i = (\text{resistance at time } n - \text{resistance in the absence of cells}) / \text{nominal resistance value}$ . An increase in  $C_i$  over time reflects cell proliferation, eventually plateauing at 100 % confluence. Introducing an apoptosis inducer or cytotoxic substance decreases  $C_i$  to zero, reflecting the detachment of cells from the well bottom. Thus, the RTCA method provides quantitative data on cell number, their proliferation, size/shape, and quality of attachment to the substrate;  $C_i$  is a cell index based on the measurement of cellular impedance during cell culture growth, the change in which is interrelated with proliferation, CPE, cytostatic effect or cytotoxicity.

RTCA was chosen as an additional method for determining cytotoxicity. For this purpose, cMSCs were seeded at a density of 10,000 cells/cm<sup>2</sup> (well area 0.32 cm<sup>2</sup>) into 16-well E-plates equipped with gold electrodes to measure the cellular index ( $C_i$ ). After that, the onset of the active growth phase was expected, and materials were added in accordance with Table 2. Cultivation was carried out until a plateau was reached. For the negative control, a 0.2 % SDS solution 1:1 to the culture medium was added to the control well after reaching the plateau. To normalize the effect of the extract or PET TM on  $C_i$ , background subtraction was performed during post-processing of the data, with negative values set to zero.

The criterion for cytotoxicity was a statistically significant difference in the  $k$  coefficient ( $C_i$ , 1/h) for samples with a weak cytotoxic effect, or a low  $C_i$  value after reaching a plateau (<50 % of the maximum) as a result of adding the test substance, for samples with a pronounced cytotoxic effect.

### Statistical Analysis

Data processing was performed in Excel (Microsoft, USA). Statistical analysis was performed in GraphPad Prism version 9.5.1 (USA). To compare the growth rate between groups, a mathematical model of exponential growth with a plateau was applied

$$y = y_m - (y_m - y_0) \times e^{-k \times x},$$

where  $y_m$  is the maximum  $C_i$ ,  $y_0$  is the initial  $C_i$ , and  $k$  is the growth rate of  $C_i$  1/h.

The acceptability of the calculated models was assessed using the  $R^2$  coefficient. Differences in growth rate ( $k$ , 1/h) between the study groups were assessed using the F criterion. The data on the graph are given as the mean  $\pm$  standard deviation (SD). Statistical significance was accepted at  $p < 0.05$ .

## Results and Discussion

### Characteristics of TM Surface Morphology

Porosity and pore diameter were determined from scanning electron microscopy (SEM) micrographs (Fig. 1). The characteristics of TMs are presented in Table 3.

### *Physical Properties of TMs*

In this study, the hydrophobic-hydrophilic and mechanical properties of PET TMs were investigated (Table 4). In addition, based on a comprehensive literature review, values for the zeta potential and surface charge of these membranes are presented. The isoelectric point (pI) of PET TMs generally lies between 3.5 and 4 [49], indicating that under physiological conditions (pH = 7.0), they carry a net negative charge. This is consistent with the findings of Sabbatovskii et al. (2012), who reported that PET TMs with a pore diameter of 25 nm exhibit a zeta potential of approximately  $-27$  mV (pore density  $\sim 2 \times 10^9$  pores/cm<sup>2</sup>, measured in 0.25 M KCl solution). Furthermore, the same study demonstrated that membranes with pore diameters ranging from 13 to 80 nm consistently possess a negative surface charge, with surface charge density ( $\sigma$ ) values on the order of  $(1-100) \times 10^4$  C/m<sup>2</sup> under varying electrolyte concentrations [50]. The observed negative values of zeta potential and surface charge have been attributed to the presence of carboxyl functional groups on the membrane surface [51]. Importantly, the magnitude of the surface zeta potential, and thus the surface charge density of PET TMs, can be strongly influenced by parameters such as membrane pore size, the pH of the surrounding medium, and ionic strength of the solution [52, 53]. Taken together, the negative zeta potential and associated surface charge characteristics facilitate favorable electrostatic interactions between PET TM surfaces and cellular membranes, thereby promoting enhanced cell adhesion on the PET TM substrate [54, 55].

The contact angle was found to range from  $67^\circ$  to  $75^\circ$ , indicating that PET TMs possess moderately hydrophilic properties. This degree of wettability is considered optimal for efficient cell adhesion to the polymer surface, as demonstrated for mouse fibroblast cell lines [56] and HUVEC cells [57]. Such wettability provides a balance between adhesive and repulsive interfacial forces, thereby enhancing cellular attachment. Moreover, a surface contact angle of approximately  $70^\circ$  was reported to promote increased migration of HUVECs [57]. Similarly, Margel et al. (1993) demonstrated using canine endothelial cells that contact angle values within this range correspond to high levels of adhesion and proliferative activity [58].

Substrates with varying mechanical properties are used for culturing different cell lines [59]. In this study, the Young's modulus of the PET TMs was determined to be  $2871 \pm 157$  MPa. Materials with stiffness comparable to that of TM ( $\sim 3$  GPa) used in the present study have been previously employed to investigate the behavior of vascular smooth muscle cells, endothelial cells, and chondrogenic cells, demonstrating the relevance of high-stiffness substrates in modulating cellular responses [60–62].

Therefore, PET TMs physical properties enable its effective application in cell biology research and tissue engineering by providing optimal conditions for cell adhesion, migration, and proliferation.

### *Sterilization of PET TM*

After autoclaving at  $121^\circ\text{C}$  for 1 h, PET TMs showed no visible changes in shape, remained intact, and retained their transparency. These observations confirm the suitability of this sterilization method for subsequent sample preparation.

### *Cytotoxicity*

Culturing MCF7 and 3T3 cells with the extracts of the tested samples, as well as under direct contact conditions, revealed no effect on the growth rate of the cell cultures (Fig. 2 a, b). MCF7 cells exposed to both extract and direct contact retained their cuboidal, epithelial-like morphology. The samples did not affect cell proliferation, and no differences in confluence were observed at the end of the experiment. Thus, no cytotoxic effect on MCF7 cells was detected. Similarly, 3T3 cells maintained their elongated, fibroblast-like morphology under both conditions. The samples did not affect proliferation, and no cytotoxic effect on 3T3 cells was detected.

The RTCA method and measurement of the cellular index  $C_i$  on the culture of cMSC cells also showed no significant effect on the rate of cell proliferation (Table 5, Fig. 3 a, b). For comparison, to induce a pronounced cytotoxic response, sodium dodecyl sulfate (SDS) was added to the control group 164 h after the start of cultivation. This treatment, which disrupts cell membranes, causes detachment from the culture surface, and releases cellular proteins, DNA, lipids, and other components into the medium, led to a sharp decline in  $C_i$ .

It was noted that the studied samples slightly reduced the maximum value of the cellular index  $C_i$ . The growth rate of  $C_i$  in the groups (coefficient  $k$ ) of extract, direct contact, and control was 0.01531, 0.01568, and 0.01877 per hour, respectively. There was no statistically significant difference in the coefficient  $k$  between the groups ( $p$  value = 0.138).

Table 1

## Scheme for adding samples and cell cultures to a 24-well plate

	1	2	3	4	5	6
A	–	–	MCF7, Extract 1:1	MCF7, Direct contact	3T3, Extract 1:1	3T3, Direct contact
B	–	–	MCF7, Extract 1:1	MCF7, Direct contact	3T3, Extract 1:1	3T3, Direct contact
C	–	–	MCF7, Extract 1:1	MCF7, Direct contact	3T3, Extract 1:1	3T3, Direct contact
D	–	–	MCF7, Control	MCF7, Control	3T3, Control	3T3, Control

Table 2

## Scheme of adding samples and cell cultures to a 16-well e-plate

No.	1	2
A	MSC, Extract 1:1	MSC, Extract 1:1
B	MSC, Extract 1:1	MSC, Extract 1:1
C	MSC, Extract 1:1	MSC, Direct contact
D	MSC, Direct contact	MSC, Direct contact
E	MSC, Direct contact	MSC, Direct contact
F	MSC, Control	MSC, Control
G	MSC, Control	Direct contact
H	Extract 1:1	PBS

Table 3

## Characteristics of TM obtained by SEM

PET TM	Thickness, $\mu\text{m}$	Pore density, $\text{cm}^{-2}$	Pore diameter, nm	Porosity, %
	$10.8 \pm 0.3$	$(8 \pm 0.7) \times 10^9$	$25 \pm 5$	$3.68 \pm 0.21$

Table 4

## Physical properties of PET TM

Parameter	Young's modulus, $E$ (MPa)	Ultimate strength, $\sigma_B$ (MPa)	Contact angle, $\theta^\circ$ (side A/ side B)
Value	$2871 \pm 157$	$71 \pm 5$	$67.31 \pm 1.97 / 75.02 \pm 1.40$

Table 5

Results of mathematical modeling of rabbit MSC cell culture growth ( $C_i$ )

Parameters	Extract 1:1	Direct contact	Control	$p$ value, (F [DFn, DFd])
$k$ (1/h)	$0.015 \pm 0.003$	$0.016 \pm 0.002$	$0.019 \pm 0.002$	0.138 (1.986 [2, 693])
$R^2$	0.89	0.96	0.97	

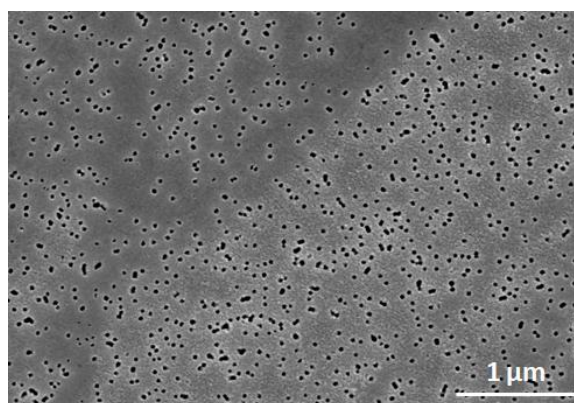


Figure 1. SEM micrographs of the PET TM surface



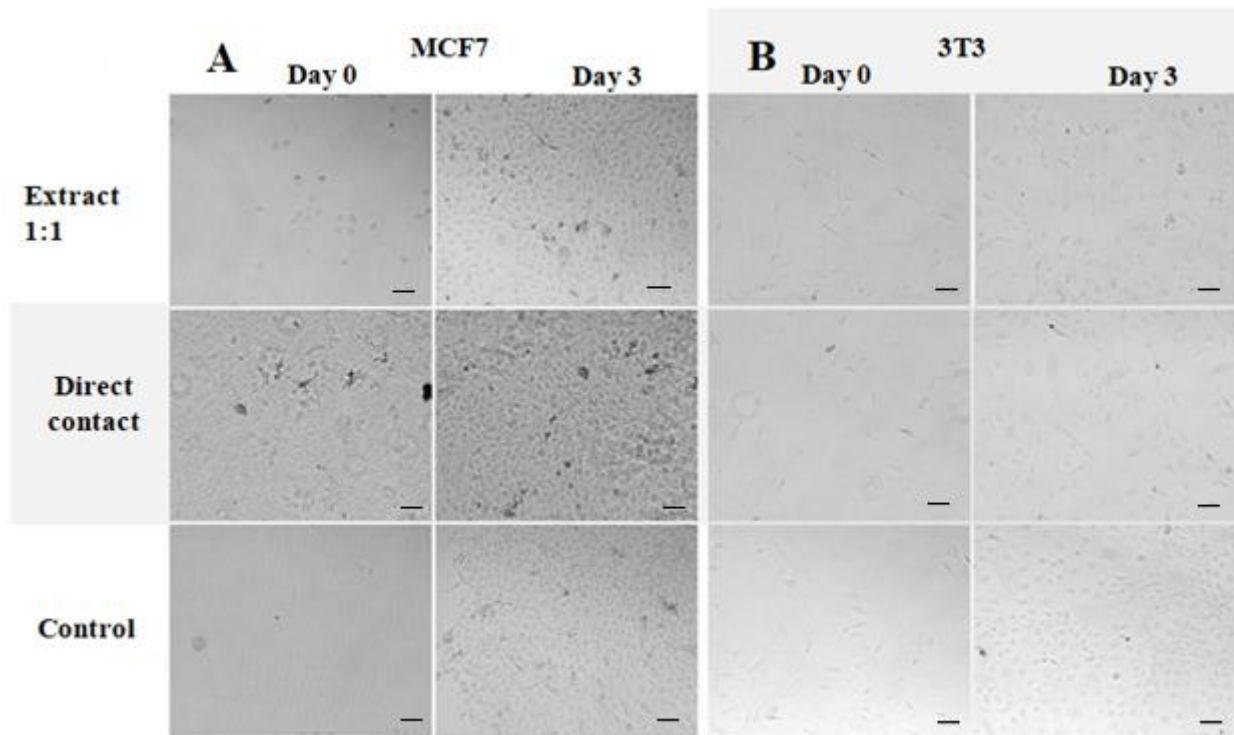


Figure 2. (a) — Effect of the extract and direct contact on the growth of the MCF7 cell culture compared to the control group during interaction with the test substance for 5 days; (b) — Effect of the extract and direct contact on the growth of the 3T3 cell culture compared to the control group during interaction with the test substance for 5 days; Objective 10× (Ph), timelapse 78 hours, shooting interval 40 minutes. Scale bar: 50 μm

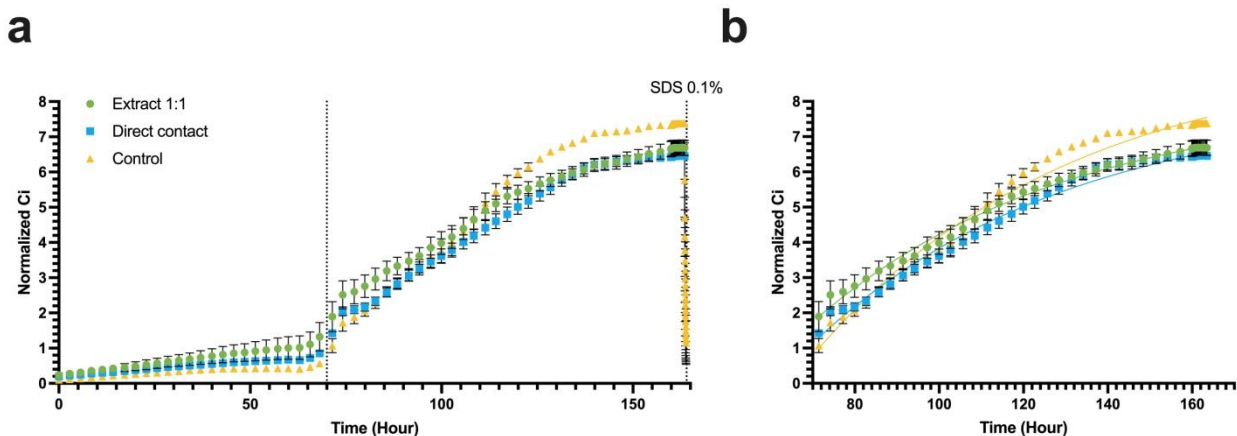


Figure 3. (a) — A growth rate of rabbit MSC cell culture, the dependence of  $C_i$  on time; (b) — interval 70–164 hours selected for subsequent statistical analysis, point 70 hours is taken as 0; data are presented as mean  $\pm$  SD

### Conclusions

The cytotoxicity of PET TM was assessed using two methods on three cell cultures (the epithelial line MCF7, the 3T3 fibroblast-like line, and primary rabbit MSC BM culture) in accordance with the Interstate standard ISO 10993-5-2011, IDT, medical devices. Evaluation of the biological effect of medical devices, Part 5, cytotoxicity studies: *in vitro* methods. The results demonstrated that PET TM samples did not affect cell cultures, the proliferation rate and cell morphology. The cytotoxicity assessment confirmed that PET TM samples are non-cytotoxic. Based on these findings, PET TMs can be recommended for further biomedical research, including their application in tissue-engineered constructs and for the encapsulation of cellular preparations intended for long-term therapeutic use.

### *Funding*

This research was funded by JINR Project No. 07-5-131-2-2024/2028.

### *Author Information\**

*\*The authors' names are presented in the following order: First Name, Middle Name and Last Name*

**Maksim Vitalievich Balyasin** — Junior Researcher, Peoples' Friendship University of Russia named after Patrice Lumumba, Miklukho-Maklaya Street, 6, 117198, Moscow, Russia; e-mail: [b.maxim4432@yandex.ru](mailto:b.maxim4432@yandex.ru); <https://orcid.org/0000-0002-3097-344X>

**Genrikh Vladimirovich Serpionov** (*corresponding author*) — Candidate of Biological Sciences, Researcher, Joint Institute for Nuclear Research (JINR), Joliot-Curie Street, 6, Dubna, Moscow Region, 141980, Russia; e-mail: [genrihserpionov@gmail.com](mailto:genrihserpionov@gmail.com); <https://orcid.org/0009-0001-4545-8811>

**Mikhail Evgenievich Krashennnikov** — Candidate of Biological Sciences, Leading Researcher, Peoples' Friendship University of Russia named after Patrice Lumumba, Miklukho-Maklaya Street, 6, 117198, Moscow, Russia; e-mail: [krashen@rambler.ru](mailto:krashen@rambler.ru); <https://orcid.org/0000-0002-3574-4013>

**Alexey Valerievich Lyundup** — Candidate of Medical Sciences, Director of the Research and Educational Center "Cell Technologies", Peoples' Friendship University of Russia named after Patrice Lumumba, Miklukho-Maklaya Street, 6, Moscow, 117198, Russia; e-mail: [lyundup2020@gmail.com](mailto:lyundup2020@gmail.com); <https://orcid.org/0000-0002-0102-5491>

**Alexander Nikolaevich Nechaev** — Candidate of Chemical Sciences, Deputy Director for Science, Centre of Applied Physics, Joint Institute for Nuclear Research (JINR), Joliot-Curie Street, 6, 141980, Dubna, Moscow Region, Russia; e-mail: [nechaeffalexander@yandex.ru](mailto:nechaeffalexander@yandex.ru); <https://orcid.org/0000-0002-5138-4265>

### *Author Contributions*

The manuscript was prepared with contributions from all authors, and all authors have approved the final version for submission. **CRedit**: **Maksim Vitalievich Balyasin** data curation, investigation, conducting biological experiments, methodology, validation, visualization, writing-review & editing; **Genrikh Vladimirovich Serpionov** data curation, investigation, characterization of physical properties of TMs, methodology, validation, visualization, writing-review & editing; **Mikhail Evgenievich Krashennnikov** investigation, methodology, validation, formal analysis, supervision, validation, writing-review & editing; **Alexey Valerievich Lyundup**, **Alexander Nikolaevich Nechaev** conceptualization, writing-review & editing, funding acquisition, resources, supervision, validation, writing-review & editing.

### *Acknowledgments*

The authors sincerely thank Pavel Apel for his valuable and precise feedback during the manuscript preparation, Oleg Orelovich for supplying the electron micrographs, and Maria Kuvaytseva for her assistance with the contact angle measurements.

### *Conflicts of Interest*

The authors declare no conflict of interest.

### *References*

- 1 Apel, P. (2001). Track etching technique in membrane technology. *Radiation Measurements*, 34(5), 559–566. [https://doi.org/10.1016/S1350-4487\(01\)00228-1](https://doi.org/10.1016/S1350-4487(01)00228-1)
- 2 Dolfus, C., Piton, N., Toure, E., & Sabourin, J. C. (2015). Circulating tumor cell isolation: The assets of filtration methods with polycarbonate track-etched filters. *Chinese Journal of Cancer Research*, 27(5), 479–487. <https://doi.org/10.3978/j.issn.1000-9604.2015.09.01>
- 3 Kaya, D., & Keçeci, K. (2020). Review—Track-Etched Nanoporous Polymer Membranes as Sensors: A Review. *Journal of The Electrochemical Society*, 167(3), 037543. <https://doi.org/10.1149/1945-7111/ab67a7>
- 4 Mizuguchi, H., Sasaki, K., Ichinose, H., Seino, S., Sakurai, J., Iiyama, M., Kijima, T., Tachibana, K., Nishina, T., Takayanagi, T., & Shida, J. (2017). A triple-electrode based dual-biosensor system utilizing track-etched microporous membrane elec-

trodes for the simultaneous determination of l-lactate and d-glucose. *Bulletin of the Chemical Society of Japan*, 90(11), 1211–1216. <https://doi.org/10.1246/bcsj.20170193>

5 Torati, S. R., Reddy, V., Yoon, S. S., & Kim, C. (2016). Electrochemical biosensor for Mycobacterium tuberculosis DNA detection based on gold nanotubes array electrode platform. *Biosensors and Bioelectronics*, 78, 483–488. <https://doi.org/10.1016/j.bios.2015.11.098>

6 Barashkova, P. S., Molodkina, L. M., & Korovina, M. D. (2017). Both sided irradiated track membrane in local water supply. *Magazine of Civil Engineering*, 71(3), 68–75. <https://doi.org/10.18720/MCE.71.8>

7 Russakova, A. V., Altynbaeva, L. Sh., Barsbay, M., Zheltov, D. A., Zdorovets, M. V., & Mashentseva, A. A. (2021). Kinetic and isotherm study of As(III) removal from aqueous solution by PET track-etched membranes loaded with copper microtubes. *Membranes*, 11(2), 116. <https://doi.org/10.3390/membranes11020116>

8 Novo, P., Dell'Aica, M., Jender, M., Höving, S., Zahedi, R. P., & Janasek, D. (2017). Integration of polycarbonate membranes in microfluidic free-flow electrophoresis. *Analyst*, 142(22), 4228–4239. <https://doi.org/10.1039/C7AN01514C>

9 Friedman, L. I., Hardwick, R. A., Daniels, J. R., Stromberg, R. R., & Ciarkowski, A. A. (1983). Evaluation of Membranes for Plasmapheresis. *Artificial Organs*, 7(4), 435–442. <https://doi.org/10.1111/j.1525-1594.1983.tb04223.x>

10 Wright, C. W., Li, N., Shaffer, L., Fowler, S. C., Howell, K. L., Kumar, G., Nelson, E., Seddon, J. M., & George, M. (2023). Establishment of a 96-well transwell system using primary human gut organoids to capture multiple quantitative pathway readouts. *Scientific Reports*, 13, 16357. <https://doi.org/10.1038/s41598-023-43656-z>

11 Yamashita, T., Inui, T., Yokota, J., Kawakami, K., Morinaga, G., Takatani, M., Kishimoto, W., Tomita, J., & Mizuguchi, H. (2021). Monolayer platform using human biopsy-derived duodenal organoids for pharmaceutical research. *Molecular Therapy — Methods & Clinical Development*, 22, 263–278. <https://doi.org/10.1016/j.omtm.2021.05.005>

12 George, J. H., Nagel, D., Waller, S., Hill, E. J., Parri, H. R., Coleman, M. D., Cui, Z., & Ye, H. (2018). A closer look at neuron interaction with track-etched microporous membranes. *Scientific Reports*, 8, Article 15552. <https://doi.org/10.1038/s41598-018-33710-6>

13 Ippolitov, D., Arreza, L., Munir, M. N., & Hombach-Klonisch, S. (2022). Brain Microvascular Pericytes—More Than By-standers in Breast Cancer Brain Metastasis. In *Cells*, 11(8), 1263. <https://doi.org/10.3390/cells11081263>

14 Kumar, R., Harris-Hooker, S., Kumar, R., & Sanford, G. (2011). Co-culture of retinal and endothelial cells results in the modulation of genes critical to retinal neovascularization. *Vascular Cell*, 3, 27. <https://doi.org/10.1186/2045-824X-3-27>

15 Lu, Y., Ma, J., & Lin, G. (2019). Development of a two-layer transwell co-culture model for the in vitro investigation of pyrrolizidine alkaloid-induced hepatic sinusoidal damage. *Food and Chemical Toxicology*, 129, 391–398. <https://doi.org/10.1016/j.fct.2019.04.057>

16 Nishi, M., Tateishi, K., Sundararaj, J. S., Ino, Y., Nakai, Y., Hatayama, Y., Yamaoka, Y., Mihana, Y., Miyakawa, K., Kimura, H., Kimura, Y., Yamamoto, T., & Ryo, A. (2023). Development of a contacting transwell co-culture system for the in vitro propagation of primary central nervous system lymphoma. *Frontiers in Cell and Developmental Biology*, 11. <https://doi.org/10.3389/fcell.2023.1275519>

17 Haynes, J., Palaniappan, B., Tsopmegha, E., & Sundaram, U. (2022). Regulation of nutrient and electrolyte absorption in human organoid-derived intestinal epithelial cell monolayers. *Translational Research*, 248, 22–35. <https://doi.org/10.1016/j.trsl.2022.04.008>

18 Dokladny, K., In, J. G., Kaper, J., & Kovbasnjuk, O. (2021). Human epithelial stem cell-derived colonoid monolayers as a model to study shiga toxin-producing Escherichia coli–host interactions. *Methods in Molecular Biology*, 2291, 285–296. [https://doi.org/10.1007/978-1-0716-1339-9\\_13](https://doi.org/10.1007/978-1-0716-1339-9_13)

19 Kozuka, K., He, Y., Koo-McCoy, S., Kumaraswamy, P., Nie, B., Shaw, K., Chan, P., Leadbetter, M., He, L., Lewis, J. G., Zhong, Z., Charmot, D., Balaa, M., King, A. J., Caldwell, J. S., & Siegel, M. (2017). Development and Characterization of a Human and Mouse Intestinal Epithelial Cell Monolayer Platform. *Stem cell reports*, 9(6), 1976–1990. <https://doi.org/10.1016/j.stemcr.2017.10.013>

20 Bhatt, A. P., Gunasekara, D. B., Speer, J., Reed, M. I., Peña, A. N., Midkiff, B. R., Magness, S. T., Bultman, S. J., Allbritton, N. L., & Redinbo, M. R. (2018). Nonsteroidal Anti-Inflammatory Drug-Induced Leaky Gut Modeled Using Polarized Monolayers of Primary Human Intestinal Epithelial Cells. *ACS infectious diseases*, 4(1), 46–52. <https://doi.org/10.1021/acsinfecdis.7b00139>

21 Lyck, R., Enzmann, G., Lécuyer, M. A., Abadier, M., Bradfield, P. F., Biechele, T., Wegner, A., Rüegg, S., Shimshek, D. R., Herich, L. C., Merz, P. A., Engelhardt, B., & Weksler, B. (2016). ALCAM (CD166) is involved in extravasation of monocytes rather than T cells across the blood–brain barrier. *Journal of Cerebral Blood Flow & Metabolism*, 37(8), 2894–2909. <https://doi.org/10.1177/0271678x16678639>

22 Wimmer, I., Tietz, S., Nishihara, H., Deutsch, U., Sallusto, F., Gosselet, F., Lyck, R., Muller, W. A., Lassmann, H., Engelhardt, B. (2019). PECAM-1 stabilizes blood-brain barrier integrity and favors paracellular T-cell diapedesis across the blood-brain barrier during neuroinflammation. *Front. Immunol.*, 10, 711. <https://doi.org/10.3389/fimmu.2019.00711>

23 Wilhelm, I., & Krizbai, I. A. (2014). In vitro models of the blood–brain barrier for the study of drug delivery to the brain. *Molecular Pharmaceutics*, 11(7), 1949–1963. <https://doi.org/10.1021/mp500046f>

24 Wong, A. D., Ye, M., Levy, A. F., Rothstein, J. D., Bergles, D. E., & Searson, P. C. (2013). The blood–brain barrier: an engineering perspective. *Frontiers in Neuroengineering*, 6, 7. <https://doi.org/10.3389/fneng.2013.00007>

25 Li, H.-X., Sun, X.-Y., Yang, S.-M., Wang, Q., & Wang, Z.-Y. (2018). Peroxiredoxin 1 promoted tumor metastasis and angiogenesis in colorectal cancer. *Pathology Research and Practice*, 214(5), 655–660. <https://doi.org/10.1016/j.prp.2018.03.026>

- 26 Zhao, J., Ma, X., & Xu, H. (2022). miR-29b-3p inhibits 22Rv1 prostate cancer cell proliferation through the YWHA/BCL-2 regulatory axis. *Oncology Letters*, 24(2), 289. <https://doi.org/10.3892/ol.2022.13409>
- 27 Wei, Y., Wang, Y., Zang, A., Shang, Y., Song, Z., Wang, Z., Wang, Y., & Yang, H. (2018). Inducible T-cell co-stimulators regulate the proliferation and invasion of human hepatocellular carcinoma HepG2 cells. *Biological research*, 51(1), 2. <https://doi.org/10.1186/s40659-017-0150-7>
- 28 Pang, J., Li, G., Qian, H., Wu, Y., & Chen, Y. (2022). Secretory type II cGMP-dependent protein kinase blocks activation of PDGFR $\beta$  via Ser254 in gastric cancer cells. *Cell biology international*, 46(5), 747–754. <https://doi.org/10.1002/cbin.1176629>
- 29 Jeon, J. H., Kim, D. K., Shin, Y., Kim, H. Y., Song, B., Lee, E. Y., & Kim, J. K. (2016). Migration and invasion of drug-resistant lung adenocarcinoma cells are dependent on mitochondrial activity. *Experimental & Molecular Medicine*, 48, e277. <https://doi.org/10.1038/emmm.2016.129>
- 30 Wasielewska, J. M., Chaves, J. C. S., Johnston, R. L., Milton, L. A., Hernández, D., Chen, L., Song, J., Lee, W., Leinenga, G., Nisbet, R. M., Pébay, A., Götz, J., White, A. R., & Oikari, L. E. (2022). A sporadic Alzheimer's blood-brain barrier model for developing ultrasound-mediated delivery of Aducanumab and anti-Tau antibodies. *Theranostics*, 12(16), 6826–6847. <https://doi.org/10.7150/thno.72685>
- 31 Varshavskaya, K. B., Petrushanko, I. Y., Mitkevich, V. A., Barykin, E.P., Makarov, A. A. (2024). Post-translational modifications of beta-amyloid alter its transport in the blood–brain barrier in vitro model. *Frontiers in Molecular Neuroscience*, 17, 1362581. <https://doi.org/10.3389/fnmol.2024.1362581>
- 32 Guo, B. B., Bellingham, S. A., & Hill, A. F. (2016). Stimulating the release of exosomes increases the intercellular transfer of prions. *Journal of Biological Chemistry*, 291(10). <https://doi.org/10.1074/jbc.M115.684258>
- 33 Rodrigues, P.V., de Godoy, J.V.P., Bosque, B.P., Carvalho, H.F. & Castro-Fonseca, M. (2022). Transcellular propagation of fibrillar  $\alpha$ -synuclein from enteroendocrine to neuronal cells requires cell-to-cell contact and is Rab35-dependent. *Scientific Reports*, 12, 4168. <https://doi.org/10.1038/s41598-022-08076-5>
- 34 Hartmann, E. S., Schluessel, S., Köhler, M. I., Beck, F., Redeker, J. I., Summer, B., Schönlitzer, V., Fottner, A., & Mayer-Wagner, S. (2020). Fibroblast-like cells change gene expression of bone remodelling markers in transwell cultures. *European Journal of Medical Research*, 25(1), 52. <https://doi.org/10.1186/s40001-020-00453-y>
- 35 Juste-Lanas, Y., Díaz-Valdivia, N., Llorente, A., Ikemori, R. & Alcaraz, J. (2023). 3D collagen migration patterns reveal a SMAD3-dependent and TGF- $\beta$ 1-independent mechanism of recruitment for tumour-associated fibroblasts in lung adenocarcinoma. *British Journal of Cancer*, 128(6), 967–981. <https://doi.org/10.1038/s41416-022-02093-x>
- 36 Bhatia, S. N., & Ingber, D. E. (2014). Microfluidic organs-on-chips. *Nature Biotechnology*, 32(8), 760–772. <https://doi.org/10.1038/nbt.2989>
- 37 Shimasaki, T., Yamamoto, S., Omura, R., & Takahiro Ochiya, T. (2021). Novel platform for regulation of extracellular vesicles and metabolites secretion from cells using a multi-linkable horizontal co-culture plate. *Micromachines*, 12(11), 1431. <https://doi.org/10.3390/mi12111431>
- 38 Henry, O. Y. F., Villenave, R., Crouce, M. J., Leineweber, W. D., Benz, M. A., & Ingber, D. E. (2017). Organs-on-chips with integrated electrodes for trans-epithelial electrical resistance (TEER) measurements of human epithelial barrier function. *Lab on a Chip*, 17(13), 2264–2271. <https://doi.org/10.1039/c7lc00155j>
- 39 Srinivasan, B., Kolli, A. R., Esch, M. B., Abaci, H. E., Shuler, M. L., & Hickman, J. J. (2015). TEER measurement techniques for in vitro barrier model systems. *Journal of laboratory automation*, 20(2), 107–126. <https://doi.org/10.1177/2211068214561025>
- 40 Ahmed Al-Tameemi, Z. K., Khanam, R., & Shetty, P. (2024). Bisphenol-A Leaching from Polycarbonate 5-Gallon Water Bottles in the UAE: A Comprehensive Study. *Nepal Journal of Epidemiology*, 14(1), 1301–1309. <https://doi.org/10.3126/nje.v14i1.59934>
- 41 Le, H. H., Carlson, E. M., Chua, J. P., & Belcher, S. M. (2008). Bisphenol A is released from polycarbonate drinking bottles and mimics the neurotoxic actions of estrogen in developing cerebellar neurons. *Toxicology letters*, 176(2), 149–156. <https://doi.org/10.1016/j.toxlet.2007.11.001>
- 42 Hoekstra, E. J., & Simoneau, C. (2013). Release of bisphenol A from polycarbonate: a review. *Critical reviews in food science and nutrition*, 53(4), 386–402. <https://doi.org/10.1080/10408398.2010.536919>
- 43 Wang, T., Han, J., Duan, X., Xiong, B., Cui, X. S., Kim, N. H., Liu, H. L., & Sun, S. C. (2016). The toxic effects and possible mechanisms of Bisphenol A on oocyte maturation of porcine in vitro. *Oncotarget*, 7(22), 32554–32565. <https://doi.org/10.18632/oncotarget.8689>
- 44 Cimmino, I., Fiory, F., Perruolo, G., Miele, C., Beguinot, F., Formisano, P., & Oriente, F. (2020). Potential Mechanisms of Bisphenol A (BPA) Contributing to Human Disease. *International journal of molecular sciences*, 21(16), 5761. <https://doi.org/10.3390/ijms21165761>
- 45 Li, T., Bian, B., Ji, R., Zhu, X., Wo, X., Song, Q., Li, Z., Wang, F., & Jia, Y. (2024). Polyethylene Terephthalate Microplastic Exposure Induced Reproductive Toxicity Through Oxidative Stress and p38 Signaling Pathway Activation in Male Mice. *Toxics*, 12(11), 779. <https://doi.org/10.3390/toxics12110779>
- 46 Zhang, H., Zhang, S., Duan, Z., & Wang, L. (2022). Pulmonary toxicology assessment of polyethylene terephthalate nanoplastic particles in vitro. *Environment international*, 162, 107177. <https://doi.org/10.1016/j.envint.2022.107177>
- 47 Apel, P., Bondarenko, M., Yamauchi, Y., & Yaroshchuk, A. (2021). Osmotic Pressure and Diffusion of Ions in Charged Nanopores. *Langmuir*, 37(48), 14089–14095. <https://doi.org/10.1021/acs.langmuir.1c02267>



- 48 International Organization for Standardization. (2011). ISO 10993-5:2011 IDT, medical devices. Evaluation of the biological effect of medical devices, Part 5, Cytotoxicity studies: in vitro methods.
- 49 Apel, P. Y., Velizarov, S., Volkov, A. V., Eliseeva, T. V., Nikonenko, V. V., Parshina, A. V., & Yaroslavl'tsev, A. B. (2022). Fouling and Membrane Degradation in Electromembrane and Baromembrane Processes. *Membranes and Membrane Technologies*, 4(2), 69–92. <https://doi.org/10.1134/S2517751622020032>
- 50 Sabbatovskii, K. G., Vilenskii, A. I., Sobolev, V. D., Kochnev, Y. K., & Mchedlishvili, B. V. (2012). Electrosurface and structural properties of poly(ethylene terephthalate) track membranes. *Colloid Journal*, 74(3), 328–333. <https://doi.org/10.1134/S1061933X12010139>
- 51 Apel, P. Y. (2013). *Track-etching. Encyclopedia of membrane science and technology*. Wiley. <https://doi.org/10.1002/9781118522318.emst040>
- 52 Lettmann, C., Mo E'ckel, D., & Staude, E. (1999). Permeation and tangential flow streaming potential measurements for electrokinetic characterization of track-etched microfiltration membranes. *Journal of Membrane Science*, 159, 243–251. [https://doi.org/10.1016/S0376-7388\(99\)00067-8](https://doi.org/10.1016/S0376-7388(99)00067-8)
- 53 D'ejardin, P., Vasina, E. N., Berezkin, V. V., Sobolev, V. D., & Volkov, V. I. (2005). Streaming potential in cylindrical pores of poly(ethylene terephthalate) track-etched membranes: Variation of apparent  $\zeta$  potential with pore radius. *Langmuir*, 21(10), 4680–4685. <https://doi.org/10.1021/la046913e>
- 54 Chang, H. Y., Huang, C. C., Lin, K. Y., Kao, W. L., Liao, H. Y., You, Y. W., Lin, J. H., Kuo, Y. T., Kuo, D. Y., & Shyue, J. J. (2014). Effect of surface potential on NIH3T3 cell adhesion and proliferation. *Journal of Physical Chemistry C*, 118(26), 14464–14470. <https://doi.org/10.1021/jp504662c>
- 55 Chang, H. Y., Kao, W. L., You, Y. W., Chu, Y. H., Chu, K. J., Chen, P. J., Wu, C. Y., Lee, Y. H., & Shyue, J. J. (2016). Effect of surface potential on epithelial cell adhesion, proliferation and morphology. *Colloids and Surfaces B: Biointerfaces*, 141, 179–186. <https://doi.org/10.1016/j.colsurfb.2016.01.049>
- 56 Tamada, Y., Ikada, Y. (1993). Cell adhesion to plasma-treated polymer surfaces. *Polymer*, 34(10), 2208–2212.
- 57 Qiu, L., Hughes-Brittain, N., Bastiaansen, C., Peijs, T., & Wang, W. (2016). Responses of Vascular Endothelial Cells to Photoembossed Topographies on Poly(Methyl Methacrylate) Films. *Journal of Functional Biomaterials*, 7(4), 33. <https://doi.org/10.3390/jfb7040033>
- 58 Margel, S., Vogler, E. A., Firment, L., Watt, T., Haynie, S., & Sogah, D. Y. (1993). Peptide, protein, and cellular interactions with self-assembled monolayer model surfaces. *Journal of Biomedical Materials Research*, 27(12), 1463–1476. Portico. <https://doi.org/10.1002/jbm.820271202>
- 59 Rahmati, M., Silva, E. A., Reseland, J. E., A. Heyward, C., & Haugen, H. J. (2020). Biological responses to physicochemical properties of biomaterial surface. *Chemical Society Reviews*, 49(15), 5178–5224. <https://doi.org/10.1039/d0cs00103a>
- 60 Yi, B., Shen, Y., Tang, H., Wang, X., & Zhang, Y. (2020). Stiffness of the aligned fibers affects structural and functional integrity of the oriented endothelial cells. *Acta biomaterialia*, 108, 237–249. <https://doi.org/10.1016/j.actbio.2020.03.022>
- 61 Yi, B., Shen, Y., Tang, H., Wang, X., Li, B., & Zhang, Y. (2019). Stiffness of Aligned Fibers Regulates the Phenotypic Expression of Vascular Smooth Muscle Cells. *ACS applied materials & interfaces*, 11(7), 6867–6880. <https://doi.org/10.1021/acsami.9b00293>
- 62 Ghosh, S., Laha, M., Mondal, S., Sengupta, S., & Kaplan, D. L. (2009). In vitro model of mesenchymal condensation during chondrogenic development. *Biomaterials*, 30(33), 6530–6540. <https://doi.org/10.1016/j.biomaterials.2009.08.019>



Sergey A. Bedin<sup>1\*</sup> , Elizaveta P. Kozhina<sup>1</sup> , Ilya M. Doludenko<sup>2</sup> , Vladimir P. Drachev<sup>1</sup> 

<sup>1</sup>Skolkovo Institute of Science and Technology (Skoltech), Moscow, Russia;

<sup>2</sup>A.V. Shubnikov Institute of Crystallography of the Kurchatov Complex Crystallography and Photonics of the NRC "Kurchatov Institute", Moscow, Russia

(\*Corresponding author's e-mail: [bserg5@gmail.com](mailto:bserg5@gmail.com))

## Track-Etched Membranes for Gold Nanowire SERS Substrates

In this study, a novel and reliable method for the production of bimetallic Ni–Au segmented nanowires by template-assisted electrochemical deposition was developed. Track-etched membranes were used as templates for the synthesis of gold nanowires with a diameter of about 100 nm by electrochemical deposition. To enhance structural stability, a modified approach was proposed, wherein gold nanowires were grown on nickel nanowire cores instead of being deposited directly onto the copper layer, as is commonly practiced. The morphology and composition of the resulting nanostructures were characterized by scanning electron microscopy (SEM) combined with energy-dispersive X-ray analysis (EDX). Elemental mapping analysis was performed to visualize the spatial distribution of constituent metals within the nanowires, revealing a well-defined segmented architecture: copper was localized at the base, nickel occupied the central region, and gold was selectively deposited on the top surface. The Surface-Enhanced Raman Scattering (SERS) activity of the substrates was evaluated using Rhodamine 6G at the concentration of  $10^{-4}$  M, confirming their effectiveness for signal enhancement. The developed approach allows precise control of the nanostructures morphology and composition by separating the deposition stages for nickel and gold segments. By eliminating direct contact between gold and copper layers, this strategy effectively suppresses intermetallic diffusion, thereby enhancing the structural stability of the resulting bimetallic nanowires.

**Keywords:** track-etched membrane, template synthesis, gold nanowires, copper layer, SERS substrates, electrochemical deposition, nanostructures, signal enhancement, intermetallic diffusion

### Introduction

Development of stable and reproducible SERS substrates is critical for rapid and reliable detection of organic compounds in field conditions [1]. While silver-based substrates provide higher signal enhancement due to superior plasmonic response in the visible region, gold substrates are preferred for practical applications due to their better chemical stability and biocompatibility [2]. Au inertness under ambient conditions prevents oxidation and sulfidation. That preserves its surface integrity and plasmonic properties over time, thereby ensuring consistent SERS performance and signal reproducibility.

Conventional methods of SERS substrates fabrication include chemical reduction and physical deposition techniques, which are commonly employed due to their simplicity and scalability [3]. However, these methods often lack precise control over the size, shape, and spatial distribution of gold nanostructures, leading to inhomogeneous surface morphologies and inconsistent signal enhancement across the substrate. To address these limitations and enable the development of reproducible and reliable SERS platforms, template-assisted synthesis in porous materials has emerged as a promising approach. Specifically, porous alumina oxide and track-etched membranes allow a controlled fabrication of ordered gold nanowire arrays with well-defined dimensions and improved uniformity of a SERS signal [4–6].

Due to the optical transparency of anodic aluminum oxide (AAO) in the visible spectral range it serves as a suitable template for the direct fabrication and in situ characterization of gold nanostructures. Study [4] demonstrates that variations in the size and aspect ratio of gold nanoparticles synthesized within AAO pores result in a pronounced color shift of the template, attributed to the localized surface plasmon resonance. Furthermore, research [5] reported the emergence of a magneto-optical effect in hybrid gold–nickel nanostructures, suggesting their potential for applications in optoelectronic and spintronic devices.

In comparison to AAO, polymer track-etched membranes fabricated via ion-track technology offer greater versatility and control over pore morphology. These polymer membranes allow precise tailoring of the pore geometry, including cylindrical, conical, and other predefined shapes [7, 8]. Moreover, this method enables forming a calibrated metallic nanostructure array, including multi-material and composite ones [9].

An additional advantage is the ability to fabricate three-dimensional nanowire networks, which can be integrated as polymer-based composites [10] or employed as self-supporting porous metallic meshes [6, 11]. Such a structural flexibility makes track-etched membranes a promising platform for the development of reproducible and functionally tailored SERS substrates.

Several studies have reported the fabrication of gold nanostructures as SERS-active substrates using track-etched membranes as templates [12, 13]. However, a key limitation of such approaches lies in the usage of copper as a conductive base layer which is unsuitable for direct gold electrodeposition due to the interdiffusion between the two metals, leading to structural and chemical instability [14, 15].

A method for fabricating hollow conical gold nanostructures was demonstrated, exhibiting strong SERS performance with detection of Rhodamine 6G at concentrations as low as  $10^{-8}$  M [16]. But, a long-term stability of the resulting substrates was compromised by the choice of copper as a base material, which facilitates interfacial diffusion and degradation over time.

To address this issue, alternative strategies have been proposed. One common solution involves a deposition of a thin metallic coating, not copper, onto the polymer template prior to the electrochemical growth. In [17], electrodeposition from sulfide-based electrolytes was shown to yield predominantly polycrystalline gold nanoparticles, whereas cyanide-based electrolytes favored the formation of (110)-textured monocrystalline structures. The process included sputtering a thin gold film onto a polycarbonate template, followed by galvanic strengthening with a copper layer. Also, gold sputtering is described in the work [18].

An alternative approach was proposed in [19], where a mercury drop was used as a liquid cathode base, eliminating the need for any intermediate metal coating. This method enables a synthesis of stable gold nanowires within polymer templates without diffusion-related degradation.

In this work, we demonstrated a structurally stable alternative through the electrochemical growth of gold onto pre-formed nickel nanowire cores, effectively preventing interfacial diffusion and phase transformation of gold. The resulting bimetallic Ni–Au segmented nanowires exhibit both chemical robustness and pronounced SERS activity, as evidenced by consistent signal enhancement of Rhodamine 6G at concentrations as low as  $10^{-4}$  M. This approach enables the fabrication of scalable, uniform, and functionally reliable SERS substrates, suitable for high-performance sensing applications where stability, reproducibility, and environmental resistance are critical.

### Experimental

Polyethylene terephthalate (PET) track-etched membranes (TMs) with a pore diameter of 100 nm were selected as a templates for the synthesis. The membranes were fabricated at the Flerov Laboratory of Nuclear Reactions, Joint Institute for Nuclear Research (JINR, Dubna). The film thickness was 12  $\mu\text{m}$  for two types of the TMs with intersecting and parallel pore systems. The surface density of the pore was  $1.2 \times 10^9 \text{ cm}^{-2}$ .

Nickel deposition was carried out using a Watts-type electrolyte with the following composition:  $\text{NiSO}_4 \times 7 \text{ H}_2\text{O}$  — 300 g/L;  $\text{NiCl}_2 \times 6 \text{ H}_2\text{O}$  — 45 g/L;  $\text{H}_3\text{BO}_3$  boric acid — 38 g/L. The pH of the nickel electrolyte was 4. Electrodeposition was performed at an electrolyte temperature of 60  $^\circ\text{C}$ , using a nickel anode grade NPA1 (purity above 99 %).

Gold deposition was conducted using a commercial gold plating electrolyte. The pH of the solution was maintained at 9, and the deposition temperature was set to 70  $^\circ\text{C}$ . A gold wire was used as an anode.

Thermally stable electrochemical cells for deposition were fabricated from polycarbonate using 3D printing [20].

The obtained nanostructures were characterized using a JEOL JSM-6000 plus electron microscope in secondary and backscattered electron scanning modes. The accelerating voltage was 15 kV. The survey was carried out using a special holder to set the samples at different angles. Elemental analysis was performed using an attached EDX spectroscopy system.

Raman and surface-enhanced Raman scattering (SERS) spectra of Rhodamine 6G (R6G) at a concentration of  $10^{-4}$  M were recorded on aluminum foil and SERS substrates based on Ni–Au segmented nanowires. The measurements were carried out using a Horiba LabRam Evolution confocal spectrometer equipped with a single-mode continuous-wave (CW) laser operating at 633 nm, with a maximum output power of 100 mW. A 100 $\times$  objective lens was used to focus the laser beam, resulting in a spot size of approximately 1  $\mu\text{m}$  in diameter.

For conventional Raman measurements on aluminum foil, the laser power was attenuated to 1 mW to minimize thermal effects and photodegradation of the analyte. In SERS experiments, two excitation power levels — 0.1 mW and 1 mW — were employed to assess signal dependence on laser intensity and to ensure

reliable detection under low-power conditions. Each spectrum was obtained by averaging five individual acquisitions, with an integration time of 20 seconds per scan, to enhance spectral reproducibility and signal-to-noise ratio.

Spectra were additionally recorded from rhodamine deposited on nickel nanowires at laser powers of 1 mW and 5 mW in order to demonstrate the absence of any significant signal enhancement, confirming the lack of SERS activity in nickel-based structures.

## Results and Discussion

### Growth and Deposition Curves

Bimetallic Ni–Au segmented nanowires were grown in several stages (Figure 1). In the first step, a 100 nm thick copper layer was sputtered onto the surface of the track-etched membrane to provide a conductive base. Subsequently, an additional copper layer with a thickness of 3–5  $\mu\text{m}$  was electrodeposited onto the initial sputtered layer (Figure 1b). This step was carried out to mechanically improve the copper layer and ensure its structural integrity during further processing. In the second step, nickel was deposited into the pores of the track-etched membrane (Figure 1c). The deposition was performed in a galvanostatic mode at a current density of 2  $\text{mA}/\text{cm}^2$ . The deposition time was chosen such that the pores were filled approximately halfway.

The deposition rate of nickel nanoparticles is 225  $\text{nm}/\text{min}$ .

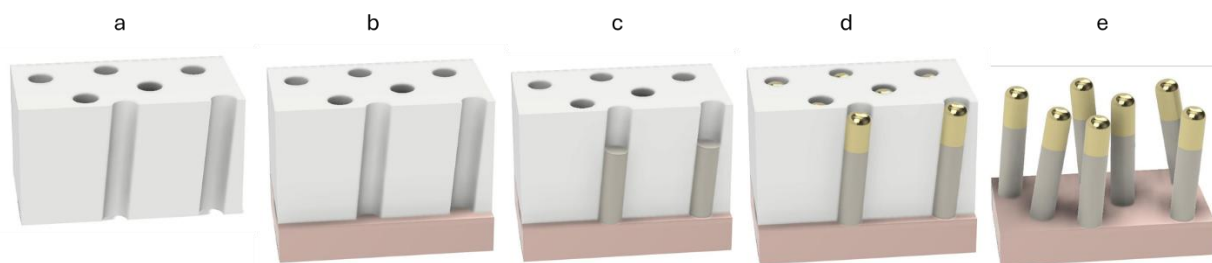


Figure 1. Stages of bimetallic Ni–Au segmented nanowire deposition

The degree of pore filling can be determined experimentally, taking into account the time required for complete pore filling, or theoretically based on the total charge passed through the electrochemical cell.

Examples of volts of time dependencies removed during nickel and gold deposition are shown in Figure 2.

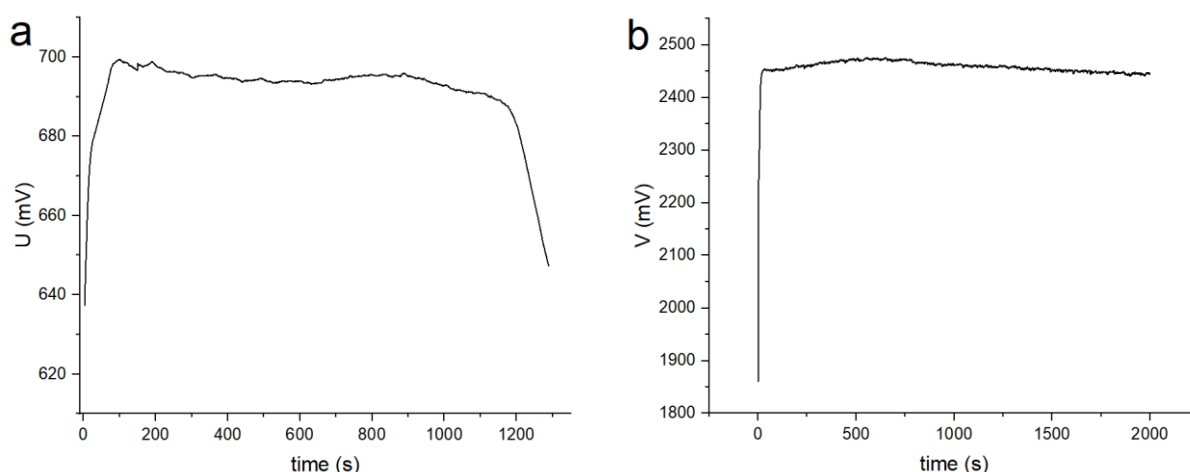


Figure 2. Changes in the electrochemical cell potential during metal deposition into 100 nm pores of track-etch membranes at a fixed current density of 2  $\text{mA}/\text{cm}^2$ : a) complete pore filling with nickel; b) partial pore filling with gold

At the third step, a gold segment was electrodeposited onto the nickel nanowires core (Figure 1d). The deposition was carried out in a galvanostatic mode at a current density of 2 mA/cm<sup>2</sup>. The deposition time varied between 500 and 2000 seconds. Figure 2b presents the deposition curve for the gold segment. The deposition rate of gold nanoparticles is 60 nm/min.

After deposition of the gold segments, the polymer template was dissolved in a concentrated alkaline solution (6M NaOH) at 80 °C for 2 hours (Figure 1e).

Following membrane dissolution, the resulting nanostructures were characterized using electron microscopy techniques.

#### Scanning Electron Microscopy (SEM) Analysis

Scanning electron microscopy (SEM) analysis revealed that the synthesized nanowires had an average total length of approximately 6.5  $\mu$ m and a diameter of 100 nm (Figure 4). Backscattered electron scanning clearly showed distinct contrast along the nanowire axis, indicating the presence of multiple metallic segments. The nickel segment was measured to be approximately 4.5  $\mu$ m in length, while the gold segment is about 2  $\mu$ m.

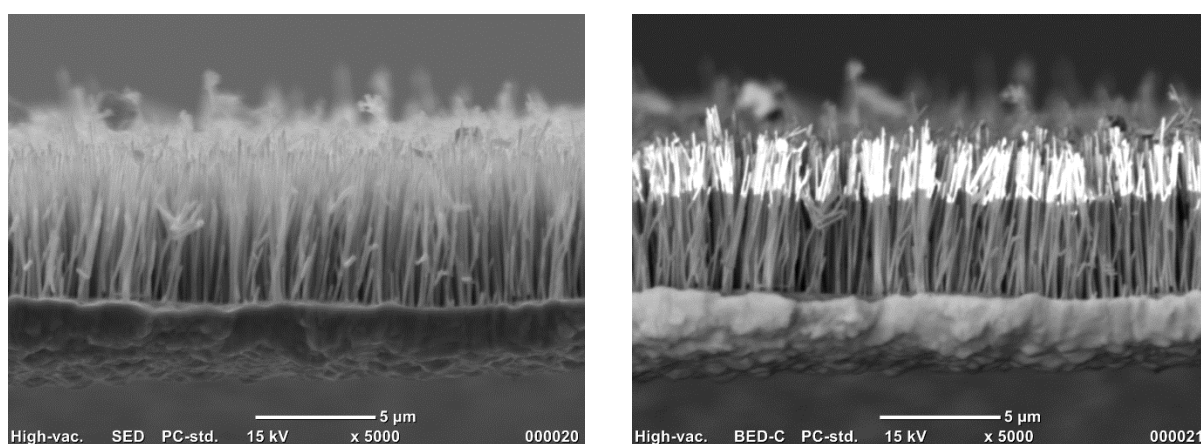


Figure 4. SEM images of the substrate with nanowires in secondary electron (SED) mode and backscattered electron (BED-C) mode

Energy-dispersive X-ray spectroscopy (EDX) analysis confirmed the presence of copper, nickel, and gold along the nanowire structure (Figure 5). Furthermore, elemental mapping was performed to visualize the spatial distribution of constituent metals (Figure 6). The results demonstrate a well-defined architecture, with copper localized at the base, nickel in the central segment, and gold selectively deposited at the top surface of the nanowires.

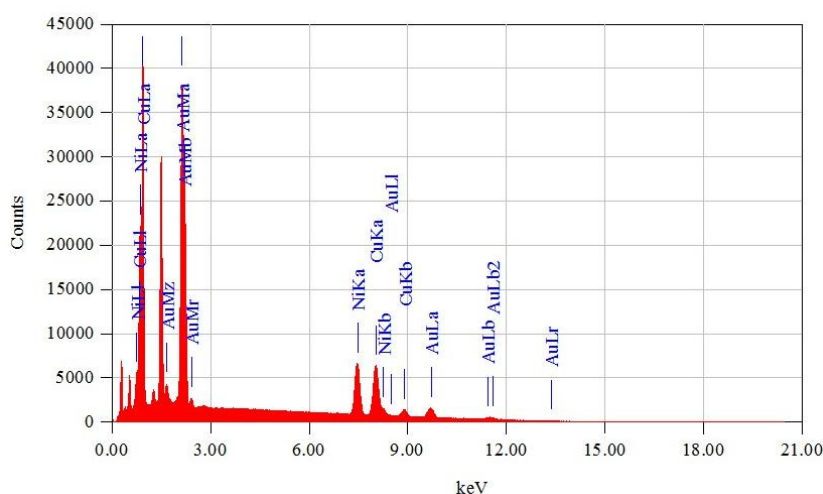


Figure 5. EDX analysis results for the bimetallic Ni–Au segmented nanowires



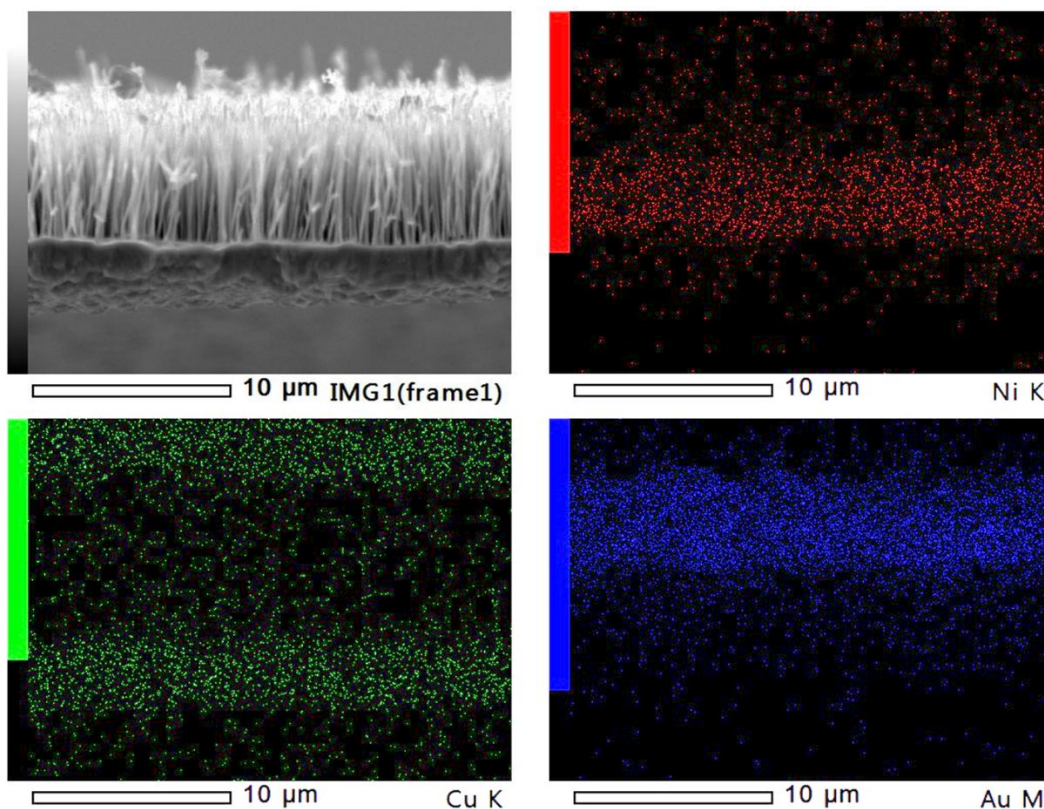


Figure 6. Elemental mapping of the nanowires showing spatial distribution of copper (green), nickel (red), and gold (blue)

### Raman Scattering

Raman and SERS measurements of Rhodamine 6G (R6G) at a concentration of  $10^{-4}$  M were performed on aluminum foil and Ni–Au segmented nanowire-based substrates. The results are summarized in Figure 7.

Figure 7a presents Raman spectra obtained from a dried droplet of R6G on aluminum foil. Clear vibrational features are observed only at the droplet edge, where the analyte is concentrated due to the coffee-ring effect, but signal still is dominated by a strong photoluminescence background. In contrast, no distinct spectral features are detected at the center of the droplet. These findings highlight the limitations of conventional Raman spectroscopy for detection that analyte concentration without plasmonic enhancement. All observed Raman bands are consistent with previously reported data for R6G known in literature.

As shown in Figure 7b, Raman spectra collected from R6G adsorbed on nickel nanowires exhibit no signal enhancement. This confirms that nickel nanostructures alone do not provide measurable SERS activity under the given experimental conditions.

In contrast, Figure 7c demonstrates a substantial improvement in spectral quality when using Ni–Au segmented nanowires as SERS-active substrates. The photoluminescence background is effectively suppressed, and the characteristic Raman peaks of R6G become clearly resolved. Spectra were acquired at two different laser powers — 0.1 mW and 1 mW — to evaluate the sensitivity and feasibility of low-power operation. Even at the reduced power level, the Raman signal remains well above the noise floor, indicating high substrate sensitivity. This feature is particularly relevant for practical sensing applications, including portable or field-deployable devices where low-power excitation is often required.

The overall performance of the Ni–Au segmented nanowire substrates suggest potential for the detection of even lower analyte concentrations and for the analysis of fluorescent compounds, which are typically challenging to detect using conventional Raman spectroscopy.



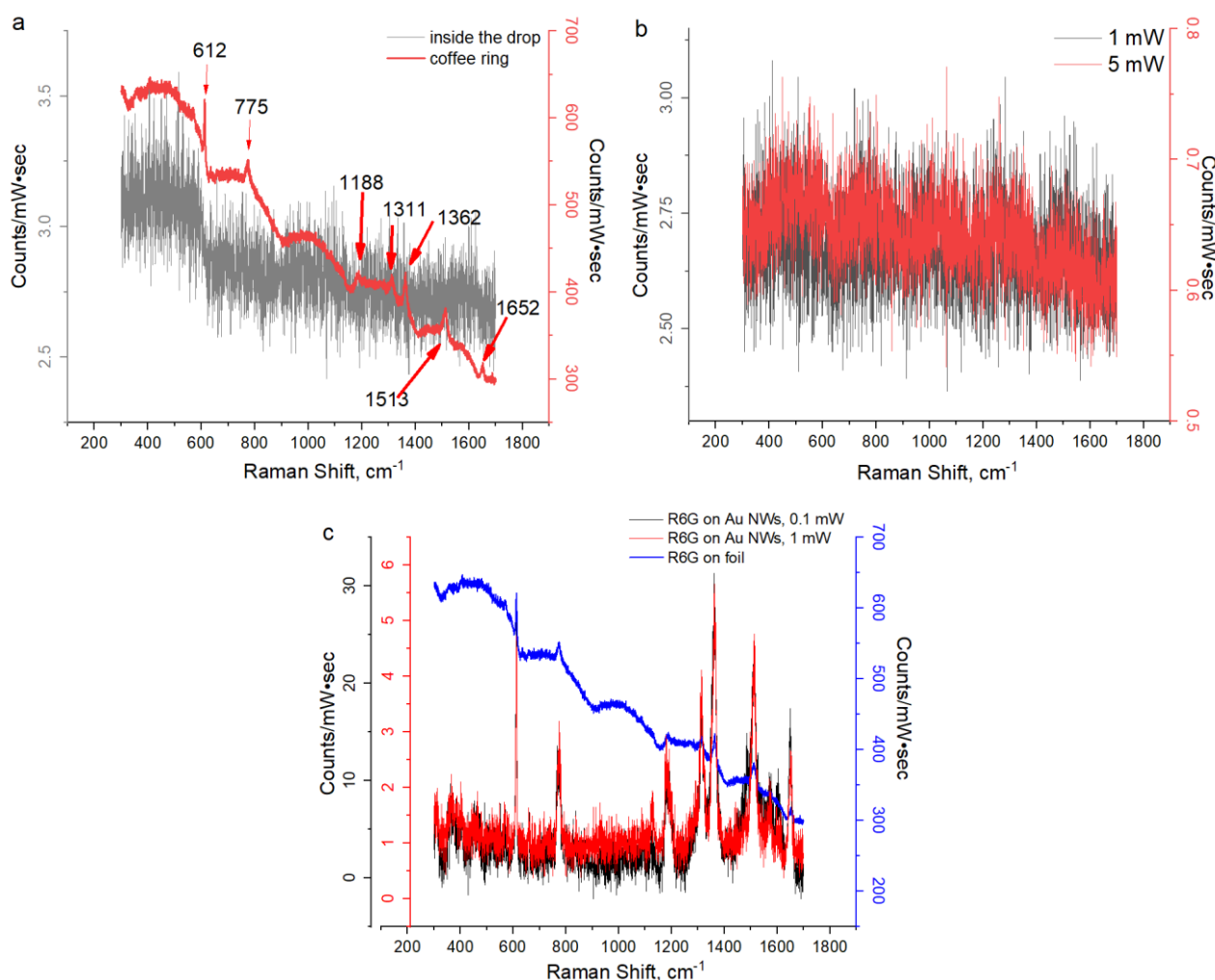


Figure 7. *a* — Raman spectra of R6G ( $10^{-4}$  M) on aluminum foil, showing signal variation at the droplet edge (coffee-ring region) and center. *b* — Raman spectrum of R6G ( $10^{-4}$  M) on Ni NWs. *c* — Comparison of R6G spectra on Al foil and Ni–Au segmented nanowires

### Conclusions

In this work, a novel and reliable approach for the fabrication of bimetallic Ni–Au segmented nanowires via template-assisted electrochemical deposition was developed. The proposed method enables precise control over the morphology and composition of the nanostructures by separating the deposition stages for nickel and gold segments. This strategy effectively avoids direct contact between gold and copper layers, thereby preventing intermetallic diffusion and significantly improving structural stability.

The resulting Ni–Au segmented nanowires demonstrated strong SERS activity, allowing for the sensitive detection of  $10^{-4}$  M Rhodamine 6G. Notably, SERS signals were obtained even at very low laser power (0.1 mW), highlighting the potential of these substrates for portable and field-deployable sensing applications. This study demonstrates that the combination of controlled template-based synthesis and bimetallic design offers a promising route toward the development of stable, reproducible, and highly sensitive SERS substrates suitable for practical analytical tasks, including trace-level detection of organic compounds with inherent fluorescence.

### Funding

SEM was made in the state assignment of NRC “Kurchatov Institute”.

### Author Information\*

\*The authors' names are presented in the following order: First Name, Middle Name and Last Name

**Sergey Aleksandrovich Bedin** (*corresponding author*) — Candidate of Physico-Mathematical Sciences, Senior Researcher, Skolkovo Institute of Science and Technology (Skoltech), Bolshoy Boulevard 30, bld. 1, 121205, Moscow, Russia; e-mail: [bserg5@gmail.com](mailto:bserg5@gmail.com); <https://orcid.org/0000-0002-7342-124X>

**Elizaveta Pavlovna Kozhina** — Junior Researcher, Skolkovo Institute of Science and Technology (Skoltech), Bolshoy Boulevard 30, bld. 1, 121205, Moscow, Russia; e-mail: [Elizaveta.Kozhina@skoltech.ru](mailto:Elizaveta.Kozhina@skoltech.ru); <https://orcid.org/0000-0003-4199-5334>

**Ilia Mikhailovich Doludenko** — Candidate of Technical Sciences, Resercher, A.V. Shubnikov Institute of Crystallography of the Kurchatov Complex Crystallography and Photonics of the NRC “Kurchatov Institute”, Akademika Kurchatova Square, 1, 123182, Moscow, Russia; e-mail: [doludenko.i@yandex.ru](mailto:doludenko.i@yandex.ru); <https://orcid.org/0000-0003-2738-3905>

**Vladimir Prokopevich Drachev** — Doctor of Physical and Mathematical sciences, Professor, Skolkovo Institute of Science and Technology (Skoltech), Bolshoy Boulevard 30, bld. 1, 121205, Moscow, Russia; e-mail: [V.Drachev@skoltech.ru](mailto:V.Drachev@skoltech.ru); <https://orcid.org/0000-0002-6205-7497>

### Author Contributions

The manuscript was written through contributions of all authors. All authors have given approval to the final version of the manuscript. **CRedit**: **Sergey Aleksandrovich Bedin** conceptualization, data curation, investigation, methodology, validation, visualization, writing-review & editing; **Elizaveta Pavlovna Kozhina** conceptualization, data curation, formal analysis, funding acquisition, resources, validation, writing-original draft, writing-review & editing.; **Ilia Mikhailovich Doludenko** investigation, methodology, validation, editing; **Vladimir Prokopevich Drachev** formal analysis, funding acquisition, resources, supervision, validation, writing-review & editing.

### Conflicts of Interest

The authors declare no conflict of interest.

### References

- 1 Wang, L., Wang, X., Cheng, L., Ding, S., Wang, G., Choo, J., & Chen, L. (2021). SERS-based test strips: Principles, designs and applications. *Biosens Bioelectron*, 189, 113360. <https://doi.org/10.1016/j.bios.2021.113360>
- 2 Augustine, S., Saini, M., K.P. S., Parida, B. K., Hans, S., Pachchigar, V., Satpati, B., & Ranjan, M. (2023). Au/Ag SERS active substrate for broader wavelength excitation. *Optical Materials*, 135. <https://doi.org/10.1016/j.optmat.2022.113319>
- 3 Lopez-Lorente, A. I. (2021). Recent developments on gold nanostructures for surface enhanced Raman spectroscopy: Particle shape, substrates and analytical applications. A review. *Anal Chim Acta*, 1168, 338474. <https://doi.org/10.1016/j.aca.2021.338474>
- 4 Martin, C. R. (1994). Nanomaterials: a membrane-based synthetic approach. *Science*, 266(5193), 1961–1966. <https://doi.org/10.1126/science.266.5193.1961>
- 5 Kolmychek, I. A., Napolskii, K. S., Leontiev, A. P., Sotnichuk, S. V., & Malysheva, I. V. (2022). Magneto-optical effects in composite hyperbolic metamaterials. *Physics of the Solid State*, 64(10). <https://doi.org/10.21883/pss.2022.10.54226.34hh>
- 6 Li, M., Ulrich, N., Schubert, I., Sigle, W., Peter Wagner, M. F., Trautmann, C., & Toimil-Molares, M. E. (2023). Three-dimensional free-standing gold nanowire networks as a platform for catalytic applications. *RSC Adv*, 13(7), 4721–4728. <https://doi.org/10.1039/d2ra08035d>
- 7 Apel, P. (2001). Track etching technique in membrane technology. *Radiation Measurements*, 34(1–6), 559–566. [https://doi.org/10.1016/s1350-4487\(01\)00228-1](https://doi.org/10.1016/s1350-4487(01)00228-1)
- 8 Oleinikov, V. A., Tolmachyova, Y. V., Berezkin, V. V., Vilensky, A. I., & McHedlishvili, B. V. (1995). Polyethyleneterephthalate track membranes with conical pores: Etching by water-alcohol alkali solutions. *Radiation Measurements*, 25(1–4), 713–714. [https://doi.org/10.1016/1350-4487\(95\)00227-6](https://doi.org/10.1016/1350-4487(95)00227-6)
- 9 Cherkasov, D. A., Zagorskii, D. L., Khaibullin, R. I., Muslimov, A. E., & Doludenko, I. M. (2020). Structure and Magnetic Properties of Layered Nanowires of 3d-Metals, Fabricated by the Matrix Synthesis Method. *Physics of the Solid State*, 62(9), 1695–1705. <https://doi.org/10.1134/s1063783420090048>
- 10 Kozhina, E., Panov, D., Kovalets, N., Apel, P., & Bedin, S. (2023). A thin-film polymer heating element with a continuous silver nanowires network embedded inside. *Nanotechnology*, 35(3), 035601. <https://doi.org/10.1088/1361-6528/ad0247>

- 11 Li, M., Bonart, H., Zellner, D., & Toimil-Molares, M. E. (2025). 3D Gold Nanowire Networks with Tailorable Surface Wetting State: From Rose-Petal Effect to Super-Hydrophilicity. *Small*, 8, Article 2411971. <https://doi.org/10.1002/sml.202411971>
- 12 Kozhina, E. P., Bedin, S. A., Nechaeva, N. L., Podoyntsyn, S. N., Tarakanov, V. P., Andreev, S. N., Grigoriev, Y. V., & Naumov, A. V. (2021). Ag-Nanowire Bundles with Gap Hot Spots Synthesized in Track-Etched Membranes as Effective SERS-Substrates. *Applied Sciences*, 11(4), 1375. <https://doi.org/10.3390/app11041375>
- 13 Mashentseva, A. A., Borgekov, D. B., Niyazova, D. T., & Migunova, A. A. (2015). Study of the structural features of nanocomposite materials based on PET track-etched membranes and gold nanotubes. *Bulletin of the University of Karaganda-Chemistry*, 79(3), 33–40.
- 14 Paunovic, M., & Schlesinger, M. (2006). *Fundamentals of Electrochemical Deposition*. John Wiley & Sons, Inc.
- 15 Gruyev, I. D., Matveev, N. I., & Sergeeva, N. G. (1988). *Elektrokhimicheskie pokrytiya izdeliy radioelektronnoi apparatury. Spravochnik* [Electrochemical Coatings for Radioelectronic Equipment: A Handbook]. Radio i Svyaz. [in Russian]
- 16 Cui, S., Su, G., Ren, X., Wu, X., Peng, L., & Fu, Y. (2023). Plasmon Hybridization of Au Hollow Nanocone Array for SERS Sensing. *Plasmonics*, 19(3), 1395–1402. <https://doi.org/10.1007/s11468-023-02080-9>
- 17 Liu, J., Duan, J. L., Toimil-Molares, M. E., Karim, S., Cornelius, T. W., Dobrev, D., Yao, H. J., Sun, Y. M., Hou, M. D., Mo, D., Wang, Z. G., & Neumann, R. (2006). Electrochemical fabrication of single-crystalline and polycrystalline Au nanowires: the influence of deposition parameters. *Nanotechnology*, 17(8), 1922–1926. <https://doi.org/10.1088/0957-4484/17/8/020>
- 18 Karimian, N., Moretto, L. M., & Ugo, P. (2016). Nanobiosensing with Arrays and Ensembles of Nanoelectrodes. *Sensors (Basel)*, 17(1). <https://doi.org/10.3390/s17010065>
- 19 Sharma, M. K., Ambollikar, A. S., & Aggarwal, S. K. (2012). Electrochemical synthesis of gold nanorods in track-etched polycarbonate membrane using removable mercury cathode. *Journal of Nanoparticle Research*, 14(9). <https://doi.org/10.1007/s11051-012-1094-z>
- 20 Bedin, S., & Kozhina, E. (2024). *Ustroïstvo dlya elektrokhimicheskogo osazhdeniya materiala pri shablonnom sinteze (varianty)* [Device for electrochemical deposition of material in template synthesis (variants)] (Patent No. RU2820470C1). *Federal'noe gosudarstvennoe byudzhethoe uchrezhdenie nauki Fizicheskii institut im. P.N. Lebedeva Rossiiskoi akademii nauk*. [in Russian]

## TEMs BASED COMPOSITES AND ITS PRACTICAL APPLICATIONS








### Article

Received: 27 May 2025 | Revised: 15 August 2025 |

Accepted: 28 August 2025 | Published online: 25 September 2025

UDC 66.081.6

<https://doi.org/10.31489/2959-0663/3-25-7>

Nikita A. Drozhzhin<sup>1, 2\*</sup> , Olga Yu. Ponomareva<sup>1, 2</sup> , Ilya I. Vinogradov<sup>2</sup> ,  
Genrikh V. Serpionov<sup>2</sup> , Abubakir Kanet<sup>3</sup> , Daria V. Nikolskaya<sup>2</sup> , Tatiana N. Vershinina<sup>1, 2</sup> 

<sup>1</sup>Dubna University, Dubna, Russia;

<sup>2</sup>Joint Institute for Nuclear Research, Dubna, Russia;

<sup>3</sup>Institute of Batteries, Astana, Kazakhstan

(\*Corresponding author's e-mail: [dna.17@uni-dubna.ru](mailto:dna.17@uni-dubna.ru))

### Nickel (II) Based Metal-Organic Framework Consolidated on Nanofibers Modified Track-Etched Membrane for Dye Removal

Metal-organic frameworks (MOFs) are promising adsorption agents with many potential applications. However, most experiments exploring the potential applications of MOFs have used powders, which limits the range of possible applications. To solve this problem, an approach to design hybrid membrane (HM) based on track-etched membrane, electrospun nanofibers and MOF based on L-tryptophan, 1,2-bis(4-pyridyl)ethylene and Ni (II) (Ni-MOF) was proposed in the current paper. An investigation of Ni-MOF morphology on hydrophilic chitosan and hydrophobic polyvinylidene fluoride nanofibers showed that the Ni-MOF tends to form superstructures — spherical conglomerates consisting of flaky crystallites on both types of nanofibers. The HMs and Ni-MOF powder were characterized by SEM and PXRD. The adsorption properties of the Ni-MOF powder towards model anionic methyl orange (MO) and cationic rhodamine B (Rh B) including kinetics and isotherm were studied. An investigation of dyes removal by HMs in dead-end filtration mode indicates the effectiveness of MO and Rh B adsorption as high as ~97 % (~380 µg/cm<sup>2</sup>) and ~9 % (~37 µg/cm<sup>2</sup>), respectively. The possibility of regeneration was also investigated. Thus, the HMs may find a potential application for advanced wastewater treatment processes to provide removal of MO in microfiltration mode.

**Keywords:** track-etched membranes, metal-organic frameworks, hybrid membranes, nanofibers, electrospinning, dye removal, adsorption, water treatment

### Introduction

Water pollution caused by industries is one of the most significant global problems. Water may contain numerous hazardous compounds such as dyes, heavy metal ions, or drugs, which pose severe risks to the environment and human health. Methyl Orange (MO), an anionic dye is commonly used in textile, printing industries and in laboratory practice. Despite this, MO is recognized as low biodegradable, toxic, carcinogenic and mutagenic compound. It is reduced into aromatic amines by intestinal microorganisms which can lead to intestinal cancer [1–3]. Rhodamine B (Rh B) is a cationic dye employed in textile, paper, paint industry. It is toxic, carcinogenic and non-biodegradable. The presence of MO or Rh B in water can negatively affect aquatic organisms due to toxicity and ability to inhibit photosynthesis by reducing light penetration [4–7]. Various techniques have been used for removal of dyes from water media: membrane filtration, adsorption, photocatalysis, sedimentation, electrochemical methods and so on. Among them, adsorption is one of the most simple and effective methods for wastewater treatment [8, 9]. Nevertheless, disadvantages of numerous traditional adsorbents are still poor selectivity, retrievability or stability and slow removal rate [10]. Thus, design of novel systems for dye removal is highly demanded.

Metal-organic frameworks (MOFs) are crystalline compounds consisting of metal ions or clusters that are held together by organic ligands. These compounds can form one-, two- or three-dimensional frameworks that may be porous. Since the 1990s and to the present day, they have been attracting great research interest due to the unique properties such as high surface area and tunability of structure [11]. There are a variety of papers studied MOFs as dyes adsorbent. Most experiments of MOFs application in this field were carried out using MOFs powders [12, 13]. However, for improving processability and realization of MOFs practical application in wastewater treatment, depositing MOFs on porous supports to form hybrid membranes (HMs) could be a promising solution [14]. Recent studies have proposed a novel approach to creating functional HMs based on track-etched membranes (TMs) modified by electrospun nanofibers (NFs) layer. This approach has proven suitable for designing materials for removal of harmful ions and dyes from wastewater, seawater desalination processes and wound dressings [9, 15–19].

Herein we present an approach to design novel hybrid membrane based on nanofiber-modified track-etched membrane and MOF synthesized via a low temperature solvothermal method. The MOF based on L-tryptophan, 1,2-bis(4-pyridyl)ethylene and Ni (II) (Ni-MOF) as it can be synthesized under mild conditions that exclude membrane damage. TMs modified with chitosan (Ch) and polyvinylidene fluoride (PVDF) NFs were used as models of hydrophilic and hydrophobic substrates, respectively. The well-defined pore architecture and thoroughly studied physicochemical properties make it possible to use TMs as a convenient model for investigating the processes of designing HMs. To study the adsorption performance two dyes, anionic methyl orange and cationic rhodamine B, were selected as model compounds. The adsorption characteristics such as kinetics and isotherms of adsorption by the Ni-MOF powder were investigated. Dye removal by HMs in filtration mode and regeneration potential were evaluated. Schematically the synthesis process and application in dye adsorption of HMs is illustrated in Figure 1.

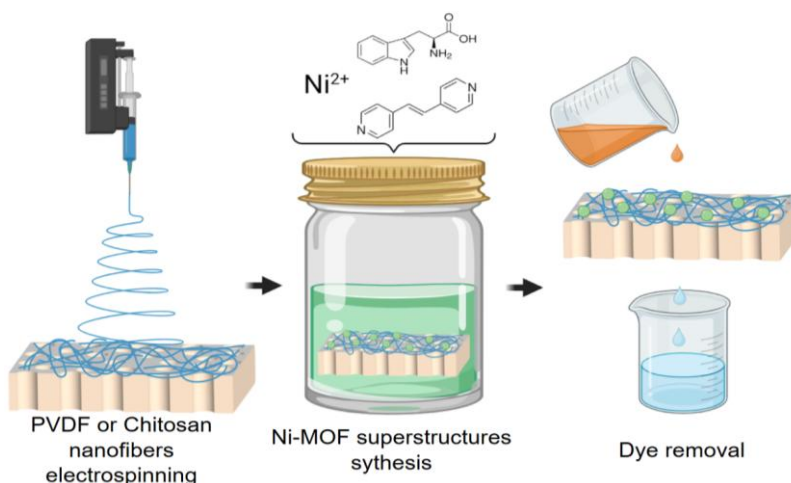


Figure 1. Schematic illustration of HMs preparation and application process

### Experimental

#### Materials

Polyethylene terephthalate (PET) TM with a thickness of 23  $\mu\text{m}$ , pores diameter of 0.3  $\mu\text{m}$  and pores density of  $(2.7 \pm 0.3) \times 10^8 \text{ cm}^{-2}$  was made from Hostaphan RNK film in Flerov Laboratory of Nuclear reactions of Joint Institute for Nuclear Research. This membrane was covered by  $40 \pm 4 \text{ nm}$  thick Ti layer in Ivtekhnomash, LLC and used as a support for future studies [20]. The titanium layer is used as collecting electrode during the electrospinning process to improve uniformity and adhesion of NFs to the TM surface [16, 17].

The following reagents were used: chitosan ( $M_w = 200000 \text{ g/mol}$ ), polyethylene oxide ( $M_w = 300000 \text{ g/mol}$ ), 99.8 % acetic acid, 25 % glutaraldehyde, polyvinylidene fluoride ( $M_w = 600000 \text{ g/mol}$ ), 99.8 % dimethylformamide, 99.8 % acetone were used for electrospinning of NFs; L-tryptophan (98 %), 1,2-bis(4-pyridyl)ethylene (97 %), nickel nitrate ( $\text{Ni}(\text{NO}_3)_2 \cdot 6\text{H}_2\text{O}$ , chemically pure), methanol (analytical grade) were used for Ni-MOF synthesis; methyl orange (97 %), rhodamine B (95 %), deionized Milli-Q water, acetate buffer were used for adsorption investigations.



### Nanofibers Electrospinning

Ch and PVDF NFs were electrospun on the TM surface according to the methods reported previously [16, 19]. Membranes with Ch or PVDF NF layers were designated as TM+Ch and TM+PVDF, respectively. Density of NFs layer was found to be  $0.37 \pm 0.03$  mg/cm<sup>2</sup> for TM+Ch and  $0.55 \pm 0.05$  mg/cm<sup>2</sup> for TM+PVDF.

### Ni-MOF Synthesis

The method described previously was used for synthesis Ni-MOF as a powder and on the membrane surface [21, 22]. Membranes modified by Ni-MOF were marked as TM+Ch+Ni-MOF or TM+PVDF+Ni-MOF. The density of Ni-MOF on the membrane surface was amounted to be  $3.4 \pm 0.6$  mg/cm<sup>2</sup> for TM+Ch+Ni-MOF and  $3.8 \pm 0.5$  mg/cm<sup>2</sup> for TM+PVDF+Ni-MOF.

### Characterization Techniques

The morphology of the membranes was studied by scanning electron microscopy (SEM, Hitachi S-3400N). The crystal structure was analyzed by powder X-ray diffraction (PXRD) using PANalytical Empyrean powder diffractometer (CoK $\alpha$  radiation) with a high-efficiency Pixel3D position-sensitive detector at a tube voltage of 40 kV and a current of 40 mA. The  $2\theta$  angle range was from 8° to 50° with steps  $\Delta\theta = 0.026^\circ$ . Hydrophobic-hydrophilic properties of membranes were estimated by water contact angle measurements using DSA-100. The Brunauer–Emmett–Teller specific surface area of the Ni-MOF powder was measured as 4.5 m<sup>2</sup>/g (N<sub>2</sub>, ASAP 2020).

### Adsorption Experiments

Two dyes were selected for adsorption experiments: anionic methyl orange and cationic rhodamine B. For batch adsorption experiments the Ni-MOF powder was used. Adsorption kinetics was studied in duplicate by 15 mg of Ni-MOF in 10 ml of dye aqueous solution with initial concentration 50 mg/L for MO and 10 mg/L for Rh B at 23 °C. Dyes solutions were analyzed by UV-Vis spectrophotometer (Evolution 600) and the adsorption capacity at certain time ( $q_t$ , mg/g) was calculated using Eq (1):

$$q_t = \frac{(C_0 - C_t)V}{m}, \quad (1)$$

where  $C_0$  is the initial concentration (mg/L),  $C_t$  is the concentration after adsorption for a certain time (mg/L),  $V$  is a solution volume (L),  $m$  is an adsorbent mass (g). To quantify the adsorption kinetics pseudo-first-order (PFO) model (Eq 2) and pseudo-second-order (PSO) model (Eq 3) were used to fit the experimental data:

$$q_t = q_e (1 - e^{-k_1 t}); \quad (2)$$

$$q_t = \frac{q_e^2 k_2 t}{1 + q_e k_2 t}, \quad (3)$$

where  $q_e$  is the adsorption capacity at equilibrium (mg/g),  $k_1$  is the rate constant of the PFO model (1/min),  $k_2$  is the rate constant of the PSO model (g/mg·min),  $t$  is the time (min).

The adsorption isotherm measurements were performed in duplicate by varying the initial dye concentration from 10 to 300 mg/L for MO and from 1 to 30 mg/L for Rh B. Three the most widely applied isotherm models, Langmuir (Eq 4), Freundlich (Eq 5) and Temkin (Eq 6) were employed to fit the experimental data:

$$q_e = \frac{q_{max} K_L C_e}{1 + K_L C_e}; \quad (4)$$

$$q_e = K_F C_e^{1/n}; \quad (5)$$

$$q_e = q_{max} \frac{RT}{b} \ln(K_T C_e), \quad (6)$$

where  $q_{max}$  is a monolayer capacity of Ni-MOF (mg/g),  $K_L$  is the Langmuir adsorption constant (L/mg),  $C_e$  is the concentration at equilibrium (mg/L),  $K_F$  is the Freundlich adsorption constant ((mg/g)·(L/mg)<sup>1/n</sup>),  $n$  is an exponent of the Freundlich model,  $b$  is the Temkin isotherm constant (J/mol),  $K_T$  is the Temkin adsorption constant (L/mg).

The fitting quality and error analysis of the models were carried out by calculating chi-squared parameter (Eq 7) and hybrid fractional error function (Eq 8):

$$\chi^2 = \sum_{i=1}^n \frac{(q_{cal} - q_{exp})^2}{q_{exp}}; \quad (7)$$

$$HYBRID = \frac{100}{n-p} \sum_{i=1}^n \frac{(q_{exp} - q_{cal})^2}{q_{exp}}, \quad (8)$$

where  $q_{cal}$  is the calculated adsorption capacity (mg/g),  $q_{exp}$  is the experimental adsorption capacity (mg/g),  $n$  is a number of measured experimental points,  $p$  is a number of variable parameters in the equation.

For adsorption investigations in dead-end filtration mode the 25 mm membrane (working diameter 22 mm) was installed in a polycarbonate filter holder. Using tubes, the holder was connected to the syringe containing 30 ml of selected dye with initial concentration 50 mg/L. The syringe was placed into a syringe pump and flow rate was set as 2 ml/min. The solution passed through the membrane was collected in a beaker and placed back into the syringe. The described procedure was repeated throughout 2, 4, 8 and 12 cycles. The adsorption losses as  $a$ , % and  $A$ ,  $\mu\text{g}/\text{cm}^2$  was calculated using Eq (9, 10):

$$a = \frac{C_0 - C_n}{C_0} \times 100; \quad (9)$$

$$A = \frac{(C_0 - C_n)V}{S}, \quad (10)$$

where  $C_n$  is the concentration after a certain cycle (mg/L),  $S$  is a membrane working area ( $\text{cm}^2$ ).

For regeneration studies, the membrane was kept in the 10 ml MO solution with concentration of 50 mg/L for 24 hours. After that the membrane was immersed in acetate buffer solution with pH = 4 for 3 hours. Adsorption ( $E_A$ , %) and desorption efficiencies ( $E_D$ , %) were calculated throughout 3 adsorption-desorption cycles using Eq (11, 12):

$$E_A = \frac{m_{ads}}{m_0} \times 100; \quad (11)$$

$$E_D = \frac{m_{des}}{m_{ads}} \times 100, \quad (12)$$

where  $m_{ads}$  is the mass of adsorbed MO ( $\mu\text{g}$ ),  $m_0$  is the initial mass of MO ( $\mu\text{g}$ ),  $m_{des}$  is the mass of desorbed MO ( $\mu\text{g}$ ).

## Results and Discussion

### Characterization

The surface morphology of TMs modified by Ch and PVDF was described in detail previously [16, 17, 19]. Both Ch and PVDF NFs on the TM surface possess a smooth and uniform morphology. The average diameters of the NFs calculated by the Gaussian approximation were  $164 \pm 4$  nm for Ch NFs and  $216 \pm 18$  nm for PVDF NFs (Fig. 2 a, b). After Ni-MOF synthesis on the membranes, superstructures — spherical conglomerates consisting of flaky crystallites, were formed (Fig. 2 c, d). Average diameter of Ni-MOF superstructures was measured as  $19 \pm 2$   $\mu\text{m}$  for the TM+Ch+Ni-MOF and  $22 \pm 2$   $\mu\text{m}$  for the TM+PVDF+Ni-MOF samples. The results suggest that the morphology of superstructures is independent of the hydrophobic-hydrophilic properties of the substrate.

To confirm that the crystal structure of Ni-MOF is identical in powder form and on the membrane surface, PXRD analysis was performed. As shown in Figure 3, the patterns of the TM+Ch, TM+PVDF, TM+Ch+Ni-MOF and TM+PVDF+Ni-MOF samples contain an amorphous halo in the region up to  $20^\circ$  and the twin peak around  $27^\circ$  and  $30^\circ$  was interpreted as PET [18]. The remaining peaks for the TM+Ch+Ni-MOF and TM+PVDF+Ni-MOF membranes correspond to Ni-MOF [21, 22]. No significant differences were observed between patterns of the Ni-MOF powder and the HMs. Thus, successful deposition of Ni-MOF on the TMs modified by Ch and PVDF NFs was achieved.

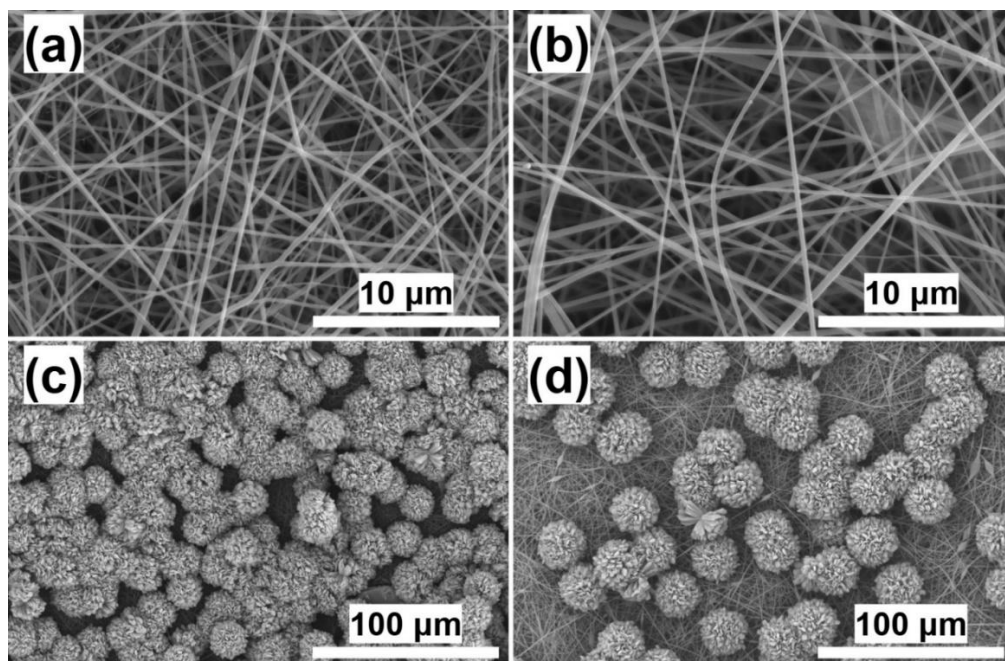


Figure 2. SEM images: (a) TM+Ch membrane, (b) TM+PVDF membrane, (c) hybrid TM+Ch+Ni-MOF membrane, (d) hybrid TM+PVDF+Ni-MOF membrane

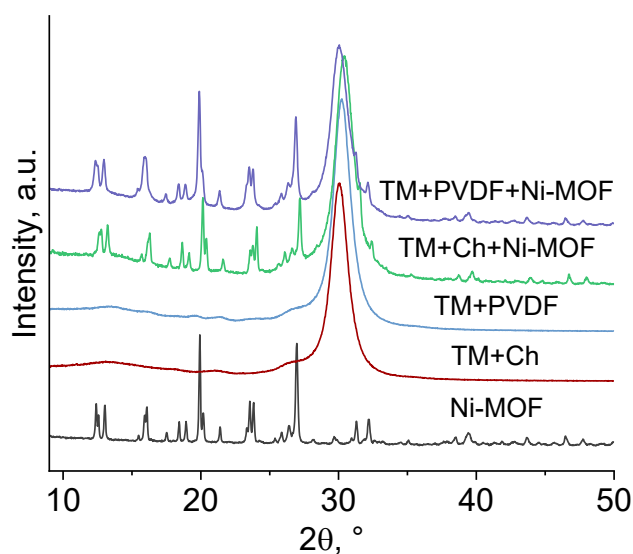


Figure 3. PXRD patterns of Ni-MOF powder, TM+Ch and TM+PVDF membranes, hybrid TM+Ch+Ni-MOF and TM+PVDF+Ni-MOF membranes

To determine hydrophobic-hydrophilic properties of the HMs and substrates, the water contact angle (CA) measurements were performed (Fig. 4). It was found that the synthesizing Ni-MOF on the membrane's surface increases its hydrophilic properties. The CA of TM+Ch was difficult to measure due to the rapid adsorption of water droplets caused by the NFs. However, this value was estimated as  $\sim 15^\circ$  (Fig. 4, a). The synthesis of Ni-MOF on the surface leads to complete wettability of the HM surface (Fig. 4, b). The CA of TM+PVDF was measured as  $140 \pm 1^\circ$  that determines the membrane surface as hydrophobic (Fig. 4, c). The modified sample TM+PVDF+Ni-MOF showed the CA value of  $123 \pm 9^\circ$  (Fig. 4, d). The relatively large deviation suggests non-uniform coverage of Ni-MOF on the TM+PVDF surface. However, the CA of TM+PVDF+Ni-MOF was decreased up to 20 % in comparison with the pristine one.

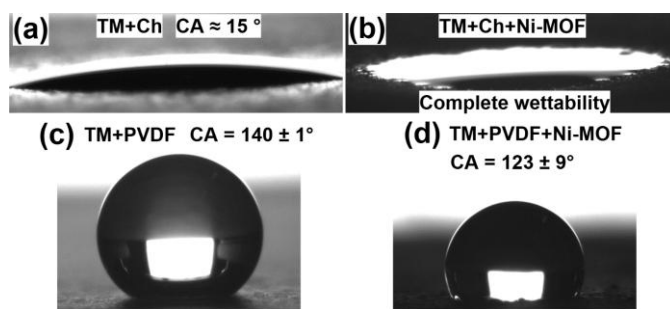


Figure 4. Photos of a water droplet on membranes: (a) TM+Ch membrane, (b) hybrid TM+Ch+Ni-MOF membrane, (c) TM+PVDF membrane, (d) hybrid TM+PVDF+Ni-MOF membrane

### Dye Adsorption

To explore the adsorption characteristics of the Ni-MOF powder and hybrid membranes HMs, two model contaminants were selected: anionic MO and cationic Rh B. Firstly, adsorption kinetics of the Ni-MOF powder was studied. As shown in Figure 5 the curve reaches a plateau through 120 minutes, corresponding to  $95.1 \pm 0.1$  % MO removal. The time taken for Rh B to reach equilibrium was also estimated as 120 minutes, corresponding to  $8.4 \pm 1.2$  % Rh B removal. The adsorption kinetics was evaluated using the PFO and PSO models. For both MO and Rh B, the adsorption process kinetics were well fitted by the PSO model characterized by the lowest  $\chi^2$  values and relatively small deviations between the experimental and calculated adsorption capacities (Table 1). Therefore, the adsorption of MO and Rh B was proportional to the square of the dye concentration and probably based on chemical interactions [23, 24].

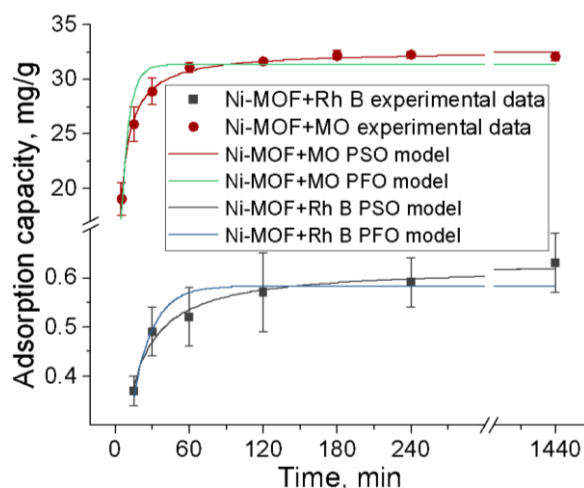


Figure 5. Adsorption kinetics curves of MO and Rh B by Ni-MOF powder

Table 1

Adsorption kinetics model parameters of Ni-MOF powder

Dye	Pseudo-first-order model					Pseudo-second-order model				
	$q_{e, exp}$	$q_{e, cal}$	$k_1$	$\chi^2$	<i>HYBRID</i>	$q_{e, exp}$	$q_{e, cal}$	$k_2$	$\chi^2$	<i>HYBRID</i>
MO	32.1	31.3	0.16	0.6896	9.8514	32.1	32.6	0.0085	0.0188	0.2685
Rh B	0.6	0.58	0.063	0.0092	0.2296	0.6	0.62	0.16	0.0018	0.0453

Adsorption isotherms were evaluated for future investigations. As shown in Figure 6, the adsorption capacity increases with the dye concentration increasing that typical property of many adsorbents. The maximum experimental adsorption capacity toward MO was amounted to be  $120.2 \pm 1.5$  mg/g at initial MO concentration of 300 mg/L. However, the adsorption capacity did not reach its plateau within the studied concentration range. Thus, there are still adsorption sites which can be occupied by MO. The maximum experi-

mental adsorption capacity of Rh B removal was significantly lower and amounted to be  $0.67 \pm 0.11$  mg/g. The adsorption curve reached saturation at dye concentration of 10 mg/L.

For better understanding of the adsorption process, isotherms were fitted by Freundlich, Langmuir and Temkin models. It should be noted that employment of Temkin isotherm requires the  $q_{max}$  value. Herein  $q_{max}$  value was derived from the Langmuir model [27]. The order of the  $\chi^2$  and *HYBRID* values of the models corresponded to the following trend: Freundlich > Langmuir > Temkin for MO and Freundlich > Temkin > Langmuir for Rh B contaminant (Table 2). Freundlich isotherm suggests heterogeneity of adsorbent surface and exponential distribution of binding sites energies [25]. Seen in Table 2, the Freundlich model exhibited the highest  $\chi^2$  and *HYBRID* values for both contaminants which indicates that the model is not capable of adequately describing the experimental data. The values of  $\chi^2$  and *HYBRID* calculated for the Langmuir model are lower in the comparison with the Freundlich model. Therefore, the assumption of uniformly distributed binding energies and constant adsorption heat is more favorable for the experimental data [26]. The calculated Langmuir maximum adsorption capacity for MO was 115.9 mg/g that is less than the experimental value by ~4 %. This may be caused by an implicit plateau. The best fit of the MO adsorption experimental data was obtained for the Temkin model. The Temkin isotherm assumes uniform distribution of binding energies and linearly decreasing of the adsorption heat along with surface coverage. A value of  $b > 0$  constant associated with the heat of adsorption indicates that the process is exothermic [27]. The best fit of the Rh B adsorption experimental data was obtained for the Langmuir model. The calculated Langmuir maximum adsorption capacity for Rh B was 0.74 mg/g that is higher than the experimental value by ~10 %.

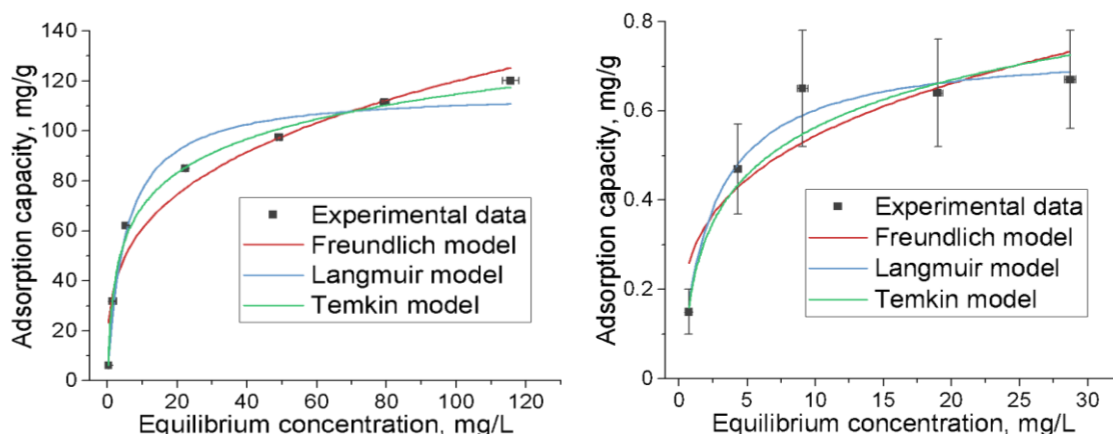


Figure 6. Adsorption isotherms of MO and Rh B by Ni-MOF powder

Table 2

Adsorption isotherm model parameters of Ni-MOF powder

Dye	Freundlich model				Langmuir model				
	$K_F$	$n$	$\chi^2$	<i>HYBRID</i>	$q_{m, exp}$	$q_{m, cal}$	$K_L$	$\chi^2$	<i>HYBRID</i>
MO	30.7	3.4	51.4495	1028.9902	120.2	115.9	0.19	3.6965	73.9302
Rh B	0.28	3.5	0.1112	3.7056	0.67	0.74	0.42	0.0106	0.3521

Dye	Temkin model			
	$b$	$K_T$	$\chi^2$	<i>HYBRID</i>
MO	14560	3.5	0.6533	13.0669
Rh B	11865	3.9	0.0246	0.8190

In summary, the Ni-MOF powder is characterized by relatively slow kinetics of dye adsorption (~2 hours). The PSO model was found to be able to adequately describe the experimental data. This may suggest that the adsorption process is chemical in nature. The Temkin model could adequately describe the Ni-MOF dye adsorption isotherms. Thus, the adsorption occurs on uniformly distributed binding sites. At an initial dye concentration of 10 mg/L, the experimental adsorption capacities were approximately ~6 mg/g for anionic MO and ~0.6 mg/g for cationic Rh B. These results suggest that Ni-MOF might exhibits selectivity towards MO.



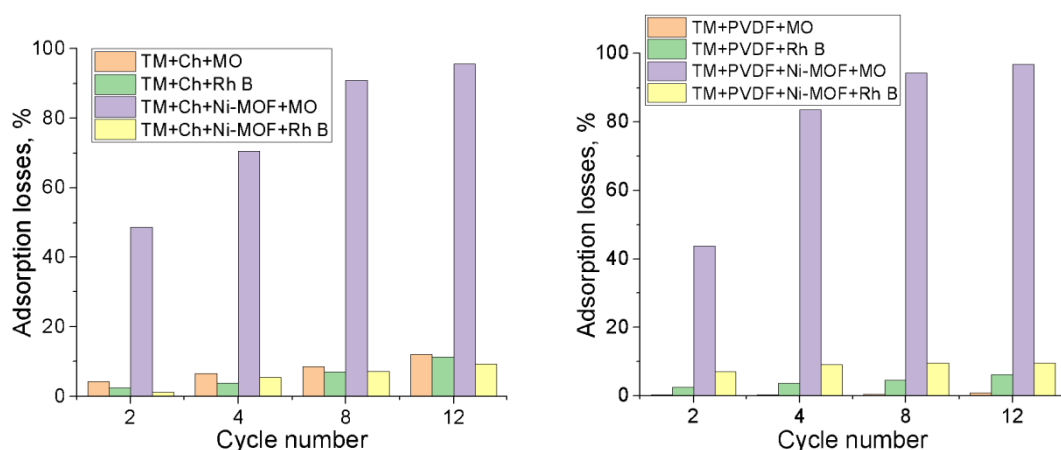


Figure 7. Adsorption losses of MO and Rh B at passing through membranes

The efficiency of dye removal by HMs was studied in dead-end filtration mode. The results are shown in Figure 7. The highest values of adsorption losses were observed for the TM+Ch+Ni-MOF and TM+PVDF+Ni-MOF samples. After 12 cycles, the adsorption losses of MO were 95.7 % for TM+Ch+Ni-MOF and 96.8 % for TM+PVDF+Ni-MOF which corresponds to the specific adsorption losses value of  $380.3 \mu\text{g}/\text{cm}^2$  and  $382.2 \mu\text{g}/\text{cm}^2$ , respectively. The differences in the adsorption kinetics of TM+Ch+Ni-MOF and TM+PVDF+Ni-MOF may be caused by the higher density of the Ni-MOF layer on the TM+PVDF+Ni-MOF surface. The adsorption losses of Rh B were significantly less: 9.3 % ( $36.7 \mu\text{g}/\text{cm}^2$ ) for TM+Ch+Ni-MOF and 9.4 % ( $37.1 \mu\text{g}/\text{cm}^2$ ) for TM+PVDF+Ni-MOF. Thus, the adsorption follows the above-mentioned trend: the adsorption of MO is more active than that of Rh B. To estimate the influence of the porous support on the adsorption, the dye removal by TM+Ch and TM+PVDF was studied. The adsorption losses of MO and Rh B on TM+Ch were 12.1 % ( $47.6 \mu\text{g}/\text{cm}^2$ ) and 11.4 % ( $45.1 \mu\text{g}/\text{cm}^2$ ), respectively. The TM+PVDF membrane showed lower maximum adsorption losses values of 0.9 % ( $3 \mu\text{g}/\text{cm}^2$ ) and 6.1 % ( $24.2 \mu\text{g}/\text{cm}^2$ ) for MO and Rh B. Therefore, the Ni-MOF layer mainly contributes to the adsorption of MO by the HMs.

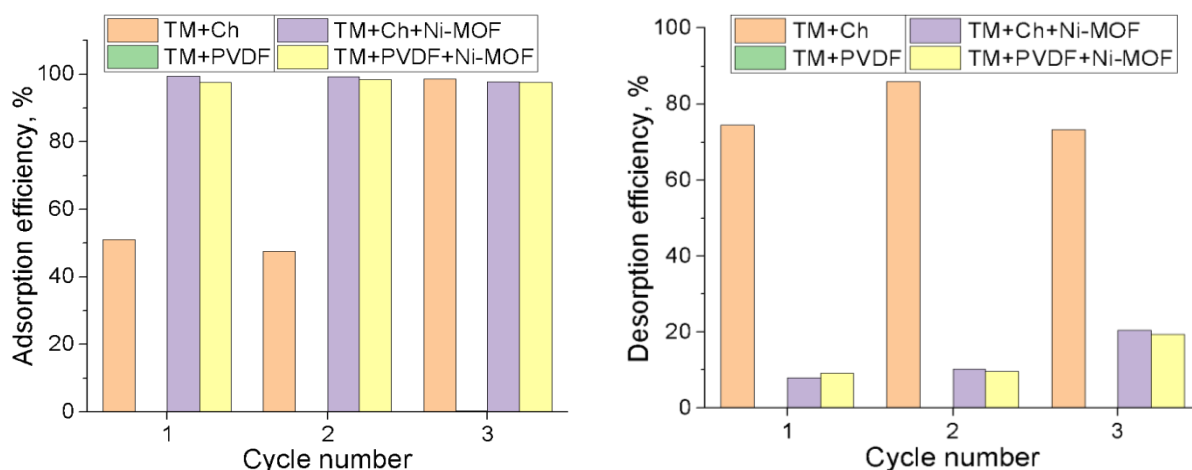


Figure 8. The efficiency of adsorption and desorption of MO by membranes

Batch adsorption-desorption experiments were used to investigate the possibility of regeneration for MO only. The results are shown in Figure 8. The adsorption efficiency of HMs was consistently high during the experiments and amounted to an average of  $98.8 \pm 0.9 \%$  ( $127.1 \pm 2.2 \mu\text{g}/\text{cm}^2$ ) for TM+Ch+Ni-MOF and  $97.9 \pm 0.5 \%$  ( $125.9 \pm 1 \mu\text{g}/\text{cm}^2$ ) for TM+PVDF+Ni-MOF. The desorption efficiency of HMs was  $\sim 10 \%$  during 2 cycles and doubled by the 3rd cycle. The desorption efficiency increase may mean degradation of the Ni-MOF crystal structure during adsorption-desorption cycles. The adsorption efficiency of the TM+Ch membrane was  $49.3 \pm 2.5 \%$  ( $63.3 \pm 3.8 \mu\text{g}/\text{cm}^2$ ) during 2 cycles and reached 98.5 % ( $125.7 \mu\text{g}/\text{cm}^2$ ) by the 3rd cycle. This result may indicate the process of chitosan swelling which leads to the reduction in the degree of crosslinking and increasing in the number of binding sites. The average desorption efficiency of the TM+Ch

membrane was  $77.9 \pm 7 \%$  during the experiments. No adsorption and desorption activity of the TM+PVDF membrane was observed. Summing up, the highest values of adsorption efficiency were measured for HMs while the desorption efficiency was relatively low. Nevertheless, the HMs are able to provide effective dye removal within 3 cycles.

### Conclusions

In summary, the design of HMs based on Ch and PVDF NFs modified TMs and Ni-MOF was successfully implemented. Morphology, structure and performance parameters of HMs were investigated. It was found that Ni-MOF has an ability to form uniform superstructures with average diameter  $\sim 20 \mu\text{m}$  on the surface of hydrophilic Ch and hydrophobic PVDF NFs. The adsorption characteristics were studied both for the Ni-MOF powder and for HMs. The adsorption process was best described by the PSO kinetic model for both contaminants, while the Temkin isotherm fitted well for MO, and the Langmuir isotherm was more suitable for Rh B. The Ni-MOF powder exhibited maximum experimentally found adsorption capacity towards MO and Rh B as high as  $120.2 \pm 1.5 \text{ mg/g}$  (at  $300 \text{ mg/L}$  of initial concentration) and  $0.67 \pm 0.11 \text{ mg/g}$  (at  $30 \text{ mg/L}$  of initial concentration), respectively. The adsorption measurements in dead-end filtration mode showed maximum values of dye adsorption by HMs as high as  $\sim 97 \%$  ( $\sim 380 \mu\text{g/cm}^2$ ) for MO and  $\sim 9 \%$  ( $\sim 37 \mu\text{g/cm}^2$ ) for Rh B. Investigations of regeneration possibilities have shown that the HMs are able to provide effective dye removal within 3 cycles. This study demonstrates an approach to design practical HMs for the application in wastewater treatment. It can be noted that the described approach might be used in the future to design innovative and processable materials for wound healing, racemic mixtures separation and sensing applications.

### Funding

This research was fulfilled as part of the Topical plan of the Joint Institute for Nuclear Research, No. 07-5-1131-2-2024/2028 “Nanocomposite and Functional Track Etched Membranes”.

### Author Information\*

*\*The authors' names are presented in the following order: First Name, Middle Name and Last Name*

**Nikita Alekseevich Drozhzhin** (*corresponding author*) — PhD Student, Department of Chemistry, New Technologies and Materials, Dubna University, Universitetskaya Street, 19, 141982, Dubna, Russia; Engineer, Joint Institute for Nuclear Research, Joliot-Curie Street, 6, 141980, Dubna, Russia; e-mail: [dna.17@uni-dubna.ru](mailto:dna.17@uni-dubna.ru); <https://orcid.org/0009-0008-5687-5822>

**Olga Yuryevna Ponomareva** — Candidate of Chemical Sciences, Researcher, Joint Institute for Nuclear Research, Joliot-Curie Street, 6, 141980, Dubna, Russia; e-mail: [oyuivanshina@mail.ru](mailto:oyuivanshina@mail.ru); <https://orcid.org/0000-0001-8551-5246>

**Ilya Igorevich Vinogradov** — Candidate of Chemical Sciences, Head of sector, Joint Institute for Nuclear Research, Joliot-Curie Street, 6, 141980, Dubna, Russia; e-mail: [ily7345@gmail.com](mailto:ily7345@gmail.com); <https://orcid.org/0000-0002-3056-2165>

**Genrikh Vladimirovich Serpionov** — Candidate of Biological Sciences, Researcher, Joint Institute for Nuclear Research, Joliot-Curie Street, 6, 141980, Dubna, Russia; e-mail: [genrihserpionov@gmail.com](mailto:genrihserpionov@gmail.com); <https://orcid.org/0009-0001-4545-8811>

**Abubakir Kanet** — Researcher, Institute of Batteries, Kabanbay Batyr Avenue, 53, Z00X8P9, Astana, Kazakhstan; e-mail: [kanet707vhs@gmail.com](mailto:kanet707vhs@gmail.com); <https://orcid.org/0009-0006-7914-6628>

**Daria Vladimirovna Nikolskaya** — Engineer, Joint Institute for Nuclear Research, Joliot-Curie Street, 6, 141980, Dubna, Russia; e-mail: [nikolskaya@jinr.ru](mailto:nikolskaya@jinr.ru); <https://orcid.org/0009-0004-2181-1002>

**Tatiana Nikolaevna Vershinina** — Candidate of Physical and Mathematical Sciences, Senior Researcher, Joint Institute for Nuclear Research, Joliot-Curie Street, 6, 141980, Dubna, Russia; e-mail: [vershinina@nf.jinr.ru](mailto:vershinina@nf.jinr.ru); <https://orcid.org/0000-0002-7748-5443>

### Author Contributions

The manuscript was written through contributions of all authors. All authors have given approval to the final version of the manuscript. **CRedit**: **Nikita Alekseevich Drozhzhin** investigation, methodology, visualization, writing-original draft; **Olga Yuryevna Ponomareva** conceptualization, investigation, methodology, validation, editing; **Ilya Igorevich Vinogradov** conceptualization, investigation, methodology, validation, editing; **Genrikh Vladimirovich Serpionov** investigation, methodology, validation; **Abubakir Kanet** investigation, methodology, editing; **Daria Vladimirovna Nikolskaya** investigation, methodology; **Tatiana Nikolaevna Vershinina** investigation, editing.

### Acknowledgments

Authors thank the team of Center of Applied Physics of Joint Institute for Nuclear Research for support and especially grateful to A.N. Nechaev for original idea and valuable remarks.

### Conflicts of Interest

The authors declare no conflict of interest.

### Notes

The graphical abstract was created in BioRender.

### References

- 1 Farhan Hanafi, M., & Sapawe, N. (2020). A review on the water problem associate with organic pollutants derived from phenol, methyl orange, and remazol brilliant blue dyes. *Materials Today: Proceedings*, 31, A141–A150. <https://doi.org/10.1016/J.MATPR.2021.01.258>
- 2 Habtemariam, T. H., Raju, V. J. T., & Chebude, Y. (2023). Pillared-Layer Metal-Organic Frameworks (MOFs) for Photo-degradation of Methyl Orange in Wastewater. *Advanced Optical Materials*, 11(10). <https://doi.org/10.1002/adom.202202843>
- 3 Kishor, R., Purchase, D., Saratale, G. D., Romanholo Ferreira, L. F., Hussain, C. M., Mulla, S. I., & Bharagava, R. N. (2021). Degradation mechanism and toxicity reduction of methyl orange dye by a newly isolated bacterium *Pseudomonas aeruginosa* MZ520730. *Journal of Water Process Engineering*, 43, 102300. <https://doi.org/10.1016/J.JWPE.2021.102300>
- 4 Ali, I., Burakova, I., Galunin, E., Burakov, A., Mkrtchyan, E., Melezhi, A., Kurnosov, D., Tkachev, A., & Grachev, V. (2019). High-Speed and High-Capacity Removal of Methyl Orange and Malachite Green in Water Using Newly Developed Mesoporous Carbon: Kinetic and Isotherm Studies. *ACS Omega*, 4(21), 19293–19306. <https://doi.org/10.1021/acsomega.9b02669>
- 5 Behera, A. K., Shadangi, K. P., & Sarangi, P. K. (2024). Efficient removal of Rhodamine B dye using biochar as an adsorbent: Study the performance, kinetics, thermodynamics, adsorption isotherms and its reusability. *Chemosphere*, 354, 141702. <https://doi.org/10.1016/J.CHEMOSPHERE.2024.141702>
- 6 Ghibate, R., Senhaji, O., & Taouil, R. (2021). Kinetic and thermodynamic approaches on Rhodamine B adsorption onto pomegranate peel. *Case Studies in Chemical and Environmental Engineering*, 3, 100078. <https://doi.org/10.1016/J.CSCEE.2020.100078>
- 7 Oladoye, P. O., Kadhon, M., Khan, I., Hama Aziz, K. H., & Alli, Y. A. (2024). Advancements in adsorption and photodegradation technologies for Rhodamine B dye wastewater treatment: fundamentals, applications, and future directions. *Green Chemical Engineering*, 5(4), 440–460. <https://doi.org/10.1016/J.GCE.2023.12.004>
- 8 Bal, G., & Thakur, A. (2022). Distinct approaches of removal of dyes from wastewater: A review. *Materials Today: Proceedings*, 50, 1575–1579. <https://doi.org/10.1016/J.MATPR.2021.09.119>
- 9 Bode-Aluko, C. A., Pereao, O., Ameh, A. E., Omoniyi, E., Nechaev, A., & Petrik, L. (2025). Removal of rhodamine 6G from aqueous solution in a continuous mode using nano-micro composite membranes. *Nano Trends*, 9, 100096. <https://doi.org/10.1016/J.NWNANO.2025.100096>
- 10 Xiang, W., Wang, Q., Li, Z., Dong, J., Liu, J., Zhang, L., Xia, T., He, Y., & Zhao, D. (2024). Water-stable methyl-modified MOF and mixed matrix membrane for efficient adsorption and separation of cationic dyes. *Separation and Purification Technology*, 330, 125268. <https://doi.org/10.1016/J.SEPPUR.2023.125268>
- 11 Jiao, L., Seow, J. Y. R., Skinner, W. S., Wang, Z. U., & Jiang, H. L. (2019). Metal-organic frameworks: Structures and functional applications. *Materials Today*, 27, 43–68. <https://doi.org/10.1016/J.MATTOD.2018.10.038>
- 12 Ramírez, D. J., Alfonso Herrera, L. A., Colorado-Peralta, R., Rodríguez, R. P., Camarillo Reyes, P. K., Chiñas, L. E., Sánchez, M., & Rivera, J. M. (2021). Highly efficient methyl orange adsorption by UV-012, a new crystalline Co(II) MOF. *CrystEngComm*, 23(19), 3537–3548. <https://doi.org/10.1039/D0CE00741B>
- 13 Sağlam, S., Türk, F. N., & Arslanoğlu, H. (2023). Use and applications of metal-organic frameworks (MOF) in dye adsorption: Review. *Journal of Environmental Chemical Engineering*, 11(5), 110568. <https://doi.org/10.1016/J.JECE.2023.110568>

- 14 Huang, J., Huang, D., Zeng, F., Ma, L., & Wang, Z. (2021). Photocatalytic MOF fibrous membranes for cyclic adsorption and degradation of dyes. *Journal of Materials Science*, 56(4), 3127–3139. <https://doi.org/10.1007/s10853-020-05473-x>
- 15 Markov, P. A., Vinogradov, I. I., Kostromina, E., Eremin, P. S., Gilmutdinova, I. R., Kudryashova, I. S., Greben, A., Rachin, A. P., & Nechaev, A. N. (2022). A wound dressing based on a track-etched membrane modified by a biopolymer nanoframe: physicochemical and biological characteristics. *European Polymer Journal*, 181, 111709. <https://doi.org/10.1016/J.EURPOLYMJ.2022.111709>
- 16 Perea, O., Uche, C., Bublikov, P. S., Bode-Aluko, C., Rossouw, A., Vinogradov, I. I., Nechaev, A. N., Opeolu, B., & Petrik, L. (2021). Chitosan/PEO nanofibers electrospun on metallized track-etched membranes: fabrication and characterization. *Materials Today Chemistry*, 20, 100416. <https://doi.org/10.1016/J.MTCHEM.2020.100416>
- 17 Vinogradov, I. I., Petrik, L., Serpionov, G. V., & Nechaev, A. N. (2021). Composite Membrane Based on Track-Etched Membrane and Chitosan Nanoscaffold. *Membranes and Membrane Technologies*, 3(6), 400–410. <https://doi.org/10.1134/S2517751621060093>
- 18 Vinogradov, I. I., Andreev, E. V., Yushin, N. S., Sokhatskii, A. S., Altynov, V. A., Gustova, M. V., Vershinina, T. N., Zin'kovskaya, I., Nechaev, A. N., & Apel', P. Yu. (2023). A Hybrid Membrane for the Simultaneous Selective Sorption of Cesium in the Ionic and Colloid Forms. *Theoretical Foundations of Chemical Engineering*, 57(4), 549–562. <https://doi.org/10.1134/S0040579523040498>
- 19 Vinogradov, I. I., Drozhzhin, N. A., Kravets, L. I., Rossouw, A., Vershinina, T. N., & Nechaev, A. N. (2024). Formation of Hybrid Membranes for Water Desalination by Membrane Distillation. *Colloid Journal*, 86(5), 667–679. <https://doi.org/10.1134/S1061933X24600519>
- 20 Rossouw, A., Olejniczak, A., Olejniczak, K., Gorberg, B., Vinogradov, I., Kristavchuk, O., Nechaev, A., Petrik, L., Perold, W., & Dmitriev, S. (2022). Ti and TiO<sub>2</sub> magnetron sputtering in roll-to-roll fabrication of hybrid membranes. *Surfaces and Interfaces*, 31, 101975. <https://doi.org/10.1016/J.SURFIN.2022.101975>
- 21 Ivashina, O. Yu., Zuba, I., Sumnikov, S. V., Nabiye, A. A., & Pawlukojć, A. (2021). L-Tryptophan metal-organic frameworks based on transition metals: Preparation, characterization and application for ruthenium 3+ ions sorption. 020001. <https://doi.org/10.1063/5.0063607>
- 22 Ponomareva, O. Yu., Drozhzhin, N. A., Vinogradov, I. I., Vershinina, T. N., Altynov, V. A., Zuba, I., Nechaev, A. N., & Pawlukojć, A. (2024). Metal–Organic Framework Based on Nickel, L-Tryptophan, and 1,2-Bis(4-Pyridyl)Ethylene, Consolidated on a Track-Etched Membrane. *Russian Journal of Inorganic Chemistry*, 69(6), 914–924. <https://doi.org/10.1134/S0036023624600667>
- 23 Ho, Y. S. (2006). Review of second-order models for adsorption systems. *Journal of Hazardous Materials*, 136(3), 681–689. <https://doi.org/10.1016/J.JHAZMAT.2005.12.043>
- 24 Lu, H., Yang, Q., Huang, B., Qi, J., Wang, R., Zhou, Q., Chen, Q., Zhu, L., Jin, J., & Kong, Y. (2023). Removal performance and adsorption kinetics of dyes by a Co-based metal organic framework. *Microporous and Mesoporous Materials*, 360, 112665. <https://doi.org/10.1016/J.MICROMESO.2023.112665>
- 25 Abin-Bazaine, A., Campos Trujillo, A., & Olmos-Marquez, M. (2022). Adsorption Isotherms: Enlightenment of the Phenomenon of Adsorption. In *Wastewater Treatment*. *IntechOpen*. <https://doi.org/10.5772/intechopen.104260>
- 26 Sahoo, T. R., & Prelot, B. (2020). Adsorption processes for the removal of contaminants from wastewater: the perspective role of nanomaterials and nanotechnology. *Nanomaterials for the Detection and Removal of Wastewater Pollutants*, 161–222. <https://doi.org/10.1016/B978-0-12-818489-9.00007-4>
- 27 Li, X., Wang, J., Zhang, X., & Chen, C. (2015). Powdered activated carbon adsorption of two fishy odorants in water: Trans, trans-2,4-heptadienal and trans, trans-2,4-decadienal. *Journal of Environmental Sciences*, 32, 15–25. <https://doi.org/10.1016/J.JES.2015.01.001>

Saniya R. Rakisheva<sup>1,2</sup> , Dinara T. Nurpeisova<sup>1,2</sup> , Alisher M. Zhumabayev<sup>1,2</sup> ,  
Nursanat Parmanbek<sup>1</sup> , Murat Barsbay<sup>3</sup> , Anastasiya A. Mashentseva<sup>1,2\*</sup> 

<sup>1</sup>Institute of Nuclear Physics of the Republic of Kazakhstan, Almaty, Kazakhstan;

<sup>2</sup>L.N. Gumilyov Eurasian National University, Astana, Kazakhstan;

<sup>3</sup>Department of Chemistry, Polymer Chemistry Division, Hacettepe University, Ankara, Türkiye

(\*Corresponding author's e-mail: [a.mashentseva@inp.kz](mailto:a.mashentseva@inp.kz))

## Galvanic Replacement-Assisted Synthesis of Cu–Ag Composite Membrane Catalysts for Potassium Ferricyanide Reduction

This study investigates the catalytic properties of mono- and bimetallic composite track-etched membranes (CTeMs) fabricated using a galvanic replacement strategy. Two bimetallic architectures, Ag/Cu@PET and Cu/Ag@PET, were synthesized by sequentially depositing copper and silver onto poly(ethylene terephthalate) (PET) templates. X-ray diffraction analysis revealed that doping Cu@PET with silver nanoparticles formed a substitutional solid solution (Ag<sub>97</sub>Cu<sub>3</sub>), which increased crystallinity by >45 % compared to monometallic Cu@PET. In contrast, doping Ag@PET with copper produced a two-layer tubular structure with phase-separated copper co-deposited along silver microtubes. The catalytic performance was evaluated through the pseudo-first-order reduction of potassium ferricyanide (PFC) by sodium borohydride. The Cu/Ag@PET composite with separate phases demonstrated superior activity, achieving 94.3 % PFC reduction within 40 minutes, significantly exceeding the performance of monometallic Ag@PET and Cu@PET. Kinetic analysis indicated that the rate constant and activation energy strongly depended on membrane structure and silver doping time in case of formation of substitutional solid solution phase. A minimum doping duration of 20 minutes was required for performance enhancement, with 30-minute Ag/Cu@PET samples reducing activation energy from 62.35 kJ/mol to 32.67 kJ/mol. These findings highlight the critical role of metal deposition order and structural configuration in optimizing catalytic activity, demonstrating the efficacy of galvanic replacement for designing high-performance, multi-metallic membrane catalysts.

**Keywords:** composite, track-etched membranes, galvanic replacement, reduction, photocatalysts, bimetallic, poly(ethylene terephthalate), silver, copper

### 1. Introduction

The development of hybrid and multicomponent nanostructured materials has gained increasing attention due to their superior performance compared to monometallic systems in fields such as catalysis, sensing, energy storage, and water purification [1–4]. Among various synthesis strategies, template-based electroless deposition provides a versatile and scalable approach to fabricate metal micro- and nanostructures with controllable dimensions and morphology [5, 6]. Depending on the type of redox pathway, the chemical deposition techniques within polymeric templates can be categorized into classical electroless deposition [7], galvanic replacement [8], and radiation-induced chemical reduction [9], as schematically summarized in Figure 1.

In electroless deposition, a reducing agent chemically reduces metal ions to form a metallic layer on the template surface. The process typically requires sensitization and activation steps and has been widely used for the fabrication of uniform metal microtubes inside track-etched membranes (TeMs). This technique allows for precise control over the geometry and composition of micro/nanotubes by adjusting factors such as temperature, time [10], and the composition of complexing agents in the plating bath [11, 12]. Notably, copper-based CTeMs have demonstrated significant promise in applications such as catalysis [13, 14], and heavy metal adsorption [15, 16].

Galvanic replacement (GR), is an efficient method of introducing a second, more noble metal into pre-formed structures of a less noble metal. During this spontaneous redox reaction, the less noble metal (M<sub>I</sub>) serves as a sacrificial reductant, donating electrons to the more noble metal ion (M<sub>II</sub>). This ion then deposits onto the surface while partially dissolving the base material [17, 18]. This process enables the synthesis of bimetallic and even trimetallic structures with improved catalytic, electronic, or optical properties. For ex-



ample, a Cu<sub>2</sub>O/ZnO@PET composite was previously synthesized using this method, forming a multiphase material with a solid-solution phase of CuZn and enhanced photocatalytic performance [19].

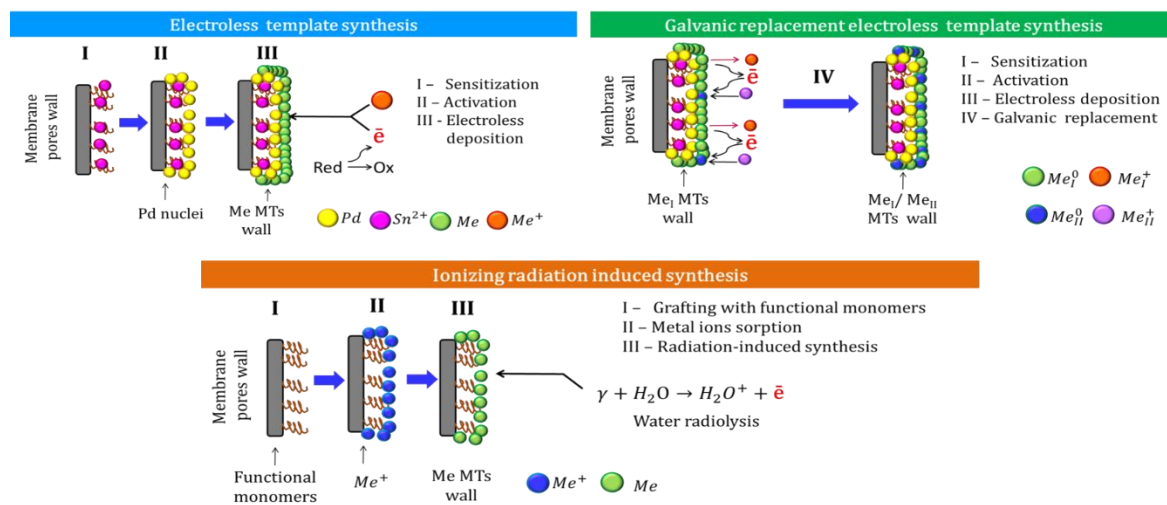


Figure 1. Schemes of CTeM synthesis using different synthesis approaches

Radiation-induced synthesis is an alternative approach that uses high-energy radiation (e.g.,  $\gamma$ -rays, e-beam) to generate solvated electrons for the in-situ reduction of metal ions immobilized on functionalized templates. This technique has been successfully used to synthesize various metallic nanostructures including copper [20], silver, and gold [21] within grafted polymer matrices. However, its application is more specialized and often requires elaborate pretreatment steps.

While many of these methods have been explored individually, fewer studies have systematically examined the effect of combining sequential deposition and galvanic replacement strategies within the same membrane system. In particular, bimetallic systems such as Ag/Cu or Cu/Ag, where one metal overlays the other, offer potential synergistic effects due to modified surface electronic structures and enhanced interfacial reactivity. In this study, we explore for the first time the catalytic performance of Ag/Cu@PET and Cu/Ag@PET composite TeMs synthesized via a combination of electroless plating and galvanic replacement. The structural features, crystallinity, and phase composition of these materials are correlated with their ability to catalyze the reduction of potassium ferricyanide (PFC), a model inorganic pollutant.

PFC is a redox-active compound known for its environmental persistence and toxicity [22, 23]. In aqueous systems, PFC acts as a stable source of highly toxic Fe(III) [24], which upon reduction to Fe(II) becomes significantly less harmful and can even be beneficial to metabolic processes [25]. The Fe(III) to Fe(II) reduction is relevant not only for environmental detoxification but also in various industrial processes such as tin refining copper extraction [26], wine and citric acid production [27], pigment formation [28, 29], anti-oxidant activity [30], and chemical sensing [31].

Previously, we demonstrated that Cu-based CTeMs synthesized via electroless deposition with ascorbic acid could achieve over 90 % conversion of Fe(III) to Fe(II) in PFC solutions [32]. Building upon this work, we hypothesize that doping such structures with a second metal via galvanic replacement could lower activation barriers, increase electron transfer rates, and improve overall catalytic efficiency. We therefore investigate both Ag/Cu@PET and Cu/Ag@PET configurations to assess how synthesis pathway and metal combination influence catalytic activity, crystallinity, and morphology. To the best of our knowledge, this is one of the first comparative studies to systematically examine the effects of metal sequence (Cu  $\rightarrow$  Ag vs. Ag  $\rightarrow$  Cu), doping time, and solid solution formation (Ag<sub>97</sub>Cu<sub>3</sub>) in the context of PFC reduction using CTeMs. The results may offer valuable insights into the design of next-generation multicomponent membrane catalysts for environmental applications.

## 2. Experimental

### 2.1 Chemicals

All chemicals were used as received without further purification. Analytical grade reagents including copper(II) sulfate pentahydrate (CuSO<sub>4</sub>·5H<sub>2</sub>O), silver nitrate (AgNO<sub>3</sub>), formaldehyde (CH<sub>2</sub>O), sodium boro-

hydride ( $\text{NaBH}_4$ ), potassium ferricyanide ( $\text{K}_3[\text{Fe}(\text{CN})_6]$ ), sodium-potassium tartrate ( $\text{KNaC}_4\text{H}_4\text{O}_6 \cdot 4\text{H}_2\text{O}$ ), pyridine, and palladium chloride ( $\text{PdCl}_2$ ) were purchased from Sigma-Aldrich. Deionized water (resistivity  $18.2 \text{ M}\Omega \cdot \text{cm}$ , Aqualon D-301) was used throughout all experiments.

## 2.2 Synthesis of Composite Track-Etched Membranes (CTeMs)

Commercial poly(ethylene terephthalate) (PET) track-etched membranes with a nominal thickness of  $12 \mu\text{m}$  and a pore density of  $4 \times 10^7$  pores/ $\text{cm}^2$  were used as the template. Following chemical etching in  $2.2 \text{ M NaOH}$  at  $70^\circ\text{C}$ , gas permeability analysis determined the average pore diameter to be  $410 \pm 12 \text{ nm}$ . Prior to metal deposition, the membranes were sensitized and activated using standard procedures. For silver plating, the PET templates were immersed sequentially in sensitization solution ( $50 \text{ g/L SnCl}_2$  in  $60 \text{ mL/L}$  concentrated  $\text{HCl}$  for  $15 \text{ min}$ ) and activation solution ( $59 \text{ mM AgNO}_3$  and  $230 \text{ mM NH}_3$  for  $3 \text{ min}$ ) [33]. For copper plating, a more robust activation protocol was applied, consisting of three sequential sensitization-activation cycles [34]. Composite membranes were fabricated in two configurations: (i)  $\text{Ag/Cu@PET}$ : Silver was deposited onto  $\text{Cu@PET}$  templates using a galvanic exchange reaction in an  $\text{AgNO}_3$ -containing bath; (ii)  $\text{Cu/Ag@PET}$ : Copper was deposited onto  $\text{Ag@PET}$  templates via galvanic replacement in a  $\text{CuSO}_4$ /formaldehyde bath. The detailed compositions of the plating baths, pH, temperature, and deposition times are summarized in Table 1.

Table 1

Experimental details of the synthesis of composite TeMs

Composite	Plating Bath Composition	Plating Conditions			Ref.
		Adjusted pH	$T$ ( $^\circ\text{C}$ )	Plating Time (min)	
$\text{Ag@PET}$	$\text{AgNO}_3$ ( $17 \text{ mM}$ ), potassium tartrate ( $120 \text{ mM}$ ), pyridine ( $50 \text{ mM}$ )	—	$3 \pm 1$	300	[33]
$\text{Cu@PET}$	$\text{CuSO}_4 \cdot 5\text{H}_2\text{O}$ ( $5 \text{ g/L}$ ), $\text{KNaC}_4\text{H}_4\text{O}_6 \cdot 4\text{H}_2\text{O}$ ( $18 \text{ g/L}$ ), $\text{NaOH}$ ( $7 \text{ g/L}$ ), $\text{CH}_2\text{O}$ ( $0.13 \text{ M}$ )	12.45 ( $\text{H}_2\text{SO}_4$ )	$3 \pm 1$	40	[34]
$\text{Cu/Ag@PET}$	Same as Cu plating bath, using $\text{Ag@PET}$ as the template	12.45 ( $\text{H}_2\text{SO}_4$ )	$3 \pm 1$	20	This work
$\text{Ag/Cu@PET}$	Same as Ag plating bath, using $\text{Cu@PET}$ as the template	—	$3 \pm 1$	5–30	

## 2.3 Catalytic Activity Evaluation

Catalytic activity was assessed by measuring the reduction of potassium ferricyanide (PFC) using sodium borohydride in aqueous medium. A  $2 \times 2 \text{ cm}^2$  CTeM sample was immersed in a 1:1 mixture of PFC ( $6.0 \times 10^{-5} \text{ M}$ ,  $20 \text{ mL}$ ) and  $\text{NaBH}_4$  ( $5.3 \times 10^{-3} \text{ M}$ ,  $20 \text{ mL}$ ). The reaction was carried out at room temperature with gentle stirring. Aliquots ( $350 \mu\text{L}$ ) were withdrawn at 10-minute intervals, and the optical absorbance at  $420 \text{ nm}$  was recorded using a Specord-250 spectrophotometer (Analytik Jena, Germany) in the wavelength range of  $250\text{--}500 \text{ nm}$ .

The reduction percentage ( $D$ , %) was calculated using:

$$D, \% = \frac{C_0 - C_t}{C_0} \times 100 \% = \frac{A_0 - A_t}{A_0} \times 100 \%, \quad (1)$$

where  $A_0$  and  $A_t$  are the absorbance values at time 0 and time  $t$ , respectively, and  $C_0$  and  $C_t$  are the concentration values of PFC at the initial time and time  $t$  [13].

A series of experiments were conducted within the temperature range of  $20$  to  $30^\circ\text{C}$  to investigate the influence of temperature on the catalytic efficiency of PFC reduction. The reduction reaction was monitored spectrophotometrically for each experiment, and the rate constants ( $k$ , in  $\text{min}^{-1}$ ) were determined based on the pseudo-first-order kinetic model.

The activation energy ( $E_a$ ) was calculated by applying the Arrhenius equation [19]:

$$\ln k = \ln A - (E_a / RT), \quad (2)$$

where  $k$  is the apparent rate constant ( $\text{min}^{-1}$ ),  $A$  is the pre-exponential factor,  $E_a$  is the activation energy ( $\text{J/mol}$ ),  $R$  is the universal gas constant ( $8.314 \text{ J/mol} \cdot \text{K}$ ), and  $T$  is the absolute temperature in Kelvin ( $\text{K}$ ). A linear plot of  $\ln k$  versus  $1000/T$  was constructed, and the slope ( $-E_a/R$ ) was used to calculate the activation energy graphically.

## 2.4 Investigation of the Composition and Structure of Composite Catalysts

The morphology and dimensional features of the synthesized composite track-etched membranes (CTeMs) were examined using a JEOL JFC-7500F field-emission scanning electron microscope (FE-SEM). Prior to analysis, membrane samples were sputter-coated with a thin layer of gold to enhance conductivity. The energy-dispersive X-ray spectroscopy (EDX) was performed using a Hitachi TM3030 SEM equipped with a Bruker XFlash MIN SVE detector, operating at an acceleration voltage of 15 kV. Elemental mapping and point analysis were used to confirm the distribution and relative abundance of metal phases (Ag and Cu) within the composite membranes.

The inner diameters and wall thicknesses of the metal microtubes, as well as the initial pore size of the PET template, were estimated by gas-flow porometry. The calculation was performed using the Hagen–Poiseuille equation [35], which relates the pressure-driven gas permeability through cylindrical pores to their geometric dimensions. The deposition rate of copper ( $R$ ) was calculated as the mass gain per unit area per hour, expressed in  $\text{mg}/\text{cm}^2\cdot\text{h}$ , based on the difference in membrane weight before and after plating.

Crystallographic analysis of the deposited metallic structures was carried out using an X-ray diffractometer (Bruker D8 Advance, Germany) equipped with a Cu  $K_\alpha$  radiation source ( $\lambda = 1.5406 \text{ \AA}$ ). XRD patterns were collected in the  $2\theta$  range of  $30^\circ$  to  $80^\circ$ , with a step size of  $0.02^\circ$  and a counting time of 1 second per step. The system operated at 40 kV and 40 mA.

The average crystallite size ( $L$ ) was estimated using the Scherrer equation, applied to the full width at half maximum (FWHM) of the most prominent diffraction peaks. The FWHM values were determined through peak fitting using pseudo-Voigt functions, which enabled accurate quantification of crystallinity and phase identification.

## 3. Results and Discussion

### 3.1 Synthesis and Structural Analysis of Composite TeMs

The changes in the structural parameters of the synthesized mono- and bimetallic composite track-etched membranes (CTeMs) are summarized in Table 2. The data demonstrate that the deposition rates ( $R$ ) obtained during the second stage of synthesis (i.e., galvanic replacement) were comparable for both Ag/Cu@PET and Cu/Ag@PET composites, with values of 0.557 and 0.593  $\text{mg}/\text{cm}^2\cdot\text{h}$ , respectively, in addition to Ag@PET (0.255  $\text{mg}/\text{cm}^2\cdot\text{h}$ ) and Cu@PET (0.251  $\text{mg}/\text{cm}^2\cdot\text{h}$ ) composites. These values indicate that the kinetics of metal substitution or secondary deposition are relatively unaffected by whether silver is deposited on copper or vice versa under the given conditions.

Despite similar deposition rates, the wall thickness of the Ag-based hybrid microtubes was found to be significantly higher than that of the Cu-based analogs. Specifically, the silver layer in Ag@PET was  $120.6 \pm 4.2 \text{ nm}$  thick, which is almost double the thickness of the copper layer in Cu@PET ( $64.2 \pm 10.9 \text{ nm}$ ). This discrepancy is likely attributed to differences in the precursor concentration, ion reduction potential, and metal nucleation/growth behavior in the respective plating baths.

Interestingly, for the Ag/Cu@PET composite, a notable reduction in the net silver mass increment ( $\Delta m = 5.2 \text{ mg}$ ) was observed compared to the monometallic Ag@PET ( $\Delta m = 25.5 \text{ mg}$ ). This decrease suggests that partial dissolution of the underlying copper microtubes occurs during galvanic replacement, reducing the overall mass gain. Such dissolution is consistent with the spontaneous redox nature of the galvanic process, where the less noble metal (Cu) acts as the sacrificial anode, donating electrons to reduce  $\text{Ag}^+$  ions. A similar trend was reported in other galvanic systems where structural hollowing or mass loss accompanies deposition of a more noble metal [17].

Table 2

Structural Parameters of Mono- and Bicomponent CTeMs

Sample	Inner Diameter of MTs (nm)	MT Wall Thickness (nm)		Deposition Rate $R$ ( $\text{mg}/\text{cm}^2\cdot\text{h}$ )		$\Delta m$ (mg)	
		$l(\text{Cu})$	$l(\text{Ag})$	$R_{\text{Cu}}$	$R_{\text{Ag}}$	Cu	Ag
Ag@PET	153.9±8.36	–	120.6±4.2	–	0.255	–	25.5
Cu/Ag@PET	144.4±1.8	56.9±0.9	–	0.593	–	7.9	–
Cu@PET	276.0±21.8	64.2±10.9	–	0.251	–	11.7	–
Ag/Cu@PET*	91.9±5.0	–	31.3±2.5	–	0.557	–	5.2

\*Deposition time for silver doping: 20 minutes.

Scanning electron microscopy (SEM) images (Fig. 3) confirmed the successful formation of hollow metal microtubes within the PET template in all samples. The observed tube structures were continuous and aligned along the template pores. There were distinguishable differences in wall thickness which were consistent with the porometry and gravimetric data presented in Table 2.

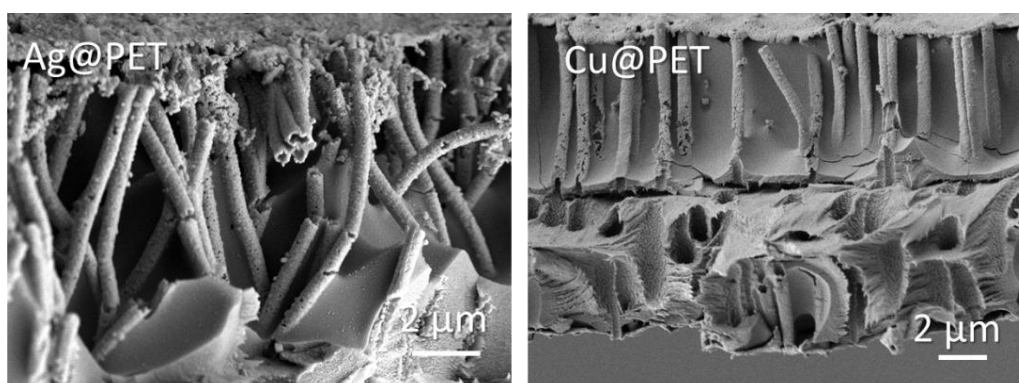


Figure 3. SEM images of cross sections of monocomponent CTeMs

The phase structure and crystallinity of the synthesized CTeMs were further analyzed using X-ray diffraction (XRD), and the results are presented in Table 3. The diffraction patterns for all samples (see Figure S1 in the Supplementary information file) showed good agreement with the standard JCPDS cards for face-centered cubic (fcc) silver (JCPDS 04-0783) and copper (JCPDS 04-0836), confirming the successful formation of the target phases.

Table 3

Crystal Structure Parameters of CTeMs

Sample	Phase	Struc- ture	Space group	<i>hkl</i>	2θ (°)	<i>d</i> (Å)	<i>L</i> (nm)	FWHM	Lattice parameter (Å)	CD (%)	Phase con- tent (%)	<i>V</i> (Å <sup>3</sup> )
Ag@PET	Ag	Cubic	Fm-3m(225)	111	38.20	2.35	36.33	0.26	<i>a</i> =4.07408	76.5	100	67.62
				200	44.25	2.05	24.45	0.39				
				220	64.48	1.44	35.13	0.30				
				311	77.36	1.23	33.98	0.33				
Cu/Ag@PET	Cu	Cubic	Fm-3m(225)	111	43.49	2.08	28.04	0.34	<i>a</i> =3.60662	79.6	27.9	46.91
	Ag	Cubic	Fm-3m(225)	111	38.05	2.36	33.20	0.28	<i>a</i> =4.07889		72.1	67.89
				200	44.25	2.05	21.99	0.43				
				220	64.48	1.44	27.89	0.37				
				311	77.43	1.23	23.79	0.48				
				111	43.49	2.08	28.04	0.34				
				200	44.33	2.04	34.30	0.28				
				220	64.48	1.44	39.67	0.26				
				311	77.59	1.23	37.57	0.30				
				222	81.50	1.18	45.62	0.26				
Cu@PET	Cu	Cubic	Fm-3m(225)	111	43.41	2.08	20.36	0.47	<i>a</i> =3.60579	67.9	100	46.88
				200	50.54	1.80	17.37	0.56				
				220	74.14	1.28	41.94	0.29				
Ag/Cu@PET	Ag <sub>97</sub> Cu <sub>3</sub>	Cubic	Fm-3m(225)	111	38.12	2.36	55.74	0.17	<i>a</i> =4.08490	78.9	100	68.16
				200	44.25	2.05	25.52	0.37				
				220	64.41	1.45	49.32	0.21				
				311	77.28	1.23	51.21	0.22				
				222	81.50	1.18	59.01	0.20				

Changes in the full width at half maximum (FWHM) of the diffraction peaks provided insights into the degree of crystallinity (CD) and average crystallite size (*L*). The FWHM values were obtained by fitting the

peaks using symmetric pseudo-Voigt functions, allowing accurate deconvolution of overlapping reflections. As expected, broader peaks indicated smaller crystallite sizes and lower structural order, while narrower peaks suggested better-defined crystalline domains.

XRD analysis of the Ag/Cu@PET sample revealed the formation of a substitutional solid solution with the nominal composition Ag<sub>97</sub>Cu<sub>3</sub> when Cu@PET was doped with silver nanoparticles. This membrane exhibited a high crystallinity degree (CD = 78.9 %) and large crystallite sizes (L), reaching to  $\approx 59$  nm, exceeding those observed in pure Cu@PET samples (CD = 67.9 %, L  $\approx 20$ –42 nm). The lattice parameter of the Ag<sub>97</sub>Cu<sub>3</sub> phase ( $a = 4.0849$  Å) was slightly expanded compared to pure Ag ( $a = 4.0741$  Å), reflecting Cu incorporation into the Ag lattice. In contrast, the Cu/Ag@PET membrane contained distinct and co-existing Cu and Ag phases without forming a solid solution. The copper phase exhibited smaller crystallites ( $L \approx 28$  nm) and broader FWHM values, while the silver phase maintained relatively higher crystallinity. These observations are consistent with partial deposition of copper over a preformed Ag structure and are in line with previously reported galvanic systems [17].

These structural differences suggest that the route of deposition (Ag over Cu vs. Cu over Ag) significantly influences the resulting crystallinity and phase homogeneity of the composite membranes. The formation of a single-phase solid solution in Ag/Cu@PET, as opposed to phase-segregated structures in Cu/Ag@PET, is likely to impact their respective catalytic performances, which will be discussed in the subsequent sections.

The elemental composition and spatial distribution of metal phases within the CTEMs were examined via energy-dispersive X-ray spectroscopy (EDX) (Fig. 4). Elemental mapping revealed a uniform and continuous distribution of the deposited metals (Ag and Cu) throughout the microtube walls in all membrane types. Notably, even after the sequential doping of monometallic membranes, the second metal phase exhibited homogenous incorporation, without any evidence of phase segregation or surface agglomeration.

Point analysis from EDX indicated that the average atomic concentrations of the dopant elements were approximately 0.6 at.% for copper in Ag@PET, and 29.4 at.% for silver in Cu@PET, confirming the success of the galvanic replacement reactions and the effective incorporation of the secondary metal phase.

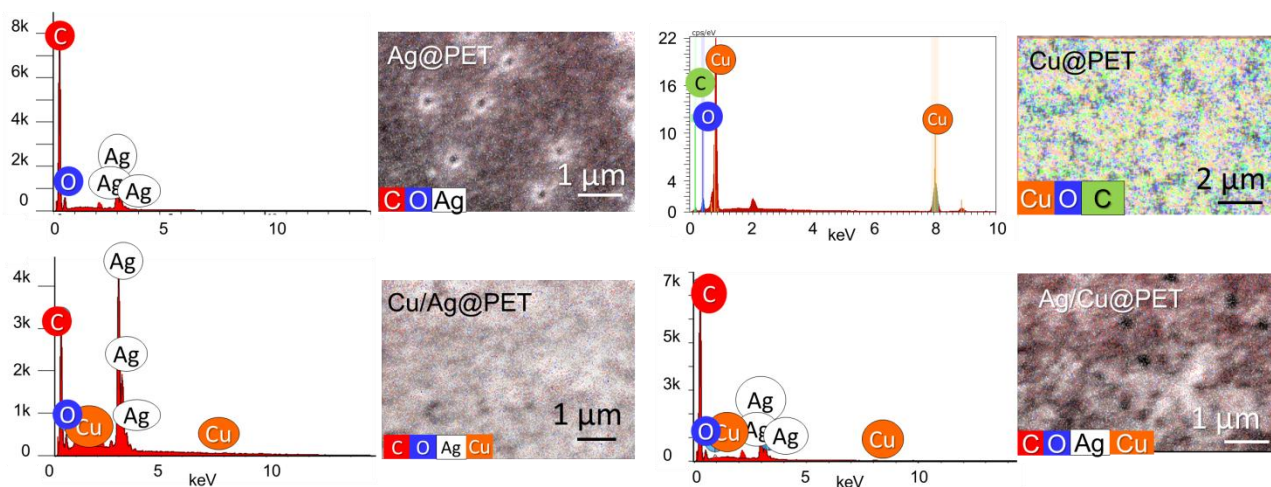


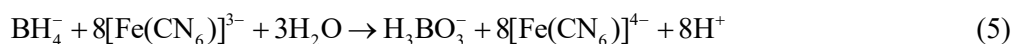
Figure 4. Energy-dispersive X-ray spectroscopy (EDX) analysis of CTEMs

### 3.2 Evaluation of Catalytic Activity via PFC reduction

The reduction of potassium ferricyanide ( $K_3[Fe(CN)_6]$ ) was employed as a model reaction to assess the catalytic performance of the synthesized membranes. This system is widely used to evaluate redox-active nanomaterials due to its well-defined electrochemical behavior and straightforward spectrophotometric monitoring [36].

In this reaction, either sodium borohydride ( $NaBH_4$ ) [25] or thiosulfate [37] acts as the reducing agent, converting ferricyanide ( $Fe^{3+}$ ) to ferrocyanide ( $Fe^{2+}$ ). This process is accompanied by a visible color change from yellow to colorless. The absorbance of  $Fe(III)$  species at 420 nm decreases progressively as the reaction proceeds, allowing real-time monitoring of the conversion degree. The overall redox reaction between ferricyanide and borohydride ions in aqueous solution is represented by the following equation [32].





This electron transfer is thermodynamically favorable due to the large difference in standard redox potentials:  $E^0(\text{Fe}^{3+} \text{ in } [\text{Fe}(\text{CN})_6]^{3-} / \text{Fe}^{2+} \text{ in } [\text{Fe}(\text{CN})_6]^{4-})$  is +0,44 V, while  $E^0(\text{BH}_4^-/\text{H}_3\text{BO}_3)$  is -1,24 V. This results in a highly exergonic process ( $\Delta G \ll 0$ ), which drives the reduction efficiently in the presence of an appropriate catalyst [32]. It is important to note that borohydride ions are also susceptible to hydrolysis, especially under acidic or neutral conditions, via:



This side reaction competes with the desired redox process and may reduce the effective reducing capacity of the system. However, in the present study, the catalytic tests were conducted at  $\text{pH} \approx 9$ , which significantly suppresses borohydride hydrolysis, rendering its effect negligible under experimental conditions.

Figure 5 shows the time-resolved UV–Vis absorption spectra for potassium ferricyanide (PFC) reduction, which were used to assess the catalytic efficiency of the synthesised CTEMs. The corresponding conversion efficiencies ( $D$ , %) are plotted in Figure 6. As expected, the monometallic Cu@PET membranes exhibited a high level of catalytic activity, achieving over 75 % reduction within the first 10 minutes of reaction. This observation is in agreement with previous studies that demonstrated the redox capabilities of copper microtubes prepared via electroless deposition [32]. When copper microtubes were subjected to galvanic replacement with silver to produce Ag/Cu@PET composites, XRD analysis confirmed that a substitutional solid solution ( $\text{Ag}_{97}\text{Cu}_3$ ) had formed. As shown in Figure 6a, the catalytic activity of Ag/Cu@PET was initially lower than that of pure Cu@PET, especially during the early stages of the reaction. Although the final PFC conversion after 40 minutes was comparable (94.3 % for Ag/Cu@PET vs. 90.8 % for Cu@PET), the overall enhancement in performance was modest. This suggests that the formation of a structurally ordered  $\text{Ag}_{97}\text{Cu}_3$  phase does not significantly enhance catalytic activity and may even inhibit it at shorter reaction times, possibly due to slower reduction rate as indicated by its lower rate constant ( $k$ ) of  $7.43 \times 10^{-2} \text{ min}^{-1}$ , compared to  $9.29 \times 10^{-2} \text{ min}^{-1}$  of Cu@PET (Section 3.3).

In contrast, the Cu/Ag@PET composites, composed of silver microtubes coated with a distinct ~60 nm copper layer, demonstrated a clear and substantial improvement in catalytic performance relative to their parent Ag@PET membranes. The monometallic Ag@PET system was the least active among all membranes tested, achieving only 79.4 % PFC reduction after 40 minutes. However, upon deposition of copper, the Cu/Ag@PET composites achieved up to 94.3 % conversion, reflecting a ~19 % improvement over Ag@PET. This performance gain can be attributed to the presence of physically separated Ag and Cu domains, rather than a uniform alloyed structure. The phase-separated nature of Cu/Ag@PET likely enables localized synergistic interactions at the Ag–Cu interfaces, facilitating enhanced electron transfer and increasing the density of catalytically active sites. Interestingly, while the  $\text{Ag}_{97}\text{Cu}_3$  solid solution formed in Ag/Cu@PET is structurally well-defined, it does not outperform the heterogeneous phase structure of Cu/Ag@PET (27.9 % Cu and 72.1 % Ag). This indicates that structural order alone does not guarantee improved catalytic behavior; rather, interfacial effects and compositional heterogeneity may be more critical in determining activity.

Previous studies have shown that silver in close proximity to copper can stabilize copper in a partially oxidized  $\text{Cu}^{\delta+}$  state, which binds reactants more strongly, thus enhancing surface reactivity [38, 39]. Additionally, silver nanoparticles are known to promote the reduction of surface copper oxides [40], leading to a process of in situ regeneration of active  $\text{Cu}^0$  sites, which is a more efficient phase in catalyzing this type of reactions [14]. This mechanism is particularly effective in biphasic or phase-segregated systems such as Cu/Ag@PET, where mutual electronic interactions between adjacent Cu and Ag phases can continuously sustain catalytic performance.

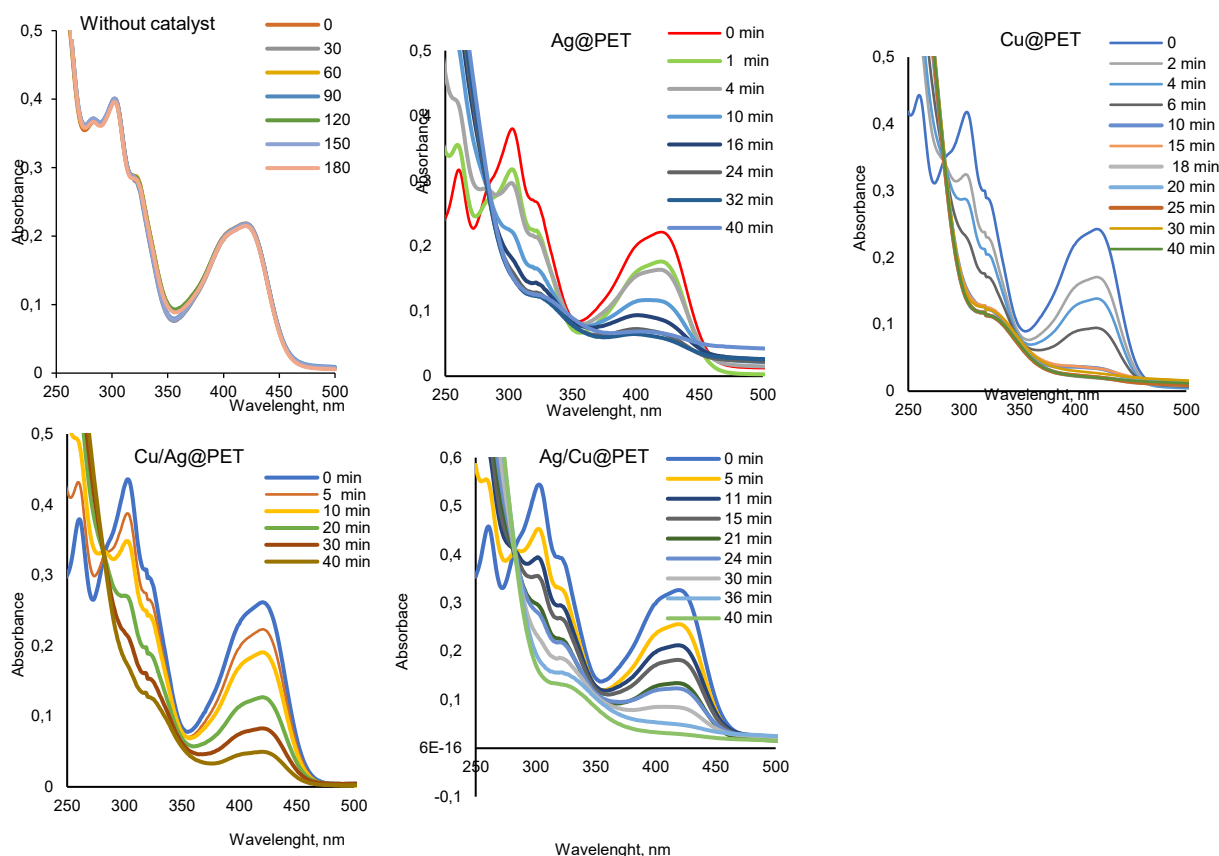


Figure 5. UV-Vis spectra of the PFC reduction reaction without the addition of a catalyst and in the presence of the studied composite catalysts

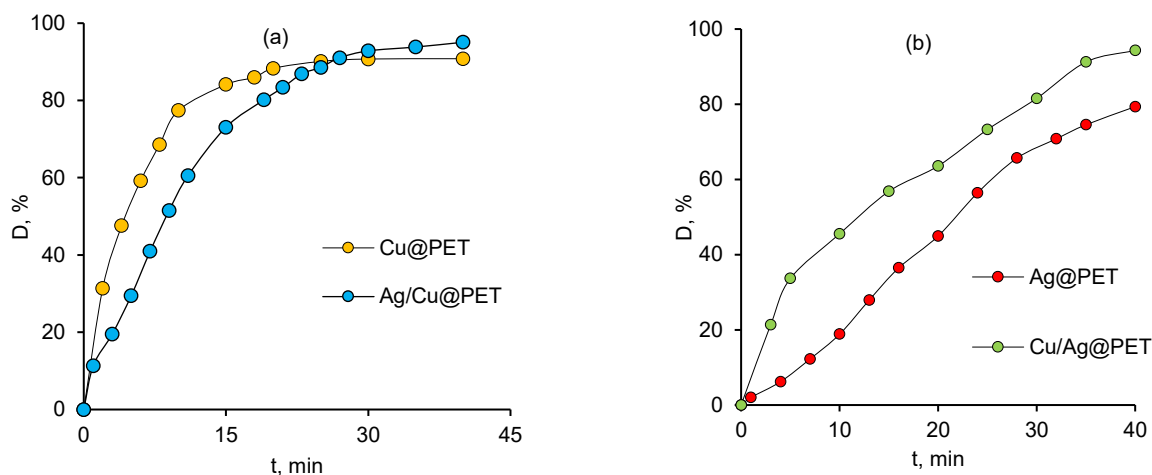


Figure 6. Change in the efficiency of PFC reduction for initial and modified samples based on MT of copper (a) and silver (b) (the doping time of the second component is 20 minutes)

### 3.3 Kinetics, Doping Time Effect, and Activation Energy

As expected for this class of redox reactions, the catalytic reduction of potassium ferricyanide (PFC) in the presence of nanoscale composite membranes was found to follow pseudo-first-order kinetics under conditions of excess sodium borohydride ( $\text{NaBH}_4$ ), [32]. The rate constants ( $k$ ) were determined from the slope of the linear plots of  $\ln(C_0/C)$  versus reaction time ( $t$ ), as shown in Figure 7. The high linearity of all curves confirms the proposed reaction order.

Among all studied membranes, the Ag@PET sample exhibited the lowest reaction rate constant, calculated as  $3.48 \times 10^{-2} \text{ min}^{-1}$ . In comparison, the Cu/Ag@PET composite, composed of a silver microtube sub-

strate coated with copper, exhibited a slightly higher rate of  $3.92 \times 10^{-2} \text{ min}^{-1}$ , indicating the beneficial influence of copper addition. Notably, the Cu@PET membranes demonstrated significantly greater reactivity, with a  $k$  value of  $9.29 \times 10^{-2} \text{ min}^{-1}$ , consistent with the well-established redox behavior of copper surfaces. The Ag/Cu@PET membranes, featuring a solid solution structure of  $\text{Ag}_{97}\text{Cu}_3$ , a lower rate constant of  $7.43 \times 10^{-2} \text{ min}^{-1}$  compared to its monometallic precursor membrane, i.e. Cu@PET.

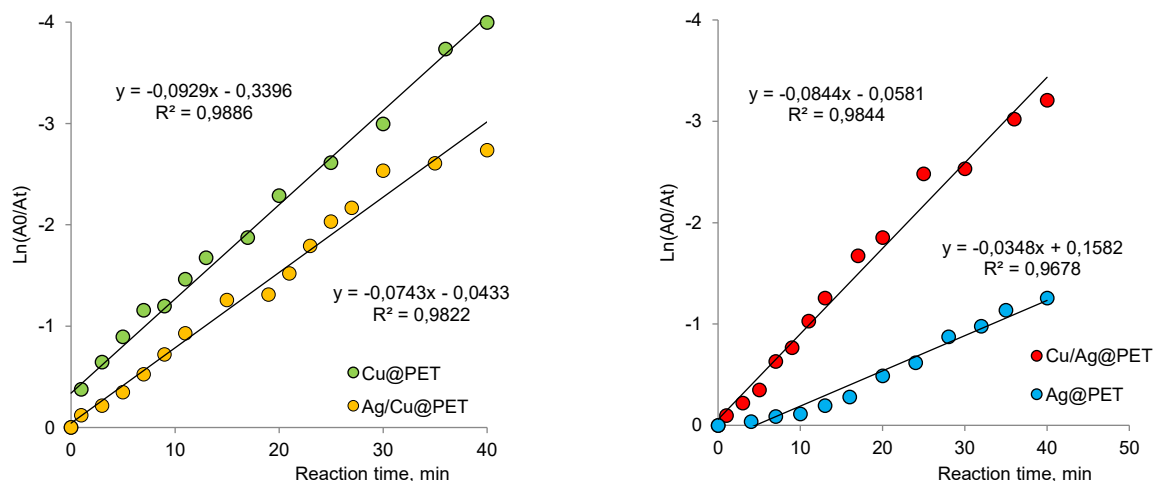


Figure 7. Kinetic curves of PFC reduction at 25 °C and change in the reaction rate constant for all types of composites studied

To investigate the effect of the time taken for silver doping on the catalytic performance of Ag/Cu@PET membranes, a series of samples were prepared with doping durations ranging from 5 to 30 minutes. The XRD analysis results in Table 4 confirmed that all samples had a cubic crystal structure corresponding to  $\text{Ag}_{97}\text{Cu}_3$ , with high degrees of crystallinity. However, a slight decrease in crystallinity (CD%) was observed as doping time increased. This reduction is likely due to the electroless deposition process, where thicker metal layers tend to become more amorphous within the confined pore geometry of the membrane.

Table 4

Data on the structure and properties of Ag/Cu@PET composites with different doping times

Doping time, min	CD, %	MT wall width, nm		Catalytic performance of CTeMs		
		$l(\text{Cu})$	$l(\text{Ag})$	$D^*$ , %	$k$ , $\text{min}^{-1}$	$E_a$ , kJ/mol
0	67.9	$64.19 \pm 10.91$	0	90.8	0.093	62.35
5	82.7		$26.11 \pm 6.13$	67.7	0.032	69.24
10	81.4		$28.38 \pm 2.66$	88.4	0.054	40.90
20	78.9		$31.30 \pm 2.50$	94.3	0.074	35.00
30	74.5		$42.5 \pm 3.8$	98.9	0.129	32.67

\* — at 25°C

As presented in Figure 8, prolonged silver doping led to improved catalytic activity. Samples doped for 30 minutes achieved almost total PFC reduction (98.9 %) within 30 minutes, while those doped for less than 20 minutes showed only marginal gains compared to monometallic Cu@PET. Thus, a minimum doping threshold appears necessary to achieve significant enhancement in catalytic efficiency.

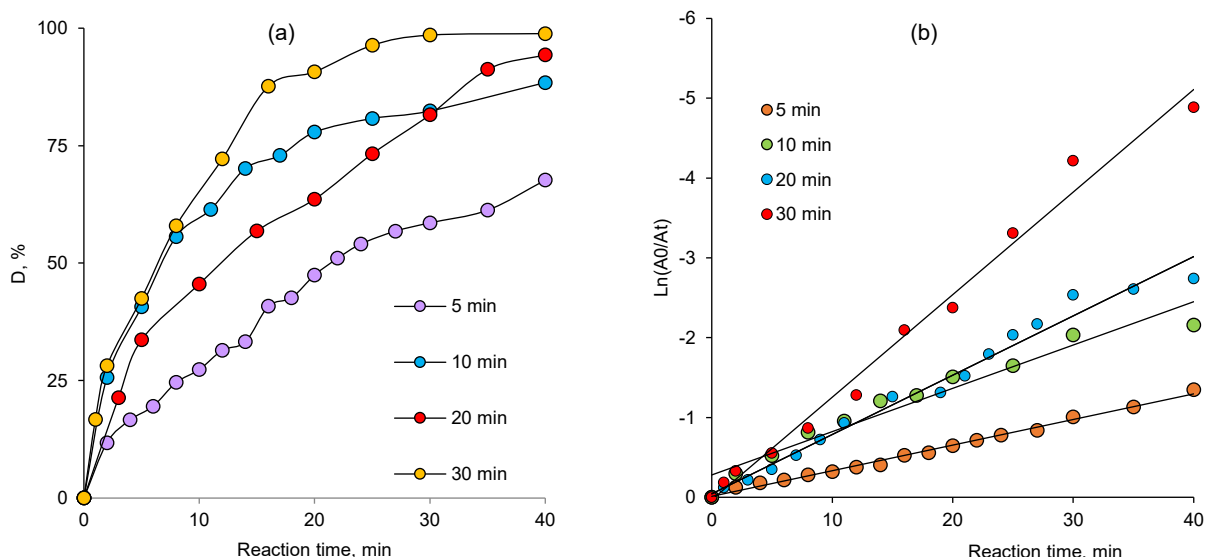


Figure 8. Change in the efficiency (a) and kinetic curves (b) of PFC reduction and change in the rate constant of the PFC reduction reaction in the presence of Ag/Cu@PET composites with different doping times

The activation energy ( $E_a$ ) values, calculated from Arrhenius plots [41], further support this observation. A clear decreasing trend in  $E_a$  was observed with increasing silver doping time (Table 4). The  $E_a$  for the undoped Cu@PET sample was 62.35 kJ/mol, whereas the 30-minute doped Ag/Cu@PET membrane exhibited a markedly lower  $E_a$  of 32.67 kJ/mol, corresponding to a reduction of over 47 %. This substantial decrease confirms that silver incorporation facilitates electron transfer, lowers energy barriers, and enhances reaction kinetics under the applied conditions. Although the reduction in  $E_a$  with increased silver doping time indicates improved electron transfer characteristics and more favorable reaction kinetics within the Ag/Cu@PET system, this does not necessarily translate to superior catalytic performance. Although the lower  $E_a$  indicates a reduced energy barrier for the redox reaction; however, catalytic activity is governed by a combination of kinetic and surface phenomena. In phase-separated structures such as Cu/Ag@PET, the presence of distinct Cu and Ag domains provide enhanced interfacial interactions, greater active surface area, and more efficient redox cycling between  $\text{Cu}^0$  and  $\text{Cu}^{\delta+}$  states. Thus, while Ag doping improves the intrinsic kinetics in Ag/Cu@PET, phase-separated architectures may remain more effective in promoting surface catalysis.

The issue of the stability of new catalysts is crucial when recommending them for further practical use outside the laboratory. Figure 9 shows the efficiency of PFC decomposition in the presence of the Cu/Ag@PET and Ag/Cu@PET (doping time — 30 min) composite membranes over multiple cycles. Notably, all samples maintained consistent performance across 5 test cycles without significant activity loss. After the 5th cycle, Cu/Ag@PET sample experienced around 8.7 % decline in degradation efficiency ( $D$  value). Similarly, the Ag/Cu@PET maintained exceptional stability, with only a 4.7 % reduction in efficiency over 5 cycles.

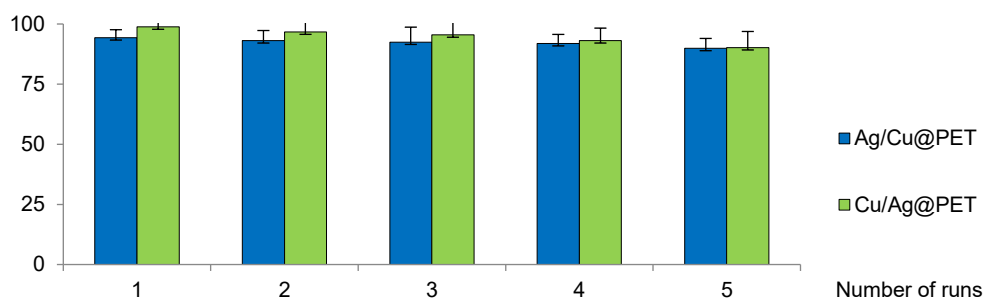


Figure 9. Catalyst reusability of composites membranes over multiple cycles (Experimental conditions: PFC concentration of  $6.0 \times 10^{-5}$  M, temperature at 25 °C, reaction time — 40 min, catalyst membrane size of  $2 \times 2$  cm)

### Conclusions

In this study, we demonstrated the use of the galvanic substitution method in the electroless synthesis of multicomponent composite track-etched membranes (CTeMs) as a template. It is shown that when MT copper is doped with silver nanoparticles, a solid substitution solution of the composition  $\text{Ag}_{97}\text{Cu}_3$  with a high degree of crystallinity is formed. The formation of a two-layer MT of the composition  $\text{Cu}/\text{Ag}@PET$  is observed at the doping of the MT silver with copper nanoparticles. The effect of dopant phases on the catalytic properties of CTeM in the PFC reduction reaction showed that in both cases, polycomponent membranes accelerate the reaction under study more effectively than the initial samples.

Catalytic evaluation using potassium ferricyanide (PFC) reduction as a model reaction demonstrated that both bimetallic systems offered improved performance over monometallic  $\text{Ag}@PET$ . However,  $\text{Cu}/\text{Ag}@PET$  membranes outperformed all other configurations, achieving 94.3 % PFC reduction in 40 minutes. This enhancement is attributed to the synergistic effects at the Cu–Ag interface, where spatial phase separation promotes active site generation, electron transfer, and surface regeneration.

In contrast,  $\text{Ag}/\text{Cu}@PET$  membranes displayed only modest performance gains despite their high crystallinity. This suggests that single-phase alloy structures do not provide the same degree of catalytic synergy as heterogeneous phase interfaces. Kinetic studies confirmed pseudo-first-order behavior, and established a clear dependence of both the rate constant ( $k$ ) and the activation energy ( $E_a$ ) on membrane architecture and silver doping time was the time of silver doping. Importantly,  $\text{Ag}/\text{Cu}@PET$  samples doped for at least 20 minutes were necessary to observe significant performance gains. Membranes doped for 30 minutes showed nearly complete PFC conversion and an  $E_a$  reduction of over 47 % compared to undoped  $\text{Cu}@PET$ . These findings highlight the importance of both structural design and processing parameters in developing next-generation composite catalysts.

### Supporting Information

The Supporting Information is available free at <https://ejc.buketov.edu.kz/index.php/ejc/article/view/374/277>

### Funding

This research was funded by the Science Committee of the Ministry of Science and Higher Education of the Republic of Kazakhstan (Grant No. BR28713053).

### Author Information\*

\*The authors' names are presented in the following order: First Name, Middle Name and Last Name

**Saniya Renatovna Rakisheva** — Engineer, Technological Track-Etched Membranes Laboratory, Institute of Nuclear Physics of the Republic of Kazakhstan, Ibragimov Street, 1, 050032, Almaty, Kazakhstan; e-mail: [saniya.rakisheva58@gmail.com](mailto:saniya.rakisheva58@gmail.com); <https://orcid.org/0000-0003-3618-4828>

**Dinara Temirbayevna Nurpeisova** — PhD, Senior Lecturer, Chemistry Department, L.N. Gumilyov Eurasian National University, Satpayev street, 2, 010008 Astana, Kazakhstan; e-mail: [nurpeisova\\_dt\\_1@enu.kz](mailto:nurpeisova_dt_1@enu.kz); <https://orcid.org/0000-0001-8789-1798>

**Alisher Madiyevich Zhumabayev** — Engineer, Technological Track-Etched Membranes Laboratory, Institute of Nuclear Physics of the Republic of Kazakhstan, Ibragimov street, 1, 050032, Almaty, Kazakhstan; e-mail: [a.zhumabayev@inp.kz](mailto:a.zhumabayev@inp.kz); <https://orcid.org/0009-0007-4431-5468>

**Nursanat Parmanbek** — PhD, Engineer, Technological Track-Etched Membranes Laboratory, Institute of Nuclear Physics of the Republic of Kazakhstan, Ibragimov street, 1, 050032, Almaty, Kazakhstan; e-mail: [nursanat0509@mail.ru](mailto:nursanat0509@mail.ru); <https://orcid.org/0000-0002-9860-1087>

**Murat Barsbay** — Professor, PhD, Department of Chemistry, Hacettepe University, 06800, Ankara, Turkey; e-mail: [mbarsbay@hacettepe.edu.tr](mailto:mbarsbay@hacettepe.edu.tr); <https://orcid.org/0000-0003-0788-4446>

**Anastassiya Alexandrovna Mashentseva** (corresponding author) — Prof., PhD, head of the technological track-etched membranes laboratory, Institute of Nuclear Physics of the Republic of Kazakhstan, Ibragimov street, 1, 050032 Almaty, Kazakhstan; e-mail: [a.mashentseva@inp.kz](mailto:a.mashentseva@inp.kz); <http://orcid.org/0000-0003-4393-5845>



### Author Contributions

The manuscript was written through contributions of all authors. All authors have given approval to the final version of the manuscript. **CRedit: Saniya Renatovna Rakisheva and Alisher Madiyevich Zhumabayev** conceptualization, data curation, investigation, methodology, validation, visualization, writing-review & editing; **Dinara Temirbayevna Nurpeisova, Nursanat Parmanbek** data curation, formal analysis; **Anastassiya Alexandrovna Mashentseva** conceptualization, formal analysis, funding acquisition, resources, supervision, validation, writing-original draft, writing-review & editing; **Murat Barsbay** supervision, validation, writing-review & editing

### Conflicts of Interest

The authors declare no conflict of interest.

### References

- Wellmann, P. J. (2021). The search for new materials and the role of novel processing routes. *Discover Materials*, 1(1), 14. <https://doi.org/10.1007/s43939-021-00014-y>
- Magliaro, J., Altenhof, W., & Alpas, A. T. (2022). A review of advanced materials, structures and deformation modes for adaptive energy dissipation and structural crashworthiness. *Thin-Walled Structures*, 180, 109808. <https://doi.org/10.1016/j.tws.2022.109808>
- Kumari, S., Raturi, S., Kulshrestha, S., Chauhan, K., Dhingra, S., András, K., Singh, T. (2023). A comprehensive review on various techniques used for synthesizing nanoparticles. *Journal of Materials Research and Technology*, 27, 1739–1763. <https://doi.org/10.1016/j.jmrt.2023.09.291>
- Baig, N., Kammakam, I., & Falath, W. (2021). Nanomaterials: a review of synthesis methods, properties, recent progress, and challenges. *Materials Advances*, 2(6), 1821–1871. <https://doi.org/10.1039/D0MA00807A>
- Lahiri, A., Pulletikurthi, G., & Endres, F. (2019). A Review on the Electroless Deposition of Functional Materials in Ionic Liquids for Batteries and Catalysis. *Frontiers in Chemistry*, 7, 85. <https://doi.org/10.3389/fchem.2019.00085>
- Muench, F. (2023). Direct surface functionalization with metal and metal oxide nanostructures. In *Encyclopedia of Nanomaterials* (pp. 318–336). Elsevier. <https://doi.org/10.1016/B978-0-12-822425-0.00048-8>
- Felix, E., Muench, F., & Ensinger, W. (2014). Green plating of high aspect ratio gold nanotubes and their morphology-dependent performance in enzyme-free peroxide sensing. *RSC Adv.*, 4(47), 24504. <https://doi.org/10.1039/c4ra03377a>
- Schaefer, S., Muench, F., Mankel, E., Fuchs, A., Brötz, J., Kunz, U., & Ensinger, W. (2015). Double-Walled Ag — Pt Nanotubes Fabricated by Galvanic Replacement and Dealloying: Effect of Composition on the Methanol Oxidation Activity. *Nano*, 10(06), 1550085. <https://doi.org/10.1142/S179329201550085X>
- Parmanbek, N., Aimanova, N. A., Mashentseva, A. A., Barsbay, M., Abuova, F. U., Nurpeisova, D. T., ... & Zdorovets, M. V. (2023). e-Beam and  $\gamma$ -rays Induced Synthesis and Catalytic Properties of Copper Nanoclusters-Deposited Composite Track-Etched Membranes. *Membranes*, 13(7), 659. <https://doi.org/10.3390/membranes13070659>
- Mashentseva, A. A., Kozlovskiy, A. L., Turapbay, K. O., Temir, A. M., Seytbaev, A. S., & Zdorovets, M. V. (2018). Determination of Optimal Conditions for Electroless Synthesis of Copper Nanotubes in the Polymer Matrix. *Russian Journal of General Chemistry*, 88(6), 1213–1218. <https://doi.org/10.1134/S1070363218060270>
- Muench, F., Rauber, M., Stegmann, C., Lauterbach, S., Kunz, U., Kleebe, H. -J., & Ensinger, W. (2011). Ligand-optimized electroless synthesis of silver nanotubes and their activity in the reduction of 4-nitrophenol. *Nanotechnology*, 22(41), 415602. <https://doi.org/10.1088/0957-4484/22/41/415602>
- Muench, F., Oezaslan, M., Svoboda, I., & Ensinger, W. (2015). Electroless plating of ultrathin palladium films: Self-initiated deposition and application in microreactor fabrication. *Materials Research Express*, 2(10), 105010. <https://doi.org/10.1088/2053-1591/2/10/105010>
- Mashentseva, A. A., Nurpeisova, D. T., & Barsbay, M. (2024). Effect of copper doping on the photocatalytic performance of  $\text{Ni}_2\text{O}_3/\text{PC}$  membrane composites in norfloxacin degradation. *RSC Advances*, 14(7), 4424–4435. <https://doi.org/10.1039/d3ra07471d>
- Nurpeisova, D. T., Mashentseva, A. A., Abuova, F., Aleskhanova, S. H., & Barsbay, M. (2025). Results in Materials Highly efficient  $\text{CuO} / \text{Cu}$  @ PC composite membranes for the photocatalytic degradation and sorption of roxithromycin from aqueous solutions. *Results in Materials*, 26(June 2025), 100677. <https://doi.org/10.1016/j.rinma.2025.100677>
- Altynbaeva, L. S., Mashentseva, A. A., Aimanova, N. A., Zheltov, D. A., Shlimas, D. I., Nurpeisova, D. T., ... Zdorovets, M. V. (2023). Eco-Friendly Electroless Template Synthesis of Cu-Based Composite Track-Etched Membranes for Sorption Removal of Lead(II) Ions. *Membranes*, 13(5), 495. <https://doi.org/10.3390/membranes13050495>
- Russakova, A. V., Altynbaeva, L. S., Barsbay, M., Zheltov, D. A., Zdorovets, M. V., & Mashentseva, A. A. (2021). Kinetic and Isotherm Study of As(III) Removal from Aqueous Solution by PET Track-Etched Membranes Loaded with Copper Microtubes. *Membranes*, 11(2), 116. <https://doi.org/10.3390/membranes11020116>

- 17 Cheng, H., Wang, C., Qin, D., & Xia, Y. (2023). Galvanic Replacement Synthesis of Metal Nanostructures: Bridging the Gap between Chemical and Electrochemical Approaches. *Accounts of Chemical Research*, 56(7), 900–909. <https://doi.org/10.1021/acs.accounts.3c00067>
- 18 da Silva, A. G. M., Rodrigues, T. S., Haigh, S. J., & Camargo, P. H. C. (2017). Galvanic replacement reaction: recent developments for engineering metal nanostructures towards catalytic applications. *Chemical Communications*, 53(53), 7135–7148. <https://doi.org/10.1039/C7CC02352A>
- 19 Altynbaeva, L., Barsbay, M., Aimanova, N., Jakupova, Z., Nurpeisova, D., Zdorovets, M., & Mashentseva, A. (2022). A Novel Cu<sub>2</sub>O/ZnO@PET Composite Membrane for the Photocatalytic Degradation of Carbendazim. *Nanomaterials*, 12(10), 1724. <https://doi.org/10.3390/nano12101724>
- 20 Korolkov, I. V., Güven, O., Mashentseva, A. A., Atıcı, A. B., Gorin, Y. G., Zdorovets, M. V., & Taltenov, A. A. (2017). Radiation induced deposition of copper nanoparticles inside the nanochannels of poly(acrylic acid)-grafted poly(ethylene terephthalate) track-etched membranes. *Radiation Physics and Chemistry*, 130, 480–487. <https://doi.org/10.1016/j.radphyschem.2016.10.006>
- 21 Korolkov, I. V., Mashentseva, A. A., Güven, O., Gorin, Y. G., Kozlovskiy, A. L., Zdorovets, M. V., ... Chlach, S. O. (2018). Electron/gamma radiation-induced synthesis and catalytic activity of gold nanoparticles supported on track-etched poly(ethylene terephthalate) membranes. *Materials Chemistry and Physics*, 217(April), 31–39. <https://doi.org/10.1016/j.matchemphys.2018.06.039>
- 22 Sut, M., Repmann, F., & Raab, T. (2014). Stability of Prussian Blue in Soils of a Former Manufactured Gas Plant Site. *Soil and Sediment Contamination: An International Journal*, 23(5), 504–522. <https://doi.org/10.1080/15320383.2014.839626>
- 23 Pearce, J. (1994). Studies of any toxicological effects of Prussian blue compounds in mammals—A review. *Food and Chemical Toxicology*, 32(6), 577–582. [https://doi.org/10.1016/0278-6915\(94\)90116-3](https://doi.org/10.1016/0278-6915(94)90116-3)
- 24 Hantson, P., N'Geye, P., Laforge, M., Clemessy, J. -L., & Baud, F. (1996). Suicide Attempt by Ingestion of Potassium Ferri-cyanide. *Journal of Toxicology: Clinical Toxicology*, 34(4), 471–473. <https://doi.org/10.3109/15563659609013821>
- 25 Veerakumar, P., Salamalai, K., Thanasekaran, P., & Lin, K. C. (2018). Simple Preparation of Porous Carbon-Supported Ruthenium: Propitious Catalytic Activity in the Reduction of Ferrocyanate(III) and a Cationic Dye. *ACS Omega*, 3(10), 12609–12621. research-article. <https://doi.org/10.1021/acsomega.8b01680>
- 26 Paoella, A., Faure, C., Timoshevskii, V., Marras, S., Bertoni, G., Guerfi, A., ... Zaghib, K. (2017). A review on hexacyano-ferrate-based materials for energy storage and smart windows: challenges and perspectives. *Journal of Materials Chemistry A*, 5(36), 18919–18932. <https://doi.org/10.1039/C7TA05121B>
- 27 Caballero, B., Toldra, P., & Fidel, F. (Eds.). (2003). *Encyclopedia of Food Sciences and Nutrition* (2nd-ed ed.). Academic Press Inc.
- 28 Huo, M., Zhao, R., Ying, Z., Jin, X., Zhu, Y., Wei, Q., & Ren, X. (2025). Efficient separation of Fe<sup>3+</sup> and Cr<sup>3+</sup> from chromium sludge leaching solution based on hydrogen bonding using trialkyl Phosphorus oxide. *Separation and Purification Technology*, 364, 132462. <https://doi.org/10.1016/j.seppur.2025.132462>
- 29 Touzi, N., & Horchani-Naifer, K. (2023). A study on the preparation and characterization of pigment quality from mill scale steel wastes. *Environmental Science and Pollution Research*, 31(28), 40538–40553. <https://doi.org/10.1007/s11356-023-25594-5>
- 30 Berker, K. I., Güçlü, K., Tor, İ., & Apak, R. (2007). Comparative evaluation of Fe(III) reducing power-based antioxidant capacity assays in the presence of phenanthroline, batho-phenanthroline, tripyridyltriazine (FRAP), and ferricyanide reagents. *Talanta*, 72(3), 1157–1165. <https://doi.org/10.1016/j.talanta.2007.01.019>
- 31 Cheong, Y. H., Ge, L., Zhao, N., Teh, L. K., & Lisak, G. (2020). Ion selective electrodes utilizing a ferrocyanide doped redox active screen-printed solid contact — impact of electrode response to conditioning. *Journal of Electroanalytical Chemistry*, 870, 114262. <https://doi.org/10.1016/j.jelechem.2020.114262>
- 32 Altynbaeva, L. S., Mendibaeva, A. Z., Aimanova, N. A., Nurmakhan, A. E., Dzakupova, Z. E., Tuleuov, B. I., & Mashentseva, A. A. (2021). Kinetic and thermodynamic characteristics of the potassium hexationoferrate (III) decomposition catalytic reaction in the presence of composite track-etched membranes. *NNC RK Bulletin*, (1), 15–24. <https://doi.org/10.52676/1729-7885-2021-1-15-24>
- 33 Mashentseva, A. A., Barsbay, M., Aimanova, N. A., & Zdorovets, M. V. (2021). Application of Silver-Loaded Composite Track-Etched Membranes for Photocatalytic Decomposition of Methylene Blue under Visible Light. *Membranes*, 11(1), 60. <https://doi.org/10.3390/membranes11010060>
- 34 Mashentseva, A. A. (2019). Effect of the Oxidative Modification and Activation of Templates Based on Poly(ethylene terephthalate) Track-Etched Membranes on the Electroless Deposition of Copper and the Catalytic Properties of Composite Membranes. *Petroleum Chemistry*, 59(12), 1337–1344. <https://doi.org/10.1134/S0965544119120089>
- 35 Borgekov, D., Mashentseva, A., Kislitsin, S., Kozlovskiy, A., Russakova, A., & Zdorovets, M. (2015). Temperature Depend-ent Catalytic Activity of Ag/PET Ion-Track Membranes Composites. *Acta Physica Polonica A*, 128(5), 871–875. <https://doi.org/10.12693/APhysPolA.128.871>
- 36 Susana, C. R., Jorge, P. J., Pablo, H., Luis, M. L. M., & Paul, M. (2010). Colloidal gold-catalyzed reduction of ferrocyanate (III) by borohydride ions: A model system for redox catalysis. *Langmuir*, 26(2), 1271–1277. <https://doi.org/10.1021/la902442p>
- 37 Yen, C. W., & El-Sayed, M. A. (2009). Plasmonic field effect on the hexacyanoferrate (III)-thiosulfate electron transfer cata-lytic reaction on gold nanoparticles: Electromagnetic or thermal? *Journal of Physical Chemistry C*, 113(45), 19585–19590. <https://doi.org/10.1021/jp905186g>

- 38 Martić, N., Reller, C., Macauley, C., Löffler, M., Reichert, A. M., Reichbauer, T., ... Schmid, G. (2020). Ag<sub>2</sub>Cu<sub>2</sub>O<sub>3</sub> — a catalyst template material for selective electroreduction of CO to C<sub>2</sub><sup>+</sup> products. *Energy & Environmental Science*, 13(9), 2993–3006. <https://doi.org/10.1039/D0EE01100B>
- 39 Wang, L., Higgins, D. C., Ji, Y., Morales-Guio, C. G., Chan, K., Hahn, C., & Jaramillo, T. F. (2020). Selective reduction of CO to acetaldehyde with CuAg electrocatalysts. *Proceedings of the National Academy of Sciences*, 117(23), 12572–12575. <https://doi.org/10.1073/pnas.1821683117>
- 40 Rollier, F. A., Muravev, V., Kosinov, N., Wissink, T., Anastasiadou, D., Ligt, B., ... Hensen, E. J. M. (2025). Cu–Ag interactions in bimetallic Cu–Ag catalysts enhance C<sub>2</sub><sup>+</sup> product formation during electrochemical CO reduction. *Journal of Materials Chemistry A*, 13(3), 2285–2300. <https://doi.org/10.1039/D4TA04263H>
- 41 Kim, Y., Dumett Torres, D., & Jain, P. K. (2016). Activation Energies of Plasmonic Catalysts. *Nano Letters*, 16(5), 3399–3407. <https://doi.org/10.1021/acs.nanolett.6b01373>

Evgeny V. Andreev<sup>1</sup> , Irina N. Fadeikina<sup>1, 2\*</sup> ,  
Alisher K. Mutali<sup>1, 3</sup> , Vladimir I. Kukushkin<sup>4</sup> 

<sup>1</sup>Joint Institute for Nuclear Research, Dubna, Russia;

<sup>2</sup>Dubna State University, Dubna, Russia;

<sup>3</sup>Laboratory of Solid State Physics, The Institute of Nuclear Physics, Almaty, Kazakhstan;

<sup>4</sup>Osipyan Institute of Solid State Physics, Russian Academy of Sciences, Chernogolovka, Russia

(\*Corresponding author's e-mail: [fadeikina@yandex.ru](mailto:fadeikina@yandex.ru))

## Comparison of SERS Effect on Composite Track-Etched Membranes with Silver Nanostructures Obtained by Vacuum Deposition and Chemical Synthesis

Track-etched membranes (TMs) represent a universal platform for the development of advanced sensor systems due to their tunable pore architecture, chemical functionalization, and compatibility with different nanostructures. In particular, their modification with plasmonic silver nanostructures enables the creation of efficient solid-state substrates for surface-enhanced Raman scattering (SERS), providing high sensitivity and potential for selective analyte detection. Solid substrates based on TMs can be a good compromise for SERS systems. This article is devoted to the study of the SERS effect on track-etched membranes with silver nanostructures. Silver nanostructures on track-etched membranes were obtained by thermal evaporation, magnetron sputtering thin silver film with subsequent annealing. Other samples were received by deposition of colloidal silver nanoparticles stabilized with sodium citrate and  $\beta$ -cyclodextrin. 4-aminothiophenol was used as a test substance. All samples exhibited the SERS effect. The intensity of the Raman scattering signal in the obtained samples was compared and enhancement factors and standard deviations were estimated. Samples obtained both by deposition of nanoparticles and by sputtering show high values of the enhancement factors, which will allow them to be used in the future as substrates for biosensors.

**Keywords:** silver nanoparticles, track-etched membranes, vacuum deposition, surface-enhanced Raman scattering, biosensors, nanostructures, sensor system, composite

### Introduction

Track-etched membranes (TMs) are a promising material for the advanced sensors development. TMs are produced from thin polymer films in which channels are created by irradiating heavy with ions and etching out destructed regions. Due to the unique technology of TMs production, they have special characteristics compared to other membranes. TMs are characterized by a uniform distribution of pore diameters, tunable pore geometry and a wide range of pore size (20 nm – 10  $\mu$ m) [1]. In addition, it is possible to change the shape of pores in TMs and obtain both symmetric and asymmetric channels [2]. In addition to adjusting the structural properties, the material from which the TMs are made polyethylene terephthalate, polycarbonate, polyvinylidene fluoride, polyimide can also be selected. TMs have a wide possibility of functionalization, for example, it is possible to modify TMs with polymers [3], biomolecules [4], low molecular weight compounds [5] using functional groups on the TMs surface. It is possible to sputter metals [6], create nanofiber coatings on TMs and form metal-organic frameworks [7]. It is also possible to realize the technology of polymer grafting on TMs due to residual radicals [8]. All the above-mentioned allows to create a large number of TMs-based sensors: electrochemical sensors for heavy metal ions [9, 10], glucose [11]. In addition, nanoporous TMs are suitable for the resistive-pulse sensing method [12], to carry out digital loop mediated isothermal amplification [13]. Furthermore, sensors based on TMs with SERS-effect (surface-enhanced Raman scattering) could be designed after creating of plasmonic structures on the TMs surface [14].

Currently, SERS is a promising tool for analyzing substances, allowing the detection of extremely low concentrations down to single molecules [15]. Raman signal amplification is possible due to the formation of plasmon-polariton waves on the surface of a dielectric substrate with nanostructures plasmonic metals, or by the formation of localized plasmons (“hot spots”) in colloidal solutions containing aggregates of metallic nanoparticles [16]. The most popular SERS-systems are colloidal solutions of silver nanoparticles. The main

problem of application of this type of systems is related to instability, tendency to aggregation, influence of colloidal solutions composition on Raman signal enhancement [17]. The consequence of this is the irreproducibility of measurement results and the difficulty of using colloidal systems in sensorics. Solid substrates can be a good compromise for SERS-systems.

Solid SERS-substrates are commonly based on glass, silicon or metals. The formation of nanostructures for the SERS-effect is carried out by immobilization of metal nanoparticles from solution or by deposition of metal films using PVD methods with subsequent treatment [18–22]. Recently, flexible materials such as polymer films as SERS-substrates attracted research interest due to a number of advantages. Flexible substrates are easier to manipulate and can be used with roll-to-roll technology [23, 24].

Composite silver nanoparticles and TMs show significant potential in the development of highly efficient SERS-systems. Of particular importance is the ability of TM not only to act as a flexible substrate for the preparation of SERS-active nanostructures, but also the ability to concentrate the analyte. Even without modification, TMs can be used in the design of sensors for filtration of analyte [25, 26]. Numerous works have been presented on the development of SERS-active structures on TMs. Methods for synthesis, deposition or immobilization of colloidal nanoparticles of different composition and geometry [27–30]; sputtering of metal films by PVD methods [31–33], variants of using TMs as templates for the formation of nanostructures in pores with subsequent membrane etching [34, 35]. TMs with aptamer-modified SERS-surface can significantly improve the selectivity and efficiency of analysis and create an aptasensor for the virus [36].

Despite the existing studies, there is still a challenge to design robust TM-based SERS systems with high enhancement factor, signal reproducibility and homogeneity.

The aim of the present paper is to study the features of the formation of the SERS-active silver nanostructures on the TMs surface using various methods and to compare the performance characteristics for the design of high-performance analytical systems.

## Experimental

### *Reagents and Materials*

The following reagents and materials were used in this work: sodium citrate 5.5-hydrate  $\text{Na}_3\text{C}_6\text{H}_5\text{O}_7 \cdot 5.5\text{H}_2\text{O}$  (98 %, PanReac);  $\beta$ -cyclodextrin  $\text{C}_{42}\text{H}_{70}\text{O}_{35}$  (98 %, Sigma-Aldrich); Branched polyethyleneimine (PEI) ( $M_n = 60.000$ , 50 % aqueous solution, Acros Organics); 4-Aminothiophenol (4-ATP) (97 %, Sigma Aldrich); Ethanol (99.9 %, Merc);  $\text{AgNO}_3$  (99.9 %, LenReaktiv); NaOH (99.9 %, LenReaktiv); Deionized water (Milli-Q, Millipore) with a resistivity of  $18 \text{ M}\Omega \cdot \text{cm}$  at  $22^\circ\text{C}$ ; Track-etched membranes made of polyethylene terephthalate (thickness  $19 \mu\text{m}$ , pore density  $2.7 \cdot 10^8 \text{ cm}^{-2}$ , pore diameter  $0.4 \mu\text{m}$ ), obtained at the Flerov Laboratory of Nuclear Reactions of the Joint Institute for Nuclear Research.

### *Formation of Nanostructures from Silver Nanoparticles obtained by Chemical Synthesis*

Spherical silver nanoparticles were prepared using the citrate method, based on the procedure [29]. For this, 50 ml of  $10^{-3} \text{ M}$  sodium citrate solution, heated to  $95^\circ\text{C}$ , was gradually added with 12.5 ml of  $10^{-3} \text{ M}$  silver nitrate solution. Before the synthesis began, 1 M sodium hydroxide solution was added to the sodium citrate solution to achieve a pH of 9.8. The resulting mixture was kept at constant stirring and temperature for one hour.

The synthesis of silver nanoparticles using  $\beta$ -cyclodextrin was carried out as follows [29]. A  $10^{-3} \text{ M}$   $\beta$ -cyclodextrin solution was prepared and adjusted to pH 11 using 1 M NaOH. Subsequently,  $10^{-3} \text{ M}$  silver nitrate solution was gradually added while stirring at  $70^\circ\text{C}$ . The solution was incubated under these conditions for 30 minutes and then left at room temperature for one day.

The TMs were washed in ethanol and water, then immersed in a 0.1 % aqueous solution of PEI and left on a laboratory shaker for 30 minutes. After modification, the TMs were washed in water for 5 minutes. Subsequently, the silver nanoparticles solution was passed through the modified TMs using an Amicon Stirred Cells filtration cell (Millipore) [37].

### *Formation of Silver Nanostructures by Physical Methods*

Magnetron sputtering was performed using a Q 150T S (Quorum) setup. A 10 nm silver layer was deposited at an argon residual pressure of  $10^{-2} \text{ mbar}$  and a deposition rate of  $5 \text{ nm/min}$ .

Thermal evaporation was performed using a thin film deposition system Nano 38 (Kurt J. Lesker Company, Jefferson Hills, Pennsylvania, USA). A 10 nm silver layer was deposited at a pressure of  $8 \cdot 10^{-7} \text{ Torr}$  and a deposition rate of  $2.4 \text{ nm/min}$ .



The formation of nanostructures was achieved through annealing in a muffle furnace (Bender) at 120 °C for 10 minutes.

The deposition of silver nanoparticles on TMs was monitored spectrophotometrically using a double-beam spectrophotometer (Evolution 600, Thermo Scientific). Spectra of colloidal solutions were recorded after filtration against deionized water. Measurements were conducted at room temperature with an optical path length of 1 cm and a slit width of 2 nm.

The zeta potential of silver nanoparticles was measured using laser Doppler microelectrophoresis (Zetasizer Nano ZSP, Malvern). A U-shaped cuvette with built-in gold electrodes was used for measurements.

Scanning electron microscopy (SEM) was performed using a microscope (SU 8020, HITACHI) with a cold field emission cathode. Cross-sectional were obtained by irradiating the TMs samples with ultraviolet light until they became brittle. To improve resolution and contrast, a 5 nm-thick layer of platinum-palladium alloy was deposited on the samples by magnetron sputtering.

The geometric parameters (diameter, shape) of nanoparticles were studied using transmission electron microscopy (TEM). TEM was performed using a microscope (Talos F200iS/TEM, Thermo Scientific). Copper grid with a thin film of amorphous carbon (SPI supplies) were used as the supporting substrate. To precipitate the nanoparticles, the grid was immersed in the solution, taken out and dried. Nanoparticle sizes were calculated from the micrographs using JMicroVision 1.3.4 software.

Raman spectroscopy was used as an additional confirmation of silver nanoparticles deposition on TMs and to evaluate the possibility of using the obtained substrates for detection of the test substance. Raman spectroscopy was performed on a spectrometer R532 (Enspectr). The excitation laser wavelength was 532 nm, the spot diameter of the focused beam was 4 µm. The test substance used was 4-ATP at a concentration of  $10^{-5}$  M in ethanol. One drop of 2 µl was applied to the membrane for measurement and left to dry completely. The enhancement factor ( $K_2$ ) was calculated from a comparative experiment in which the ratio of the Raman line intensities of 4-ATP on commercially produced Enspectr substrates (with a known enhancement factor,  $K_1 = 7 \cdot 10^6$ ) was determined. For this purpose, measurements were performed under the same laser operating conditions (radiation power density 20 mV, exposure time 300 msec, number of scans 10) on the Enspectr substrate and TMs. The intensity values of the  $1435 \text{ cm}^{-1}$  band were averaged over 5 measurements on 5 replicate samples.  $K_2$  calculated according to the formula:

$$K_2 = K_1 \cdot N,$$

where  $N$  — is the coefficient showing how many times the values of the obtained band intensities at  $1435 \text{ cm}^{-1}$  differ from each other. The standard deviation and relative standard deviation were calculated for the measured enhancement factors using the formulas:

$$S = \sqrt{\frac{\sum (x - \bar{x})^2}{(n-1)}};$$

$$Sr = \frac{S}{\bar{x}},$$

where  $\bar{x}$  — denotes the sample mean, and  $n$  — represents the sample size.

### Results and Discussion

The study investigated two principal approaches to obtaining SERS-active surfaces on TMs. The first approach involves the forming of nanoparticles from thin silver films through their aggregation upon heating. The second approach comprises the deposition of chemically synthesized colloidal silver nanoparticles onto the TMs surface via filtration.

#### *Silver Nanoparticle Formation via Sputtering*

Thin silver films were produced using thermal and magnetron sputtering techniques. Thermal evaporation was selected due to its ease of implementation and widespread use. A viable alternative to thermal evaporation is magnetron sputtering, which yields films with improved adhesion, greater uniformity, thickness consistency, and reduced roughness [38]. An important advantage of magnetron sputtering is lower substrate heating and the absence of droplet phase and microparticles in the deposited material flux, unlike thermal sputtering [39]. Previous research was conducted to optimize film thickness and annealing conditions for thermally deposited films [40]. It was determined that the optimal conditions for nanoparticle formation were

a film thickness of 10 nm and annealing at 120 °C. Similar studies were performed for magnetron-deposited films. The findings revealed that the optimal conditions for nanoparticle formation were identical to those of thermally deposited films, with a film thickness of 10 nm and annealing at 120 °C. Figure 1 presents micrographs of the original and annealed silver films with a thickness of 10 nm.

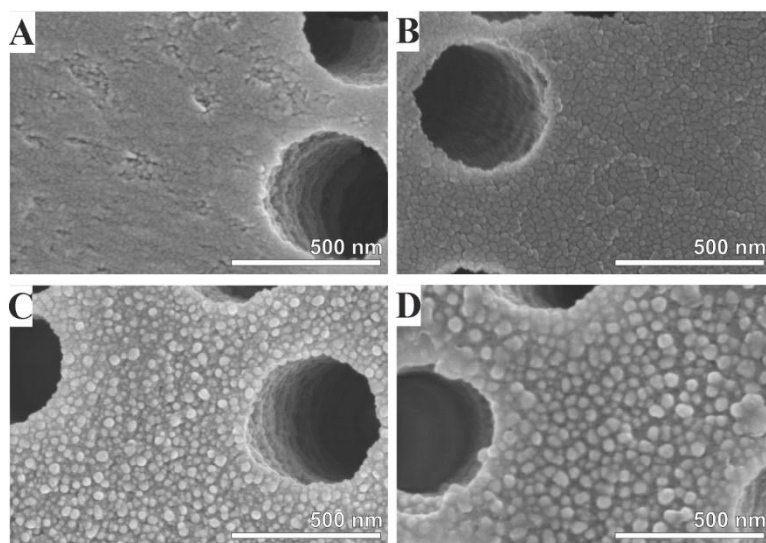


Figure 1. Micrographs obtained by SEM of a TMs with a 10 nm silver layer: Magnetron-sputtered before annealing (A) and after annealing (C); Thermal evaporation before annealing (B) and after annealing (D)

It can be observed that the initial films do not contain nanoparticles, yet a noticeable difference in morphology exists between the films produced by magnetron sputtering (Figure 1A) and thermal evaporation methods (Figure 1B). The films obtained via magnetron sputtering exhibit a smoother surface, while those produced by thermal evaporation show the presence of islands. These differences are inherent to the deposition methods and are typical of them.

The formation of nanostructures from thin films was achieved through heating to 120 °C, after which the film aggregated into silver nanoparticles. The nanoparticle size for films produced by magnetron sputtering (TM-Ag-M) was  $21 \pm 6$  nm (Figure 1C), whereas for films obtained by thermal evaporation (TM-Ag-T) was  $28 \pm 7$  nm (Figure 1D).

#### *Silver Nanoparticle Deposition from Solution onto Track-Etched Membrane*

The second approach to forming silver nanostructures on a TMs involved filtering a solution of nanoparticles through a PEI-modified TMs. During filtration, silver nanoparticles deposit onto the TMs surface via electrostatic and donor-acceptor interactions with PEI.

This study examined two types of silver nanoparticles. The first were nanoparticles stabilized with sodium citrate, and the second were nanoparticles stabilized with  $\beta$ -cyclodextrin. Both types of nanoparticles had negatively charged surfaces to prevent electrostatic repulsion from the PEI-modified TMs. The zeta potential of citrate nanoparticles was  $-51 \pm 5$  mV (pH = 10), while that of cyclodextrin nanoparticles was  $-35 \pm 8$  mV (pH = 11).

The citrate synthesis method was chosen for its simplicity, allowing for the production of nanoparticles of a specific size without the use of toxic reagents. A drawback of this method is the presence of other nanoparticle shapes, such as nanorods and triangular nanoprisms. As an alternative, the synthesis of silver nanoparticles using  $\beta$ -cyclodextrin as a stabilizer and reducing agent was selected. This method also avoids the use of toxic reagents and produces particles with good stability and spherical shape.

A notable feature of this method is the presence of a hydrophobic cavity in the  $\beta$ -cyclodextrin molecule, which can accommodate various molecules for applications in drug delivery systems and biosensing [41, 42]. Figure 2 presents micrographs of silver nanoparticles produced using sodium citrate (AgNPs-Cit) (Figure 2A) and  $\beta$ -cyclodextrin (AgNPs-CD) (Figure 2B).

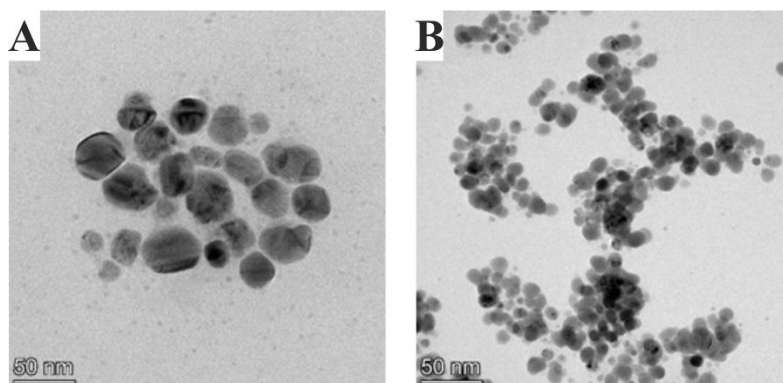


Figure 2. Micrographs of AgNPs-Cit (A) and AgNPs-CD (B) obtained by TEM

According to TEM data, the size of AgNPs-Cit and AgNPs-CD was  $24 \pm 10$  nm and  $28 \pm 4$  nm, respectively.

The UV-visible absorption spectra of the AgNPs-Cit and AgNPs-CD are presented in Figure 3. The characteristic plasmon resonance for silver nanoparticles was observed in the region of 400 nm.

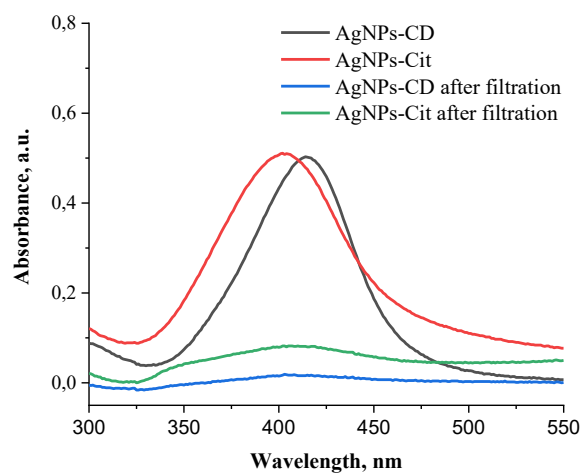


Figure 3. UV-visible absorption spectra of silver nanoparticles before and after filtration through TMs

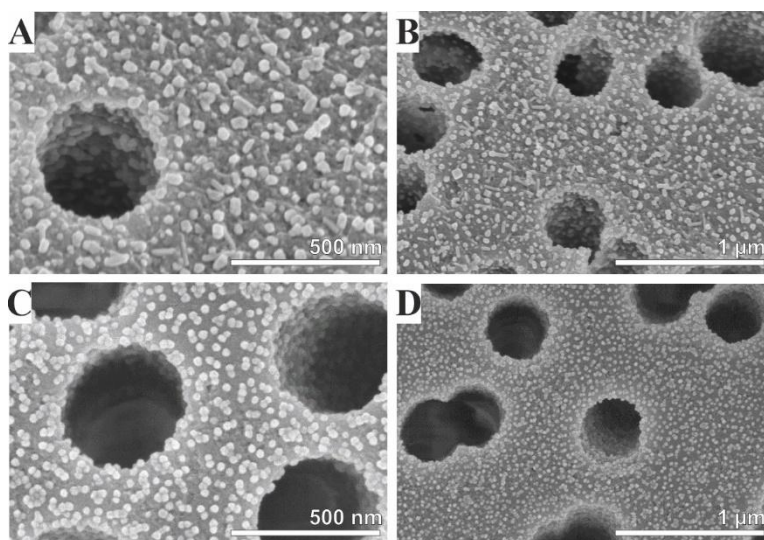


Figure 4. Micrographs of AgNPs-Cit (A, B) and AgNPs-CD (C, D) obtained by SEM

The concentration of nanoparticles was equalised by dilution based on the intensity of the plasmon resonance peak. Also, the change in intensity peak of the plasmon resonance was used to evaluate the completeness of deposition. The deposition efficiency was 90 % and 95 % for AgNPs-Cit and AgNPs-CD, respectively.

Figure 4 shows SEM of the surface of TMs after deposition AgNPs-Cit (Fig. 4 A, B) и AgNPs-CD (Fig. 4 C, D).

In the micrographs of the TMs surfaces after silver nanoparticle deposition, it can be observed that both AgNPs-Cit (Fig. 4 A, B) and AgNPs-CD (Fig. 4 C, D) are deposited uniformly across the entire surface. However, almost all nanoparticles stabilized with  $\beta$ -cyclodextrin are present as agglomerates on the TMs surface, while those stabilized with sodium citrate predominantly appear as single particles with lesser aggregation. In the AgNPs-Cit samples, particles of not only spherical shape but also in the form of rods, cubes, and triangular nanoprisms can be discerned.

#### *Comparison of Chemical and Physical Approaches in the Formation of Silver Nanostructures on Track-Etched Membranes*

When comparing the approaches to the formation of silver nanostructures on track-etched membranes, the depth of nanoparticle deposition in the pores, the intensity of the giant Raman scattering signal, and the relative standard deviation of the amplification coefficient were assessed. Micrographs of TMs cross-sections at angles of 90° and 70° are presented in figure 5.

The fundamental difference in the coatings can be observed in the cross-sections of TMs with silver nanoparticles obtained via physical and chemical methods. When nanoparticles are produced from sputtered films, predominantly only the frontal surface of the TMs is filled. Within the pores, a small number of nanoparticles are observed from one edge, with deposition depths of approximately 1  $\mu\text{m}$  for TM-AgNPs-T (Fig. 5A, B) and 0.5  $\mu\text{m}$  for TM-AgNPs-M (Fig. 5C, D).

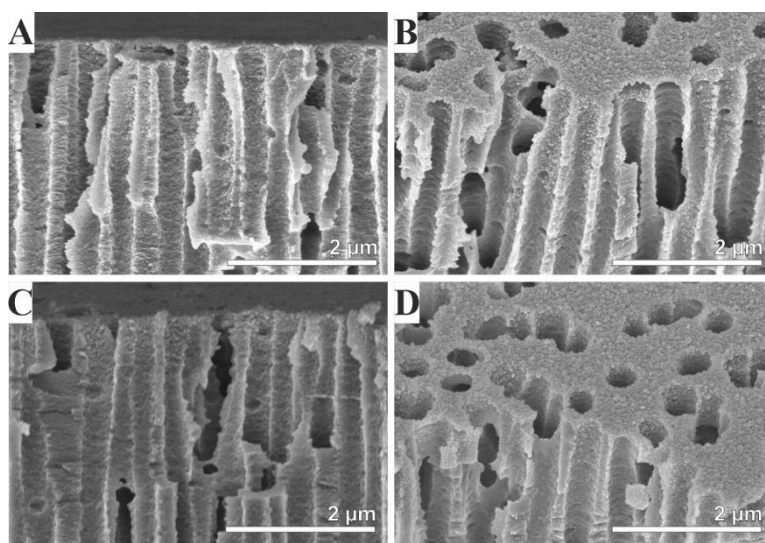


Figure 5. Micrographs of TMs cross-sectional by SEM: TM-AgNPs-T (A, B), TM-AgNPs-M (C, D)

The location of nanoparticle formation can be associated with different positions of the silver target when obtaining films relative to different sections of the membrane. The depth of nanoparticle location is also affected by different slopes of the pore channels of the TMs. With distance from the front surface, the thickness of the deposited film decreases, and as a consequence, the size and density of the particle distribution decrease. Nanoparticles are present, as a rule, at one edge of the pore, and at different depths. Part of the pore channel is inaccessible for filling with nanoparticles. The filling of membrane surface areas is schematically shown in Figure 6 (A).



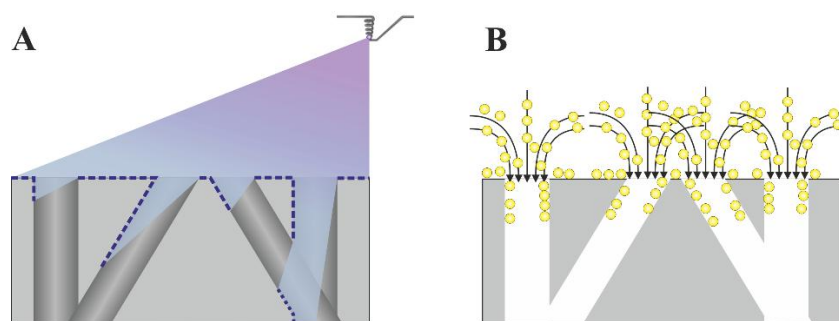


Figure 6. Schematic representation of the process of deposition of silver films (A) and the process of filtration of silver nanoparticles through a TMs (B)

Formation of a nanoparticle layer by precipitation from a solution differs fundamentally from the method of formation from thin films. The presence of silver nanoparticles both on the front surface and in the pores of the track-etched membranes, down to a depth of 3  $\mu\text{m}$ , is observed on the cross-sectional of the TM-AgNPs-Cit (Fig. 7 A, B) and TM-AgNPs-CD (Fig. 7 C, D) samples.

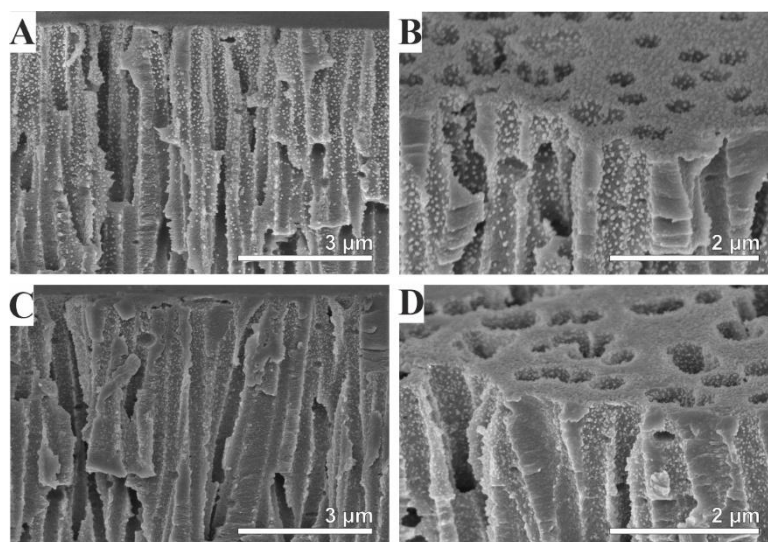


Figure 7. Micrographs of TMs cross-sectional by SEM: TM-AgNPs-Cit (A, B), TM-AgNPs-CD (C, D)

The density of the nanoparticles layer in the pore is comparable to the density of nanoparticles on the front surface of the TMs. This behavior of the nanoparticles can be associated with the fact that during filtration, the nanoparticles carried away by the flow move along the pore channel for a significant distance. At the same time, the amount of nanoparticles in the solution is sufficient to densely fill the front surface of the TMs and the pore channels (Fig. 6 B).

#### *SERS Effect on Track-Etched Membranes with Silver Nanostructures*

The SERS effect was studied on the composite TMs with silver nanostructures. The polymer material of the track membrane does not interfere with analyte detection due to the layer of silver nanoparticles on the surface. 4-ATP with a concentration of  $10^{-5}$  M was used as a test substance. Due to the presence of a thiol group, 4-ATP is well adsorbed on the surface of silver nanoparticles. The presence of a benzene ring increases the SERS activity of the substance. These factors make 4-ATP a common standard for measuring the SERS signal [43].

The averaged Raman spectra of 4-ATP on samples SERS-substrates are shown in Figure 8.



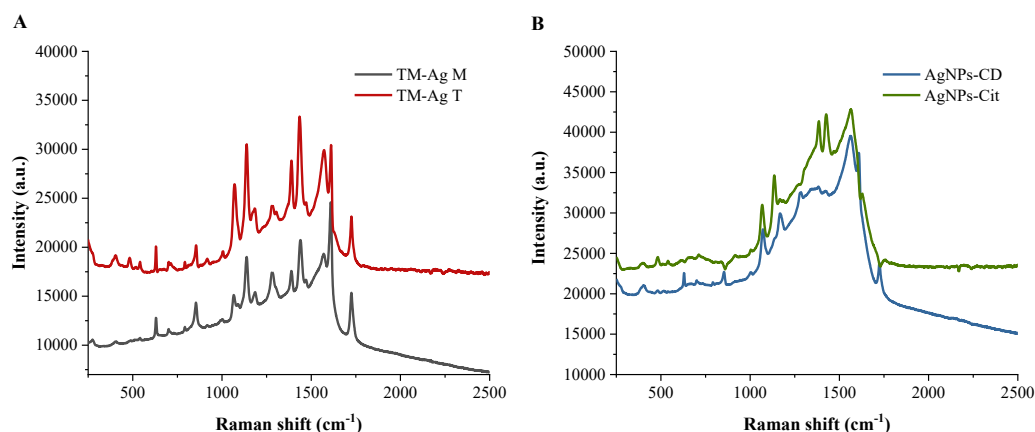


Figure 8. Raman spectra of 4-ATP ( $10^{-5}\text{M}$ ): TM-Ag-T, TM-Ag-M (A); TM-AgNPs-Cit, TM-AgNPs-CD (B)

All samples of TMs exhibit vibrational bands corresponding to 4-ATP in the regions of 1145, 1390, 1435, 1575  $\text{cm}^{-1}$ , which are consistent with similar bands from the literature data obtained on silver nanoparticles upon excitation by a laser with a wavelength of 532 nm [44]. The intensities of the Raman scattering signals were comparable. The maximum signal intensity was observed on the TM-Ag-T sample obtained by thermal evaporation, and the minimum Raman signal intensity was recorded for the TM-AgNPs-CD sample. Higher signal intensities on TMs with nanoparticles obtained from thin films can be explained by a denser arrangement of silver nanoparticles. For TM-Ag-T, the average density of nanoparticles on the front surface was  $\approx 700 \text{ pcs}/\mu\text{m}^2$ , for TM-AgNPs-CD  $\approx 600 \text{ pcs}/\mu\text{m}^2$ .

Based on the averaged Raman spectra, the enhancement factors and their relative standard deviations were calculated, the values of which are presented in Figure 9.

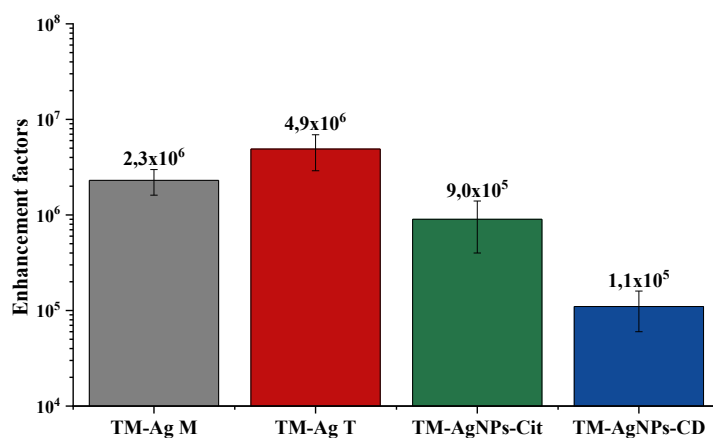


Figure 9. Histogram of the enhancement factors values on the samples TM-Ag-T, TM-Ag-M, TM-AgNPs-Cit, TM-AgNPs-CD

The enhancement factors on TMs were determined to be  $2.3 \cdot 10^6 \pm 30\%$ ,  $4.9 \cdot 10^6 \pm 41\%$ ,  $9.0 \cdot 10^5 \pm 56\%$ , and  $1.1 \cdot 10^5 \pm 45\%$  for TM-Ag M, TM-Ag T, TM-AgNPs-Cit, and TM-AgNPs-CD, respectively.

It can be observed that TMs with silver nanoparticles produced by physical methods exhibited lower relative standard deviations compared to samples containing nanoparticles produced by chemical methods. The lowest relative standard deviation was achieved with magnetron sputtering samples, which can be attributed to the more homogeneous structure and uniform thickness distribution of the initial films.

The highest standard deviation was observed for TMs with silver nanoparticles synthesized using sodium citrate. This phenomenon can be explained by the greater polydispersity and presence of non-spherical shapes in citrate-stabilized silver nanoparticles.

For TM-AgNPs-Cit and TM-AgNPs-CD, there are fewer nanoparticles on the surface, but particles within the pores also contribute to the signal enhancement, which results in a higher relative standard deviation of the enhancement factor.

It can be noted that the enhancement factors of all samples are comparable in magnitude and are consistent with the enhancement values observed on other non-porous SERS substrates with silver nanostructures [45, 46].

### Conclusions

Creation of a composite material based on TMs and silver NPs with the SERS effect was carried out using thermal evaporation, magnetron sputtering and deposition from solution. It was demonstrated that physical deposition methods (magnetron sputtering and thermal evaporation) enable the creation of a homogeneous coating of the frontal surface with silver nanoparticles, wherein the particles are in close contact with each other. However, within the pores, the nanoparticles formed unevenly, with the filling dependent on the position of the target relative to the examined track-etched membranes region.

Comparison of thermal evaporation and magnetron sputtering methods shows that silver nanostructures capable of exhibiting the SERS effect are formed in both cases. However, magnetron sputtering demonstrates better reproducibility of the analytical signal.

Filtration of the solution containing chemically synthesized nanoparticles through the porous material allows covering the surface with a complex relief with a sufficiently dense layer of nanoparticles and depositing the nanoparticles into the pores. The filling of the pore channels with nanoparticles occurs uniformly and to a greater depth compared to sputtering.

The highest enhancement factor of  $4.9 \cdot 10^6 \pm 41\%$  was achieved with the sample featuring thermal evaporation of a silver film followed by annealing. Track-etched membranes with citrate silver nanoparticles had the highest value of the relative standard deviation of the enhancement factor,  $9.0 \cdot 10^5 \pm 56\%$ . The obtained enhancement factors were comparable to those of other substrates.

### Funding

This research was funded by the Russian Science Foundation, grant No. 24-65-00015 (<https://rscf.ru/project/24-65-00015>) and JINR Project No 07-5-1131-2-2024/2028.

### Author Information\*

\*The authors' names are presented in the following order: First Name, Middle Name and Last Name

**Evgeny Valerievich Andreev** — Junior Researcher, Flerov Laboratory of Nuclear Research, Joint Institute for Nuclear Research, 141980, Dubna, Russia; e-mail: [evandreev@jinr.ru](mailto:evandreev@jinr.ru); <https://orcid.org/0009-0003-6924-2622>

**Irina Nikolaevna Fadeikina** (*corresponding author*) — Candidate of Technical Sciences, Researcher, Flerov Laboratory of Nuclear Research, Joint Institute for Nuclear Research, 141980, Dubna, Russia; Dubna State University; e-mail: [fadeikina@yandex.ru](mailto:fadeikina@yandex.ru); <https://orcid.org/0009-0006-5094-6760>

**Alisher Kassymbekuly Mutali** — Researcher, Flerov Laboratory of Nuclear Research, Joint Institute for Nuclear Research, 141980, Dubna, Russia; Laboratory of Solid State Physics, Institute of Nuclear Physics, 050032 Almaty, Kazakhstan; e-mail: [mutali@jinr.ru](mailto:mutali@jinr.ru); <https://orcid.org/0000-0003-2889-5785>

**Vladimir Igorevich Kukushkin** — Candidate of Physical and Mathematical Sciences, senior scientist, Osipyan Institute of Solid State Physics, Russian Academy of Sciences, Chernogolovka, Russia; e-mail: [ku-kushvi@mail.ru](mailto:ku-kushvi@mail.ru); <https://orcid.org/0000-0001-6731-9508>

### Author Contributions

The manuscript was prepared with contributions from all authors, and all authors have approved the final version for submission. **CRedit**: **Evgeny Valerievich Andreev** writing — original draft, investigation, formal analysis, review & editing, conceptualization; **Irina Nikolaevna Fadeikina** writing — original draft, investigation, formal analysis, review & editing, project administration, conceptualization; **Alisher Kassymbekuly Mutali** writing — review, investigation; **Vladimir Igorevich Kukushkin** writing — review, investigation.

### Acknowledgments

The authors thank O. Orelovich for the help with SEM examination of track-etched membrane samples, scientific supervisor A.Nechaev for support and stimulating ideas, Prof. P. Apel for fruitful discussions and critical review of the manuscript.

### Conflicts of Interest

The authors declare no conflict of interest.

### References

- 1 Apel, P. Y. (2018). Fabrication of functional micro- and nanoporous materials from polymers modified by swift heavy ions. *Radiation Physics and Chemistry*, 159, 25–34. <https://doi.org/10.1016/j.radphyschem.2019.01.009>
- 2 Apel, P.Yu., Blonskaya, I.V., Dmitriev, S.N., Orelovich, O.L., Sartowska, B.A. (2015). Ion track symmetric and asymmetric nanopores in polyethylene terephthalate foils for versatile applications. *Nuclear Instruments and Methods in Physics Research Section B*, 359, 1–7. <https://doi.org/10.1016/j.nimb.2015.07.016>
- 3 Fadeikina, I. N., Andreev, E. V., Kristavchuk, O. V., et al. (2023). Electric Discharge Synthesis of Colloidal Silver Nanoparticle Solutions Using Various Modifiers for Immobilization on the Surface of Track-Etched Membranes. *Inorganic Materials*, 59(3), 337–347. <https://doi.org/10.1134/s0020168523030056>
- 4 Zarubin, M., Andreev, E., Kravchenko, E., et al. (2024). Developing tardigrade-inspired material: Track membranes functionalized with Dsup protein for cell-free DNA isolation. *Biotechnology Progress*. <https://doi.org/10.1002/btpr.3478>
- 5 Yamauchi, Y., Blonskaya, I. V., Apel, P. Y. (2017). Adsorption of nonionic surfactant on porous and nonporous poly(ethylene terephthalate) films. *Colloid Journal*, 79(5), 707–714. <https://doi.org/10.1134/S1061933X17050167>
- 6 Rossouw, A., Vinogradov, I. I., Serpionov, G. V., Gorberg, B. L., Molokanova L. G., Nechaev A. N. (2022). Composite Track Membrane Produced by Roll Technology of Magnetron Sputtering of Titanium Nanolayer. *Bulletin of the Russian Academy of Sciences: Physics*, 86(3), 251–255. <https://doi.org/10.1134/S2517751622030039>
- 7 Ponomareva O.Y., Drozhzhin N.A., Vinogradov I.I., Vershinina T.N., Altyinov V.A., Zuba I., Nechaev A.N., Pawlukojć, A. (2024). Metal-organic framework based on nickel, L-tryptophan and 1,2-bis(4-pyridyl)ethylene, consolidated on a track-etched membrane. *Bulletin of the Russian Academy of Sciences: Physics*, 88(6), 543–547. <https://doi.org/10.31857/S0044457X24060132>
- 8 Pinaeva, U., Lairez, D., Oral, O., et al. (2019). Early warning sensors for monitoring mercury in water. *Journal of Hazardous Materials*, 375, 120–128. <https://doi.org/10.1016/j.jhazmat.2019.05.023>
- 9 Pinaeva, U., Dietz, T.C., Sheikhy M. Al. (2019). Bis[2-(methacryloyloxy)ethyl]phosphate radiografted into track-etched PVDF for uranium (VI) determination by means of cathodic stripping voltammetry. *Reactive and Functional Polymers*, 140, 104–112. <https://doi.org/10.1016/j.reactfunctpolym.2019.06.006>
- 10 Zhumanazar, N., Korolkov, I.V., Yeszhanov, A. B. (2022). Enhancement of electrochemical detection of Pb<sup>2+</sup> by sensor based on track-etched membranes modified with interpolyelectrolyte complexes. *Sensors and Actuators B: Chemical*, 353, 114094. <https://doi.org/10.1016/j.sna.2022.114094>
- 11 Zhumanazar, N., Korolkov, I.V., Yeszhanov, A. B. (2023). Electrochemical sensors based on modified track-etched membrane for non-enzymatic glucose determination. *Microchemical Journal*, 188, 109003. <https://doi.org/10.1016/j.microc.2023.109003>
- 12 Kaya, D., Keçeci, K. (2020). Track-Etched Nanoporous Polymer Membranes as Sensors: A Review. *Journal of The Electrochemical Society*, 167(11), 070525. <https://doi.org/10.1149/1945-7111/ab67a7>
- 13 Lin, X., Huang, X., Urmann, K., Xie, X., Hoffmann, M.R. (2019). Digital Loop-Mediated Isothermal Amplification on a Commercial Membrane. *ACS Sensors*, 4(1), 242–249. <https://doi.org/10.1021/acssensors.8b01419>
- 14 Taurozzi, J.S., Tarabara, V.V. (2006). Support as Flow-Through Optical Sensors for Water Quality Control. *Environmental Engineering Science*, 24(1), 122–131. <https://doi.org/10.1089/ees.2007.24.122>
- 15 Gao, T., Yachi, T., Shi, X., Sato, R., Sato, C., Yonamine, Y., Kanie, K., Misawa, H., Ijro, K., Mitomo, H. (2024). Ultrasensitive surface-enhanced Raman scattering platform for protein detection via active delivery to nanogaps as a hotspot. *ACS Nano*, 18(32), 21593–21606. <https://doi.org/10.1021/acsnano.9b04224>
- 16 Pilot, R., Signorini, R., Durante, C., Orian, L., Bhamidipati, M., & Fabris, L. (2019). A Review on Surface-Enhanced Raman Scattering. *Biosensors*, 9(2), 57. <https://doi.org/10.3390/bios9020057>
- 17 Aroca, R. F., Alvarez-Puebla, R. A., Pieczonka, N., et al. (2005). Surface-enhanced Raman scattering on colloidal nanostructures. *Advances in Colloid and Interface Science*, 116, 45. <https://doi.org/10.1016/j.cis.2005.04.007>
- 18 Mahanty, S., Majumder, S., Paul, R., Boroujerdi, R., Valsami-Jones, E., Laforsch, C. (2024). A review on nanomaterial-based SERS substrates for sustainable agriculture. *Science of The Total Environment*, 884, 174252. <https://doi.org/10.1016/j.scitotenv.2024.174252>
- 19 Peng, J., Song, Y., Lin, Y., Huang, Z. (2024). Introduction and Development of Surface-Enhanced Raman Scattering (SERS) Substrates: A Review. *Nanomaterials*, 14(20), 1648. <https://doi.org/10.3390/nano14201648>

- 20 Huang, Y., Yuan, B., Wang, X., Dai, Y., Wang, D., Gong, Z., Chen, J., Shen, L., Fan, M., Li, Z. (2023). Industrial wastewater source tracing: The initiative of SERS spectral signature aided by a one-dimensional convolutional neural network. *Water Research*, 232, 119662. <https://doi.org/10.1016/j.watres.2023.119662>
- 21 Parnsubsakul, A., Ngoensawat, U., Wutikhun, T., Sukmanee, T., Sapcharoenkun, C., Pienpinijtham, P., & Ekgasit, S. (2020). Silver nanoparticle/bacterial nanocellulose paper composites for paste-and-read SERS detection of pesticides on fruit surfaces. *Carbohydrate Polymers*, 235, 115956. <https://doi.org/10.1016/j.carbpol.2020.115956>
- 22 Zhang, L., Zhang, P., Fang, Y. (2007). An investigation of the surface-enhanced Raman scattering effect from new substrates of several kinds of nanowire arrays. *Journal of Colloid and Interface Science*, 311(2), 502–506. <https://doi.org/10.1016/j.jcis.2007.03.024>
- 23 Ma, J., Zhao, J., Liu, X., Gu, C., Zeng, S., Birowosuto, M. D., Jiang, J., Jiang, T., Wu, K. (2024). Ultrasensitive SERS-based detection of prostate cancer exosome using Cu<sub>2</sub>O–CuO@Ag composite nanowires. *Biosensors and Bioelectronics*, 243, 115775. <https://doi.org/10.1016/j.bios.2023.115775>
- 24 Mahanty, S., Majumder, S., Paul, R., et al. (2024). A review on nanomaterial-based SERS substrates for sustainable agriculture. *Science of The Total Environment*, 950, 174252. <https://doi.org/10.1016/j.scitotenv.2024.174252>
- 25 Zhdanov, G., Nyhrikova, E., Meshcheryakova, N. et al. (2022). A Combination of Membrane Filtration and Raman-Active DNA Ligand Greatly Enhances Sensitivity of SERS-Based Aptasensors for Influenza A Virus. *Frontiers in Chemistry*, 10, 937180. <https://doi.org/10.3389/fchem.2022.937180>
- 26 Wigginton, K. R., & Vikesland, P. J. (2010). Gold-coated polycarbonate membrane filter for pathogen concentration and SERS-based detection. *Analyst*, 135(4), 1320–1326. <https://doi.org/10.1039/B919270K>
- 27 Qi, X., Wang, X., Dong, Y., Xie, J., Gui, X., Bai, J., Duan, J., Liu, J., Yao, H. (2022). Fast synthesis of gold nanostar SERS substrates based on ion-track etched membrane by one-step redox reaction. *Sensors and Actuators B: Chemical*, 364, 120955. <https://doi.org/10.1016/j.saa.2022.120955>
- 28 Zhang, R., Zhang, L., Xie, S., Yang, X., Liu, Y., Wang, M., He, Y. (2025). A simple and rapid preparation of Au-Ag alloy nanourchins flexible membrane for ultrasensitive SERS detection of microplastics in water environment. *Sensors and Actuators B: Chemical*, 373, 126451. <https://doi.org/10.1016/j.saa.2025.126451>
- 29 Fadeikina, I. N., Andreev, E. V., Yurenkov, D. I., et al. (2024). Synthesis of silver nanoparticles for the production of hybrid track-etched membranes and their further use as sensory materials. *Russian Journal of Applied Chemistry*, 97(3), 244–250. <https://doi.org/10.31857/S0044461824030071>
- 30 Mashentseva, A.A., Sutekin, D.S., Rakishcheva, S.R., Barsbay, M. (2025). Composite Track-Etched Membranes: *Synthesis and Multifaced Applications*. <https://doi.org/10.3390/polym16182616>
- 31 Kovalets, N. P., Kozhina, E. P., Razumovskaya, I. V., Bedin, S. A., Piryazev, A. A., Grigoriev, Yu. V., Naumov, A. V. (2022). Toward single-molecule surface-enhanced Raman scattering with novel type of metasurfaces synthesized by crack-stretching of metallized track-etched membranes. *The Journal of Chemical Physics*, 156(3). <https://doi.org/10.1063/5.0078451>
- 32 Lyu, S., Zhang, Y., Du, G., Di, C., Yao, H., Fan, Y., Duan, J., Lei, D. (2023). Double-sided plasmonic metasurface for simultaneous biomolecular separation and SERS detection. *Spectrochimica Acta Part A: Molecular and Biomolecular Spectroscopy*, 285, 121801. <https://doi.org/10.1016/j.saa.2022.121801>
- 33 Rodrigues, D. C., Andrade, G. F. S., Temperini, M. L. A. (2013). SERS performance of gold nanotubes obtained by sputtering onto polycarbonate track-etched membranes. *Physical Chemistry Chemical Physics*, 15(4), 1169–1176. <https://doi.org/10.1039/C2CP42994A>
- 34 Ritchie, G., Burstein, E., Stephens, R.B. (1985). Optical phenomena at a silver surface with submicroscopic bumps. *Journal of the Optical Society of America B*, 2(4), 544–551.
- 35 Kozhina, E. P., Bedin, S. A., Nechaeva, N. L., Podoynitsyn, S. N., Tarakanov, V. P., Andreev, S. N., Grigoriev, Y. V., Naumov, A. V. (2021). Ag-Nanowire bundles with gap hot spots synthesized in track-etched membranes as effective SERS substrates. *Applied Sciences*, 11(4), 1375. <https://doi.org/10.3390/app11041375>
- 36 Kukushkin, V., Kristavchuk, O., Andreev, E., et al. (2023). Aptamer-coated track-etched membranes with a nanostructured silver layer for single virus detection in biological fluids. *Frontiers in Bioengineering and Biotechnology*, 10, 1076749. <https://doi.org/10.3389/fbioe.2022.1076749>
- 37 Fadeikina, I. N., Andreev, E. V., Kristavchuk, O. V., et al. (2023). Electric discharge synthesis of colloidal silver nanoparticle solutions using various modifiers for immobilization on the surface of track-etched membranes. *Inorganic Materials*, 59(3), 337–347. <https://doi.org/10.1134/s0020168523030056>
- 38 Gudmundsson, J. T. (2020). Physics and technology of magnetron sputtering discharges. *Plasma Sources Science and Technology*, 29(11), 113001. <https://doi.org/10.1088/1361-6595/abb7bd>
- 39 Glushko, S. P. (2020). Selection of technologies for metal film application using physical deposition techniques. *Advanced Engineering Research*, 20(3), 280–288. <https://doi.org/10.23947/2687-1653-2020-20-3-280-288>
- 40 Serebrennikova, S. I., Kukushkin, V. I., Morozova, E. N., Astrakhantseva, A. S., Kristavchuk, O. V., & Nechaev, A. N. (2022). Formation of island SERS films on surfaces of track membranes and silicon substrates. *Bulletin of the Russian Academy of Sciences: Physics*, 86(4), 423–433. <https://doi.org/10.3103/S1062873822040207>
- 41 Fazylov, S. D., Nurkenov, O. A., Nurmaganbetov, Z. S., et al. (2025). Synthesis of  $\beta$ -cyclodextrin-functionalized silver nanoparticles and their application for loading cytosine and its phosphorus derivative. *Molecules*, 30(6), 1337. <https://doi.org/10.3390/molecules30061337>

- 42 Yang, L., Chen, Y., Li, H., Luo, L., Zhao, Y., Zhanga, H., Tian, Y. (2015). Application of silver nanoparticles decorated with  $\beta$ -cyclodextrin in determination of 6-mercaptopurine by surface-enhanced Raman spectroscopy. *Anal. Methods*, 7, 6520–6527. <https://doi.org/10.1039/C5AY01212K>
- 43 Zhu, J., Wu, N., Zhang, F., et al. (2018). SERS detection of 4-Aminobenzenethiol based on triangular Au-AuAg hierarchical-multishell nanostructure. *Spectrochimica Acta Part A: Molecular and Biomolecular Spectroscopy*, 204, 754–762. <https://doi.org/10.1016/j.saa.2018.06.105>
- 44 Ratkajec, A., Kendel, A. (2024). Structural characterization of 4-aminothiophenol in silver and gold colloids using surface-enhanced Raman scattering. *Croatica Chemica Acta*, 97(20), 77–85. <https://doi.org/10.5562/cca4107>
- 45 Sakir, M., Pekdemir S., Karatay A. et al (2017). Fabrication of plasmonically active substrates using engineered silver nanostructures for SERS applications. *ACS Appl. Mater. Interfaces*, 9(45), 39795–39803. <https://doi.org/10.1021/acsami.7b12279>
- 46 He, L., Riassetto, D., Bouvier, P., Rapenne, L., Chaix-Pluchery, O., Stambouli, V., Langlet, M. (2014). Controlled growth of silver nanoparticles through a chemically assisted photocatalytic reduction process for SERS substrate applications. *Journal of Photochemistry and Photobiology A: Chemistry*, 277, 1–11. <https://doi.org/10.1016/j.jphotochem.2013.12.003>